RETINAL DISEASE DIAGNOSIS THROUGH COMPUTER AIDED FUNDUS IMAGE ANALYSIS

A Thesis

Submitted in the fulfilment of the requirement for the award of the degree of

DOCTOR OF PHILOSOPHY

in

ELECTRICAL AND INSTRUMENTATION ENGINEERING

Submitted by

Jaskirat Kaur

(Registration No.: 951204005)

Under the supervision of

Dr. Deepti Mittal

Associate Professor, EIED, TIET

Electrical and Instrumentation Engineering Department
Thapar Institute of Engineering & Technology,
Patiala -147004, Punjab, India

March 2019

CERTIFICATE

I, **Jaskirat Kaur** hereby certify that the work presented in this thesis report entitled "**Retinal Disease Diagnosis Through Computer Aided Fundus Image Analysis**" in fulfilment of the requirements for the award of the degree of **Doctor of Philosophy** and submitted in Electrical and Instrumentation Engineering Department of Thapar Institute of Engineering & Technology, Patiala, is an authentic record of my own research work carried out during a period from January 2013 to June 2018 under the supervision of **Dr. Deepti Mittal,** Associate Professor, Electrical and Instrumentation Engineering Department of Thapar Institute of Engineering & Technology, Patiala.

The matter presented in this thesis has not been submitted by me for the award of any other degree of this or any other Institute.

Jaskirat Kaur

(JASKIRAT KAUR)

Registration No. 951204005

This is to certify that the above statement made by the candidate is correct to the best of my knowledge and belief.

(Dr. Deepti Mittal)

Associate Professor

Electrical and Instrumentation Engineering Department

Thapar Institute of Engineering and Technology (Deemed to be University)

Patiala, Punjab, India

Acknowledgements

I would like to express my sincere gratitude to my supervisor Dr. Deepti Mittal, Associate Professor, Department of Electrical and Instrumentation Engineering, Thapar Institute of Engineering & Technology, Patiala, for introducing the present topic and for her inspiring guidance, constructive criticism, essential support, valuable suggestions and constant encouragement during the entire research work. Her dynamism and foresightedness helped me in a big way in completion of this work. I really feel privileged to have worked under her supervision.

I express my sincere thanks to the members of my doctoral research committee Dr. Amit Kumar Kohli, Associate Professor, Department of Electronics and Communication Engineering, Thapar Institute of Engineering & Technology; Dr. Gagandeep Kaur, Associate Professor, Department of Electrical and Instrumentation Engineering, Thapar Institute of Engineering & Technology; and Dr. Jainy Sachdeva, Assistant Professor, Department of Electrical and Instrumentation Engineering, Thapar Institute of Engineering & Technology for providing necessary facilities and valuable suggestions throughout this research work and in the submission of this manuscript.

I am very thankful to Dr. R.S. Kaler, Senior Professor and Head, Department of Electrical and Instrumentation Engineering, Thapar Institute of Engineering & Technology and Dr. Sanjay Jain, Associate Professor and PhD Coordinator, Department of Electrical and Instrumentation Engineering, Thapar Institute of Engineering & Technology for their constructive discussions and valuable suggestions during the meetings of my research committee. I am also thankful to all other faculty members of the Department of Electrical and Instrumentation Engineering for their support.

I extend my warm thanks to all teaching and non-teaching staff, Department of Electrical and Instrumentation Engineering, Thapar Institute of Engineering & Technology for their day-to-day co-operation.

I would like to thank Dr. Gurmeet Mangat, Medical Superintendent and Dr. Amanpreet Kaur, from the Department of Ophthalmology, Sri Guru Harkrishan Sahib Eye hospital, Mohali for granting ethical clearance to the research proposal and for their clinical advice. I am also thankful to the clinicians of the department to provide all the necessary help in collecting and providing retinal fundus images data on diabetic retinopathy.

I am indebted to my beloved parents for all their support during the PhD work. They are my pillars and without their support this work was not possible to conclude. I express my deepest appreciation for my sister Sukhpreet, brother Gauravdeep and niece Anahat whose blessings and wishes helped me to reach this end.

Finally, I owe deeply to my husband Ashu for his unwavering patience, understanding, and encouragement, as the present work is finally concluded because of his support for which I shall ever remain indebted.

Jaskirat kaur

(JASKIRAT KAUR)

Abstract

Diabetic retinopathy, an asymptomatic complication of diabetes, is one of the leading causes of blindness in the world. The early detection and diagnosis can reduce the occurrence of severe vision loss due to diabetic retinopathy. Therefore, the present research work was conducted to diagnose symptomless clinical stages of diabetic retinopathy, i.e., non-proliferative diabetic retinopathy and progressive diabetic retinopathy. The diagnostic confirmation of diabetic retinopathy depends on the reliable detection and classification of bright lesions namely: exudates and cotton wool spots, and dark lesions namely: microaneurysms and hemorrhages present in retinal fundus images. However, variability within the retinal images makes difficult to distinguish dark and bright lesions in the presence of anatomical structures (landmarks) like blood vessels and optic disk. Therefore, it is necessary to eliminate any spurious, unwanted and false regions due to anatomical structures before the segmentation of retinal lesions. In addition, to design an efficient computer-aided diagnostic method a benchmark composite database, having varying attributes such as position, dimensions, shapes and color is required. Keeping all these facts in mind, a composite database has been designed in this work to provide an efficient and generalized computer-aided solution for the diagnosis of diabetic retinopathy

In this research work, a composite database formed, includes 5048 retinal fundus images from two diverse sources: one is clinical source including 2942 images and other is six online available benchmark sources including overall 2106 images. The clinical database was developed by acquiring database of 2942 retinal images with varying color, brightness and quality from 482 different patients: 280 men (mean age: 51 years) and 202 women (mean age: 44 years) with an age range of 25 to 83 years over the period of January 2014 to July 2017. Image database comprises of 99 healthy and 2843 pathological retinal images with varying grades of diabetic retinopathy. Pathological retinal images comprise of 1351 images with hard exudates, 446 images with cotton wool spots, 1165 images with micro aneurysms and 1588 images with hemorrhages. The open-source benchmark databases of retinal images used in the present work are DRIVE, STARE, e-

OPHTHA, MESSIDOR, DIARETDB and HEI-MED. These databases have different goals, characteristics and levels of completeness. Therefore, a framework for the development of benchmark composite retinal fundus image database is also designed.

Artifacts and blur are the prime factors which degrade the contrast resolution and obstruct the meaningful information present in retinal fundus image. Their presence severely hampers the interpretation and analysis of retinal fundus images. Therefore, retinal fundus image enhancement is designed in the present work with the intention to improve the visualization of details available in retinal fundus images in order to provide accurate detection of anatomical structures and retinal lesions. This is accomplished by retaining high frequency components and enhancing the local contrast in retinal fundus images. Two-directional high pass filter is applied to retain high frequencies and then adaptive scaling factor is used for contrast enhancement. Scaling factor is adaptive in the sense that it chooses two different scaling values depending on local variations in image intensities. A threshold value is optimized to make a choice in between two scaling values by analyzing the extent of range of intensity variations in each retinal image database. The enhancement of the images was approved and confirmed by the visual interpretations of expert ophthalmologists.

The precise segmentation of blood vessels, in order to avoid spurious responses, is the first step in extracting diagnostic information for the early detection of diabetic retinopathy. Therefore, in the present work a generalized method to detect and segment blood vasculature using retinal fundus images has been designed with four phases namely, (i) initial segmentation of vasculature map to find vessel and non-vessel structures, (iii) extraction of relevant set of geometrical based features from the vasculature map and intensity based features from original retinal fundus image that differentiate vessel and non-vessel structures efficiently, (iv) supervised classification of vessel and non-vessel structures using the extracted features, and (v) joining of candidate vessel structures to create connectivity. Results of subjective evaluation are supported by the objective medically significant statistical measures. The performance of the proposed method has been

validated on composite database of 5048 images. The experimental results indicate the high performance of the proposed method with the overall average sensitivity of 84.82% revealing its ability to perform significantly in distinguishing true vessel structures from non-vessel structures. The segmentation results by the proposed method also show a high correlation with the ground truth with an accuracy of 97.58%. Furthermore, the method proves its capability on varying grades of retinal fundus images with the sensitivity of 85.13%, 85.73% and 82.41% on mild, moderate and severe diabetic retinopathy respectively. Finally, it can be emphasized that the promising results indicate the generalization ability of the blood vessels segmentation method to aid ophthalmologists in precise detection of retinal lesions for timely treatment of retinal abnormalities.

After the retinal blood vessels are segmented, they are used to segment another anatomical structure i.e. optic disk. In this work, optic disk is segmented in two-steps, viz., (i) localization using blood vessels convergence-based approach and (ii) boundary estimation using canny edge detector and iterative circular Hough transform. After the blood vessels and optic disk are segmented, they are eliminated from the original retinal fundus image. In order to eliminate blood vessels from original retinal fundus image, an adaptive blood vessels normalization method is designed in this work. Subsequently, the optic disk is also eliminated from normalized blood vessels image using morphological filling operation.

The exudates, abnormal leaked fatty deposits on retina, are one of the most prevalent clinical signs of progressive diabetic retinopathy. Therefore, computer-aided detection of progressive diabetic retinopathy requires the quantitative assessment of exudates in retinal fundus images. Additionally, during mass screening of diabetic retinopathy, it is vital to differentiate retinal images purely based on the presence or absence of exudates. Therefore, proper detection and then segmentation of exudates is important for decision making during treatment. In this work, a generalized exudates segmentation method is designed by introducing an adaptive image quantization that reduces the number of distinct colours in an image by grouping the image pixels

with similar attributes. The proposed method is adaptive in the sense that it adapts itself to the variations in intensity ranges of retinal fundus images in the composite database. In the next step, dynamic decision thresholding method is designed to discriminate pixels corresponding to true exudates from other regions of retinal image. Three parameters were optimized in the designing of decision threshold method by conducting a series of experiments with the help of expert ophthalmologist in order to achieve best combination of sensitivity/specificity. The main contribution of the proposed method is that it reliably segments exudates irrespective of associated heterogeneity, bright and faint edges. The detection capability of the proposed method is assessed using two evaluation criteria: (i) image-based evaluation and (ii) lesion-based evaluation. Image based evaluation criterion evaluates the performance of the method in discriminating images with or without exudates. Whereas, lesion-based evaluation compares the segmentation results pixel by pixel with the reference ground truths. Experimental results for lesion-based evaluation show that the proposed method outperforms other existing methods with a mean sensitivity/specificity/accuracy of 87.95/96.45/92.64 on a composite database of 5048 retinal fundus images. The segmentation results for image-based evaluation with a mean sensitivity/specificity/accuracy of 93.25/97.64/97.48 respectively prove the clinical effectiveness of the method during screening.

Experienced ophthalmologists diagnose and then grade non-proliferative diabetic retinopathy by visualizing various shape, intensity and texture-based features of retinal lesions present in retinal fundus images. Therefore, in this work, an extensive feature set is formulated based on different descriptors such as shape, size, intensity, texture of both dark and bright lesion to design an efficient computer-aided severity level detection of non-proliferative diabetic retinopathy. A set of 54 features were extracted using three methods namely: (i) geometrical features based on shape, size and contour of the retinal lesions, (ii) textural features namely: first order statistical (FOS) texture-based features, grey level run length matrix (GLRLM) texture-based features, and grey level co-occurrence matrix (GLCM) texture-based features, and (iii) RGB and

HSI model-based colour features. Furthermore, in order to achieve high classification accuracy, the proposed method is designed using a two-step neural network classifier. The main contribution of the proposed method is that it reliably judges the severity level by segmenting dark and bright lesions present in retinal fundus images regardless of types of lesions, blurred and well-contrasted lesions. The experimental results on a composite database of 5048 retinal images for lesion-based evaluation reveals high performance of the proposed method in the segmentation of dark and bright lesions with sensitivity/specificity/accuracy of 94.80/99.80/98.43 and 95.80/98.80/95.43 respectively on clinically acquired database retinal images. The image-based evaluation outcomes show the high precision in precise recognition of clinically acquired pathological images from healthy retinal images with average sensitivity/specificity/accuracy of 98.8/100/100 and 100/100/100 for dark and bright lesions respectively. The overall grading accuracy of 96.33% reveals the capability of the proposed framework in the efficient grading of severity level of non-proliferative diabetic retinopathy based on the detection of dark and bright lesions which are subtle and tough to distinguish. Furthermore, it can be emphasized that the proposed severity level detection method will aid ophthalmologists for appropriate treatment and effective preparation in the diagnosis of various stages of non-proliferative diabetic retinopathy.

Finally, it can be concluded that the present research work comprises of (i) retinal image enhancement, (ii) segmentation and elimination of anatomical structures, (iii) detection of progressive diabetic retinopathy and, (iv) detection and classification of non-proliferative diabetic retinopathy. The substantial combined performance of different experiments on clinical and open-source benchmark databases proves the generalization ability and the strong candidature of the proposed computer-aided methods in real-time diagnosis of progressive and non-proliferative diabetic retinopathy.

Contents

List of Abbreviations

MA	micro aneurysms
HEM	hemorrhages
EXU	exudates
CWS	cotton wool spots
NPDR	non-proliferative diabetic retinopathy
FFA	fundus fluorescein angiography
OCT	optical coherence tomography
2-D	two-dimensional
3-D	three-dimensional
FOV	field of view
NN	neural Network
SN	sensitivity
SP	specificity
Acc	accuracy
TPR	true positive rate
FPR	false positive rate
PPV	positive predictive value
SVM	support vector machine
AUC	area under the curve
ROC	receiver operating characteristics
RGB	red green blue
HSI	hue saturation intensity
$\mathbf{d_{FOV}}$	ratio of FOV widths
$\mathbf{I(x,y)}$	original retinal fundus image
$\mathbf{I_{fil\_H}(x,y)}$	high pass filtered image in horizontal direction
$\mathbf{I_{fil\_V}(x,y)}$	high pass filtered image in vertical direction
$\mathbf{I_F(x,y)}$	laplacian filtered image
$\boldsymbol{\sigma}\mathbf{(x,y)}$	scaling factor
$\mathbf{Var_N(x,y)}$	neighborhood variance parameter

$\bar{\mathbf{I}}_{\mathbf{N}}(\mathbf{x},\mathbf{y})$	average luminance level
$\mathbf{T}_{\mathbf{E\_Var}}$	threshold value for neighborhood variance parameter
$\mathbf{I}_{\mathbf{L\_G}}(\mathbf{x},\mathbf{y})$	local and global enhanced image
$\mathbf{I}_{\mathbf{E}}(\mathbf{x},\mathbf{y})$	final enhanced image
VM	vasculature map
MF	matched filter
MF-FDOG	matched filter and its first derivative of Gaussian
$\mathbf{D}_{\mathbf{m}}$	local mean of neighborhood elements
VM_F	vasculature map obtained after supervised classification
$\mathbf{I}_{\mathbf{BV}}$	final segmentation of blood vessels
$\mathbf{T}_{\mathbf{E\_Var}}$	threshold value of neighborhood variance parameter
$\mathbf{N}(\mathbf{x},\mathbf{y})$	normalization factor
$\mathbf{N}_{\mathbf{BV\_img}}$	normalized blood vasculature image
$\mathbf{Sub\_Num}_{\mathbf{pix}}(\mathbf{x},\mathbf{y})$	sub image around the pixel P(x,y)
$\mathbf{I}_{\mathbf{BV\_SKT}}$	vasculature skeleton image
$\mathbf{I}_{\mathbf{Les\_img}}$	lesion image
$\mathbf{I}_{\mathbf{Q\_Les\_img}}$	quantized lesion image
$\mathbf{N}_{\mathbf{Q\_Les\_img}}$	normalized and quantized lesion image
$\mathbf{T}_{\mathbf{Exu\_ref}}$	reference threshold value
$\mathbf{T}_{\mathbf{Exu\_dec}}$	decision threshold parameter
$\mathbf{I}_{\mathbf{Reg}_{\mathbf{seg}}}$	segmented region image
$\boldsymbol{\beta}$, k	number of clusters
FOS	first order statistics
GLRLM	gray level run length matrix
GLCM	gray level co-occurrence matrix
ETDRS	Early treatment diabetic retinopathy study
$\boldsymbol{\Psi}$	Lesion combination operation

List of Figures

List of Tables

Chapter 1

Introduction

1.1 PREFACE

Retinal abnormalities comprise an important public health issue having high occurrence in developing countries. Retinal abnormalities are broadly classified as systemic and non-systemic. Systemic retinal abnormalities spread in entire body and affect multiple organs in the body; whereas non-systemic retinal abnormalities are ocular manifestations that originate and reside in retina. This research work is focused on systemic retinal abnormality related to diabetes. Among a variety of retinal abnormalities, diabetes is one of the severe retinal abnormalities. Diabetes has several adverse effects on numerous parts of body such as eyes, nervous system, heart, kidneys and other organs, but the most likely first to be affected is the retina, hence the patient's sight. In addition, prolonged diabetes is the foremost cause of irreversible vision loss, accounting for almost 15% of all blindness cases [1]. Diabetic retinopathy, a retinal abnormality of diabetes mellitus, is the leading cause of vision impairment worldwide. According to International Diabetes Federation, the increase in prevalence of diabetes affects 451 million people globally and is estimated to affect vision of about 693 million people by 2045 [2]. Rapidly rising rate of obesity, sedentary lifestyles, lack of physical activity are prime contributing factors of an increased prevalence of diabetes. A survey conducted by International Diabetes Federation estimated that around 49.7% diabetic cases worldwide were undiagnosed and left untreated leading to complications such as blindness, kidney failure, heart disease, stroke etc. [3]. Globally diabetes is the seventh leading cause of death in the year 2016. India tops the list of countries with the highest number of diabetics in 2017 and represented 49 percent of the world's diabetes burden with an estimated 72 million cases, a figure expected to almost double to 134 million by 2025 [4].

Diabetic retinopathy is a chronic abnormality which is characterized by the presence of single or multiple retinal lesions like micro aneurysms (MA), haemorrhages (HEM), exudates

(EXU) and cotton wool spots (CWS). Mainly diabetic retinopathy can be categorized as non-proliferative diabetic retinopathy (NPDR), progressive diabetic retinopathy and proliferative diabetic retinopathy. Non-proliferative diabetic retinopathy advances from mild stage to moderate and severe stages [5]. Mild non-proliferative diabetic retinopathy is characterized by the presence of even one micro aneurysms. Moderate non-proliferative diabetic retinopathy is identified by the collective presence of few haemorrhages, hard exudates and cotton wool spots, whereas these lesions are found in greater quantity in severe non-proliferative diabetic retinopathy. Additionally, the only sole appearance of exudates determines the presence of progressive diabetic retinopathy. Proliferative diabetic retinopathy, an advanced stage characterized by the growth of new blood vessels in distinct regions of retina, may lead to irreversible vision loss. Also, the treatment at this stage turn out to be less effective. Individuals affected with non-proliferative diabetic retinopathy and progressive diabetic retinopathy usually exhibits no characteristic symptoms and mostly does not affect vision until a proliferative stage of diabetic retinopathy is reached. In brief, vision impairment through diabetic retinopathy is stage-dependent and the vision is least affected when retinopathy is diagnosed at early stage. It is therefore significant to diagnose diabetic retinopathy at an initial symptomless clinical stage. One major challenge in the process of diagnosing diabetic retinopathy is to diagnose the severity level of diabetic retinopathy correctly. Therefore, the present research work is focused on the diagnosis of symptomless clinical stages of diabetic retinopathy, i.e., non-proliferative diabetic retinopathy and progressive diabetic retinopathy.

1.2 RETINAL IMAGING MODALITIES

Retinal imaging modalities such as retinal fundus imaging, fundus fluorescein angiography (FFA) and optical coherence tomography (OCT) are the commonly used diagnostic techniques by the expert ophthalmologists to detect non-proliferative diabetic retinopathy and progressive diabetic retinopathy cases. There is no perfect retinal imaging

modality for all ophthalmological applications and needs. In addition, each imaging modality is limited by its mechanism and type of image being produced. Medical imaging modalities that do not penetrate the skin physically are non-invasive. The non-invasive medical imaging modalities like retinal fundus imaging and OCT plays an important role in diagnosis and treatment of retinal abnormalities by identifying the type of retinal lesion, its size, shape and number. The challenges with imaging modalities in extraction of clinically significant information related to anatomical structures and lesions have received enormous attention. Fundus fluorescein angiography has been the gold standard to understand, confirm diagnosis and treat retinal abnormalities [6]. However, being an invasive procedure, it is quite difficult to be accepted by the patients because of associated side effects such as nausea and risk of various allergies [7]. Due to this reason non-invasive imaging techniques such as fundus imaging and optical coherence tomography are frequently used for retinal disease detection during mass screening and to gather information about the particular abnormality.

The diagnostic clarification related to retinal abnormalities is a frequent problem in clinical routine. For imaging the retina, most hospitals use fundus imaging, FFA, or OCT. Currently, there is no consensus concerning the optimal strategy for imaging retina. All modalities have its advantages and limitations. The choice of which modality to use is determined based on the expert ophthalmologist, the availability of the equipment, the condition of the patient, and the experience of the ophthalmologist. To ensure the best treatment of the patient, preferably all lesions, related to particular abnormality should be detected. Therefore, choosing the modality with the most benefits and least limitations is essential. With the brief introduction of FFA, OCT and fundus imaging modalities in the following paragraphs, some comparative statements are made to get the better understanding of the preferences among imaging modalities in order to detect non-proliferative and progressive diabetic retinopathy.

Fundus fluorescein angiography is a technique to image retina using a fundus camera by injecting a fluorescent dye. Sodium fluorescein dye is added into the systemic circulation following which the retina is illuminated with blue light at a wavelength of 490 nanometres. Final angiogram image is obtained by photographing the fluorescent green light that is emitted by the dye. Fundus fluorescein angiography produces a high contrast images of retina and is mainly used to analyse pathologies related to choroid and blood circulation that reside in retina. However, FFA being an invasive technique has a wide range of complications. The most common reactions are transient nausea, vomiting, pain and redness in eyes after the procedure.

Optical coherence tomography is a procedure that uses coherent light to capture two-dimensional (2-D) and three-dimensional (3-D) images from optical scattering media. It is based on the concept of interferometry to create a cross-sectional view of the retina. Due to the transparency of the eye (i.e. the retina can be viewed through the pupil), OCT has gained wide popularity as an ophthalmic diagnostic tool. Optical coherence tomography is useful in diagnosing retinal conditions related to macula. Lesions present in macula are easier to image using OCT than lesions in the mid and far periphery of retina. It is particularly helpful in diagnosing diabetic macular oedema, macular hole, age-related macular degeneration. Optical coherence tomography is non-invasive and easy to interpret, but OCT does not identify the changes in blood vessels. Therefore, this imaging modality is unable to document a disease with bleeding in the retina such as diabetic retinopathy.

Fundus imaging is a very popular and primarily used imaging modality. Almost all the ophthalmologists in the world has fundus cameras that provide high resolution colour fundus photographs. Fundus imaging is done by using digital fundus camera to capture image of the true retinal fundus. Fundus cameras are non-invasive, easy to use, widely available, cost effective and good at documenting the front view of retina where all the retinal lesions and anatomical structures are clearly visible. The images produced by fundus photography are the

2-D representation of 3-D semi-transparent retinal tissues. They capture 30^0 to 50^0 views of the retina.

In summary, FFA, OCT and fundus photography imaging modalities of retinal imaging have its own advantages and disadvantages. Fundus photography is an attractive medical imaging technique in general because of unique set of virtues including (i) low cost making it feasible for a patient from low socio-economic status, (ii) versatility and widespread availability making its clinical relevance high worldwide, (iii) initial imaging modality due to its relative simplicity in comparison to other imaging modalities, (iv) risk-free system making it the first preference among other imaging modalities for screening of retinal abnormalities, and (v) fast and portable making it convenient to use. In continuation, the fundus images are easy to study once the observer is trained. As a result, fundus imaging is an extremely useful means of diagnostic imaging and the most widely employed imaging method for screening purposes and detection of retinal lesions related to diabetic retinopathy. Therefore, retinal fundus images are utilized in the present work to design computer-aided methods to diagnose non-proliferative diabetic retinopathy and progressive diabetic retinopathy

1.3 FUNDUS IMAGING

Fundus imaging is a procedure in which a two-dimensional representation of the three-dimensional retinal semi-transparent tissues of the back of the eye i.e. fundus is projected onto the imaging plane. This projection is obtained on the screen of a fundus machine by the image intensities that represent the amount of reflected light from retina. Fundus photographs thus obtained documents the retina, the neurosensory tissue that translates the optical visuals/images in front of our eyes into electrical impulses for our brain to understand. Fundus photography, a highly useful means of diagnostic imaging, has a wide array of clinical applications. The basis of its operation, as shown in figure 1.1, is the projection of light into the eye through cornea followed by the reflection, processing, and display of image intensities reflected from

retinal structures within the eye [9]. Ophthalmologists use these retinal photographs to follow, diagnose, and treat retinal abnormalities such as diabetic retinopathy, age-related macular degeneration, hypertensive retinopathy etc. In order to construe a fundus image of the retina, it is essential to understand how a fundus imaging system works and how reflected light is converted into an image.

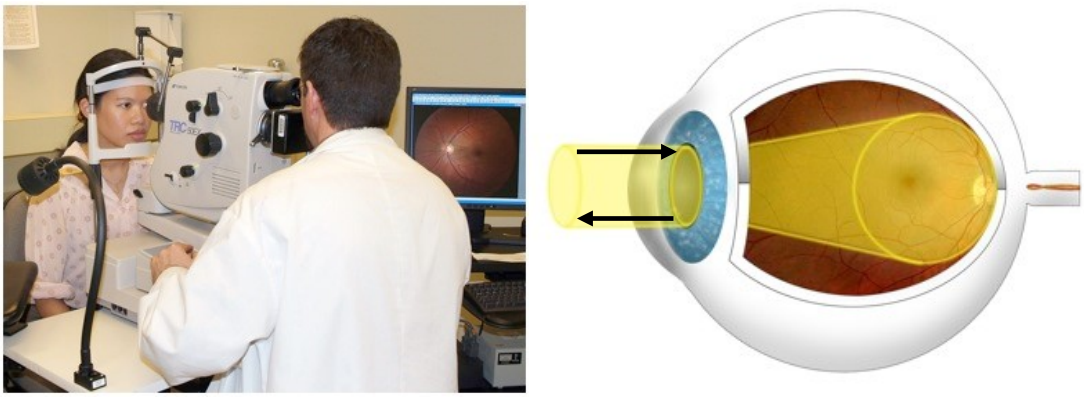

(a) **(b)**

Figure 1.1 (a) Retinal imaging with fundus camera, (b) Path of transmitted and reflected light from fundus camera

1.3.1 Fundus Image Formation

The fundus cameras comprise of an intricate microscope attached to a flash enabled camera. The design of the fundus camera is based on the working of an indirect ophthalmoscope. The observation light generated from either viewing lamp or the electronic flash is projected through a set of filters and onto a round mirror. This mirror reflects the light up into a series of lenses which focus the light. A mask on the uppermost lens shapes the light into a doughnut. The doughnut shaped light is reflected onto a round mirror with a central aperture to form a ring shape before exiting the camera through the objective lens, and proceeds into the eye through the cornea. The resulting retinal image formed from the reflected light exits the cornea through the central, un-illuminated hole of the doughnut formed by the illumination system. As the paths of the projection of light into the retina and reception of light from the retina are independent, there are minimal reflections of the light source captured in

the image. This image forming rays continue towards the low powered telescopic eye piece attached to the fundus machine. When the button is pressed to take a picture, a mirror interrupts the path of the illumination system and allows the light from the flash bulb to pass into the eye. Simultaneously, a mirror falls in front of the observation telescope, which redirects the light onto the capturing medium i.e. film or a digital CD. The produced image on the film is an upright, magnified view of the fundus described by an angle of view termed as field of view (FOV). Generally, an angle of 30^0 to 50^0 of retinal area (FOV) is used to create the retinal image 2.5 times larger than original. Wide angle fundus cameras capture images between 45^0 and 145^0 that provide comparatively low magnification of retinal area and minimizes the image to half of the original size. Whereas, narrow angle fundus cameras capture images at FOV of 20^0 or less providing five times magnification.

Fundus photography have three modes of examination:

(i) Colour fundus photography: In this mode, retina is illuminated by white light and examined in full colour. Generally, this mode is the primary mode to capture retinal fundus images during first round of diagnosis.

(ii) Red free fundus photography: The illuminating light is filtered to improve the contrast of retinal lesion structures with respect to the background. The filtering process removes red colours from the coloured retinal fundus images.

(iii) Stereo fundus photography: In this mode, image intensities represent the amount of reflected light from two or more different view angles, to create a 3-D image. The 3-D image generated by this process is used to obtain better surface characteristics than the above-mentioned photography modes.

1.4 EYE ANATOMY AND RETINAL DISEASES

The anatomical view of human eye is demonstrated in figure 1.2 [9]. The retina is a multi-layered sensory tissue that lines the back of the eye, senses light, and create electrical impulses.

These electrical impulses travel along the optic nerve to the brain which are subsequently converted into images through photoreceptors. Photoreceptors are composed of two types: rods and cones. Rods can sense changes in contrast even at low illumination but cannot sense any variation in colour. Whereas, cones are very sensitive to changes in colour. Rods and cones reside mainly in the macula, the region which is responsible for day vision. The central region of macula is termed as fovea, where the human eye is able to differentiate visual details with high precision. All these photoreceptors are connected to the brain via bundle of optic nerves. The circular region where the optic nerve leaves the eye is called as blind spot due to the absence of photoreceptors, also termed as optic disk. Retinal blood vessels having tree like structure supply nutrients to the retina. Blood vessels have lower reflectance as compared to other retinal structures, thus they appear darker with respect to the background of fundus images. The retinal measures approximately 72% of a sphere about 22mm in diameter, 0.56 mm thick near the optic disk, and thinnest at the centre of fovea in adult humans.

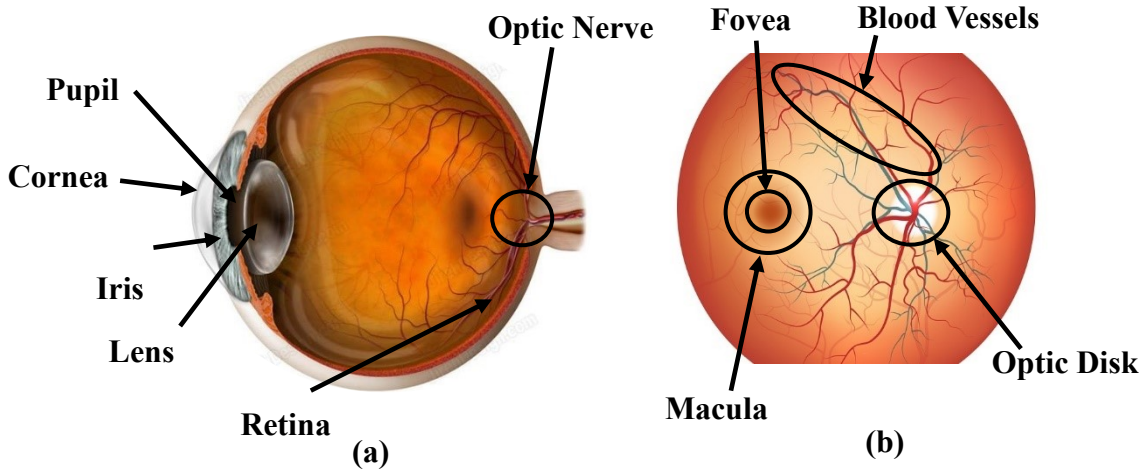

Figure 1.2 (a) Cross sectional view of right human eye (b) Photographic view of retina

The retinal image serves as window to assess many systemic abnormalities and brain related abnormalities. The structures that can be visualized on a retinal fundus image are optic disk, peripheral retina, blood vessels and retinal lesions if present. Visually extractable features on retinal fundus images to detect diabetic retinopathy are based on the presence of type, size,

shape and number of lesions. Thus, retinal fundus images are used to investigate and monitor the progression of abnormalities that affect the eye. Experienced ophthalmologists visualize these features in retinal fundus images to characterize various stages of diabetic retinopathy and normal retina.

1.4.1 Normal Retina

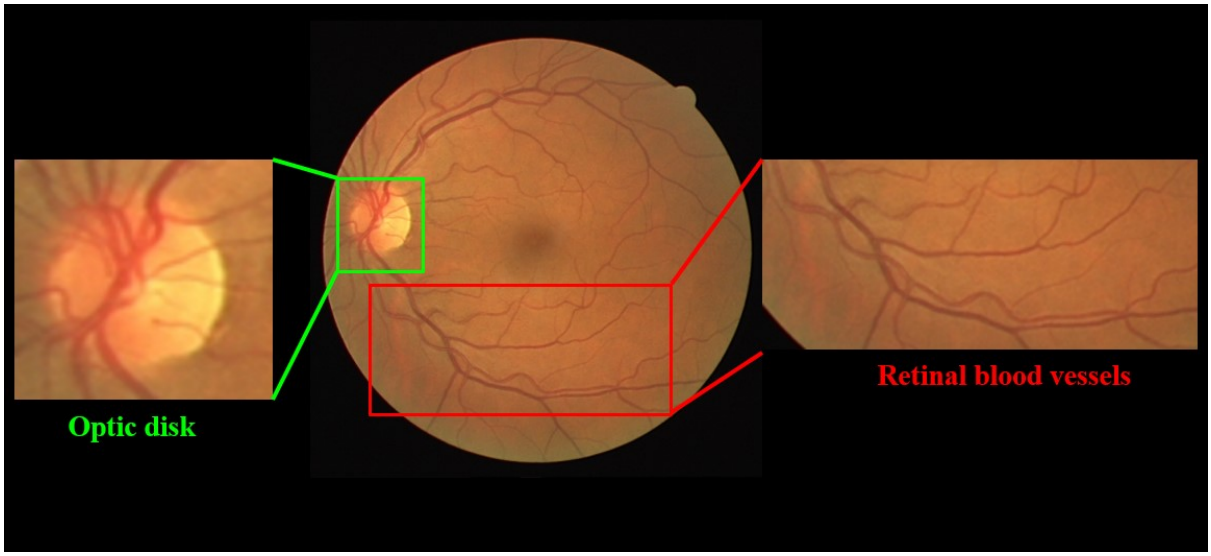

Figure 1.3 Appearance of normal retina on fundus image

On retinal fundus images, the appearance of normal retina is homogeneous and clear providing the clean view of the clinically acquired fundus as shown in figure 1.3 of the right eye. This image has no signs of any abnormality or pathology. There are no lesions, scars, or pigmentary changes in the retinal fundus. The normal retina has uniform appearance along with the presence of main distinguishing structures such as blood vessels, optic disk, macula and fovea. These main distinguishing structures are termed as landmarks or anatomical structures. Blood vessels network is the set of thin elongated structures of dark red colour. Blood vessels converge into the largest bright round area known as optic disk. The blood vessels in this fundus image are normal in course and calibre. Approximately, two and half disk diameters to the right of the optic disk, a dark circular region, the fovea, which is at the centre of the area is known

as macula. These retinal structures like optic disk and blood vessels, can provide valuable information about the health of the retina. This is the reason that it is important to analyse and detect changes in their morphology. Nevertheless, the main indicator of the presence of a particular retinal abnormality or diseases is the appearance of lesions.

1.4.2 Retinal Lesions Associated with Diabetic Retinopathy

Retinal lesions are recognized visually as alterations of the normal appearance of the retinal fundus image. Lesions appear with various attributes such as intensities, shape, colour, size etc. in retinal fundus images. They can be divided mainly into bright and dark (red) retinal lesions. Brief descriptions about these retinal lesions are given as below:

Dark Lesions:

Dark lesions are mainly categorized into micro aneurysms and haemorrhages.

Micro aneurysms:

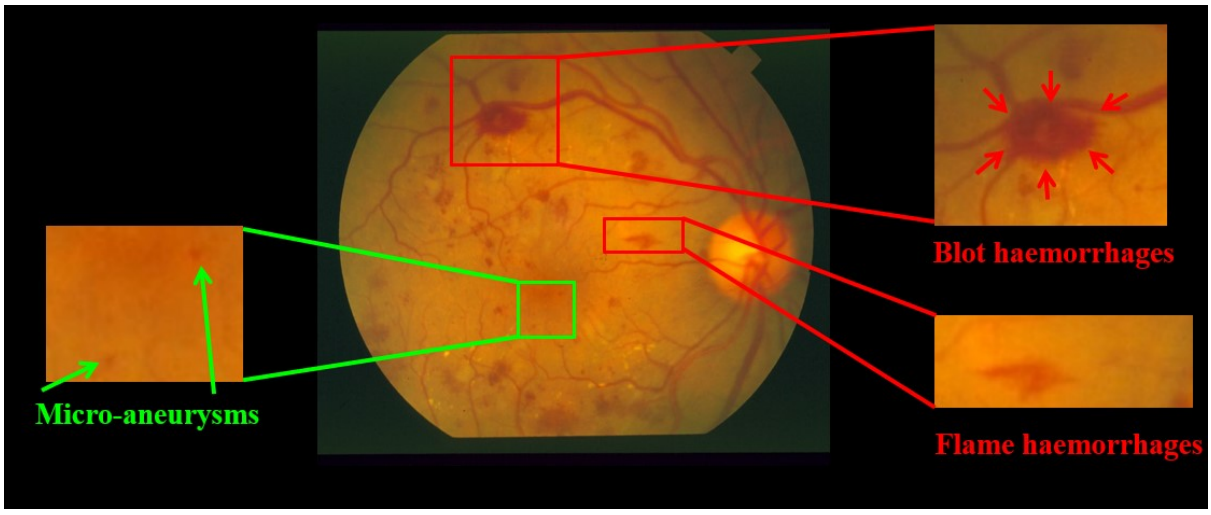

Figure 1.4 A fundus image having typical appearance of dark lesions

Microaneurysms are the first sign of diabetic retinopathy. They are dilated, aneurismal retinal vessels that appear as small red dots detached from blood vessels in coloured retinal fundus images as shown in clinically acquired figure 1.4. These lesions can leak fluid and blood into the retina, leading to vision threatening lesions such as exudates and haemorrhages. These

lesions are the smallest detectable retinal lesions and the local expansions of the weakened retinal capillaries. Microaneurysms are of variable size ranging from 10 to 100 micrometres. Any form of abnormality related to blood vessels or high blood pressure may contribute to a retinal microaneurysm, however the most common cause of it is diabetes mellitus. Microaneurysms alone are not likely to cause any external symptoms and does not require treatment. Most microaneurysms are reversible if preventive measures such as healthy lifestyle, management of diabetes etc. are taken timely.

Haemorrhages:

Retinal haemorrhages are formed due to bleeding of blood vessels in the retina. Haemorrhages can appear anywhere in retina with varying size and shapes. They are characterized by dark red colour and are of several types namely: “dot”, “blot” and “flame” haemorrhages. Dot haemorrhages are tiny red structures and are usually referred as micro aneurysms. Blot and flame haemorrhages correspond to leakage of blood in deeper layers of retina. They appear on fundus images as large and dark retinal lesions with irregular contours [8]. Figure 1.4 shows an example image highlighting different types of haemorrhages inside the marked bound regions of rectangular shape. A retinal haemorrhage can be caused by diabetes, hypertension or blockages in retinal vein. They are more serious retinal disease because they are associated with the onset of chronic diabetic retinopathy. Some of the common symptoms of haemorrhages are (i) visual disturbances producing unclear vision, (ii) presence of blind spots in vision, (ii) pain in the eye.

The detection and differentiation of microaneurysms and haemorrhages can be complex for the expert ophthalmologist as they are characterized by their poor contrast with the background. Also, these lesions have similar attributes in terms of colour and texture with anatomical structures like blood vessels.

Bright Lesions:

Bright lesions are mainly categorized as exudates and cotton wool spots.

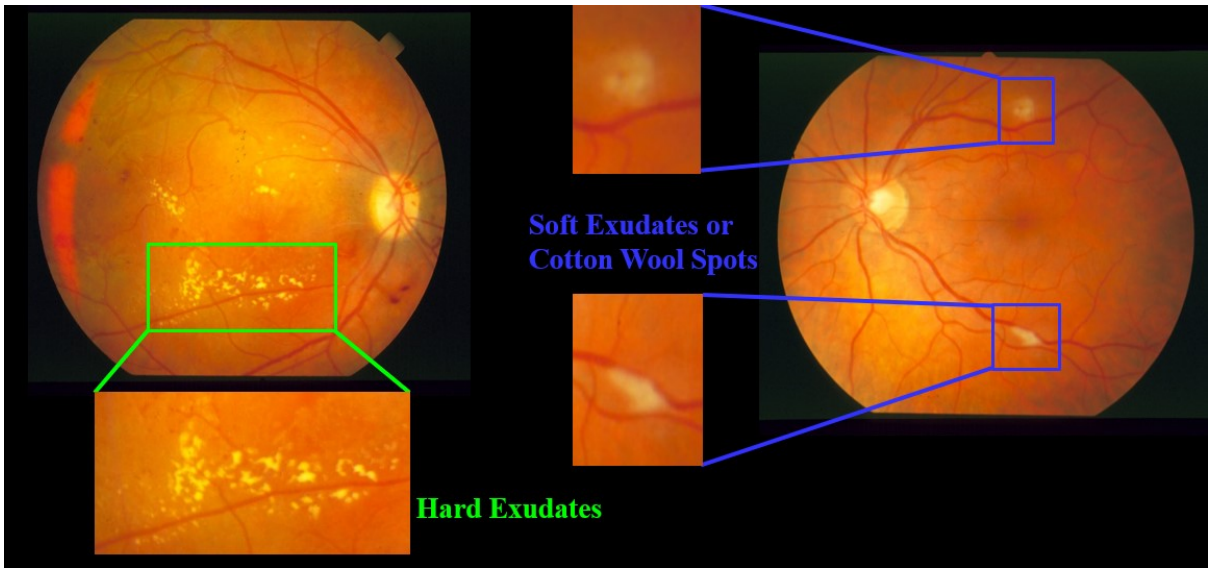

Figure 1.5 A fundus image having typical appearance of bright lesions

Exudates:

Retinal exudates are aggregates of fatty material formed from lipids and protein leaking from microaneurysms in the retina [9, 10]. The leakage of lipids and protein is due to increased pressure in the walls of microaneurysms that are thinner than normal capillaries. In retinal fundus images, exudates appear as bright yellow crystalline granules having sharper definition as shown in clinically acquired figure 1.5. Exudates can have varying shapes, sizes and locations and are the hallmark of the progressive diabetic retinopathy. Their size can vary from very few pixels, appearing as dot to as large as an optic disk. An increase in size and locations of exudates signifies the increase in severity level of the abnormality. The presence of hard exudates results in various degrees of reduced vision depending on the location of exudates. Exudates may cause rapid vision impairment if not treated on time. In order to cease the further development of exudates, retinal area comprising of exudates are exposed to laser for photocoagulation by physicians.

Cotton Wool Spots:

Cotton wool spots (or soft exudates) are small, swollen micro infarcts that appear because of obstructed blood vessels resulting in the impaired blood supply to that area. Furthermore, the decreased blood flow injures the nerve fibres in that location resulting in blood circulation in local capillaries. They appear on fundus images as yellowish or white fluffy patches with blurred edges as depicted in clinically acquired figure 1.5. Usually, their local spread is less than 1/3 optic disk areas in diameter and are generally found throughout the retina. Cotton wool spots by themselves do not cause visual difficulties, but they are highly correlated with conditions that affect the retina circulation like in the case of diabetic retinopathy. They also typically appear with other retinal abnormalities that cause significant symptoms and have long-term implications. Often cotton wool spots disappear on their own, but some localized vision loss may be permanent.

In the present work, the designing of computer-aided diagnostic method is done by extracting diagnostic information related to non-proliferative diabetic retinopathy from retinal fundus images by collectively identifying the presence of dark lesions such as micro aneurysms and haemorrhages, bright lesions such as exudates and cotton wool spots and anatomical structures such as blood vessels and optic disk. Whereas, the designing of computer-aided method to diagnose progressive diabetic retinopathy only needs to identify the presence of exudates and anatomical structures in retinal fundus images.

1.5 NEED OF COMPUTER AIDED DIABETIC RETINOPATHY DETECTION METHOD

Retinal fundus imaging is one of the valuable and non-invasive tools for imaging retina. However, due to its qualitative, subjective and experience-based nature, fundus images can be affected by imaging conditions such as illumination, machine settings. The visualization criteria for distinguishing various retinal lesions is slightly confusing and extremely based on upon the ophthalmologist's experience. This frequently results in ambiguity in the diagnostic

procedure and reduces its objectivity and reproducibility. The visualization of retinal lesions is a tedious task with retinal fundus images because of their varying sizes, shapes, contrast with respect to the background etc. Moreover, overlapping characteristics of anatomical structures and retinal lesions confuses the ophthalmologists to differentiate them. In practice, an ophthalmologist analysing a large number of retinal fundus images can have visual fatigue, resulting in the possibilities of inaccurate results. Therefore, there is a need to develop a (i) computer-aided progressive diabetic retinopathy detection method and (iii) computer aided non-proliferative diabetic retinopathy detection method that can be used by ophthalmologists as a non-invasive diagnostic tool to support their observations based on characteristic visual appearance of retinal lesions on fundus images. Diabetic retinopathy diagnosis with the assistance of an efficient and reliable computer-aided detection method may reduce the frequency of further examinations.

1.6 NEED OF RETINAL IMAGE ENHANCEMENT

It is critically essential that all the characteristic symptoms of the abnormality present in a retinal fundus image must be detected clearly to get high diagnostic accuracy. Albeit the presence of artifacts and blur, that occur during retinal image acquisition, severely hampers the interpretation and analysis of retinal fundus images. Artifacts and blur are the prime factors which degrades the contrast resolution and obstructs the meaningful information present in retinal fundus image. These artifacts are introduced due to non-uniform illumination which is further responsible for inhomogeneous intensity variations. In addition, the blur, camera dependent factors, further degrade the contrast resolution and impart a visible fuzziness to the image. The detection of retinal abnormality by an experienced ophthalmologist depends on the visualization of various lesions in a retinal fundus image. Consequently, the fuzzy edges of various retinal structures are highly undesirable at the time of accurate lesion detection. Therefore, there is a need to develop a methodology to enhance the visual quality of retinal

fundus images in such a way that the visualization of the definition of retinal structures must improve to provide efficient detection of lesions present in a retinal fundus image. Therefore, in the present work, enhancement method is designed with the intention to improve visualization of details available in retinal fundus images in order to provide accurate detection of anatomical structures and retinal lesions.

1.7 NEED OF CHARACTERIZATION OF ANATOMICAL STRUCTURES AND LESIONS

Fundus images can be influenced by qualitative and subjective variations which may lead to ambiguous analysis and identification of various retinal lesions. Furthermore, the visual criteria for differentiating retinal lesions and anatomical structures are rather subjective and highly dependent upon the ophthalmologist's experience. This often affects the diagnostic procedure by limiting its objectivity. Additionally, the visualization of retinal lesions and anatomical structures with retinal fundus images is not an easy task because of their varying sizes and limited contrast with respect to the background. Therefore, there is a need to characterize anatomical structures and retinal lesions quantitatively in order to develop a computer-aided diagnostic method to support ophthalmologists in their decision making.

1.7.1 Segmentation of Retinal Blood Vessels

Precise segmentation of blood vessels, is the first step in extracting diagnostic information for early detection of diabetic retinopathy. However, challenges faced during blood vessels segmentation from various types of pathological retinal fundus images are: (i) the presence of artifacts due to improper illumination during image acquisition, (ii) blurring due to improper focus, (iii) wide range of widths and tortuosity, (iv) the overlapping of blood vessels and lesions due to their similar intensities, and (iv) chances of missed information due to fatigue associated with the availability of large amount of data being analysed. Therefore, there is a need to develop an efficient blood vessels segmentation method to precisely segment and then eliminate blood vessels from retinal fundus images. Therefore, in this work, a generalized

blood vessels segmentation method is designed to eliminate efficiently the blood vessels from retinal fundus images.

1.7.2 Detection of Optic Disk

The accurate detection of optic disk centre and approximate removal of optic disk region can help in reducing the spurious responses during diabetic retinopathy diagnosis and screening. Challenges faced in the computer-aided detection of optic disk are: (i) similar attributes of optic disk and bright lesions in a retinal fundus image in terms of colour, intensity and contrast, (ii) partial acquisition of optic disk, (iii) hidden by major blood vessels crossings over the optic disk boundary, and (iv) ambiguous contour of optic disk. Therefore, there is a need to precisely locate and segment optic disk to avoid spurious responses during diagnosis of non-proliferative and progressive diabetic retinopathy.

1.7.3 Segmentation of Retinal Lesions

Retinal lesions are primary visual indicators of various stages and types of diabetic retinopathy. Therefore, retinal lesion identification and segmentation is an important step in diagnosing the diabetic retinopathy. However, the obstacles encountered in the identification and precise segmentation of retinal lesions are (i) the presence of shading artifacts due to improper illumination that occur during retinal image acquisition, (ii) blurred appearance of lesions due to improper focus, (iii) ambiguity in the interpretation of lesion's class, magnitude, size and exact boundary due to their similar morphologies and heterogeneity, (iv) similarity in the features of anatomical structures like optic disk and blood vessels with that of bright and dark lesions respectively, and (iv) possibility of missed information, because of human fatigue, while analysing huge number of retinal images. Therefore, there is a need to reduce the consequences of these limitations in the accurate computer-aided detection of retinal lesions. Thus, in the present work, for the detection of progressive diabetic retinopathy, a generalized exudates segmentation method is designed by introducing a novel adaptive image quantization and dynamic decision thresholding-based method. Additionally, for the detection of non-

proliferative diabetic retinopathy various dark and bright lesions are segmented irrespective of associated heterogeneity, bright and faint edges in different retinal fundus images.

1.8 NEED OF COMPUTER AIDED CLASSIFICATION AND GRADING METHOD

Experienced ophthalmologists visualize various shape, intensity and texture-based features in retinal images to classify retinal lesions and subsequently judge the severity level of diabetic retinopathy. The grading of severity level of non-proliferative diabetic retinopathy requires the subjective and quantitative validation of dark and bright lesions present in retinal image. However, the manual marking and segmentation, precision in judgement of lesions and related parameters is vastly dependent on the capability and experience of the ophthalmologist. Thus, the ambiguity lies in (i) the interpretation of precise contours due to their varied shapes and intensities resulting in confliction and (ii) the likelihood of retinal lesions of few pixels being skipped. Moreover, assessment of each patient manually becomes wearisome and is a tedious process. Furthermore, the unnecessary cost of examinations and the dearth of experts avert many patients from receiving effective treatment. Therefore, it is essential to design a computer-aided severity level detection method to aid ophthalmologists, which would reduce the cost associated with specialist graders and remove the inconsistency corresponding to manual assessment. Moreover, the detection and classification of different retinal lesions is not only helpful for diagnosis but also for treatment preparation. The experts determine the exact area of lesions to be exposed to laser for treatment. Thus, in the present work an efficient retinal lesions classification and non-proliferative diabetic retinopathy grading method is designed for fast and precise diagnosis of non-proliferative diabetic retinopathy.

The studies reported so far, in the computer-aided detection and grading of diabetic retinopathy, focuses mainly on either segmentation of anatomical structures or the segmentation of particular retinal lesions related to diabetic retinopathy [11-15]. Most of the methods use particular type of bright or dark lesions or combinations of them to diagnose

diabetic retinopathy [16-18]. In practice, expert ophthalmologists consider the information related to various combinations of lesions such as their shape, size and location to draw conclusions. Hence, there is a need to develop a more practical, accurate and precise computer-aided diagnostic method by blending information related to retinal lesions and anatomical structures present in retinal fundus images. Thus, in the present work a solution is provided in terms of computer aided diagnostic method by introducing objectivity in segmentation of retinal lesions and anatomical structures irrespective of associated heterogeneity, bright and faint edges in different retinal fundus images. The proposed computer-aided non-proliferative diabetic retinopathy detection method is designed with an extensive set of geometrical, colour and texture-based features for mathematically interpreting the visualization details of ophthalmologists. Further, the classification studies reported so far reveals that there have been very few attempts to design a computer-aided method that can provide classification among five retinal lesion classes, i.e., No DR, EXU, CWS, MA and HEM followed by grading of diabetic retinopathy. Therefore, the present computer-aided detection method is performed to classify these retinal lesion classes and grade the severity level of non-proliferative diabetic retinopathy. Clear and sharp contrasted retinal lesions are easily identified by the ophthalmologists. However, the overlapping retinal lesions with anatomical structures or among themselves may lead to misdiagnosis and confusion even for the expert ophthalmologists. Thus, the present work includes retinal images of varying attributes to provide a generalized computer-aided detection method for diabetic retinopathy diagnosis.

Further, the literature review also revealed that the neural network (NN) classifier had been used in several studies [19-21] for the classification of retinal lesions, whereas the multi-step classifiers have never been used to develop computer aided detection methods for retinal lesions in spite of the fact that multi-step classifiers had been preferred in many other clinical applications such as liver disease detection [22], brain tumour detection [23], breast cancer

detection [24] etc. Therefore, the computer aided detection and grading of non-proliferative diabetic retinopathy in the present study are designed using two-step NN classifiers.

Literature review also reveals that most of the computer-aided diagnostic methods have utilized open-source benchmark databases and the limitation in using a particular open-source benchmark database is that it remains specific to only one type of retinal lesion. Therefore, few researchers have combined various open-source databases to provide an efficient computer-aided diagnostic solution. Furthermore, images in open-source benchmark databases are of superior quality than the images encountered by ophthalmologists in their clinical practice. Therefore, there is a need to provide a practical solution that should work well with clinical retinal images. Thus, it is prerequisite to develop a composite database by combining open-source benchmark images and clinically acquired images to provide a generalized computer-aided method for the diagnosis of retinal abnormality.

1.9 OBJECTIVES OF THE PRESENT WORK

In view of the needs as discussed above, the proposed work is designed to identify and segment various retinal anatomical structures (landmarks) and lesions to detect diseases such as progressive diabetic retinopathy and grade severity level of non-proliferative diabetic retinopathy from retinal fundus images with the following objectives.

1. Development of database of clinical retinal fundus images of healthy and chronic retina of various stages
2. Study and establish the diagnostically important mathematical features to differentiate among various retinal diseases (taking expert ophthalmologist help)
3. Based on quality and grade ability of image, implement/modify algorithm for enhancement of retinal fundus image
4. Segmentation of landmarks and lesions
5. Selection of relevant set of features for lesions identification

6. Design a classifier to classify images into different types and stages of retinal diseases
7. Verify and validate the results of algorithms with the interpretation of expert ophthalmologist(s)

1.10 ORGANIZATION OF THE THESIS

This thesis contains seven chapters and two Appendices. Chapter 1 covers the introduction, need and specific research objectives. Chapter 2 covers the current status of the diabetic retinopathy diagnosis and the summary of limitations observed from literature survey. The improvements incorporated in the present work to overcome these limitations have been listed in concluding remarks. In chapter 3, the detailed methodology and the development of the composite retinal images database of the present research work is detailed. In chapter 4, the detailed procedure of the methods designed for retinal image enhancement, segmentation of blood vessels has been presented. In chapter 5, the method designed for the detection of progressive diabetic retinopathy has been discussed in detail. Chapter 6 covers the method designed for the detection and grading of non-proliferative diabetic retinopathy. Finally, Chapter 7 covers the conclusions drawn on this research work, its future scope. The segmentation results and the sample images obtained from various experiments carried out have been provided in Appendix-A and B.

1.11 CONCLUDING REMARKS

A general background about the retinal lesions related to initial stages of diabetic retinopathy (i.e. non-proliferative diabetic retinopathy and progressive diabetic retinopathy) and their characteristic visual appearance on retinal fundus images has been provided. The need of (i) computer-aided diabetic retinopathy detection, (ii) retinal image enhancement, (iii) characterization of anatomical structures, (iv) characterization of retinal lesions and (v) computer-aided diabetic retinopathy classification and grading method have also been discussed. Finally, the objectives of the present study have been presented.

Chapter 2

Literature Review

2.1 INTRODUCTION

Computer-aided diagnostic aid to an ophthalmologist plays a crucial role by carrying out repetitive tasks in the diagnosis and detection of diabetic retinopathy. Apparently, several mathematical techniques, such as morphology and thresholding, filtering, supervised methods, hybrid methods are being used to develop such aids for the quantitative analysis of retinal fundus images. Additionally, it is possible to represent visual understanding of many ophthalmologists in a single computational method. Quantification of diabetic retinopathy using computer-aided methods requires sequential application of various digital image processing steps on retinal fundus images. Specifically, these image processing steps are retinal image enhancement, anatomical structures (blood vessels and optic disk) detection and segmentation, dark and bright lesions segmentation and grading the severity level of abnormality. In order to design a computer-aided diagnostic method for the diagnosis of diabetic retinopathy it is necessary to first enhance retinal fundus images, then segment and eliminate anatomical structures, following efficient segmentation of retinal lesions. In this chapter, the reviews of significant work done in retinal blood vessels segmentation, optic disk location and detection, dark and bright lesions segmentation and diabetic retinopathy screening or grading methods with retinal fundus images are provided.

2.2 KEY STEPS OF COMPUTER-AIDED DIAGNOSTIC METHODS

Generally, the computer-aided diagnostic methods for the detection of diabetic retinopathy are based on five steps that are shown in figure 2.1.

(i) Retinal image database: Several types of open-source retinal image databases are available online that are used by researchers to evaluate the methods. But, due to their lack of completeness with respect to diabetic retinopathy screening, few researchers have

developed and used clinically acquired databases along with open-source databases to evaluate the robustness of their designed methods with respect to variability in retinal images.

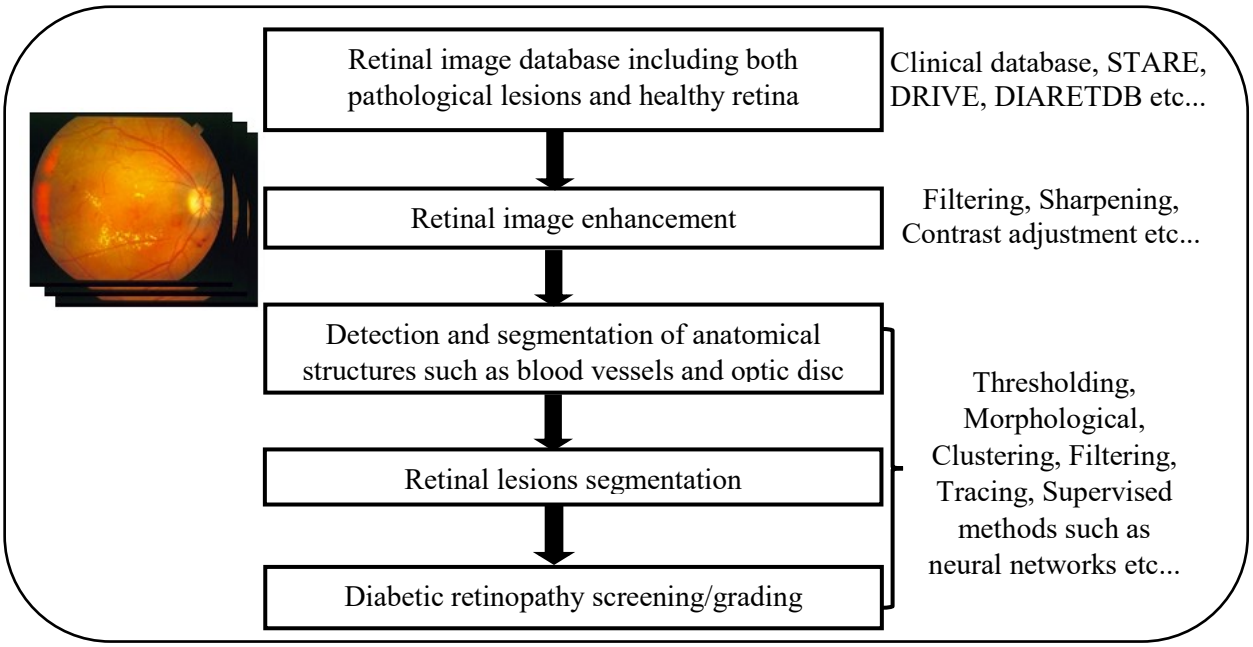

Figure 2.1 The architecture of computer-aided diagnostic method for the detection and grading of diabetic retinopathy

(ii) Retinal image enhancement: The key issues in fundus imaging are non-uniform illumination, presence of artifacts and blur. Image enhancement involves filtering, sharpening, local and global contrast improvement without destroying the significant information that is useful for diagnosis.

(iii) Detection and segmentation of anatomical structures: In this step, anatomical structures such as blood vessels and optic disk are identified, segmented and separated from background. The resulting image is then used for retinal lesions identification and classification.

(iv) Retinal lesions segmentation: In this step, bright and dark lesions are detected, segmented and distinguished from each other by specifically designed method.

(v) Diabetic retinopathy detection (screening) and grading: In this step, various classification methods are applied to classify retinal images with suspected lesions into various grades of diabetic retinopathy.

Some of the computer-aided diagnostic methods do not involve grading of diabetic retinopathy and solely discriminate images as normal and pathological. In such methods, precise retinal lesions segmentation is not carried out and only the presence or absence of lesion is obtained.

2.3 SEGMENTATION OF ANATOMICAL STRUCTURES

2.3.1 Blood Vessels Segmentation Methods

Retinal blood vessels, with varying length and widths, is one of the anatomical structures of retina. The precise segmentation of blood vessels, is the first step in extracting the diagnostic information for the early detection of various retinal abnormalities. Therefore, in the past decade numerous methods have been proposed in the literature on retinal blood vessels detection and segmentation. Table 2.1 presents the summary of these studies carried out on the segmentation of blood vessels using retinal fundus images.

Table 2.1 Brief detail of state-of-the-art methods related to blood vessels segmentation

Author (Ref.)	Method used	Performance Measures (%)	Advantages	Limitations
Chaudhuri [25]	• Gaussian function and two- dimensional Matched filter	---	• Preserves the connectivity of vessels • Computationally simple	• No objective parameters used for evaluation • Tested the algorithm with only two images
Hoover [26]	• Threshold probing method • Matched filter using Gaussian function	TPR* = 75.00	• Maintains the continuity of blood vessels	• Only one parameter used for evaluation • Unable to segment blood vessels of various widths • High level of error in pathological images
Staal [27]	• KNN classifier using feature set • Ridge detection	Acc* = 87.00	• Works satisfactorily for healthy images	• Over segmentation of blood vessels • Validated only on DRIVE database • Blood vessel connectivity is lost
Soares [28]	• Bayesian classifier • Feature vector composed of two-dimensional Gabor wavelet responses	Acc = 94.66 (DRIVE) Acc = 94.80 (STARE)	• Efficient for DRIVE database • Maintains the connectivity of vessels	• False detection due to noise • False detection of optic disk and lesions as blood vessel Structures

Contd…

Author (Ref.)	Method used	Performance Measures (%)	Advantages	Limitations
Mendonca and Campilho [29]	• Directional differential operator • Iterative region growing method • Multiscale morphology	Acc = 94.52 (DRIVE) TPR= 73.41 (DRIVE) FPR* = 23.60 (DRIVE) Acc = 94.40 (STARE) TPR= 69.96 (STARE) FPR = 27.00 (STARE)	• Detects the vessel centerline candidates	• Due to under segmentation thin blood vessel segments are missed • Unable to separate bright lesions from vessel structures
Ricci and Perfetti [30]	• Line operators • SVM based classifier	Acc = 95.62 (DRIVE) Acc = 95.82 (STARE)	• Computationally simple • Detects branching points accurately	• High number of false positives around optic disk • Strong interference of lesions with vessel structures • Weak vessels are lost during segmentation
Martinez-Perez [31]	• Geometrical features followed by spatial derivative of images • Multiscale analysis	TPR = 72.46 (DRIVE) FPR = 3.45 (DRIVE) TPR = 75.05 (STARE) FPR = 4.35 (STARE)	• Preserves the connectivity • Fine Vessels and endings are also detected	• Tested on angiography images
Zhang [32]	• Double sided thresholding • Matched filter	Acc = 94.90 (Healthy) TPR = 66.11 (Healthy) FPR = 1.52 (Healthy) Acc = 94.16 (Unhealthy) TPR =72.86 (Unhealthy) FPR = 3.72 (Unhealthy)	• Works satisfactorily for healthy images • Some of the false positives are eliminated	• Loss of connectivity of blood vessels • Optic disk rim detected as blood vessel structure
Zhang [12]	• First derivative of Gaussian filter • Matched filter	Acc = 93.82 (DRIVE) TPR = 71.20 (DRIVE) FPR = 2.76 (DRIVE) Acc = 94.84 (STARE) TPR = 71.77 (STARE) FPR = 2.47 (STARE)	• Works on eliminating small bright lesions • Preserves the thick vessels	• Many lesions are detected as vessel structures • Non-vessels structures modeled as step edges only are deleted

Contd…

Author (Ref.)	Method used	Performance Measures (%)	Advantages	Limitations
Lupascu [33]	• Adaboost classifier • 41-dimensional feature vector at multiple scale	Acc = 94.87 SN* = 52.73 SP* = 99.51	• Preserves the connectivity of blood vessels in healthy images	• Produces high amount of fragmented structures and blood vessels • Validated only on DRIVE database
Fraz [34]	• Ensemble classifier based on boosted and bagged decision trees		• Attempts to delete few of the pathological structures	• Unable to perform well on severe pathological retinal images
Li [35]	• Multiscale matched filter • Scaled multiplication for preprocessing • Double thresholding	Acc = 93.43 (DRIVE) TPR = 71.54 (DRIVE) FPR = 2.84 (DRIVE) Acc = 94.07 (STARE) TPR = 71.91 (STARE) FPR = 3.13 (STARE)	• Quite efficient on healthy retinal images • Extracted few of the weak vessel segments	• Low TPR for pathological images • Few random structures are detected with blood vessel segments
Wang [36]	• Multiscale hierarchical decomposition • Multiwavelet kernels • Adaptive thresholding	Acc = 94.61 (DRIVE) Acc= 95.21 (STARE)	• Preserves the thick blood vessels • Partially separates the bright lesions	• Many true vessel structures are lost during separation of lesions from vessels
Nguyen [37]	• Combination of line responses of each scale • Multiscale line detector	Acc = 94.07 (DRIVE) Acc = 93.24 (STARE)	• Accurate segmentation of central reflex vessels	• False vessel response in pathological regions and also in optic disk region
Salazar [38]	• Markov random field for optic disk detection • Graph cut technique	Acc = 93.43 (DRIVE) TPR = 71.54 (DRIVE) FPR = 2.84 (DRIVE) Acc = 94.07 (STARE) TPR = 71.91 (STARE) FPR = 3.13 (STARE)	• Detects optic disk to guide the algorithm for blood vessel segmentation	• Sensitive to various training datasets • No lesions have been considered for elimination
Rahebi [39]	• Multi perceptron neural network • 12-dimensional feature vector using gray level co-occurrence matrix	Acc = 94.61 (DRIVE) SN = 73.65 (DRIVE) SP = 97.07 (DRIVE) Acc = 95.27 (STARE) SN = 69.02 (STARE) SP = 98.04 (STARE)	• Maintains the connectedness of large blood vessels	• Only intensity-based features have been used • Large number of features have been computed • Validated on two standard datasets only

Contd…

Author (Ref.)	Method used	Performance Measures (%)	Advantages	Limitations
Franklin and Rajan [40]	• Multi perceptron neural network • Contrast limited adaptive histogram equalization (CLAHE) for preprocessing	Acc = 80.70 SN = 60.70 SP = 97.30	• Works well for few healthy retinal fundus images	• Tested only on DRIVE database • Unable to work for pathological images
Qian [41]	• CLAHE and 2D Gabor wavelet for enhancement • Level set and region growing method	Acc = 94.77 (DRIVE) SN = 73.54 (DRIVE) SP = 97.89 (DRIVE) Acc = 95.09 (STARE) SN = 71.87 (STARE) SP = 97.67 (STARE)	• Works well for few healthy retinal fundus images	• Produces broken blood vessel segments • Large processing time • Unable to remove non- blood vessel structures
Zhao [42]	• Hybrid region information model • Active contour modeling	Acc = 95.40 (DRIVE) SN = 74.20 (DRIVE) SP = 98.20 (DRIVE) Acc = 87.90 (STARE) SN = 78.00 (STARE) SP = 97.80 (STARE)	• Preserves the connectivity of thick blood vessels	• Over segmentation around optic disk • Testing database is limited • Unable to work for pathological retinal images
Roychowdhury [43]	• Adaptive thresholding • Top hat reconstruction	Acc = 94.90 (DRIVE) SN = 73.90 (DRIVE) SP = 98.40 (DRIVE) Acc = 95.60 (STARE) SN = 73.20 (STARE) SP = 98.40 (STARE)	• Per papillary blood vessels are taken into consideration	• Micro aneurysms detected as false blood vessel segments • Initial major blood vessel estimate is required
Imani [44]	• Wavelet and adaptive thresholding for enhancement • Morphological component analysis	Acc = 95.23 (DRIVE) SN = 75.24 (DRIVE) SP = 97.53 (DRIVE) Acc = 95.90 (STARE) SN = 75.02 (STARE) SP = 97.45 (STARE)	• Partially able to eliminate lesions from retinal fundus images	• False detections in severe pathological retinal fundus images

Contd…

Author (Ref.)	Method used	Performance Measures (%)	Advantages	Limitations
Wang [45]	• Random forest-based classifier • Convolutional neural network for feature extraction	Acc = 94.90 (DRIVE) SN = 73.90 (DRIVE) SP = 98.40 (DRIVE) Acc = 95.60 (STARE) SN = 73.20 (STARE) SP = 98.40 (STARE)	• Achieves better accuracy •	• Fragmented blood vessel structures • Very large computational time

*SN - Sensitivity, SP-Specificity, Acc-accuracy, TPR-true positive rate, FPR- false positive rate

The stated methods in table 2.1 on retinal blood vessels segmentation can be broadly classified into (i) filtering methods, (ii) vessels tracing methods, (iii) supervised methods, and (iv) hybrid methods. The following paragraphs provide a brief discussion on each class of vessel segmentation methods.

The studies based on filtering methods applied single scale matched filters followed by multiple scale filters to exploit the varying widths of retinal blood vessels. Initially single scale matched filter based on two dimensional Gaussian was employed by Chaudhuri [25]. In this method, the cross section of blood vessels is approximated by a Gaussian shaped curve and the method constructed 12 different templates to search vascular segments in all possible directions. This method was tested only for two retinal fundus images and no objective parameters were used for performance evaluation. An improvement on this method was proposed by Hoover who used local thresholding scheme for blood vessel pixel classification [26]. This improved methodology obtained a true positive rate (TPR) of 75%. The main drawback of the above mentioned single scale matched filter method is that they have similar responses for vascular and non-vascular structures and thus result in errors with overlapping blood vessels segmentation. Afterwards, several methods based on multiple scale filters have been reported to overcome this limitation. Zhang proposed a double-sided thresholding scheme to reduce the false positive detection due to the bright non-vascular structures [32]. This method

was tested on 15 clinical images depicting varying grades of diabetic retinopathy and STARE database with normal and pathological retinal images. The results showed a TPR of 79.54%. Jiang and Mojon proposed a filter based on multi threshold scheme and resulted in a TPR of 83.4% on 20 healthy and pathological retinal fundus images [46]. Sofka and Stewart have applied multiscale matched filters for vessel centerline extraction on STARE and DRIVE databases [47]. Recently, Zhang *et al*. employed a combination of matched filter and first derivative of Gaussian in order to reduce the number of false positives due to bright lesion structures in the blood vessels pixel map and produced a TPR of 71.7% [12]. A similar approach was proposed by Qin Li to deal with pathological images and he obtained a TPR of 80.69% for STARE and a TPR of 78.43% for DRIVE database respectively [35]. Also, wavelet-based filters followed by thresholding scheme have been extensively used in literature [41]. All these methods use the fact that the cross section of the retinal blood vessels can be approximated as Gaussian function. The maximum responses of the rotating Gaussian filter are taken in different positions and orientations. The main limitations of filtering-based methods are (i) they need an assumption of the optimum threshold value and, (ii) these methods fail to take into account the features of non-vascular structures to clearly differentiate true blood vessels from true non-blood vessels. Thus, these methods fail to remove many non-vascular structures present in pathological retinal fundus images and therefore cannot be generalized to wider applications.

Vessels tracing methods segment the blood vessels along the vessel center with the guidance of some local information. Zhou *et al*. used matched filtering-based method and employed initial and final points of vascular structures to detect vascular boundaries [48]. Chutatape *et al*. proposed a method in which circumference of optic disk is the initial point for the tracing of vascular structure and next point in the tracing process is estimated using Kalman filter [49]. Tolias and Can performed automatic blood vessels tracing from the information

provided by the seed points [50, 51]. The major advantage of vessels tracing based methods is that they segment blood vessels with varying vascular widths. However, these methods cannot handle bifurcations and blood vessels crossings and therefore resulting in fragmented vascular structures.

Supervised methods are based on the principle of classifying the pixels into vascular and non-vascular. Most of the supervised classification methods require images for training to decide whether the pixel belongs to a vascular structure or not. These methods attempt to extract blood vessels in the presence of different pathological signs. Soares *et al*. employed the Bayesian classifier and Gaussian mixture model for blood vessels segmentation [28]. The performance of this method resulted in an accuracy of 94.66% and 94.80% on DRIVE and STARE datasets respectively. Results show the occurrence of false detection of vascular structures in retinal fundus images due to the border of optic disk, hemorrhages and other pathological structures present in similar contrast. Ricci and Perfetti employed a two-step approach for pixel classification [30]. In this method, firstly, the response of basic line detector is thresholded for unsupervised pixel classification. Secondly, two orthogonal detectors are used to construct the feature vector for supervised classification using support vector machine (SVM). The performance evaluation showed TPR of 90.3% and 77.5% and an accuracy of 95.7% and 95.6% on STARE and DRIVE datasets respectively. The segmentation results of this method depict some false positives around the border of optic disk and in the proximity of pathological regions. You *et al*., also proposed SVM based classification approach in an attempt to reduce false positives in retinal fundus image and achieved a sensitivity of 72.6% and 77.61% on STARE and DRIVE datasets respectively [52]. Rahebi and Hardalac employed gray level co-occurrence matrix for feature extraction [39]. They used a neural network-based approach in their work and computed 12 dimensional vectors from co-occurrence matrix for

supervised pixel classification into vascular and non-vascular. Their performance results on STARE and DRIVE depict an average sensitivity of 69% and 73.6% respectively. Fraz *et al*. have used ensemble classifier and decision trees for classification [34]. Their evaluation was carried out on DRIVE and CHEST datasets and the results demonstrate that the method is unable to perform well on severe pathological retinal fundus images. The main limitations of supervised methods are that they are (i) highly dependent on the variety and number of features, and (ii) type and number of retinal images used for training the classifier.

Another set of studies employed hybrid models comprising of filtering and supervised methods. These methods take into account the advantages of both filtering and supervised methods to reduce the number of false positives in the blood vessels segmentation results. Cinsdikici *et al*. extracted retinal blood vessels using matched filter responses and ant colony algorithm [53]. This method was tested on 20 test images of the DRIVE dataset and achieved an accuracy of 92.9%. The main drawback of this study is that pathological regions in retinal fundus images have not been considered. Yao and Chen employed a two-dimensional Gaussian matched filter along with pulse coupled neural network [54]. Further, they applied two-dimensional Otsu thresholding followed by final vessel map computation using regional connectivity. The method obtained a TPR of 80% on the STARE dataset. Wang *et al*. proposed a comprehensive supervised classification using multiwavelet kernels with multiscale decomposition and adaptive thresholding [36]. Experimental results on DRIVE and STARE achieved an accuracy of 94.61% and 95.21% respectively. In the near past multidimensional feature vectors extracted were extracted and given as inputs to a supervised classifier for construction of blood vessels pixel map and the results show a significant improvement in performance of blood vessels segmentation [31, 33, 39, 45].

An analysis of the studies reported so far reveals that there have only been a few attempts to classify the retinal fundus image pixels into vascular and non-vascular in pathological retinal

fundus images comprising of different types of lesions [28, 34, 37, 39, 45]. The above-mentioned methods concentrate on eliminating one particular type of lesion among various lesions present in retinal fundus images. Therefore, these methods produce incorrect vascular structures (false positives) in retinal blood vessels segmentation when applied to images with other types of lesions. In the above-mentioned studies, the retinal fundus images used for detection and segmentation of blood vessels are from publicly available standard databases such as DRIVE and STARE. Most of the methods using these datasets perform well only on healthy retinal fundus images because these datasets do not comprise of varying pathologies. Few methods that attempt to eliminate the above limitations utilize only intensity-based features of lesions to separate them from the blood vessels, thus do not produce promising results for pathological images. Therefore, there is a need to provide a generalized solution for blood vessels detection and segmentation to ensure precise segmentation of lesions in subsequent steps.

2.3.2 Retinal Optic Disk Detection Methods

Optic disk, besides blood vessels, is another anatomical structure of retina. The optic disk appears as the brightest circular structure in a retinal fundus image. Retinal arteries and veins merge into optic disk. The knowledge of optic disk region is a significant step mainly for two tasks: (i) the precise segmentation of optic disk boundary is mainly required to detect abnormalities such as glaucoma, papilledema etc. (ii) the accurate detection of optic disk center and approximate removal of optic disk region can help in reducing the spurious responses during the detection of pathologies present in retina. The latter is mainly used for the diabetic retinopathy diagnosis and screening systems. Therefore, numerous methods have been developed not only to locate the optic disk, but also for the segmentation of optic disk boundary pertaining to particular type of application. Since optic disk is the most distinguishable of all the structures present in retina, and it shares some attributes with bright lesions, therefore, the

methods designed for diabetic retinopathy screening generally locate and eliminate optic disk region before the segmentation of retinal lesions.

Table 2.2 Brief detail of previous research works related to optic disk detection

Author (Ref.)	Method used	Number of retinal images	Optic disk location Accuracy (%)
Hoover and Goldbaum [62]	• Fuzzy convergence algorithm	81	Acc* = 89 .00
Tobin [63]	• Blood vessel features	345	Acc = 90.40
Youssif [64]	• Matched filter using blood vessels orientation	81 (STARE) 40 (DRIVE)	Acc = 98.77 Acc = 100
Niemeijer [65]	• Regression based neural network method	250	Acc = 99.20
Kauppi and Kalviainen [66]	• Template based method	61 (DIARETDB1)	Acc = 100
Niemeijer [67]	• Point distribution model	500 (Normal) 100 (Unhealthy)	Acc = 98.40 Acc = 94.00
Welfer [68]	• Hybrid snake model-based method	89 (DIARETDB1) 40 (DRIVE)	Acc = 97.75 Acc = 100
Lu [69]	• Circular transformation-based method	143 (ARIA) 1200 (MESSIDOR)	Acc = 99.50
Yu [70]	• Matched filter-based method	1200 (MESSIDOR)	Acc = 99.00

*Acc-accuracy

The earlier optic disk segmentation methods were based on the inherent geometrical and intensity properties of the retinal optic disk. By using geometrical properties such as circularity of optic disk, the methods were unable to perform well in retinal images in which optic disk was not precisely circular or was incompletely captured [55-59]. Second set of studies involved the application of intensity features of optic disk [25, 60, 61]. These methods assumed that the only region with bright pixels in the retinal image correspond to the optic disk region. Due to this, using the intensity-based features, methods were designed to search for the cluster of pixels having higher intensity values. The methods were able to detect optic disk either in only healthy retinal images or images containing red lesion structures. However, the presence of bright lesions such as exudates and cotton wool spots may result in spurious responses with the interpretation as optic disk. Recent, optic disk detection methods are designed by utilizing the fact that all retinal blood vessels originate from optic disk center. Therefore, blood vessels segmentation is considered to be one of the most reliable way to locate and then segment optic

disk method for optic disk segmentation. Therefore, an accurate blood vessels segmentation method is essential for the precise location of optic disk. Hoover *et al*., [62] proposed an optic disk detection method based on the fuzzy convergence of blood vessels. The method was based on the fact that, if it is unable to detect the optic disk center accurately based on convergence of blood vessels, the method will identify the brightest region of the retinal image as optic disk. However, the optic disk segmentation results comprised of many false positives in pathological images. Also, the authors evaluated the method on limited number of images comprising of 31 healthy retinal fundus images and 50 pathological retinal fundus images. Tobin *et al*., [63] applied a two-step approach for the optic disk location based on blood vessels segmentation. In the first step, spatial features such as density, width and orientation of blood vessels with respect to the location of optic disk are determined. Afterwards in the second step, optic disk is located by traversing the geometrical model constructed for the blood vessels with the extracted spatial features. Youssif *et al*., [64] located the optic disk center by first applying a two-dimensional Gaussian matched filter for the extraction of blood vessels orientation map. Afterwards, morphological operations and local intensity-based filtering is used to determine the candidates corresponding to optic disk center. The minimum difference between the filtered image and the blood vessels orientation around each candidate provides an estimation of the optic disk location. Niemeijer *et al*., employed a supervised approach for the location of optic disk center [65]. They used neural network-based regression method after blood vessel segmentation to approximate the optic disk location. They trained their supervised model with 200 retinal fundus images. Similarly, Kauppi *et al*. proposed a supervised method for the location of optic disk center using principle component analysis [66]. Principle component analysis is used to determine an eigenspace that characterizes the optic disk in colored retinal images. Table 2.2 shows the overall summary of the methods designed to locate optic disk. The limitation of these methods is that they rely on the assumption that the optic disk center and convergence point of blood vessels is same. Although the convergence point of blood vessels

is inside the optic disk, it is not necessarily located at its center. Therefore, in such cases incorrect estimation of optic disk area may lead to its partial elimination, thus affects the accurate detection of bright retinal lesions. Also, these methods have been evaluated with limited number of retinal images as well as each method have used different sets of retinal images. Therefore, there is a requirement of a robust optic disk detection and elimination method to reduce spurious responses during the segmentation of retinal lesions.

2.4 RETINAL LESIONS DETECTION AND SEGMENTATION

The diagnosis of diabetic retinopathy is based upon visually identifying various characteristic clinical attributes. Retinal lesions are among the primary visual indicators of various stages of diabetic retinopathy. As described in section 1.1, non-proliferative diabetic retinopathy is characterized by the presence of single or multiple retinal lesions, whereas progressive diabetic retinopathy is recognized by the sole presence of exudates. Therefore, an important step in diagnosing the diabetic retinopathy is retinal lesion identification and segmentation. Retinal fundus images consist of varying types of dark and bright lesions having different identification criteria, as discussed in section 1.4.2. These criteria provide guidelines for the designing of the computer-aided methods for the detection of various retinal lesions. There are various recent methods proposed in literature for the detection and classification of micro aneurysms, hemorrhages, hard exudates and cotton wool spots for the diagnosis of diabetic retinopathy. The detection and segmentation of retinal lesions are considered individually or in a collective way. The diagnostic capability of detection and segmentation of retinal lesions in state-of-the-art methods are assessed with two evaluation criteria: (i) per-lesion based evaluation and (ii) per-image based evaluation.

Per-Lesion Based Evaluation: Each cluster of pixels belonging to a lesion area in a retinal image is considered as a distinct lesion and each lesion may comprise of single or multiple pixels. A retinal fundus image may consist of many such cluster of lesions. These lesions are

segmented by applying an appropriate method on retinal fundus images. Then, the per-lesion results are measured in terms of sensitivity, specificity and accuracy by evaluating the segmentation outcomes in detecting every single lesion with the reference ground truths marked by the expert ophthalmologists. The per-lesion performance of the method must be as high as possible, because the number of lesions and their location is vital to judge the severity level of diabetic retinopathy.

Per-Image Based Evaluation: The prime objective of per-image evaluation is to impart a decision whether a retinal image has some evidence of retinal lesions and subsequently diabetic retinopathy or not. The decision is solely based on the absence or presence of retinal lesions. Hence, the per-image evaluation of a method is carried out by computing the number of correctly identified retinal images in proportion to the tested normal and pathological images. Per-image evaluation is primarily used in clinical applications from screening point of view since it validates the performance of the method in discerning images with any signs of diabetic retinopathy.

2.4.1 Bright Lesions Segmentation Methods

Bright lesions are broadly categorized into two types namely hard exudates and cotton wool spots (also termed as soft exudates). The diagnosis of severity level of diabetic retinopathy requires the subjective and quantitative analysis of the variations in exudates. The boundaries of exudates are detected in retinal fundus images by expert ophthalmologists using manual evaluation procedure or by using automatic segmentation methods. Generally, exudates are segmented as a first step during the detection of various retinal lesions to identify the cases of symptomless diabetic retinopathy, i.e. progressive or non-proliferative diabetic retinopathy. The reason is exudates have high contrast with respect to the background as compared to other retinal lesions. Also, the detection of exudates is not only useful for diagnosis but also for treatment planning. The physicians determine the precise area of exudates to be exposed to

laser for photocoagulation in order to control the progression of diabetic retinopathy. There are various automatic and semi-automatic methods on exudates detection and segmentation on retinal fundus images [71-101]. Table 2.3 presents the summary of the comparative study carried out on the detection and segmentation of exudates using retinal fundus images.

Table 2.3 Brief detail of previous research works related to bright lesions segmentation

Author (Ref.)	Method used	Performance Measures (%)	Advantages	Limitations
Phillips [73]	• Shade Correction • Gray level Thresholding	SN* = 87	• Applied simple technique for exudates segmentation	• Method is not robust enough to work for variety of retinal fundus images • Tested the method on 14 digital color slides
Ege [74]	• Bayesian, KNN, Mahalanobis Classifier • 31 features based on Region growing algorithm	**Location based** SN = 98.9 (Exudates) SN = 80 (Cotton Wool spots)	• Number of lesions have been taken into consideration • Designed a clinical dataset	• Tested the method on 134 retinal fundus images • False detection of optic disk as lesions • Objective parameters evaluated based on location criteria
Wang [75]	• Statistical classifier using feature space	**Image Based** Acc* = 100	• Brightness adjustment procedure for non-uniform illumination	• Classified images as abnormal and normal • Tested the algorithm on 154 (54-normal,100- abnormal) retinal fundus images
Osareh [88]	• Fuzzy c means Clustering • Neural network	**Image Based** SN = 92 SP* = 82	• Simple feature set used for training the neural network	• Trained the method on 74% and tested on only 26% of the samples of 140 images • Exudate Maculopathy is taken for consideration
Walter [79]	• Morphological Reconstruction • Watershed Transformation	**Pixel Based** SN = 92.8 SP = 92.4	• Optic disk eliminated though the process is not robust • Pixel based evaluation of objective parameters	• Tested the algorithm on only 30 retinal images • Mainly considered exudates in diabetic macular edema
Osareh [84]	• Local Contrast Enhancement • Fuzzy c means clustering • 3-layer perceptron neural network	**Image Based** SN = 95 SP = 88.9 **Exudate Based** SN = 93 SP = 94.1	• Image and exudates-based evaluation of objective parameters	• Processing time for each image is 11 minutes • 75 retinal images are used for training and 67 for testing • No information on how ground truths have been marked

Contd…

Author (Ref.)	Method used	Performance Measures (%)	Advantages	Limitations
Usher [89]	• Recursive region growing • Adaptive intensity thresholding • Artificial neural network	**Image Based** SN = 89 SP = 62.4 **Patient Based** SN = 95.1 SP = 46.3	• Trained the algorithm on 500 images and tested on 773 images • Optic disk location in variety of retinal images	• Designed clinical dataset on only one type of population • Optic disk location method is not robust
Gracia [77]	• Multilayer Perceptron • Radial basis function • Support vector machine	**Image Based** SN = 100 SP = 92.59 Acc = 97 **Lesion Based** SN = 88.14 PPV* = 80.72	• Evaluated the algorithm using both lesion and image criteria	• 50 retinal images are used for training and 67 for testing
Sopharak [80]	• CLAHE • Morphology Reconstruction • Otsu Thresholding • HSI color space	**Pixel Based** SN = 80 SP = 99.5	• Pixel based evaluation of objective parameters • Hand drawn reference ground truths have been used for evaluation	• Optic disk eliminated though the process is not robust • Tested the method on only 60 retinal images (40-with exudates, 20- normal) • Processing time for each retinal image is 3 minutes
Sopharak [83]	• CLAHE • Fuzzy c means clustering • Morphology	**Pixel Based** SN = 87.28 SP = 99.24 Acc = 99.1	• Simple feature set used for training the neural network	• Tested the algorithm on only 40 retinal images • Processing time for each retinal image is 18 minutes
Reza [90]	• Fixed and variable threshold • Morphological opening • Watershed transformation	**Pixel Based** SN = 96.7	• Tested the method in standard datasets • Detects both exudates and optic disk	• Tested only on 20 retinal images of STARE and DRIVE database • No range of variable threshold is mentioned • Unable to separate exudates and optic disk thus producing unfair results
Sanchez [76]	• Mixture Models • Dynamic Thresholding • Edge Detection	**Image Based** SN = 100 SP = 90 **Lesion Based** SN = 90.2 PPV = 96.8	• Tested for variable threshold values	• Optic disk detection using Hough transform not being robust • Tested on only clinical dataset of diabetic patients • Method not robust to detect various types of exudates
Welfer [81]	• Mathematical morphology • H maxima transform • LUV color space • Thresholding	**Pixel Based** SN = 70.48 SP = 98.8	• Hand labeled reference ground truths have been used • Coarse and fine detection of exudates	• False detection of pixels leading to decreased sensitivity • Tested the method on one standard database (DIARETDB1- 89 images)
Reza [91]	• Contrast Adjustment • Marker controlled watershed transformation	**Pixel Based** SN = 94.9 SP = 100 PPV = 92	• Distinguished hard exudates and cotton wool spots though not robust	• Tested only on 20 test images of STARE and DRIVE • Unfair comparison of methods because of different datasets

Contd…

Author (Ref.)	Method used	Performance Measures (%)	Advantages	Limitations
Youssef [92]	• Morphology • Thresholding • Edge point detection	**ROI Based** SP = 100 SN = 80	• Noise elimination which arises due to hemorrhages • Efficient detection of blood vasculature	• Only 20 ROI and 7 clinical images used for validation • Focuses more on anatomical structure detection • OD extraction algorithm not robust • Semi-automated algorithm and ROI is selected manually
Yazid [78]	• Fuzzy c means clustering • Edge detection • Otsu and inverse surface thresholding	**Pixel Based** SN = 97.8 SP = 99 Acc = 83.3 (STARE) SN = 90.7 SP = 99.4 Acc = 74	• Tested on both clinical and standard database	• Tested only on 15 images of STARE database and 15 from custom database • False detection of OD along with exudates and unable to separate them
Giancardo [86]	• Wavelet decomposition-based feature set • Support vector machine	**Image based** AUC = 0.93 (DiaretDB1) AUC = 0.90 (MESSIDOR) AUC = 0.93 (HEI-MED)	• Tested the algorithm on variety of publicly available standard databases	• Image based validation • False segmentation response at lesion level validation • No clinical dataset is used • Rough reference ground truth annotations used
Harangi [93]	• CLAHE • Naïve Bayes classifier	**Image based** SN = 63 PPV= 0.85	• More than 50 features are extracted for each candidate pixel	• Tested on DIARETDB standard database of 89 images • Image based classification of objective parameters • Specificity is not calculated
Rajput [94]	• CIELAB color space • K means clustering • Morphology	**----**	• Classified exudates based on edge energy and threshold	• No objective parameters used for evaluation • Tested on only clinical dataset of 100 retinal images with no details of pathology
Zhang [14]	• Mathematical morphology • Random forest algorithm	**Image Based** SN = 89 SP = 96 **Pixel Based** SN = 83	• Variety of features are used • Heterogeneous clinical dataset is developed	• Both Optic disk and blood vessels are roughly detected for elimination and the method is not robust • Only 47 random images were contoured by the experts
Lahmiri [95]	• Empirical mode decomposition, CLAHE • Feature set based on entropy and uniformity • SVM	**Image Based** SN = 100 SP = 100 Acc = 100	• High segmentation results on limited number of images	• Unable to detect various types of exudates • Tested on only 45 images of STARE database • Processing time for each image is 4 minutes • Image based classification of objective parameters
Figueiredo [101]	• Multiresolution feature discrimination based on wavelets • Hessian Eigen values and multi-scale image analysis	**Image Based** SN = 89.81 SP = 97.47	• Tested on 607 retinal frames for exudates segmentation • Different types of exudates are considered for segmentation	• Different criteria for identifying isolated dots of exudates, clusters of dotted exudates and large/medium exudates • Accuracy is not calculated

Contd…

Author (Ref.)	Method used	Performance Measures (%)	Advantages	Limitations
Wisaeng [96]	• Moving average threshold models • Sobel edge detector • Otsu thresholding	**Pixel Based** SN = 90.42 SP = 94.60 Acc = 93.69	• Trained on 200 images and tested on 1220 images • Hand labeled reference ground truths from multiple experts	• Comparison of algorithm with other techniques is unfair as different datasets are used • No details of types of pathology in database used are mentioned
Sidibe [87]	• Linear support vector machine • Sparse coded features	**Image Based** SN = 99.1 SP = 100 (Drusen) SN = 97.4 SP = 98.2 (Exudates)	• Discriminated exudates and drusen • Multiple images from standard and clinical dataset are used	• Only discriminated retinal images containing different bright lesions • Image based classification of objective parameters
Jaya [97]	• Fuzzy support vector machine • Circular Hough transforms • Neural Network	**Pixel Based** SN = 94.1 SP = 90	• Pixel based classification for clinical dataset	• OD extraction algorithm not robust • Tested on only clinical dataset of 200 images with no details of type of pathologies

*SN-sensitivity, SP-Specificity, AUC = Area under ROC, Acc-accuracy, PPV-positive predictive value

The initial attempt was made by Phillips *et al.* in which global and adaptive thresholding method was applied to segment exudates [73]. The method was tested only on 14 retinal images and the image-based sensitivity on a patch of size 256 x 192 pixels was reported between 61% and 100%. The authors did not provide lesion (pixel by pixel) based evaluations. A drawback of this method was that the other bright lesions such as cotton wool spots could be identified mistakenly. This drawback was addressed by Ege *et al.* [74] by applying a combination of thresholding, region growing and template matching methods for the detection of initial pathologies in retinal images. The method was tested on 38 retinal images containing bright lesions and from which only 87% of bright lesions were detected. Then, a Bayesian classifier was applied to further classify the detected bright lesions into exudates, cotton wool spots, noise and the final performance resulted in the detection of 62% for exudates. Another approach was developed by Wang *et al*. using Bayesian classifier to classify each pixel of retinal image into lesion or non-lesion [75]. As in this study, the objective was to identify bright lesions, cotton wool spots were also incorrectly classified as exudates. The image-based

evaluation sensitivity of this method on a database of 150 retinal images was reported as 100%. However, the specificity of 70% showed there was more number of wrongly detected healthy retinal images as pathological retinal images.

Another study for exudates segmentation based on adaptive thresholding using mixture model-based clustering was proposed by Sanchez *et al.* [76]. To effectively segment the exudates from background, threshold values are adaptively assigned to retinal images. Afterwards, post processing based on edge detection is applied to distinguish hard exudates from cotton wool spots and other bright structures. This method achieved the sensitivity of 90.2% for lesion-based evaluation on 80 retinal images. The major limitation of this method is that it is designed and evaluated on a database having limited number of pathological structures in their images. Moreover, despite the enhancement of hard exudates, the method fails to identify the faint exudates lesions. Gracia *et al*. developed an adaptive histogram thresholding-based candidate exudates extraction and classification using three types of neural network classifiers [77]. The image-based evaluation of the method on a database of 117 retinal images achieved a sensitivity of 100%, a specificity of 77.78% and a mean accuracy of 91.04%. Whereas the sensitivity of 88.4% was achieved for lesion-based evaluation. However, the limited number of retinal images in the database and the incapability of the algorithm to segment faint exudates makes it unsuitable for practical applications. Yazid *et al*. applied fuzzy c-means clustering algorithm to threshold the various regions of retinal images into categories namely: the background, blood vasculature, low intensity exudates and high intensity exudates [78]. Once the region containing the exudates is identified, edge detection is performed to extract the boundaries of the exudates. Afterwards, the exudates pixels are separated from others by using Otsu thresholding method. The method was evaluated on a small dataset of 15 retinal images from STARE database and achieved lesion-based sensitivity of 90.7%. The method was also evaluated on 15 clinically acquired retinal images and achieved the sensitivity

of 97.8%. However, the method misclassified the optic disk pixels as exudates pixels due to similar intensities of optic disk and exudates. Figueiredo *et al*. proposed wavelet and multiscale image analysis-based thresholding method for exudates segmentation and resulted in image-based sensitivity/specificity of 89.81/97.47 respectively [18]. However, the method proposed three binary detectors to detect distinct types of exudates such as isolated dots of exudates, clusters of dotted exudates and large/medium exudates. All these state-of-the-art methods use the fact that the exudates have maximum intensity response with respect to background to decide the threshold value. The main limitation of thresholding-based methods is to determine the optimum threshold value for the segmentation. Also, most of the above-mentioned methods do not consider the automatic detection and elimination of optic disk which tends to interfere with the intensity value of the exudates. Thus, these methods cannot be generalized to varying types of retinal fundus images as there are no unique threshold settings that can be applied on a composite database.

Morphology based methods apply morphological operations on the retinal fundus images to detect and segment various structures with predictable shapes such as blood vasculature and optic disk so that exudates can be identified in colored retinal fundus images. Walter *et al*. proposed morphology based automated identification of exudates [79]. Firstly, a morphological closing operator is used to eliminate retinal blood vasculature and then the local sliding window is employed to determine grey level variations in the neighborhood of each pixel to detect candidate exudates. Secondly, morphological reconstruction is used to determine minimum threshold value to detect exudates more precisely. The method reported a mean lesion-based sensitivity of 92.8% on a very small clinically acquired database of 15 pathological retinal images. The authors however have not compared their method with publicly available standard databases. This method also misclassifies some of the cotton wool spots as exudates. A similar approach based on morphological closing and reconstruction operator was proposed by

Sopharak *et al*. in which they initially eliminated optic disk to reduce the number of false positives [80]. Afterwards, the exudates pixels are segmented by constructing the local variability image based on local variations of exudates in retinal fundus images. The sharp contrast of exudates pixels with respect to surroundings highlights the contours of exudates lesions in local variability image. Lesion based sensitivity of 80% on a small database of 60 clinically acquired retinal images shows that many of the true exudate pixels are still too subtle to be detected by this method. Welfer *et al.* performed automatic segmentation of exudates in three steps [81]. Firstly, morphological top hat opening and closing operators are used to enhance the lightness, L, of uniform LUV color space of retinal images. Since exudates are brighter than the background region, reconstruction by dilation is performed to estimate the background region. Secondly, by subtraction of the background region from the enhanced image and by applying H-maxima transform along with threshold operator, the exudates are coarsely detected. Finally, for the precise detection of exudates, a reconstruction operator is applied on the coarsely detected exudates. The method obtained lesion-based sensitivity of 70.48% on a publicly available DIARETDB1 database. The main drawback of this approach is that it produced low specificity values and high misclassified portions for images that do not contain exudates. Recently, Zhang *et al*. not only eliminated dark structures such as blood vasculature and dark lesions in the pre-processing stage but also the interfering bright structures such as optic disk and the reflections while acquisition [82]. They extracted various features to eliminate these non-exudates pixels and train the random forest classifier. After classification of non-exudates pixels from exudates pixels, several mathematical morphology operators were applied to obtain the true candidate pixels. The method is evaluated based on both image and lesion level-based evaluation criteria. The method reported the maximum sensitivity of 83% for lesion-based evaluation. The major advantage of mathematical morphology-based methods is that the anatomical structures can be eliminated efficiently before obtaining the final

segmentation of exudates. However, these methods cannot handle retinal anatomical structures such as optic disk and blood vasculature with varying widths and thus detection failures leading to false positives.

Clustering methods are based on the principle of detecting exudates by grouping them into a set of pixels called clusters using varying types of algorithms. Most of the clustering methods are followed by supervised approaches to classify the pixels into exudates and non-exudates. Sopharak *et al*. employed a two-step approach for exudates detection [83]. Initially, exudates are coarsely detected using fuzzy c-means clustering algorithm. Afterwards, mathematical morphological operators are used to refine the exudates detection. The segmentation was carried out on a small database of 40 clinically acquired retinal fundus images and the performance evaluation showed the lesion-based sensitivity of 87.28%. However, the processing time of 18 minutes makes this method unsuitable for clinical applications. Osareh *et al*. used a three-step method for automatic identification of exudates in colored retinal images [84]. After color normalization and contrast enhancement, the retinal images are segmented using fuzzy c-means clustering algorithm. Due to non-uniformity of color distribution in retinal images, clustering algorithms may result into cluster overlapping resulting in false positives. Therefore, in the last step neural networks are employed to classify the extracted structures as exudates or non-exudates regions. The method achieves a sensitivity of 95% and a specificity of 88.9% on a dataset of 142 colored retinal images. Niemeijer *et al*. discriminated the bright lesions such as exudates, cotton wool spots and drusen from colored retinal images [85]. Firstly, a lesion probability map is constructed to determine the probability of each pixel to be a part of bright lesion. Then pixels with high probability are grouped into each lesion cluster termed as the bright lesions. Finally, these clusters are classified into exudates, cotton wool spots or drusen using a series of k-nearest neighbor classifiers. The authors reported a lesion-based sensitivity of 95.5%, 70% and 77% for exudates, cotton wool

spots and drusen respectively for a dataset of 300 retinal images. Giancardo *et al*. proposed exudates segmentation method based on support vector machine classifier trained with a single feature vector per image obtained from color and wavelet analysis [86]. The method was tested on their newly provided public database namely, HEI-MED and other publicly available databases such as MESSIDOR and DIARETDB1. It achieved the area under the curve (AUC) of 88% on HEI-MED database. Recently, Sidibe *et al*. proposed a method for discrimination of retinal images containing various bright lesions [87]. This discrimination and classification method for retinal images required no prior knowledge of location of anatomical structures for feature learning based on sparse coding principle. The evaluation for the classification of retinal images was carried on six publicly available databases and one clinically acquired database. The results demonstrate the image-based sensitivity/specificity of 97.4/98.2 respectively but still the method is unable to detect pathological structures of few pixels. A common limitation of the supervised approaches for the detection of exudates is that these methods are highly dependent on the features of exudates structures present in retinal images for training. Therefore, there is a probability of misclassification of various structures present in retinal images as exudates.

The main limitations of above state of the art methods can be summarized as: (i) These methods segment only clear and bright exudates lesions, (ii) they detect many false edges due to dull boundaries, (iii) there have been only few attempts in literature to efficiently eliminate blood vessels and optic disk prior to the detection of exudates and lead to misclassification, (iv) methods were tested either with specific database available online or only with clinically acquired database, therefore the generalized capability of these methods is questionable and (v) different methods are evaluated with different evaluation criteria, so a fair comparison cannot be made among them.

2.4.2 Dark Lesions Segmentation Methods

Dark lesions are broadly categorized into two types namely micro aneurysms and hemorrhages. The grading of severity level of non-proliferative diabetic retinopathy also requires the subjective and quantitative evaluation of dark lesions along with bright lesions present in retinal image. There are various methods proposed in literature for the detection and classification of micro aneurysms and hemorrhages for the diagnosis of non-proliferative diabetic retinopathy [102-141]. In these methods, the detection and segmentation of red lesions are considered individually or in a collective way. Table 2.4 presents the summary of the comparative study carried out on the detection and segmentation of dark lesions on retinal fundus images either individually or in a collective manner.

Table 2.4 Brief detail of previous research works related to red lesions segmentation

Author (Ref.)	Method used	Performance Measures (%)	Advantages	Limitations
		Task: Detect Images/Pixels with Microaneurysms		
Spencer [103]	• Bilinear top hat transformation • Matched filter-based threshold	**Image Based** SN = 82	• Microaneurysms were verified from five clinicians	• Tested the method on four fluorescein angiogram images with 71 microaneurysms • Identified only image areas counting microaneurysms
Cree [102]	• Registration based method	**Image Based** SN = 82 SP = 84	• Trained the classifier using varying types of 89 retinal images	• Tested the algorithm on 20 fluorescein angiogram images
Frame [112]	• Empirically derived rule-based system	**Image Based** SN = 84 SP = 85	• Trained the classifier using varying types of 68 retinal images • Different types of classifiers were tested and compared	• Tested on 20 fluorescein angiogram images • No information regarding the presence of other types of lesions in test retinal images
Hipwell [113]	• Enhancement-based method • Classification method	**Image Based** SN = 81 SP = 93	• Used digital red free color images • Background variations in intensity are removed	• No information regarding the presence of other lesions in test retinal images • Trained the classifier using 102 retinal images
Yang [114]	• Top hat transformation • Threshold and region growing-based method	**Image Areas Based** SN = 80 SP = 90	• Performs well for low resolution images	• Tested on only 3 retinal images

Contd…

Author (Ref.)	Method used	Performance Measures (%)	Advantages	Limitations
Walter [104]	• Thresholding method • Bounding box closing method	**Image Areas Based** SN = 86 Acc = 75	• Used colored retinal fundus images	• Tested on only 5 retinal images counting microaneurysms
Pallawala [115]	• Eigen vectors-based affinity matrix approach	**Image Segments Based** SN = 93	• Simple mathematical approach • An attempt to suppress the overlapping retinal structures	• Tested on only 70 image segments with microaneurysms • Limited number of parameters are calculated
Quellec [116]	• Wavelet Transform • Sub-bands decomposition	**Image Areas Based** SN = 88 SP = 96	• Trained and tested the method on 995 retinal images • Method can be extended to other small lesion structures	• Unable to extract microaneurysms when other types of prominent lesions are present
Walter [117]	• Diameter closing • Thresholding method • Feature extraction	**Lesion Based** SN = 88.5	• Varying types of features were used • Trained the algorithm using 21 images • Can be extended for the detection of other lesions	• Tested the algorithm on only 94 images
Bhalero [118]	• Circular symmetric based linear filters • Morphological analysis-based method	**Pixel Based** SN = 82.6 SP = 92.4	• Requires tuning of two parameters	• Tested the method on DIARETDB1 database consisting of 89 images only
Quellec [107]	• Template matching • Wavelet transforms • Genetic algorithm-based optimization	**Lesion Based** SN = 90.24 PPV = 89.75	• Method is not sensitive to quality variations within images	• Mistakenly detect microaneurysms clustered with blood vessels • Some hemorrhages are detected as microaneurysms
Zhang [119]	• Multiscale correlation filter • Dynamic thresholding	**Pixel Based** FPR = 35.7	• Two public databases (DIARETDB1 and ROC) are used for evaluation • Varying types of features were used for classification	• Selection of scales at the first level is tedious • High number of features were used for training the classifier
Sanchez [120]	• Mixture model clustering • Logistic regression classification • Thresholding	**Image Segments based** FROC score = 0.33	• Evaluated the algorithm on ROC dataset comprising of 100 images with varying quality and characteristics	• Missed microaneurysms adjacent to blood vessels • High number of false positives due to non-removal of blood vessels
Giancardo [121]	• Radon transforms • Radon cliff operator	**Image Based** SN = 41	• Ability to distinguish between vessels and microaneurysms • Microaneurysms of different sizes can be detected	• Tested on a ROC database comprising on 100 colored images • Unable to detect microaneurysms in the presence of other lesions • Low sensitivity

Contd…

Author (Ref.)	Method used	Performance Measures (%)	Advantages	Limitations
Zhang [122]	• Supervised classification • Ultimate opening method • Top hat transformation method	NA	• A new approach based on ultimate opening was implemented	• No single parameter was selected for the whole database • Number and type of testing images were not mentioned
Hatanka [123]	• Double ring filter-based approach	**Image Based** SN = 68	• 126 features were used for training	• Only 25 test images were used for evaluation of the method
		Task: Detect Images/Pixels with Hemorrhages		
Gardner [124]	• Back propagation neural network	**Image Segments based** SN = 73.8 SP = 73.8	• Simple neural network for the detection of hemorrhages	• Trained and tested on 179 images in total • Detection accuracy is highly dependent on the images used for training • Unable to distinguish vessels from hemorrhages and microaneurysms • High computational time
Zhang and Chutatape [125]	• SVM classifier • Boot strapping sample selection algorithm	**Image Segments based** SN = 90	• Good classification accuracy is achieved	• Interference with other objects due to similar attributes and non-uniform illumination
Hatanka [126]	• Co-occurrence matrix-based features	**Image Based** SN = 85 SP = 21	• Interfering blood vessels are eliminated prior to the segmentation of hemorrhages • Varying features used for classification	• Unable to detect hemorrhages that overlap with blood vessels • Tested the method on limited number of retinal images
Hatanka [127]	• Gamma correction • HSV space • Density analysis	**Image Based** SN = 80 SP = 88	• Anatomical structures were detected and eliminated prior to lesion segmentation • Elimination of false positives using feature analysis	• Tested on only 35 pathological images • Unable to detect lesions in clinical retinal images
Fleming [128]	• Multiscale morphology • Region growing	**Pixel Based** SN = 98.6 SP = 95.5	• Blood vessels were detected prior to hemorrhages detection • 10,846 images were used for testing	• Only one type of hemorrhage has been considered for segmentation • Unable to distinguish microaneurysms and hemorrhages
Bae [129]	• Template matching • CLAHE • Region growing method	**Pixel Based** SN = 85	• Algorithm tested on images with varying resolution of 52 images • False positives were reduced using bounding box	• Various thresholds were used for segmentation of hemorrhages • Unable to distinguish blood vessels from hemorrhages

Contd…

Author (Ref.)	Method used	Performance Measures (%)	Advantages	Limitations
Joshi [130]	• Splat feature algorithm • KNN classifier	**Lesion Based** SN = 84.84 PPV = 90.30	• 200 images were used for testing • 43 features were used for training the classifier	• False positives due to overlapping of hemorrhages and blood vessels • Poor performance for severe cases • High computational time
Tang [131]	• Splat feature supervised classification • Wrapper approach	**Image Based** SN = 93 SP = 66 AUC = 87	• 1200 images from MESSDOR database were used for testing • Over segmentation at edges has been dealt using edge effects method	• Unable to detect hemorrhages overlapping with blood vessels • Unable to distinguish lesions from the background
		Task: Detect Images/Pixels with Red Lesions		
Ege [74]	• Mahalanobis classification method	**Image Segments Based** SN = 69 (MA) SP = 83 (HEM)	• Varying types of classifier have been tested • Simple neural network approach	• Tested on 134 images comprising 161 image segments • Low sensitivity depicting incorrect segmentations
Sinthanayothin [132]	• Moat operator • Recursive region growing	**Pixel Based** SN = 77.5 SP = 88.7	• Anatomical structures were detected and eliminated prior to lesion segmentation	• Tested the method on only 14 retinal images • Overlapping of blood vessels and red lesions resulting in spurious responses
Niemeijer [108]	• Mathematical morphology • Pixel based classification	**Image Based** SN = 100 SP = 87	• Varying types of features such as color and contextual features were considered	• Red lesions corresponding to few pixels are missed. • Unable to distinguish hemorrhages and microaneurysms
Zhang and Fan [133]	• Entropy thresholding • Adaptive multiscale mathematical morphology	**Lesion Based** SN = 84.1 PPV = 89.2	• Over segmentation have been removed using scale map generation • Blood vessels removal prior to hemorrhages detection	• Tested on only 30 retinal images • Unable to distinguish hemorrhages and microaneurysms
Grisan and Ruggeri [134]	• Local thresholding • Spatial density of pixels	**Image Areas Based** SN = 94	• High performance on very few images	• Tested on only 6 retinal images • Doesn't distinguish red lesion structures • Cannot be extended to varying types of images
Marino [135]	• Correlation filters • Region growing segmentation method • Shape and intensity-based approach	**Lesion Based** SN = 78.5	• Method is able to adapt to different resolutions • False positives due to overlapping of blood vessels and red lesions are removed using four matched filters	• Algorithm tested on only 75 retinal images

Contd…

Author (Ref.)	• Method used	Performance Measures (%)	• Advantages	• Limitations
Pradhan [136]	• Local thresholding • Region growing • KNN classifier • Gaussian mixture model	**Pixel Based** SN = 87 SP = 95.53	• Removal of blood vessels reduce the number of false positives • Four types of classifiers were used for optimized performance	• Limited number (33) of testing images were used • Unable to distinguish small red lesions
Gracia [138]	• Multilayer perceptron classification	**Image Based** SN = 100 SP = 60 Acc = 80 **Lesion Based** SN = 86.1 SP = 71.4	• Feature selection and optimization of the parameters reduces computational complexity	• Trained and tested on 100 retinal images in total • Unable to distinguish between hemorrhages and microaneurysms
Kande [137]	• Morphology top hat transform • SVM classifier • Entropy thresholding	**Pixel Based** SN = 96.22 SP = 99.53	• Multiple channel information is utilized for red lesions detection • Ability to segregate red lesion structures from the background	• Selected 80 random train and test images from public databases • Detected red lesion on well contrasted images • Unable to distinguish hemorrhages and red lesions
Gracia [110]	• Multilayer perceptron • Radial basis function • Support vector machine • Majority voting scheme	**Image Based** SN = 100 SP = 100 Acc = 83.08 **Lesion Based** SN = 86.01 PPV = 51.99	• Various types of supervised classifiers were tested • Both image and pixel parameters were calculated	• Well contrasted testing images were used • Unable to distinguish dark lesions from the background
Kande [139]	• Pixel classification using support vector machine • Mathematical morphology	**Pixel Based** SN = 100 SP = 91	• 54 clinically acquired retinal images from hospital were used • Intensity information from various channels have been utilized	• Tested on 35 images from public database • Images are resized to same scale, resulting in incorrect detections • Unable to detect lesions in low contrast images
Seoud [111]	• Entropy approach • Dynamic shape features • Random forest classifier	**Image Based** SN = 87.7 SP = 85.9 **Pixel based** SN = 38	• Private database of 1006 images and publicly available database are used • Both lesion and image-based evaluation is carried out • Can be extended for other lesions	• Pixel based low sensitivity implies most of the lesions were not detected • Unable to distinguish between hemorrhages and microaneurysms

*SN - Sensitivity, SP-Specificity, Acc-accuracy, TPR-true positive rate, FPR- false positive rate

The initial attempt on the detection and segmentation of micro aneurysms was made by Cree *et al*. and Spencer *et al.* [102, 103]. They applied top hat transformation to discriminate

retinal lesions and blood vessels. Afterwards, they applied region growing method to segment candidate lesions. Although top hat transformation was very sensitive to microaneurysms, it resulted into many false positives because of the used linear structuring element that tends to detect blood vessels as microaneurysms. Spencer *et al*. applied shade correction and dynamic range normalization as preprocessing steps to improve the sensitivity of the segmentation of candidate microaneurysms using top hat transformation. Afterwards, the true microaneurysms were segregated from the spurious responses using a rule-based classifier trained using various intensity and shape-based features. The primary difference between the method proposed by Spencer and Cree is in the classification step, where varying classifiers and features were used. A similar approach for red lesions based on feature extraction and classification was also studied and implemented by Ege *et al*. [74]. Another approach to overcome the shortcomings of the top hat transformation-based methods was proposed by Walter and Klein [104, 105]. They applied bounding box closing method instead of linear structuring element for the detection of candidate microaneurysms. Similar technique was developed by Sinthanayothin *et al.* for the segmentation of dark lesions where recursive region growing and Moat operator was used for optimal recognition of micro aneurysms and hemorrhages [106]. Another approach to detect micro aneurysms based on Gaussian template matching in wavelet space was developed by Quellec *et al.* [107]. Images were partitioned into sub bands having complementary information of micro aneurysms. However, these methods reported low sensitivity and spurious responses due to overlapping of blood vessels with the dark lesions. A solution to this problem was addressed by feature extraction-based methods in which a set of features were extracted from the candidate regions of retinal images, and classification algorithms were used to obtain the final segmentation of dark lesions.

Niemeijer *et al*. combined the candidates detected using mathematical morphology with the candidates detected from pixel classification-based system [108]. Afterwards, to achieve

the best performance, number of classifiers were tested to classify each of the objects as either a dark lesion or non-dark lesion. However, the computational time of 15 minutes for final classification limits the method for practical applications. Usher *et al.*, after the identification of anatomical structures, classified each retinal image as normal and abnormal according to the presence of number of micro aneurysms and hemorrhages [109]. Another method based on feature extraction and classification was proposed by Gracia *et al*. [110]. Initially, a set of features were extracted from candidate regions, and a feature selection algorithm was applied to choose the adequate feature subset for the effective detection of dark lesions. Afterwards, number of neural network classifiers were used for final segmentation. However, the low specificity of these methods proves that there were more incorrectly detected healthy retinal fundus images as pathological retinal fundus images. Recently, Seoud *et al*., proposed a three-step algorithm for dark lesion detection [111]. Firstly, an entropy-based approach is used to locate and eliminate optic disk followed by the candidate lesion extraction to extract a set of features. Secondly, to discriminate false positives from true lesion structures dynamic shape-based features were used. Finally, to distinguish between lesion and non-lesion, random forest classifier is used on the test retinal image. The method obtained the per-image sensitivity/specificity of 87.7/85.9 on a private database of 1006 retinal images. However, per-lesion sensitivity of 38% implies that most of the lesions were not detected in retinal images. The literature review of dark lesions reveals certain limitations which can be summarized as: (i) These methods segment clear and well-contrasted red lesions especially microaneurysms, (ii) they are incapable of differentiating dull and small lesions from the background of retinal image, resulting in many false detections, (iii) limited number of attempts have been made in literature to precisely eliminate retinal blood vessels and optic disk prior to the segmentation of lesions and lead to misclassification, (iv) most of the methods focused exclusively in the detection of either microaneurysms or particular type of hemorrhage, (v) methods were

evaluated either with open source benchmark databases or only with clinically acquired private database, therefore their generalization capability is uncertain, and (vi) ambiguity in the identification of number, size and precise boundary among red lesions due to their similar morphology and associated heterogeneity.

2.5 DIABETIC RETINOPATHY SCREENING AND GRADING

Numerous computer-aided diagnostic methods have been developed for disease detection from various body using medical images such as mammograms, ultrasound, ECG, MRI, fundus etc. [142-151]. In the sections, as previously mentioned, different methods were described to address the detection of various anatomical structures and lesions present in retina. The identification of these structures is necessary to judge the severity level of diabetic retinopathy. As a result, numerous computer-aided diagnostic methods were proposed for the detection of diabetic retinopathy using these methods. Such computer-aided diagnostic methods are summarized in Table 2.5 [152-161,18].

Table 2.5 Brief detail of previous research works related to diabetic retinopathy screening

Author (Ref.)	Method used	Task	Number of retinal images	Performance Measures (%)
Pires [152]	• Bag of visual words • Semi soft coding • Max pooling Techniques	Detection of lesions related to diabetic retinopathy	1077 (DR1) 520 (DR2) 1200 (MESSIDOR)	AUC = 94 .20
Mookiah [153]	• Multi resolution analysis • Feature ranking framework • Wavelet transform	Differentiated between normal and diabetic retinal images	340 (Clinical)	(Image based) Acc = 94.17 SN = 92.81 SP = 96.27
Welikala [154]	• Dual classification • SVM classifier • Genetic algorithm	Detection of only proliferative diabetic retinopathy	45 (MESSIDOR) 15 (Clinical)	(Region based) SN = 91.38 SP = 96.00 (Image based) SN =100 SP = 97.50
Prakash [155]	• Morphological operations • Region growing method and SVM	Graded images into mild, moderate, severe NPDR and PDR	10 (Clinical)	(Image based) SN =80 SP = 100 ACC = 90

Contd…

Author (Ref.)	Method used	Task	Number of retinal images	Performance Measures (%)
Akram [157]	• m-Mediods based approach • Gaussian mixture model • Hybrid classifier	Graded images into mild, moderate and severe NPDR	89 (DIARETDB) 40 (DRIVE) 81 (STARE) 1200 (MESSIDOR)	(Image based) SN = 99.17 SP = 97.07 ACC = 98.52 (Lesion based) SN = 96.41 SP = 93.86 ACC = 94.98
Wong Li Yun [158]	• Backpropagation neural network	Graded images into mild, moderate, severe NPDR and PDR	124 (Clinical)	(Image based) SN = 91.7 SP = 100 PPV = 84
Mishra [159]	• K nearest neighbor classifier	Detected severity level based on identification of limited number of lesions	Not mentioned	Not evaluated
Verma [160]	• Random forest classifier	Detection of mild, moderate and sever NPDR based on identification of limited number of lesions	65 (STARE)	ACC = 87.50
Ahmad Fadzil [161]	• Gaussian Bayes classifier • CLAHE based enhancement	Detected only no DR and severe NPDR/PDR	256 (Clinical)	(Image based) SN = 84 SP = 97 ACC = 95
Sohini Roychowdhury [156]	• Gausian mixture Model • K nearest neighbor • Support vector machine	Graded images into four stages of diabetic retinopathy	1200 (MESSIDOR)	(Image based) SN =100 SP = 53.16 AUC = 90.4
Figueiredo [18]	• Hessian multiscale analysis • Cartoon and texture decomposition	Detected patients with the presence or absence of diabetic retinopathy	2870 (DR images) 42900 (Normal images)	(Patient based) SN = 95.32 SP = 65.05

*SN - Sensitivity, SP-Specificity, Acc-accuracy, AUC-Area under the curve

Pires *et al*. screened retinal images with diabetic retinopathy solely based on the presence or absence of retinal lesion. They detected various dark and bright lesions using bag-of-visual words, semi soft coding and max pooling techniques [152]. The authors however did not classify the type of lesion detected and assessed only the presence or absence of the diabetic retinopathy. The method reported the area under the ROC curve of 94.2%. Whereas, Mookiah *et al*. proposed a similar diabetic retinopathy screening method to discriminate between normal and pathological retinal image using feature extraction and reported AUC of 94.17% [153]. Welikala *et al*. applied four-dimensional feature vector to feed an SVM classifier and recognized only severe stage of diabetic retinopathy with sensitivity/specificity of 91/96

respectively [154]. Prakash *et al.* classified retinal images into five severity grades of diabetic retinopathy by applying dual-stage classification using NN-SVM and achieved accuracy of 80% [155]. However, these methods were computationally expensive. Roychowdhury detected dark and bright retinal lesions using 30 set of optimized features [156]. They applied hierarchical classification approach to eliminate the false positives and then final classification of dark and bright lesion structures is carried out. Per-image sensitivity of 100% and low specificity of 53.16% proves the incapability of the algorithm to detect normal images as healthy during classification process. Akram *et al*. proposed a three-step method consisting of preprocessing, extraction of candidate lesions, feature set formulation and final classification for grading the severity of diabetic retinopathy [157]. The method combines m-Medoids modeling using Gaussian mixture model in an ensemble to form a hybrid classifier. The proposed system achieved per-image and per-lesion sensitivity/specificity/accuracy of 99.17/97.07/98.5 and 96.41/93.86/94.88 respectively. However, the process of hybridization of classifiers proves it to be a computationally expensive. The diabetic retinopathy screening system developed by Wong Li *et al*., identified four stages corresponding to normal retina, moderate and severe non-proliferative diabetic retinopathy, and proliferative diabetic retinopathy in 124 retinal fundus images [158]. Classification of these four stages was achieved using a three-layer feed forward network. The authors reported the sensitivity/specificity of 91.7/100 respectively. However, the major limitation of this method is that the authors used the limited number of test images used for training the classifier which makes it unsuitable for practical applications. A similar approach based on diabetic retinopathy related features was proposed by Mishra *et al*. [159]. Four stages of severity related to diabetic retinopathy were identified using a KNN classifier. However, the authors did not calculate the performance parameters making the method incapable to demonstrate the accuracy. Verma *et al*. classified retinal images into normal, moderate and severe non-proliferative diabetic retinopathy stages by quantifying blood vessels and hemorrhages [160]. The authors reported the classification

accuracy of 87.5% for pathological images using random forests classifier. However, the method did not segment other lesions necessary for the precise grading of non-proliferative diabetic retinopathy. Recently, Figueiredo *et al*. applied a wavelet and multiscale image analysis-based thresholding method for the segmentation of dark and bright lesions and resulted in collective per-image sensitivity/specificity of 95/70 respectively [18]. The method was also evaluated for detecting the presence or absence of diabetic retinopathy in a patient and resulted in an average sensitivity/specificity of 95.32/65.05 respectively. However, the method proposed different binary detectors to detect distinct types of lesions such as isolated dots, clusters of dotted lesions and large/medium lesions. Also, separate mathematical settings for each type of retinal lesion demonstrates that the method is incapable for practical applications.

The studies on diabetic retinopathy screening and grading methods have some shortcomings such as: (i) most of the state-of-the-art screening methods rely on the detection of specific retinal lesion, whereas diagnostic interpretation for diabetic retinopathy involves the detection of all dark and bright lesions, (ii) limited number of methods have been designed to grade diabetic retinopathy after elimination of anatomical structures. A better grading system can be designed with the segmentation of retinal lesions related to diabetic retinopathy after removal of spurious responses generated from anatomical structures, (iii) there have been only few methods in literature to provide objective performance parameters calculated on sufficient number of images, therefore their generalization capability is uncertain and (iv) there have been only few attempts in literature devoted to the classification of retinal images into different severity levels of diabetic retinopathy based on quantitative evaluation of dark and bright retinal lesions. Therefore, it is challenging to identify the severity levels of non-proliferative diabetic retinopathy in retinal fundus images for general clinical use.

2.6 CONCLUDING REMARKS

Based on the critical review of the literature, the following conclusions have been drawn:

(i) Literature related to blood vessels segmentation indicates that different filtering, morphological, supervised, thresholding-based methods are commonly used for the segmentation of retinal blood vessels. Hybrid models using thresholding and supervised methods provide the idea of multiscale implementation and have shown good segmentation results for pixel wise classification of blood vessel and non-blood vessel structures. The connectivity in geometrical structure of blood vessels was not preserved in most of these hybrid approaches. Thus, in the present work, this research gap related to the proper connectivity of segmented blood vessels is taken care of.

(ii) A comprehensive literature survey on optic disk detection and segmentation reveals that the blood vessels convergence-based methods are best suitable for optic disk detection. The efficiency of precise location of optic disk using blood vessels convergence-based method is improved in the present work by extracting and then incorporating other optic disk related features such as its contour, circularity and blood vessel crossings of optic disk.

(iii) Exudates segmentation methods (specially designed for the detection of progressive diabetic retinopathy) and bright lesions segmentation methods, as proposed in literature, have their own advantages and disadvantages. It was also observed after extensive literature review on the combination of two or more methods, to utilize the advantages of each method, aids in reducing false positives due to spurious responses during segmentation of exudates. Also, most of the previous work segment the exudates without elimination of anatomical structures, and so result into overlapping responses. Therefore in the present work, to increase accuracy and preciseness of the segmentation of exudates, adaptive quantization and dynamic thresholding-based methods are combined after the segmentation and elimination of anatomical structures.

(iv) Extensive literature available on bright and dark lesions segmentation methods indicates that geometrical and morphological features are common in providing differentiation

among various retinal lesions to detect non-proliferative diabetic retinopathy cases. Even though these features have shown good results in segmentation of retinal lesions, still there is a need of improvement. That improvement can be obtained in the present work by the inclusion of diverse type of features such as shape, size, intensity and texture. The extracted set of diverse features is applied on specifically designed two-step neural network classifier to improve the accuracy of proposed computer-aided diagnostic system.

(v) Presently, most of the methods available in literature use open-source benchmark databases comprising of clear retinal images to develop and test computer-aided diagnostic methods. An individual open-source retinal image database is designed for specific purpose such as e-Ophtha EX database consisting of only exudates is mainly designed for the evaluation of methods for exudates segmentation. Therefore, evaluation of diabetic retinopathy detection methods on such databases is not justified. Although few researchers have combined various open-source databases to remove this ambiguity, but still clinically acquired images which are encountered by ophthalmologists in day to day practice should also be the part of the database. Therefore, in order to maintain diversity of retinal images with respect to type of lesions, field of view, number of patients, machine settings etc., a composite database comprising of both clinically acquired retinal fundus images with the available open-source benchmark retinal image databases is considered in the present work. Also, the evaluation of diabetic retinopathy detection methods on a large composite database would ensure their generalization capability.

Chapter 3

Methodology and Development of Benchmark Database

INTRODUCTION

The research methodology is a systematic structure of research in order to comprehend it technically by considering all the steps collectively. It provides an outline of the procedure that is supposed to be followed in order to accomplish research objectives. A proper layout of research methodology is framed to carry out this research work related to the designing of computer-aided diagnostic solutions for progressive and non-proliferative diabetic retinopathy.

The development of benchmark retinal image database is essential for the reliable evaluation and comparison of computer-aided diabetic retinopathy detection methods. The developed database must comprise various types of retinal lesions with the verification by the experts. In addition, to measure the consistency of the computer-aided methods, information about the diagnosis related to these retinal images must also be available. This pre-information about the confirmed diagnosis is called the ground truth. The accuracy of any designed computer aided diagnostic method is tested with the help of these available ground truths. Keeping all these facts in mind, the first requisite for this work is to develop a benchmark retinal fundus image database along with annotated ground truth information for the computer-aided diagnosis of diabetic retinopathy. In this light, this chapter present the designed experimental methodology, collection of open-source benchmark databases, development of clinical retinal images database, and benchmarking of retinal fundus image database

3.1 DESIGN OF EXPERIMENT

It is required to design an experiment in an appropriate way to accomplish research objectives. The design of the experimental methodology for the present research work is described in this section. Figure 3.1 depicts the flowchart of the design of the experimental methodology. The steps carried out in the designing of the methodology are described below.

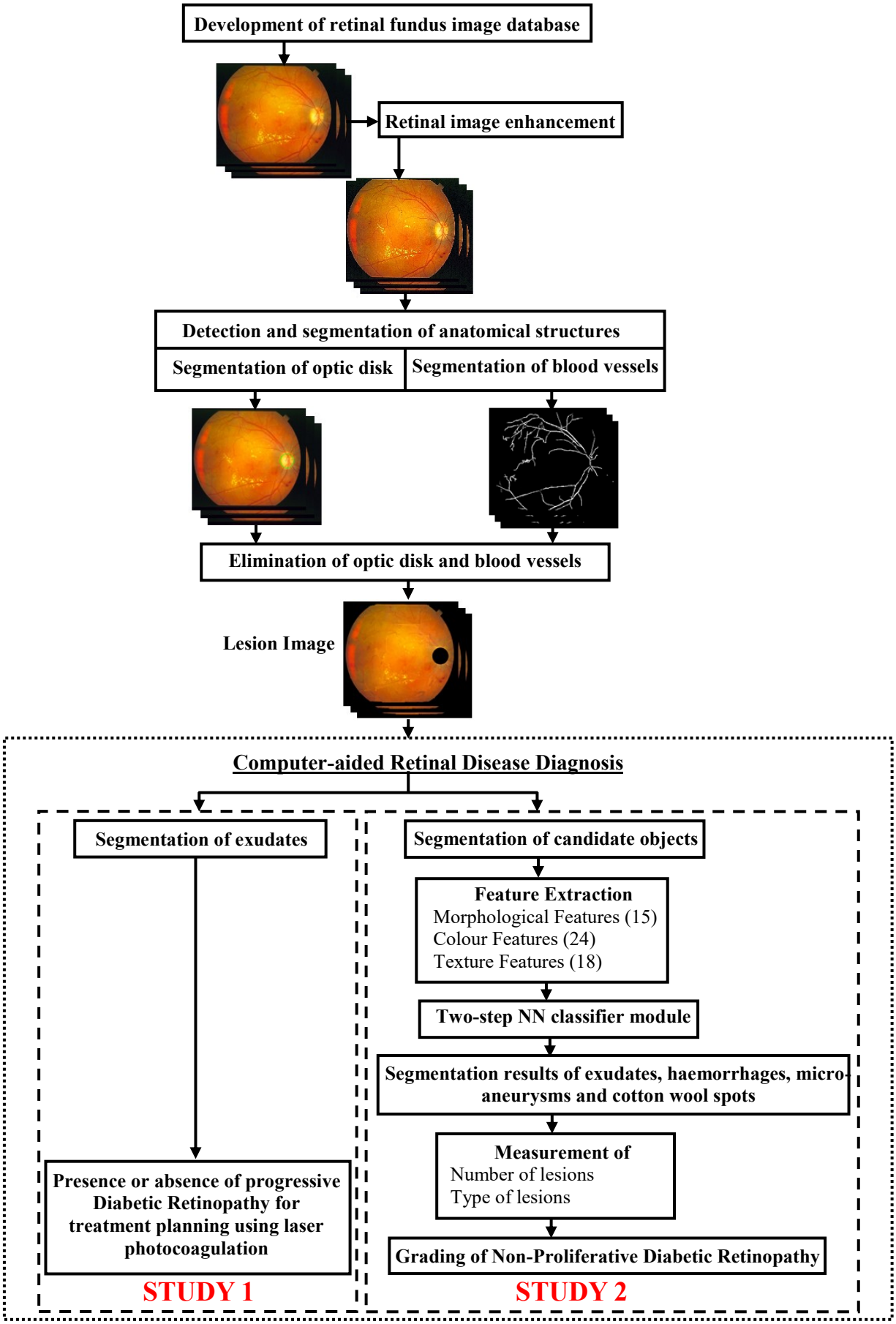

Figure 3.1 Flowchart of the design of experiment

(i) Development of Retinal Images Database:

– Retinal images database for this work, is acquired from two sources: open-source and clinically acquired. Twenty-one hundred and six retinal fundus images are taken from six open-source benchmark databases which are available online and 2942 retinal fundus images are acquired clinically. Clinical retinal fundus image database is developed over a span of two and a half years to carry out the experiments. The database, as acquired from a reputed eye hospital, comprises normal and pathological retinal images. The motivation behind to collect and use retinal image data from various sources is to make the proposed computer-aided diabetic retinopathy detection method independent of image acquisition variability and to make a fair evaluation of effectiveness of the proposed method.

– The annotations of reference ground truth of blood vessels, optic disk and various retinal lesions in retinal fundus images was done by two expert ophthalmologists with the experience of 13 and 10 years in retinal fundus imaging.

(ii) Retinal Image Enhancement:

An enhancement method for retinal fundus images is developed as per the requirement of ophthalmologists. The ophthalmologists require (a) the removal of artifacts due to non-uniform illumination inherited in retinal images up to an extent that an artifact removal method should not deteriorate the information hidden behind the artifacts, (b) the reduction of blurring in retinal images for better visualization of details, and (c) an overall good contrast of retinal fundus images to reduce the fatigue associated with visualization of retinal lesions hidden in dark background of retinal images. With all these considerations, retinal image enhancement method is designed for better visual quality as compared to the original retinal fundus images.

(iii) Segmentation and Elimination of Anatomical Structures:

In this step, anatomical structures such as blood vessels and optic disk are identified, segmented and separated from background. The resulting image, termed as lesion image, is then used for retinal lesions identification and classification. The detection and elimination of anatomical structures aids in reducing the spurious responses in the further processing steps designed for retinal lesion identification such as detection of bright and dark lesions from the retinal fundus image.

Computer-aided diagnostic methods in this work are designed for the detection of two diseases related to diabetic retinopathy, i.e. progressive diabetic retinopathy and non-proliferative diabetic retinopathy.

(iv) Detection of Progressive Diabetic Retinopathy (Study 1):

Bright retinal lesions such as exudates are one of the earliest and most prevalent signs of the onset of chronic diabetic retinopathy termed as progressive diabetic retinopathy. The ophthalmologists segment and treat exudates to cease the progression of retinopathy from reaching vision threatening complications. Therefore, to identify the presence of progressive diabetic retinopathy in retinal images bright lesions namely exudates are segmented. The method proposed in this work reliably segment exudates using adaptive image quantization and subsequently dynamic decision thresholding irrespective of associated heterogeneity, bright and faint edges. The precise detection of exudates is further used for treatment planning of progressive diabetic retinopathy where the physicians need to determine the precise area of exudates to make it expose to laser for photocoagulation.

(v) Detection and Grading of Non-Proliferative Diabetic Retinopathy (Study 2):

Experienced ophthalmologists judge the severity level of non-proliferative diabetic retinopathy to cease diabetic retinopathy at an initial symptomless clinical stage and to

diagnose other retinopathies as diabetic macular oedema and diabetic macular ischemia. The grading of severity level of non-proliferative diabetic retinopathy is based on the interpretation of dark and bright lesions present in retinal image. Therefore, an efficient detection, segmentation and classification of retinal lesions is carried out in the present work to grade non-proliferative diabetic retinopathy. The step wise description of the proposed computer-aided method is given below:

- Segmentation of candidate objects: Retinal lesions, also termed as candidate objects, are defined as group of pixels with homogeneous appearance. Therefore, in the proposed computer-aided diagnosis method, candidate objects are extracted from lesion image by grouping the image pixels with similar attributes such as colour and texture. The use of candidate objects in subsequent processing for the diagnosis of non-proliferative diabetic retinopathy reduces the complexity and redundancy as compared to pixel by pixel processing. Candidate objects, obtained from the composite retinal image database, are collectively used in study 2.
- Ophthalmologists visualize geometrical, colour and texture-based features of retinal lesions to diagnose various stages of non-proliferative diabetic retinopathy. Therefore, five feature extraction methods are taken to extract features, related to first, second and higher order statistics of texture, geometry and color of the candidate objects. The number of features chosen from these approaches are (i) eight first order statistical features, (ii) eight gray level co-occurrence matrix based second order statistical features, (iii) five gray level run length matrix based higher order statistical features, (iv) fifteen geometrical properties based morphological features, and (v) eighteen color-based features using RGB (red, green, blue) and HSI (hue, saturation and intensity) based features.

- The discrimination capability of classification system depends on how accurately the classifier classifies a particular retinal lesion category. In the present work, a two-step neural network classifier is designed for optimized performance in distinguishing various retinal lesion classes associated with non-proliferative diabetic retinopathy.
- Finally, computer-aided severity level detection method is proposed in this work for the diagnosis of early stage of non-proliferative diabetic retinopathy. This method grades the severity level of non-proliferative diabetic retinopathy by objective quantification of dark and bright retinal lesions detected in the previous step.

Table 3.1 Open source benchmark databases of retinal fundus images

Database	Image Acquisition	Number of Images	Resolution (pixels x pixels)	Types of lesions present
DRIVE [162]	3-CCD camera with 45-field of view	20 color fundus images (Test set) 20 color fundus images (Train set)	768 x 584	Exudates, hemorrhages, micro aneurysms and abnormal blood vessels
Image – Ret (DIARETDB0, DIARETDB1) [163]	50-field of view	DIARETDB0: Total of 130 images: 20 are healthy and 110 with DR DIARETDB1: Total 89 images: five are healthy and 84 with DR	1500 x 1152	Exudates, hemorrhages, micro aneurysms and abnormal blood vessels
MESSIDOR [164]	3CCD camera at 45-field of view	1200 images	1440 x 960, 2240 x 1488 and 2304 x 1536	Exudates, hemorrhages, micro aneurysms and abnormal blood vessels
e-Ophtha EX [165]	OPHDIAT Tele-medical network	It contains 47 images with exudates and 35 healthy images	2048 x 1360	Exudates
e-Ophtha MA [165]	OPHDIAT Tele-medical network	It contains 148 images with micro aneurysms or small hemorrhages and 233 healthy images	2048 x 1360	Micro aneurysms
STARE [166]	Top con TRV 50 fundus camera at 35-field of view	400 images	605 x 700	Exudates, hemorrhages, micro aneurysms and abnormal blood vessels

3.3 OPEN-SOURCE RETINAL FUNDUS IMAGE DATABASES

A well-constructed retinal image database needs to take into consideration all aspects of diversified uses of retinal images in order to diagnose various diseases. With this purpose, a

number of retinal image databases have been constructed and made public for the validation of methods proposed for the diagnosis of particular characteristic features related to retinal abnormalities [162-166]. These databases are termed as open-source benchmark databases. These databases of retinal images, as described in table 3.1, are developed with different goals and therefore images in these databases have different characteristics and levels of completeness. Some of the benchmark databases are openly available for the assessment of the computer-aided methods developed for diabetic retinopathy screening. The purpose of these databases is to check the strength of automatic screening of diabetic retinopathy by computer-aided methods with respect to the procedures used in medical domain. A brief description of all the databases and about their provided ground truths is described as follows:

(i) DRIVE: Digital retinal images for vessel extraction

The DRIVE database comprises of 40 colored retinal fundus images that had been acquired using canon non-mydriatic 3CCD camera with the resolution of 768 x 584 pixels at 45^0 FOV with 8 bits per color channel [162]. This database contains 33 healthy and 7 pathological retinal fundus images. The set of 40 images has been divided into train and test set, both containing 20 images. This database provides pixel level blood vessels ground truth annotations for the test set.

(ii) DIARETDB0 and DIARETDB1 Database

The DIARETDB0 database comprise of 130 colored retinal fundus images acquired using a fundus camera with 50^0 FOV [163]. The 130 retinal images available in the database comprise of 110 images depicting signs of diabetic retinopathy (hard exudates, soft exudates, microaneurysms, hemorrhages etc.) and 20 are normal retinal images. The DIARETDB1 database consists of 89 colored retinal fundus images and they have been acquired using a fundus camera with 50^0 FOV. The 84 retinal images available in the database contain mild signs of diabetic retinopathy including exudates and the remaining

5 are of healthy retinal images. DIARETDB0 and DIARETDB1 were one of the first publicly available databases consisting of manually marked location of exudates as reference standard. However, these annotations contain only the encirclements of the areas associated with lesions in retinal images.

(iii) MESSIDOR Database

The MESSIDOR database consists of 1200 retinal fundus images captured using a Topcon TRC NW6 non-mydriatic fundus camera with multiple resolutions of 1440 x 960, 2240 x 1488 or 2304 x 1536 pixels at 45^0 FOV using 8 bits per color plane [164]. This database provides the diagnostic findings of various retinal images. However, it does not provide reference standard for retinal lesions segmentation.

(iv) e-Ophtha EX and e-Ophtha MA Database

Images of these databases are acquired with different resolutions. Resolution range varies from 1440 x 960 pixels to 2544 x 1696 pixels. All the images are obtained from OPHIDAT telemedicine network for diabetic retinopathy. The e-Ophtha EX database consists of 82 retinal fundus images, with 35 healthy retinal images and 47 pathological retinal images [165]. Pathological retinal images consist of exudates related to mild, moderate and severe diabetic retinopathy. The e-Ophtha MA database consists of 233 healthy retinal fundus images and 148 images with microaneurysms or small hemorrhages. In addition, e-Ophtha EX and e-Ophtha MA databases are the only databases consisting of pixel level reference ground truth annotations of exudates and microaneurysms segmentation respectively. These annotations are beneficial for precise assessment of the efficiency of various exudates and microaneurysms segmentation methods.

(v) STARE: Structured analysis of the retina

The STARE database comprises of 400 colored retinal fundus images that been acquired using by a Topcon TRV-50 fundus camera with the resolution of 605 x 700 pixels at 35^0 FOV with 8 bits per RGB plane [166]. This database contains exudates, micro-aneurysms and hemorrhages of varying shapes and sizes. The database provides the diagnostic findings related to diabetic retinopathy for each retinal fundus image, but it does not contain the reference ground truth annotations of various retinal lesions like exudates, hemorrhages etc.

The main limitations of the open-source benchmark databases are that these databases (i) comprise of limited number of retinal images ranging from 40 to 1200, (ii) contains only well contrasted and clear retinal images, (iii) are constructed by considering the specific type of retinal disease diagnosis, (iv) does not include annotated ground truths of all retinal anatomical and pathological structures and (iv) does not include diversities related to disease progression. Due to these limitations, open-source benchmark databases are not complete and descriptive retinal image database sources for evaluating computer-aided systems for real time diagnosis of diseases. It is due to the fact that experts have to deal with varying types of retinal images in real time domain. Thus, in order to provide a real time solution for retinal disease diagnosis a representative clinically acquired retinal fundus image database is constructed in the present work with the help of expert ophthalmologists.

In the proposed work the aforementioned limitations are dealt with by designing a composite benchmark retinal image database: (i) including 2942 clinical and 2016 open-source images with varying attributes such as such as position, dimensions, shapes and color in retinal images, (ii) well-defined annotated ground truths of anatomical structures such as blood vessels and optic disk, dark and bright retinal lesions and stages of diabetic retinopathy. In addition, an evaluation framework is also proposed for the construction of benchmark medical image database.

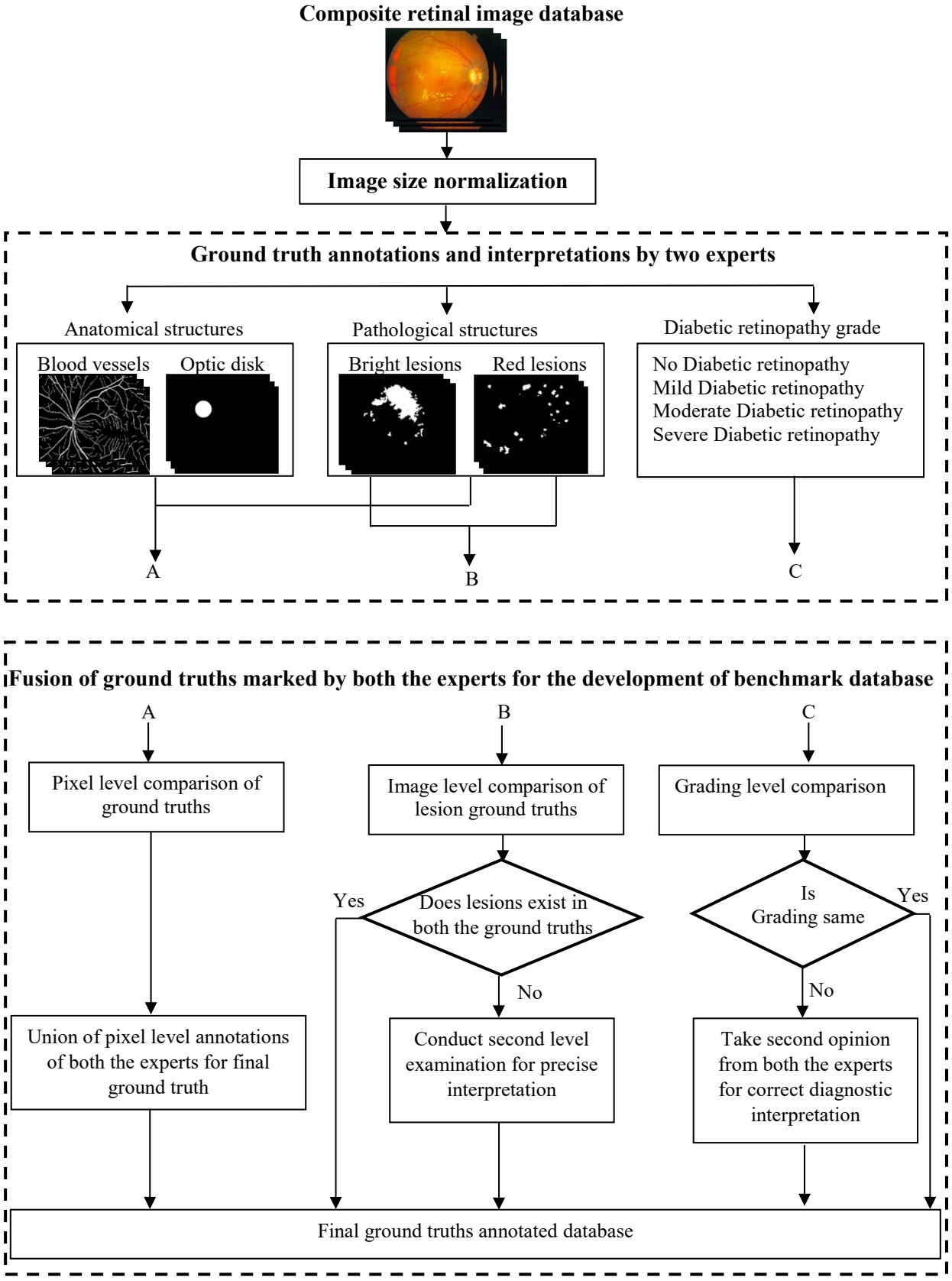

Figure 3.2 Framework for the construction of benchmark database

3.4 BENCHMARKING OF RETINAL IMAGE DATABASE

Benchmark retinal image databases are a significant resource for the development and evaluation of computer-aided diagnostic systems. Figure 3.2 illustrates the procedure of benchmarking framework which comprises of four main components, viz. (i) development of clinically acquired retinal image database, (ii) image size normalization, (iii) annotation of ground truths, and (iv) fusion of ground truths from multiple experts.

3.4.1 Development of Clinical Retinal Image Database

The database is developed to carry out diabetic retinopathy diagnosis through computer-aided fundus image analysis. The study was approved by the medical ethics committee of the Department of ophthalmology at Sri Guru Harkrishan Sahib Eye Hospital, Mohali, India. Clinical retinal images were of men and women who underwent an eye examination during the period January 2014 to July 2017. Retinal fundus image database of healthy and affected retina of these patients was developed over this period of two and half years from the images acquired during their examinations. These images were acquired using Top-Con TRC-50 DX fundus camera with 3216 x 2136 pixels resolution at 45^0 FOV with 8 bits per color channel. These settings remained unchanged except for changes made necessarily for obtaining the best field of view. Retinal image database for this work is developed with the intention to capture large variations in visual appearance of different retinopathy findings. The consents of patients for using their images for research were taken prior to image acquisition.

Collection Criteria:

A total of 2942 retinal images with varying color, brightness and quality were collected in this period from 482 patients. There were 280 men (age range: 25-83 years; mean age: 51 years) and 202 women (age range: 24-75 years, mean age: 44 years). The collection of retinal images was based on the following criteria:

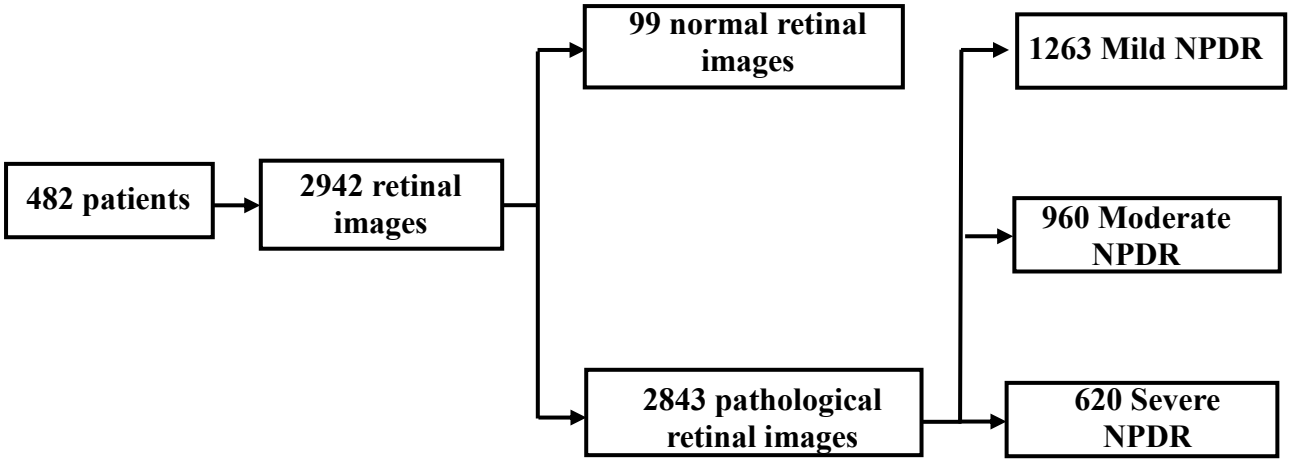

Figure 3.3 Distribution of acquired database among various stages of diabetic retinopathy

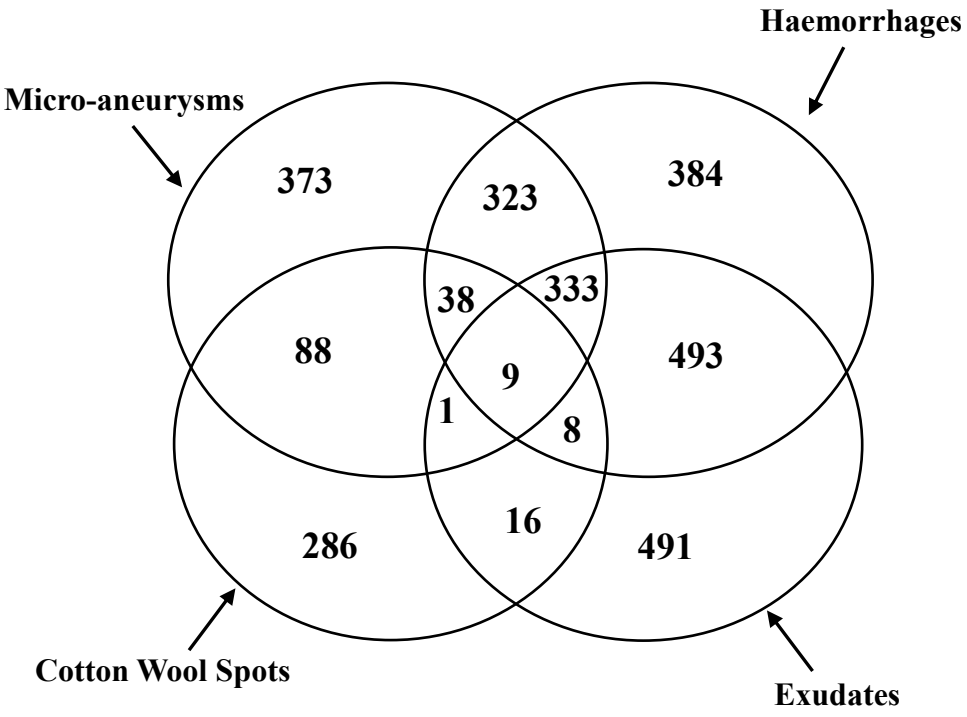

Figure 3.4 Distribution showing number of images of various retinal lesions in clinically acquired retinal image database

- Diversified clinical retinal images were acquired including (i) different age groups of men and women, (iii) various stages of progression of diabetic retinopathy, and (iv) variation in color, brightness and quality.
- Two images of each patient were collected for diabetic retinopathy diagnosis.

- Acquired retinal images should (i) be free from excessive artifacts, (ii) have complete field of view, (iii) possess diagnostic information as confirmed by an expert ophthalmologist.
- The development of database is carried out till the acquisition of sufficient number of images to provide maximum diverse combinations of lesion classes.

Categorization:

The database developed during the period of two and a half years contains 2942 retinal fundus images acquired from 482 patients for the present study. Out of these 2942 images, 99 are healthy and 2843 are pathological retinal images. Pathological retinal images comprise of 1351 images with hard exudates, 446 images with cotton wool spots, 1165 images with micro aneurysms, 1588 images with hemorrhages. Images related to non-proliferative diabetic retinopathy can be further categorized into various stages based on their grading. The need of present work is to categorize clinically acquired database among (i) various diabetic retinopathy types and grades, and (ii) various types of lesions. The categorization of database, as summarized in figure 3.3, is done according to diabetic retinopathy grades. Whereas, figure 3.4 depicts the categorization of images in database with respect to the number and types of retinal lesions present.

3.4.2 Image Size Normalization

To determine the practicability of the computer-aided method in diagnosing diabetic retinopathy, the composite database presented in this work, includes diverse types of images with varying attributes. However, the key issue in designing a generalized computer-aided diagnostic method is that it should be capable to handle various variabilities associated with image scale, contrast and quality. Therefore, to deal with heterogeneity related to image scale, the retinal fundus images from varying databases are needed to bring at same scale by rescaling the images before the construction of ground truths and further processing. Two images from composite database, as shown in figure 3.5, are taken to illustrate the need of rescaling in this

research work. Retinal image, as shown in figure 3.5 (a), is the image with the smallest size in the clinical database, whereas retinal image of figure 3.5 (b) is the largest image. It can be observed that the width of blood vessel in smallest size image is 9 pixels wide and that in the largest size image is 28 pixels wide. Similar kind of diversities can also be observed with other anatomical structures and lesions present in retinal images. Thus, an image size normalization method by rescaling retinal images is designed in such a way that same type of structures in different retinal images must represent same size to design a consistent computer-aided diagnostic method.

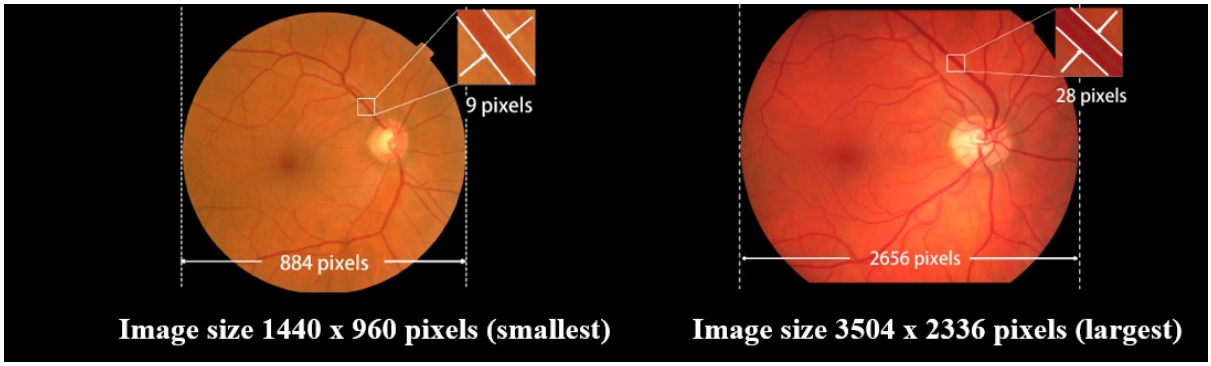

(a) **(b)**

Figure 3.5 (a) Clinically acquired smallest size image of 1440×960 pixels in which main vessel width is of 9 pixels, (b) clinically acquired largest size image of 3504×2336 pixels in which main vessel width is of 28 pixels.

One of the most general method to perform image size normalization is to use a fixed reference (based on size of images) to rescale all images to that reference [167,168]. However, the major limitation of this method is that they do not consider the expanse of information (i.e. field of view) in a retinal image. Therefore, scaling the retinal image size cannot precisely represent the scaling of the pixel size of an image. For example, as depicted in figure 3.5, the ratio between the width of blood vessels in largest and smallest size images is 3.1 (28/9). However, the ratio of the size of retinal images is 2.4 ({3504 x 2336}/{1440 x 960}). The bias in ratios due to rescaling also occurs for other surface measures such as retinal lesions. Rescaling methods related to anatomical structures, such as the diameter of the optic disk and

the width of blood vessels are hard to realize because of several limitations. One major limitation is the variations in anatomical size of structures from one person to the other. As an example, the theoretical size of the optic disk varies in the range of 1-2 mm in general. Another limitation is difficulty in obtaining a precise segmentation and measurement of retinal structures, such as blood vessels, prior to image rescaling. The distance between optic disk and fovea can also be used to rescale images as this distance is relatively constant in human eyes. But the problem is that the optic disk and fovea needs to be detected, which is tedious to locate in all the retinal images. Moreover, they may be absent from some of the retinal images.

Zhang *et al*. observed that the ratio of FOV widths, denoted by d_{FOV}, of largest and smallest images is 3 (2656/884) which is almost equal to the ratio of blood vessel widths i.e. 3.1 [178]. Therefore, the width of the FOV, is a better reference for image size rescaling, as they preserve the complete field of information in retinal images containing different shapes: circular or truncated circle as depicted in figure 3.5 (a) and (b) respectively. Thus, to eliminate the inconsistency associated with image rescaling, a simple and effective FOV based image size rescaling method is proposed that facilitates the development of generalized computer-aided diabetic retinopathy detection methods.

As described above, width of the FOV in retinal images can be considered as a suitable measure for the image size rescaling of retinal images. To measure the width of FOV it is first required to segment FOV from the background region of retinal fundus image. Generally, in ideal cases, FOV appears to be much brighter as compared to the background of the retinal image and is recognized by high intensity changes at their boundaries. Therefore, in such cases background of the retinal image is assumed to be zero. But in real time conditions, the background value is never zero due to non-uniform illumination. The presence of non-uniform illumination causes color and contrast variations in different areas of a retinal fundus image. Also, due to improper illumination in images, as depicted in figure 3.6, the FOV and the

background merge due to presence of very dark region at the border of FOV. Overlapping of FOV with the background will be responsible for false detection of FOV width at the time of image size normalization. Therefore, accurate segmentation of FOV boundary from a retinal fundus image is necessary to perform image size normalization effectively.

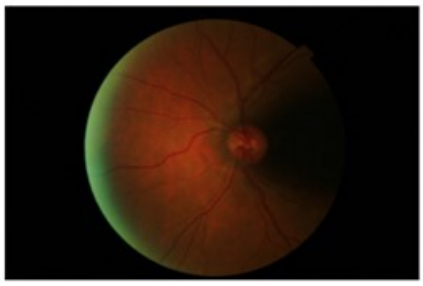

Figure 3.6 Retinal image containing dark region

The designed method, in this work, for FOV segmentation is carried out in two steps and described below:

Step 1: Firstly, the number of distinct shades of grey is reduced in the retinal fundus image by grouping the image pixels with similar attributes using k-means clustering method [169]. These attributes are basically based on grey shades intensity values of supreme of green and red channel retinal image pixels. The k-means clustering method randomly partitions the image pixels into sets of grey shades based on k initial centroids, selected arbitrarily, k being the user specified parameter and the optimum value (k=15) was determined empirically. Then the iterative process is carried out to update centroid of each cluster by taking the mean of pixel values in each cluster. This iterative process continues until all the centroid pixels satisfies the convergence criteria. According to the convergence criteria, the centroid pixels are convergent if all the pixels of an image are assigned to the clusters having the nearest centroids. Lastly, each pixel value is replaced by its corresponding centroid pixel value, resulting in a clustered image.

Step 2: In this step, adaptive thresholding method is carried out to segment FOV boundary from the background of the retinal fundus image. It is accomplished by assessing the range of intensity values of the pixels to be thresholded. Since, the aim is to distinguish FOV from the

background, the thresholding value must be greater than the intensity values of the background pixels. However, it is important how bigger the threshold parameter value should be chosen. It is accomplished by varying the threshold value from zero (corresponding to black) to 38. It was observed that initially, FOV segmentation improved with increase in thresholding value, but after a certain value, i.e. 23 there is no significant improvement in the segmentation of FOV boundary and rather FOV boundary was getting distorted. This is due to the inclusion of pixels corresponding to the inside region of FOV. Thus, the optimized threshold value, with the help of an expert ophthalmologist, for FOV segmentation was set to 23. Some of sample retinal images and the corresponding segmented FOV's are shown in figure 3.7. Figure 3.7 (a-c) shows the original retinal fundus images with dark background region, complete field of view circle and truncated circle respectively. It can be observed that the proposed method was able to segment FOV irrespective of the type of retinal fundus image as shown in figure 3.7 (d-f).

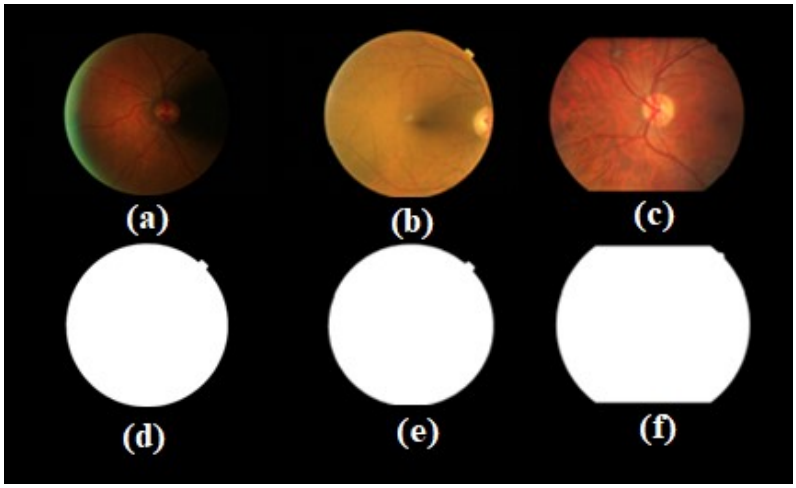

(a), (b), (c): Original retinal fundus images
(d), (e), (f): Segmented field of view structures

Figure 3.7 Original retinal fundus images and their segmented FOV

Finally, the image size rescaling is accomplished by computing the width of FOV of each retinal image, as depicted in figure 3.8. The smallest image and its corresponding FOV width is set as the reference value to resize the varying number of retinal images from a composite database. Resizing is carried out by computing the scale coefficient. Scale coefficient

determines the scaling value with which the original retinal image is to be scaled to obtain the normalized image. It is the ratio of the reference width of FOV and the FOV of original retinal image. Table 3.2 illustrate the values of varying scale coefficients corresponding to different resolutions of retinal fundus images from a composite database.

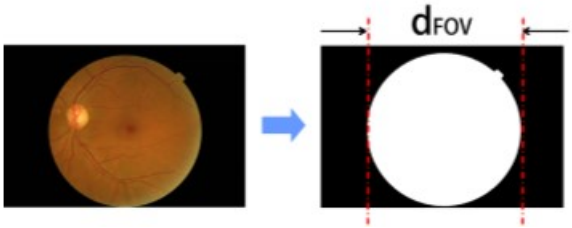

Figure 3.8 FOV width estimation for image size normalization

Table 3.2 Computation of scale coefficients depending on width of FOV

Image Size	Width of FOV	Scale Coefficients
1440 x 960	910	1
1504 x 1000	923	0.99
1728 x 1152	1305	0.70
1936 x 1288	1484	0.61
2048 x 1360	1533	0.59
2544 x 1696	1924	0.47
2816 x 1880	2159	0.42
3504 x 2336	2650	0.34

3.4.3 Ground Truths Annotations

Area of a retinal fundus image that has pixels of interest to provide diagnostically relevant information is reference ground truth. To design a computer-aided diagnostic method for the detection of diabetic retinopathy, reference ground truths of anatomical structures such as blood vessels and optic disk and pathological structures such as dark and bright lesions are required to be annotated. Reference ground truths of these structures are necessary since they are the basis to verify the results of processing related to the detection and classification of particular retinal abnormalities. Also, reference ground truth annotations are essential to perform the quantitative analysis of the methods as well as for their evaluation and comparison. In the

present work, reference ground truth of anatomical structures and lesions are annotated independently using pen & ink application by two expert ophthalmologists with the experience of 13 and 10 years' in their domain. Afterwards, the boundaries of various anatomical structures and lesions are labelled manually by using an application software. Figure 3.9 (a-d) show ground truths of anatomical structures obtained from an expert ophthalmologist corresponding to sample retinal fundus images with varying visual appearance shown in figure 3.9 (e-h) respectively. Similarly, figure 3.10 (a-d) depicts the reference ground truth annotations of bright and dark lesions corresponding to sample retinal images shown in figure 3.10 (e-h). It can be observed that, a single image can have single or multiple types of reference ground truths corresponding to different structures of retina, for example, both dark and bright lesions may appear in a retinal image and therefore different reference ground truths are constructed by an expert corresponding to different lesions. In other words, reference ground truth of a particular structure does not include the ground truth of any other structure present in a retinal image.

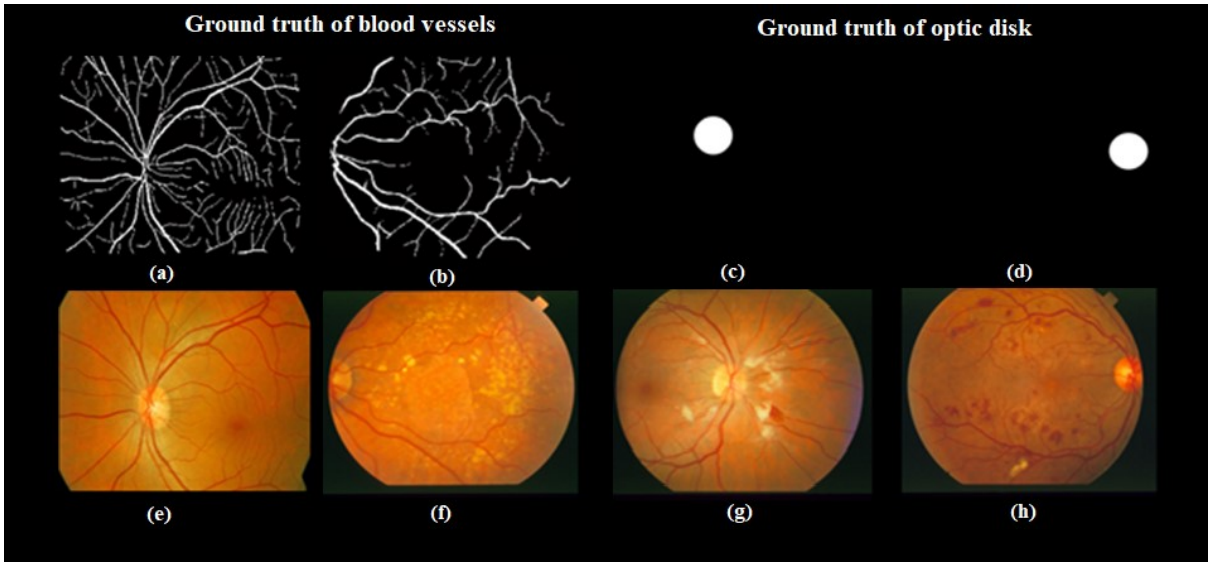

(a), (b): Ground truth of blood vessels
(c), (d): Ground truth of optic disk
(e), (f), (g), (h): Original retinal fundus images

Figure 3.9 Ground truths of various anatomical structures present in sample retinal fundus images

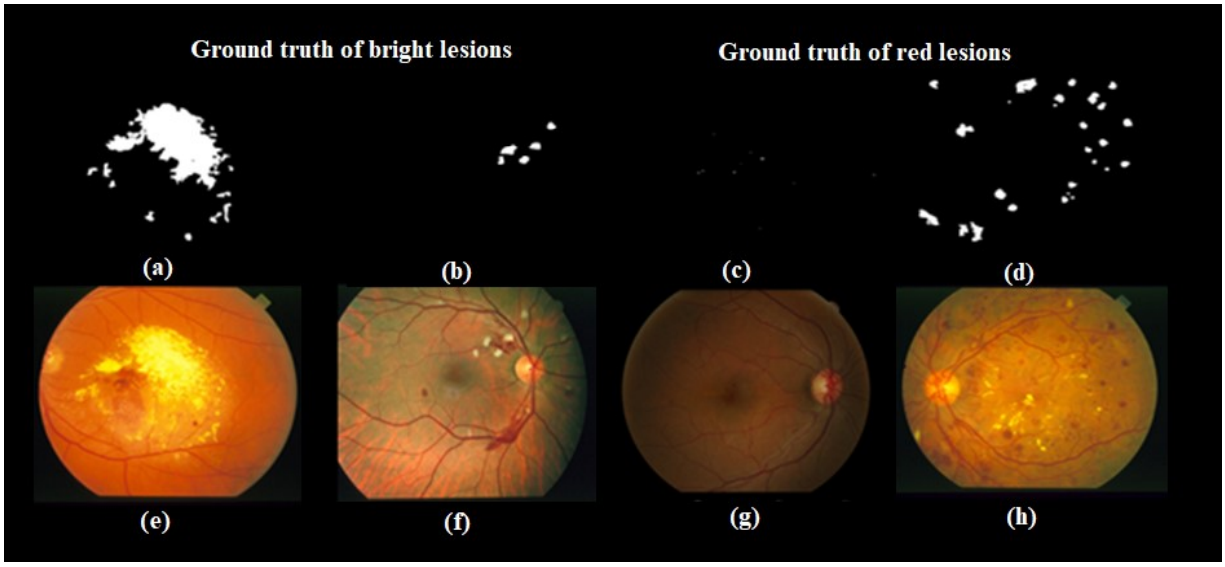

(a), (b): Ground truth of bright lesions
(c), (d): Ground truth of dark lesions
(e), (f), (g), (h): Original retinal fundus images

Figure 3.10 Ground truths of various bright and dark lesions present in sample retinal fundus images

3.4.4 Fusion of Ground Truths from Multiple Experts

In this work, a composite database of 5048 retinal images, comprising of varying types of lesions were first normalized by rescaling the image size to a fixed reference. Afterwards, the soft copy of processed images along with the list of (i) diabetic retinopathy grades such as No DR, mild, moderate and severe, (ii) anatomical structures, and (iii) dark and bright lesions were provided to each expert in their separate chambers for unbiased labeling of structures and grading of images. The ground truth annotations in the present work are manually labeled by the expert ophthalmologists using visual evaluation criteria. Visual evaluation is the ability of an expert ophthalmologist to extract significant information related to anatomical structures and lesions from a retinal image. However, there can exist variations in visual evaluation from expert to expert. Therefore, to avoid variability in the diagnosis of diabetic retinopathy, the ground truth annotations in this work were labeled by two expert ophthalmologists. Since there can exist inconsistencies in the interpretation of multiple experts, it is necessary to develop a

method to appropriately fuse ground truth annotations by both the experts for the construction of reliable ground truth image database.

The reference ground truths marked by both the ophthalmologists signify the pixels corresponding to the ground truth of blood vessels, lesions and diabetic retinopathy grade. Fusion of ground truth interpretations from both the experts was carried out by comparing the ground truths at (i) pixel level, (ii) image level, and (iii) grading level.

(i) Pixel level comparison - In pixel level comparison, ground truth annotations of blood vessels, dark and bright lesions were compared at pixel level using computer-aided tool. It was observed that there was a mismatch of only 5 percent or less in the manual segmentations provided by both the experts. Therefore, in an attempt to not discard any information, the ground truth annotations are combined by taking the union of ground truth pixels from both the experts.

(ii) Image level comparison – Image level ground truths impart information related to the evidence of type of dark and bright lesions and subsequently diabetic retinopathy or not. After analyzing the image level ground truth interpretations from both the experts, it was observed that out of 5048 images of the composite database, 122 images have mismatch in image level ground truths. It was also observed that mismatch was present in the images mainly consisting of microaneurysms. The mismatch is due to the fact that these lesions are one pixel wide and can sometimes be missed during visual interpretation by expert ophthalmologists. Therefore, for such images with inconsistent ground truths, diagnosis was confirmed by second level examination such as OCT, angiography etc.

(iii) Grading level comparison – Diabetic retinopathy grades provided by both the expert ophthalmologists for a retinal image were combined into a single file. Ground truth grades were confirmed on those images that have same opinion by both experts about their grades. After assessing the ground truth grades of all the images from both the

experts, it was observed that out of 5048 images 183 images have mismatch of grades. It was also observed that 172 images out of these 183 images have adjacent ground truth grades i.e. either mild/moderate or moderate/severe from both the experts. This mismatch is due to the subtle difference in the interpretation of mild/moderate or moderate/severe diabetic retinopathy cases. Therefore, in such cases with different interpretation of grades from both the experts, the second opinion of both the experts were taken for correct diagnostic interpretation.

3.5 CONCLUDING REMARKS

The experimental methodology to accomplish research objectives has been presented in this chapter. Its important constituents are design of experiment, collection of open-source databases, development of clinical retinal images database, and benchmarking of retinal images database. In the first subsection, the overview of experimental design has been presented which gives the framework of the studies carried out in the present research work for the diagnosis of diabetic retinopathy. The designing steps carried out such as retinal image enhancement, anatomical structures detection and elimination, retinal lesion detection and classification are presented in detail in the subsequent chapters. In the second subsection, the collection and types of retinal images from various open-source databases are presented. The last subsection describes the details of the steps carried out for the construction of benchmark retinal image database for medical image analysis. The developed clinically acquired retinal fundus image database in the duration of two and a half years is also detailed in this subsection in terms of number of patients, image acquisition, collection criteria, reference ground truth annotations and distribution of database.

Chapter 4

Retinal Image Enhancement and Blood Vessels Segmentation

4.1 INTRODUCTION

The present chapter describes retinal image enhancement and blood vessels segmentation methods for retinal fundus images. It is critically essential that all the characteristic symptoms of the abnormality present in a retinal fundus image must be detected clearly to get high diagnostic accuracy. However, the presence of artifacts and blur, that occur during retinal image acquisition, impose limitations in the accurate detection and segmentation of lesions in retinal fundus images. These artifacts are introduced due to non-uniform illumination which is further responsible for inhomogeneous intensity variations. In addition, the blur, camera dependent factors, further degrade the contrast resolution and impart a visible fuzziness to the image. The detection of retinal abnormality by an experienced ophthalmologist depends on the visualization of various lesions in a retinal fundus image. Consequently, the fuzzy edges of various retinal structures are highly undesirable at the time of accurate lesion detection. Therefore, the retinal image enhancement phase is designed in such a way that the visualization of the definition of retinal structures must improve to provide efficient detection of lesions present in a retinal fundus image. This is implemented by improving the global contrast of the overall retinal image and local contrast of minute retinal structures. Additionally, in order to enhance the visual quality of the retinal images to the optimum, number of parameters were optimized with the help of expert ophthalmologist.

The ophthalmologists visualize variations in geometrical structure of retinal blood vessels in order to diagnose various retinal abnormalities. The initial manifestations of retinal abnormalities can be seen as the deviations in retinal blood vessels from its normal appearance. Figure 4.1(a) is an example image to depict the normal appearance of retinal blood vessels. The deviations in normal blood vessels appear as changes in (i) the widths of arteries and veins, (ii)

bifurcation related parameters, (iii) tortuosity measures, and (iv) microvascular growth of the blood vessels etc. Figure 4.1(b) depicts the contraction in the width of arteries which is termed as arteriolar narrowing. Likewise, figure 4.1 (c) shows the reduction in bifurcation angle in between parent and its two daughter branches. The reduction in bifurcation angle in pathological images can be confirmed by the standard range of bifurcation angle for healthy retinal blood vessels. Lastly, figure 4.1(d) highlights the tortuosity and microvascular growth in a pathological image. Tortuosity is abnormal twists and turns in retinal blood vessels, whereas microvascular growth is the appearance of new minute blood vessel structures across the retinal surface called as neovascularization.

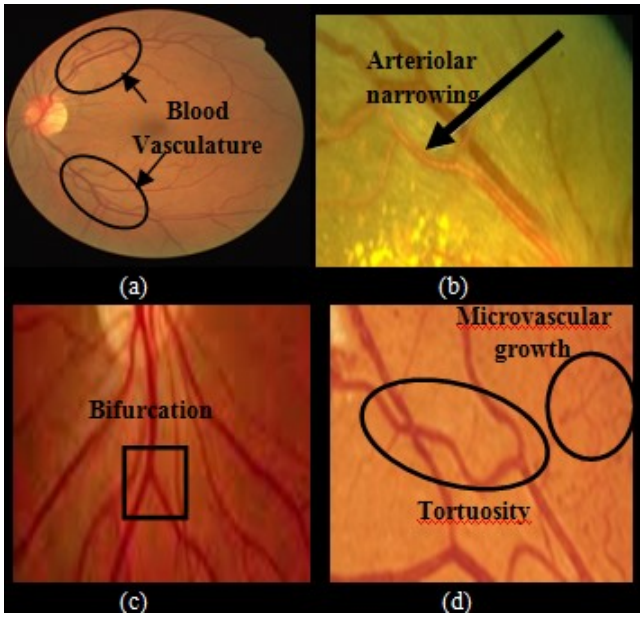

Figure 4.1 (a) Healthy retinal image, (b) Retinal image depicting variations in arteries, (c) Retinal image showing bifurcation, (d) Retinal image with tortuosity and microvascular growth

Another significant task associated with retinal blood vessels is its reliable exclusion for the accurate and efficient detection of various retinal lesions and other anatomical structures. The detection process of lesions such as micro aneurysms, haemorrhages, cotton wool spots, and exudates etc. may produce false positives if blood vessels are not properly eliminated from the retinal fundus image. False appearances occur because retinal blood vessels present similar contrast with lesions and thus interfere in its extraction. Therefore, the precise exclusion of

retinal blood vessels will highlight the minute lesions with respect to background which will be further helpful in diagnosing the possible retinal abnormality. In addition, the geometry of retinal blood vessels is such that it appears like branches of a tree merging into the optic disk. It helps in determining the location of other important anatomical structures like fovea and optic disk. Therefore, the precise segmentation of blood vessels, is the first step in extracting diagnostic information for the early detection of diabetic retinopathy. With these points in consideration an efficient blood vessels segmentation method is designed in this work by combining the responses of matched filter, its first derivative and subsequently supervised classification of pixels. The performance of the method has been evaluated on diverse types of retinal images obtained from clinical and open-source databases.

4.2 RETINAL IMAGE ENHANCEMENT

The steps involved in retinal image enhancement are: (i) Two-directional high pass filtering for determining high frequency components, (ii) variance calculation for adaptive contrast enhancement, and (iii) the formation of enhanced image.

4.2.1 Two-directional High Pass Filtering

The presence of non-uniform illumination causes colour and contrast variations in different areas of a retinal fundus image. In addition, the definitions of various retinal structures such as lesions, optic disk and blood vessels are recognized by the high changes in intensity at their boundaries. High intensity changes represent the high frequency components in an image. Therefore, two-directional high pass filtering is applied to improve the perceptual quality of an image by retaining its high frequency components. Also, this processing step emphasizes the details by reducing the blurring effect with the removal of low frequency components. The application of two-directional Laplacian high pass filter on coloured retinal fundus image $I(x, y)$ is mathematically represented as:

$$\nabla^2 = \begin{bmatrix} \nabla^2[R(x,y)] \\ \nabla^2[G(x,y)] \\ \nabla^2[B(x,y)] \end{bmatrix} \tag{4.1}$$

where $R(x,y)$, $G(x,y)$ and $B(x,y)$ are red, green and blue components of $I(x,y)$. Computation of Laplacian operator in horizontal and vertical directions are expressed in Eqs. (4.2) and (4.3) respectively, as given below

$$I_{fil\_H}(x,y) = {\partial^2 I(x,y)}/{\partial x^2} = I(x+1,y) + I(x-1,y) - 2I(x,y) \tag{4.2}$$

$$I_{fil\_V}(x,y) = {\partial^2 I(x,y)}/{\partial y^2} = I(x,y+1) + I(x,y-1) - 2I(x,y) \tag{4.3}$$

where $I_{fil\_H}(x,y)$ and $I_{fil\_V}(x,y)$ are high pass filtered images in horizontal and vertical directions respectively. Actually $\nabla^2[I(x,y)]$ also symbolized as $I_F(x,y)$, is computed from its horizontal and vertical components as shown in Eq. (4.4).

$$\nabla^2[I(x,y)] = {\partial^2 I(x,y)}/{\partial x^2} + {\partial^2 I(x,y)}/{\partial y^2} \tag{4.4}$$

or

$$I_F(x,y) = \left[I_{fil\_H}(x,y), I_{fil\_V}(x,y)\right]^T \tag{4.5}$$

Basically, the application of high pass filter improves the global contrast of a retinal fundus image. But, still there is a need of further enhancement of local areas to highlight the minute details that can be achieved in the next step, i.e. computation of variance and scaling factor.

4.2.2 Computation of Variance and Scaling Factor

Local contrast enhancement is carried out by adding a scaling factor $\sigma(x,y)$ at each spatial location of the filtered image, $I_F(x,y)$, after measuring the local variance around that pixel. The local intensity variation around a pixel of the image, $I_F(x,y)$, is computed in the neighbourhood area of 3 x 3 pixels and can be expressed mathematically as

$$\mathrm{Var_N}(x,y) = \frac{1}{9}\sum_{i=x-1}^{x+1}\sum_{j=y-1}^{y+1}[I_F(i,j) - \bar{I}_N(x,y)]^2 \tag{4.6}$$

where $\bar{I}_N(x,y)$ is the average luminance level calculated over the same neighbourhood region, N, of 3 x 3 pixels area.

Scaling factor $\sigma(x,y)$, as represented by Eq. (4.7), is obtained by choosing a threshold value T_{E_Var} of neighborhood variance parameter. Any pixel of original retinal fundus image having neighborhood variance parameter less than the threshold value T_{E_Var} is considered as a part of low frequency i.e. smooth region of retinal fundus image and hence no further high pass filtering is applied at that location and therefore $\sigma(x,y)$ is set to one. On the contrary, if variance parameter is greater than or equals to the threshold value T_{E_Var}, the corresponding pixel belongs to the detailed region of retinal fundus image and a comparatively higher scaling factor is applied to enhance that area.

$$\sigma(x,y) = \begin{cases} 1, & \mathrm{Var_N}(x,y) < T_{E\_Var} \\ \sigma(>1), & \mathrm{Var_N}(x,y) \geq T_{E\_Var} \end{cases} \tag{4.7}$$

This step contributes in further enhancement of the details by selective filtering of local areas on globally enhanced image $I_F(x,y)$ and the resultant image is expressed as

$$I_{L\_G}(x,y) = \sigma(x,y)I_{fil\_H}(x,y) + \sigma(x,y)I_{fil\_V}(x,y) \tag{4.8}$$

4.2.3 The Formation of Enhanced Image

The last step of enhancement process is the addition of original retinal fundus image with the resultant image $I_{L\_G}(x,y)$. The addition of scaled version of retinal fundus image to the original retinal image will significantly improve the visual appearance of the image with the enhancement of edges and details on smooth background. This final enhanced image is mathematically represented as

$$I_E(x,y) = I(x,y) + I_{L\_G}(x,y) \tag{4.9}$$

4.3 SEGMENTATION OF BLOOD VESSELS

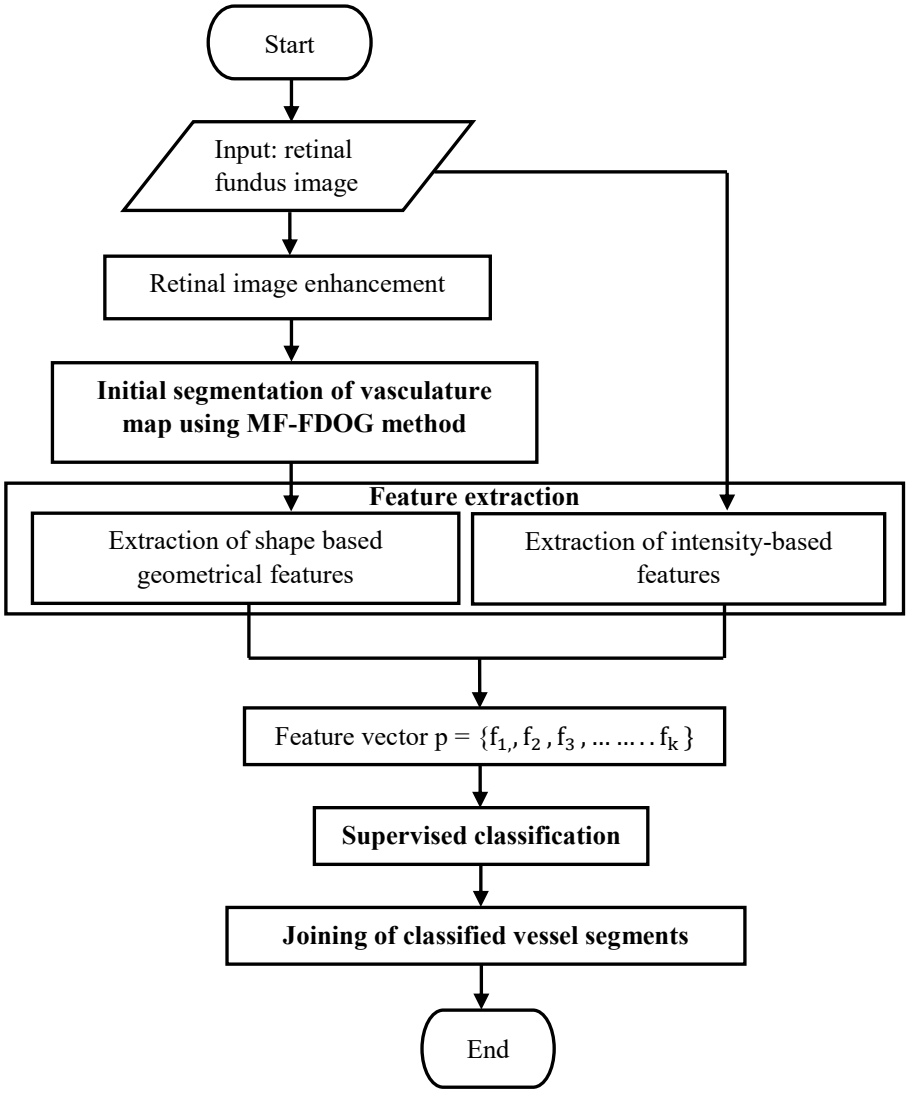

Figure 4.2 Flowchart showing the proposed blood vessels segmentation method

The proposed generalized blood vessels segmentation method after retinal image enhancement as shown in figure 4.2 consists of four phases, namely (i) initial segmentation of blood vasculature map (VM) using matched filter and its first derivative of Gaussian (MF-FDOG), (ii) feature extraction, (iii) supervised classification, and (iv) joining of classified vessel segments. The steps followed in these four phases are explained in this section.

4.3.1 Initial Segmentation of Blood Vasculature Map

The basic matched filter (MF), as described by Chaudhuri, performs comparative matching of the blood vessels and Gaussian curve by considering the fact that the vessel

structures can be approximately modelled as Gaussian probability density function and are assumed to be piece wise linear [25]. Figure 4.3 (a) shows the intensity profile of a cross section of a vessel structure compared with figure 4.3 (b) which contains the approximated Gaussian function.

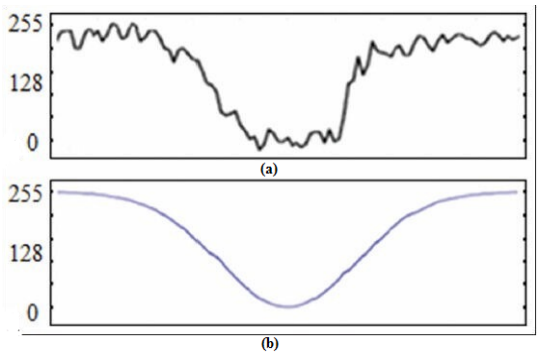

Figure 4.3 (a) Cross section of a typical vessel structure (b) Its bell-shaped approximation

The basic matched filter is defined as:

$$G(x,y) = -\frac{1}{\sqrt{2\pi}\sigma}\exp\left(-\frac{x^2}{2\sigma^2}\right) \text{ for } |y| \leq \frac{L}{2} \tag{4.10}$$

where L is the length of the vessel structure that has the same orientation. Here, the direction of the vessel structure is assumed to be aligned along the y axis and σ is the spread of the intensity profile. Chaudhuri et al., experimentally chose the best parameter values of L and σ to be 9 and 2 respectively for maximum response.

In order to detect the vessel structures in all the possible orientations, matched filter is rotated using the rotation translation matrix defined as:

$$r_i = [u\ v] = [x\ y]\begin{bmatrix}\cos\theta & -\sin\theta \\ \sin\theta & \cos\theta\end{bmatrix} \tag{4.11}$$

where [u v] denotes the new rotated coordinates of [x y] and θ is the angle with which the MF filter is rotated. Previous works show that rotating the filter with an amount of 15^0 is adequate to detect vessel structures with acceptable accuracy which results in filter bank with 12 kernels [25, 170]. Also, the maximum area within the Gaussian curve lies within the range [-3σ, 3σ].

Therefore, Gaussian curve with infinitely long double-sided trails are truncated at ± 3σ. A neighbourhood N, containing the number of elements in matrix r_i is defined as:

$$N = \{[u, v],\ |u| \leq 3\sigma,\ |v| \leq L/2\} \tag{4.12}$$

Each pixel is convolved with all the MF kernels with different orientations. According to Al-Rawi et al., the rotating set of filters can be written as

$$k_i[x\ y] = -\frac{1}{\sqrt{2\pi}\sigma}\exp\left(-\frac{u^2}{2\sigma^2}\right) \text{ for } r_i \in N \tag{4.13}$$

The mean value of the filter is normalized to zero as follows:

$$k_i[x\ y]' = k_i[x\ y] - m_i \tag{4.14}$$

where $m_i = \frac{1}{n}\sum_{r_i \in N} k_i[x\ y]$, n denotes the number of elements in N [170].

The simplicity of basic MF makes it popular for vessel structure detection. However, the MF segments regions corresponding to both vessel and non-vessel structures present in retinal fundus images. Thus, in an attempt to distinguish vessel structures from non-vessel structures Zhang et al. proposed a scheme based on pair of filters namely multiscale matched filter and its first derivative of Gaussian (MF-FDOG) [12].

The method is based on the fact that cross section of a true blood vessel structure is a symmetric Gaussian function while the non-vessel structure approximated as step edge is an asymmetric function. The response of true blood vessel structure to the MF is strongly positive and symmetric. Whereas, the response of non-vessel structure to the MF is partially strong positive and partially strong negative (i.e. asymmetric). Thus, MF will respond to both vessel and non-vessel structures, resulting in responses wrongly classified as vessel structures. Zhang et al. improved the accuracy of the MF by introducing the first derivative of Gaussian (FDOG) filter defined as:

$$G'(x,y) = -\frac{x}{\sqrt{2\pi}\sigma^3}\exp\left(-\frac{x^2}{2\sigma^2}\right) \quad |x| \leq 3\sigma, |y| \leq \frac{L}{2} \tag{4.15}$$

The response of true blood vessel structure to FDOG is antisymmetric and to that of non-vessel structure is positive and symmetric. In order to distinguish vessel structures modelled as Gaussian function from non-vessel structures approximated as step edge, a scheme based on set of pair of filters defined in Eqs. (4.10) and (4.15) is used.

The average of the neighbouring elements (i.e. local mean), denoted by D_m, is calculated by filtering the response of FDOG to the original retinal fundus image with a mean filter W of size w x w with all elements $1/w^2$. D_m is then normalized so that each element lies within the range [0,1]. Normalized image of D_m is denoted by $\overline{D_m}$. It is observed that the value of D_m for the vessel structures (i.e. Gaussian function) is very low and that of non-vessel structures (i.e. step edge) is very high. Therefore, the local mean signal D_m can be used to adjust the threshold T to detect true vessel structures while removing the non-vessel step edges from the MF response. Lower magnitude of D_m implies vessel structures, and hence threshold T applied to MF response is decreased. If the magnitude of D_m is high implying non-vessel structures threshold T is increased to eliminate the non-vessel step edges. Thus, a thresholding scheme by using MF-FDOG method is employed in which a threshold is applied to the response of MF to retinal fundus image and the threshold level is adjusted by the response of FDOG to retinal fundus image. Mathematically, thresholding scheme is defined as

$$T = (1 + \overline{D_m})T_R \tag{4.16}$$

where T_R is the reference threshold which is the mean value of the matched filter response to retinal fundus image. Initial segmentation of the vasculature map (VM) is obtained by applying T to the matched filter response.

VM = 1 if MFresponse (x, y) ≥ T (x, y) and (4.17)

VM = 0 if MFresponse (x, y) < T (x, y)

It can be seen from the above three equations that when $\overline{D_m}$ is weak, T will be lowered and the vessel structure is detected by Eq. (4.17). On the contrary, when $\overline{D_m}$ will be high, T is raised and step edges are eliminated.

4.3.2 Feature Extraction

The initial segmentation of VM obtained from MF-FDOG method on healthy and pathological retinal fundus images have major drawbacks that include

(i) MF-FDOG method does not eliminate non-vessel structures which cannot be modeled as step edges. Therefore, incorrect responses are produced for the regions containing dark and some of the bright lesions.

(ii) MF-FDOG method does not preserve the connectivity of the structures thus producing broken vessel and non-vessel structures.

Thus, the VM obtained by MF-FDOG method is further processed in the next step to eliminate the extracted non-vessel structures very precisely.

Experienced ophthalmologists differentiate blood vessel structures and lesions by visualizing their geometrical and intensity-based features. Therefore, in this work, a new relevant set of both shape and intensity-based features are used that mathematically represent the visual understanding of ophthalmologists. The first step of the algorithm extracts the initial segmentation of vasculature map consisting of vessel and non-vessel structures using MF-FDOG method. A feature set is then computed for each sample in the VM. If the VM has n samples (one sample is one connected object) extracted as vessel and non-vessel structures, then feature set representation for blood vasculature map is VM = $\{p_1, p_1, p_2, p_3, \ldots\ldots p_{n-1}, p_n\}$ where p_i is a feature vector for the i^{th} sample comprising of k features as $p = \{f_1, f_2, f_3, \ldots\ldots f_k\}$. For the present classification of the extracted samples into vessel and non-vessel structures six geometrical and intensity-based features are used.

Description of the extracted features is given below:

(i) Area: The expanse or coverage of a vessel or non-vessel structure is defined as area of a structure. The vessel structures appear like branches of a tree preserving the connectivity. However, unlike vessel structures, non-vessel structures appear as cluster of pixels concentrated over small region. Thus, this feature calculates the area of a particular structure appearing in the initial segmentation of vasculature map. Mathematically, area of the i^{th} sample can be calculated as

$$A_i = \sum_{j=1}^{j=x} VM\left[m_j, n_j\right] \tag{4.18}$$

where VM denotes the binary image extracted using MF-FDOG method which includes all the vessel and non-vessel structures, x denotes the number of pixels present in the i^{th} sample and $[m_j, n_j]$ denotes the location of the j^{th} pixel of the i^{th} sample.

(ii) Length: The measurement of the vessel or non-vessel structure from end to end is defined as a length of the structure. Vessel structures are thin and elongated in shape while non-vessel structures appear as fragmented bunches. Thus, the length will be higher for true vessel structures than non-vessel structures. Various structures present in retinal fundus images can be horizontally or vertically inclined. Therefore, maximum length of the particular sample is calculated. Mathematically, length of the i^{th} sample is calculated as

$$L_i = \left[\left[x_j(max) - x_j(min)\right], \left[\, y_j(max) - y_j(min)\right]\right]_{max} \tag{4.19}$$

where x_j and y_j are the respective rows and columns of the j^{th} pixel in the i^{th} sample.

(iii) Distance: This feature reflects the distance of the i^{th} sample from the optic disk center. Generally, lesions are less concentrated in the optic disk region as compared to the other areas of the retinal fundus image. Also, vessel tree is denser in optic disk region. Distance of the i^{th} sample is calculated as

$$D_i = \sqrt{(s - x_j(mean))^2 + (t - y_j(mean))^2} \tag{4.20}$$

where s and t denote the coordinates of the disk center, $x_j(mean)$ and $y_j(mean)$ is the center of mass of the j^{th} pixel in the i^{th} sample.

Three intensity-based features identify the intensity value of each pixel in the red, green and blue planes of original retinal fundus image. Vessel structures have high contrast in green plane of the colored retinal fundus image but non-vessel structures and artifacts may have better contrast in red and blue planes of the colored retinal fundus image. These intensity values of vessel and non-vessel structures in red, green and blue planes exhibit uniformity among various retinal fundus images. Thus, to distinguish vessel structures from non-vessel structures these features calculate the mean of all intensity values of each sample in red, green and blue planes.

(iv) Mean intensity of the i^{th} sample in the red plane of the original colored retinal fundus image is calculated as

$$R_i = \frac{\sum_{j=1}^{j=x} I\_O\_R[m_j, n_j]}{x} \tag{4.21}$$

where $I\_O\_R[m_j, n_j]$ is the red plane of the original colored retinal fundus image.

(v) Mean intensity of the i^{th} sample in the green plane of the original colored retinal fundus image is calculated as

$$G_i = \frac{\sum_{j=1}^{j=x} I\_O\_G[m_j, n_j]}{x} \tag{4.22}$$

where $I\_O\_G[m_j, n_j]$ is the green plane of the original colored retinal fundus image.

(vi) Mean intensity of the i^{th} sample in the blue plane of the original colored retinal fundus image is calculated as

$$B_i = \frac{\sum_{j=1}^{j=x} I\_O\_B[m_j, n_j]}{x} \tag{4.23}$$

where $I\_O\_B[m_j, n_j]$ is the blue plane of the original colored retinal fundus image.

4.3.3 Supervised Classification

Six-dimensional feature vector computed in the previous step is used as an input to the neural network-based classifier in order to classify the extracted samples from the initial segmentation of the vasculature map into vessel and non-vessel structures. The neural network

consists of three layers namely: input layer, hidden layer and an output layer. In order to find the appropriate number of hidden neurons, a trial-and-error process was applied. Various numbers of hidden neurons were tried, and it was found that twenty neurons in hidden layer were reasonable for classification. The desired output was set to 1 for the output neuron corresponding to the class of vessel structures and 0 for non-vessel structures. The learning of neural network was supervised and the weights were adjusted by back propagation procedure with adaptive learning rate in order to obtain desired input-output relationship [22]. A three-step methodology comprising of training, validation and testing is employed for the designing of a classifier using neural network. The training set, T_S is composed of 1685 samples of vessel or non-vessel structures. These samples, collected from 15 training images were used to select the sets of parameters for neural network architecture and weights. The samples forming the training set were collected from the ground truth of various database images under consideration. Images with varying number of vessel and non-vessel structures from each type of diabetic retinopathy grade were cautiously selected with the help of expert ophthalmologist to train the neural network. 15% of the training samples were used for the validation of trained neural network to identify the neural network structure for fine performance. The performance of the trained neural network is then evaluated on each retinal fundus image of the composite database described earlier. The output ranges between 1 and 0 indicating the probability of the sample to be a part of vessel or non-vessel structure. The segmentation of the vasculature map obtained after classification is denoted as VM_F.

4.3.4 Joining of Classified Vessel Segments

The neural network classifier detects vessel structures as isolated samples. However, the majority of the vessels are represented by one large connected structure in the binary image. Therefore, these isolated samples of true vessel structures are joined based upon their distance, defined in Eq. (4.24.), among each other. In this method, each true vessel sample searches

another true vessel sample in the vicinity of the mask of size 5 x 5 and if the sample is found, the gap between the two vessel samples is filled. True vessel samples are very close to each other in the final segmentation of the vasculature map. Thus, creation of connectivity among these samples is sensitive to the size of mask used to search another true vessel sample. Therefore, size of the mask should be small enough to be able to join the nearest true samples. After trial and interaction with expert ophthalmologists, mask of size 5 x 5 pixels was selected for the present study. If a particular sample is unable to find any true vessel structure in the vicinity then the same sample is extracted without any joining process. Pseudo code of this method is as shown below:

for i = 1 to n

for m = 1 to x

for n = 1 to y

$$d = \sqrt{(R(i) - x(m)^2 + (C(i) - y(m)^2} \tag{4.24}$$

if d < threshold then VM_F $[x(m), y(m)]$ = 1

else VM_ F $[x(m), y(m)]$= 0

end

end

end

where n represents the number of pixels found as vessel from neural network, R(i) and C(i) are the row and column of the i^{th} pixel of true vessel samples classified, $[x(m), y(m)]$ represent the pixel location of the final vasculature map extracted from neural network. The final segmentation of blood vessels after joining the classified vessel segments is termed as I_{BV}.

4.4 EVALUATION OF THE RETINAL IMAGE ENHANCEMNT METHOD

The performance evaluation of the proposed retinal image enhancement method was done after obtaining the optimal values of the parameters as described below.

4.4.1 Parameters Considered for Retinal Image Enhancement

The quality of retinal fundus image depends on several factors, such as settings and resolution of the fundus camera, acquisition angle, illumination, pixel noise etc. The database used in the present work is acquired from various sources; hence there is a large variation in the quality of retinal images. In other words, the local intensity variations (represented by neighbourhood variance parameter) around detailed regions has a good range of values. Therefore, better visualization of detailed regions, i.e. regions corresponding to blood vessels, optic disk and lesions, in retinal images requires local contrast enhancement using selective filtering. Application of selective filtering on the database images have shown that the neighbourhood variance parameter increases in the detailed regions, as compared to the smooth regions (background) of retinal images. Therefore, the approach used in this work to enhance detailed regions is to set a threshold on the value of neighbourhood variance parameter. Threshold value of the neighbourhood variance parameter, T_{E_Var}, determines the pixels corresponding to detailed structures. Therefore, to determine the optimum value of the threshold, the extent of mean intensity variations of detailed structures for each database is computed. It can be observed in the figure 4.4 that the range of intensity variations around the median value (to exclude the extremely large and small intensity variations) varies from database to database. Therefore, for the sake of generalization, a common value, i.e. average of all median values ($T_{E\_Var}\approx120$) is considered for best outcomes.

One more parameter is required for the optimal implementation of contrast enhancement using selective filtering and that is scaling factor, σ. This parameter controls the extent of local contrast enhancement at each spatial location determined by T_{E_Var}. The detailed regions identified by $T_{E\_Var}>120$ are enhanced by multiplying them with the scaling factor. Whereas for regions corresponding to $T_{E\_Var}<120$ i.e. smooth regions, scaling factor is set to 1, representing no enhancement. The value of scaling factor was decided by varying the value of

σ in the range of 2 to 5 and the assessment was done by the participating ophthalmologist. This experiment was carried out on 50 sample retinal images selected from varying databases. After visualizing the results, it was observed that initially with the increase in scaling factor, the detailed structures give better visual appearance in comparison to the original image as depicted in the marked bounded regions of figure 4.5 (b) and (c). But after $\sigma = 3$, no significant difference in enhancement was visualized as assessed by the participating ophthalmologist. Therefore, scaling factor is taken as 3 to assure desirable contrast enhancement of retinal fundus image.

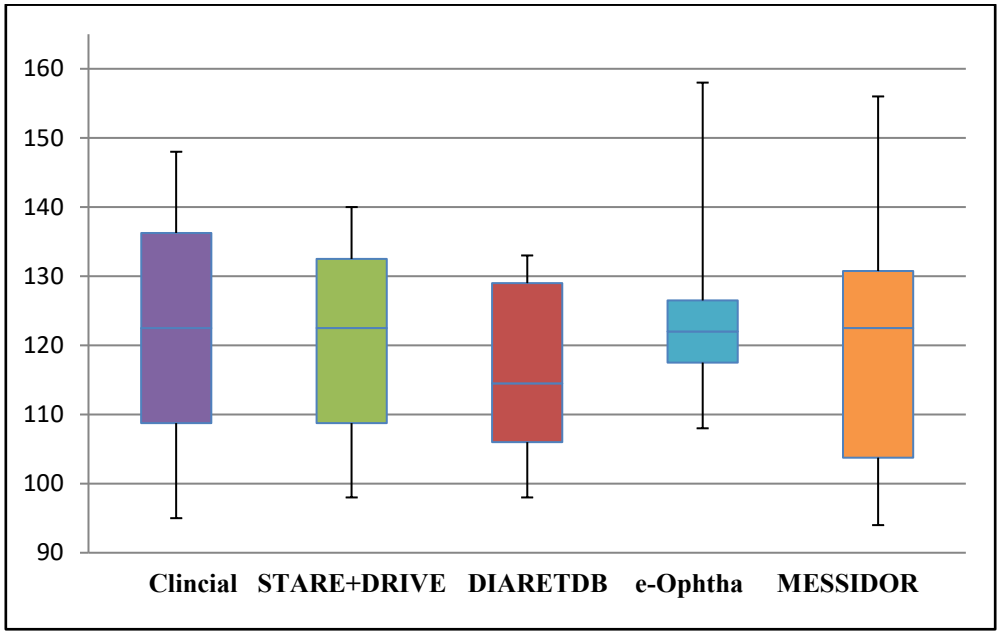

Figure 4.4 Range of intensity variations in detailed regions of sample retinal images from varying databases

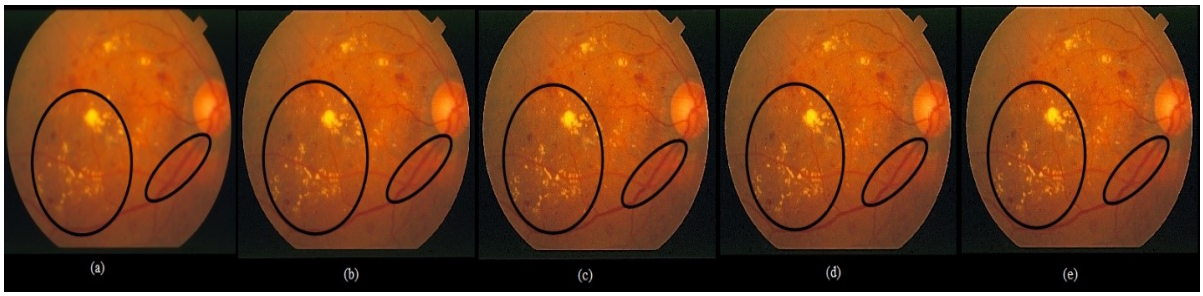

Figure 4.5 (a) Original retinal image and processed pathological image for scaling factor (b) $\sigma = 2$, (c) $\sigma = 3$, (d) $\sigma = 4$, and (e) $\sigma = 5$

4.4.2 Performance Evaluation of Retinal Image Enhancement

Figure 4.6 shows original and processed images of four lesion categories. These lesion categories are cotton wool spots, exudates, haemorrhages and micro aneurysms which are indicated by figure 4.6 (a), (b), (c) and (d) respectively. The lesions are identified by the regions encircled in original images. When the enhancement processed images denoted by figure 4.6 (e), (f), (g) and (h) are compared with their original counterparts and analysed; it is observed that the processed images provide the better visual appearance with enhanced contrast with respect to the background and reduced blurring. These enhanced images are suitable for precise lesion and anatomical structures segmentation methods carried out in subsequent steps. These improvements were more clearly observable when they were visualized on the computer screen with black background and these improvements were supported by visual interpretations of expert ophthalmologists.

4.5 RESULTS AND DISCUSSION

The proposed method is evaluated and validated on six open-source and clinically acquired retinal fundus image databases comprising of healthy images, images with mild, intermediate and severe diabetic retinopathy. A total of 5048 retinal fundus images with different resolutions and grades are used. To demonstrate the performance of the proposed method, figure 4.7 (a), (b) and (c) are three randomly chosen healthy retinal fundus images, where figure 4.7 (a) and (c) are the clinically acquired original retinal fundus images and figure 4.7 (b) is an original image from DRIVE database. Figure 4.8 (a) is randomly chosen unhealthy retinal fundus image containing exudates (bright spots) from STARE database whereas, figure 4.8 (b) and (c) are clinically acquired retinal fundus images containing hemorrhages (dark red spots) and drusen (dull yellow spots) respectively.

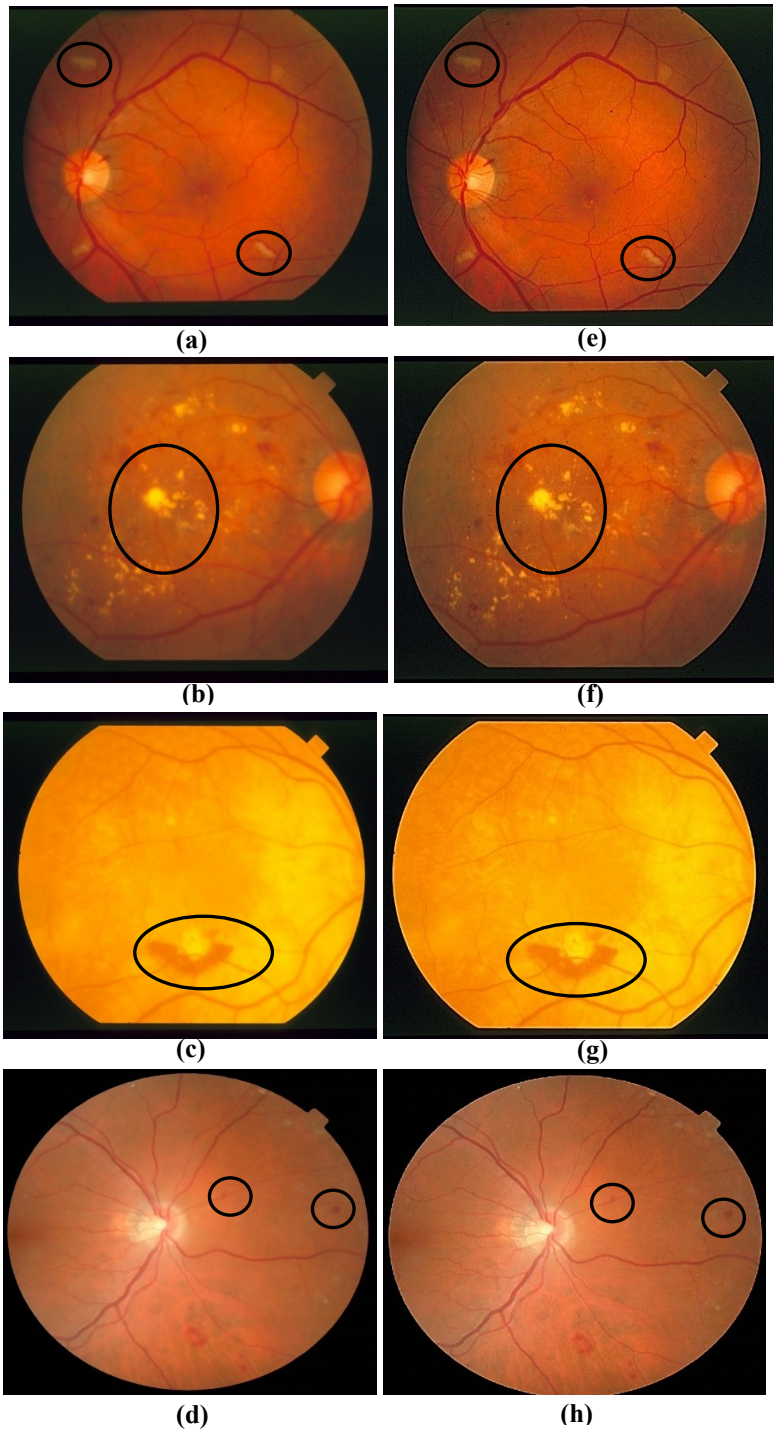

(a), (b), (c), (d): Original pathological retinal fundus images
(e), (f), (g), (h): Enhanced retinal images

Figure 4.6 Original and enhanced pathological retinal images

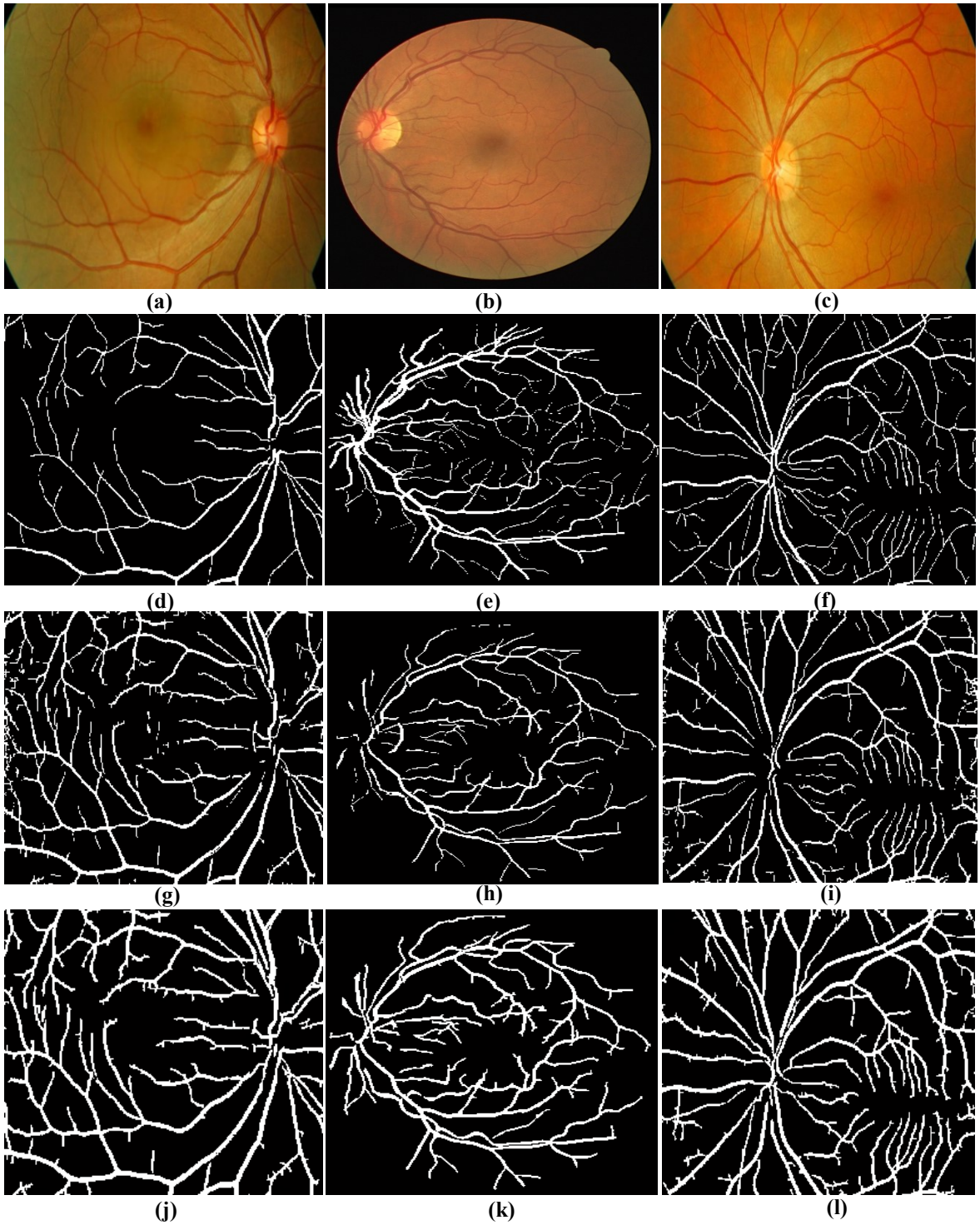

(a), (b), (c): Original Image
(d), (e), (f): Reference Ground Truth
(g), (h), (i): Results of MF-FDOG
(j), (k), (l): Results of the Proposed Method

(a): Clinically Acquired Image
(b): Image from DRIVE Database
(c): Clinically Acquired Image

Figure 4.7 Original and processed healthy images by MF-FDOG and the proposed method

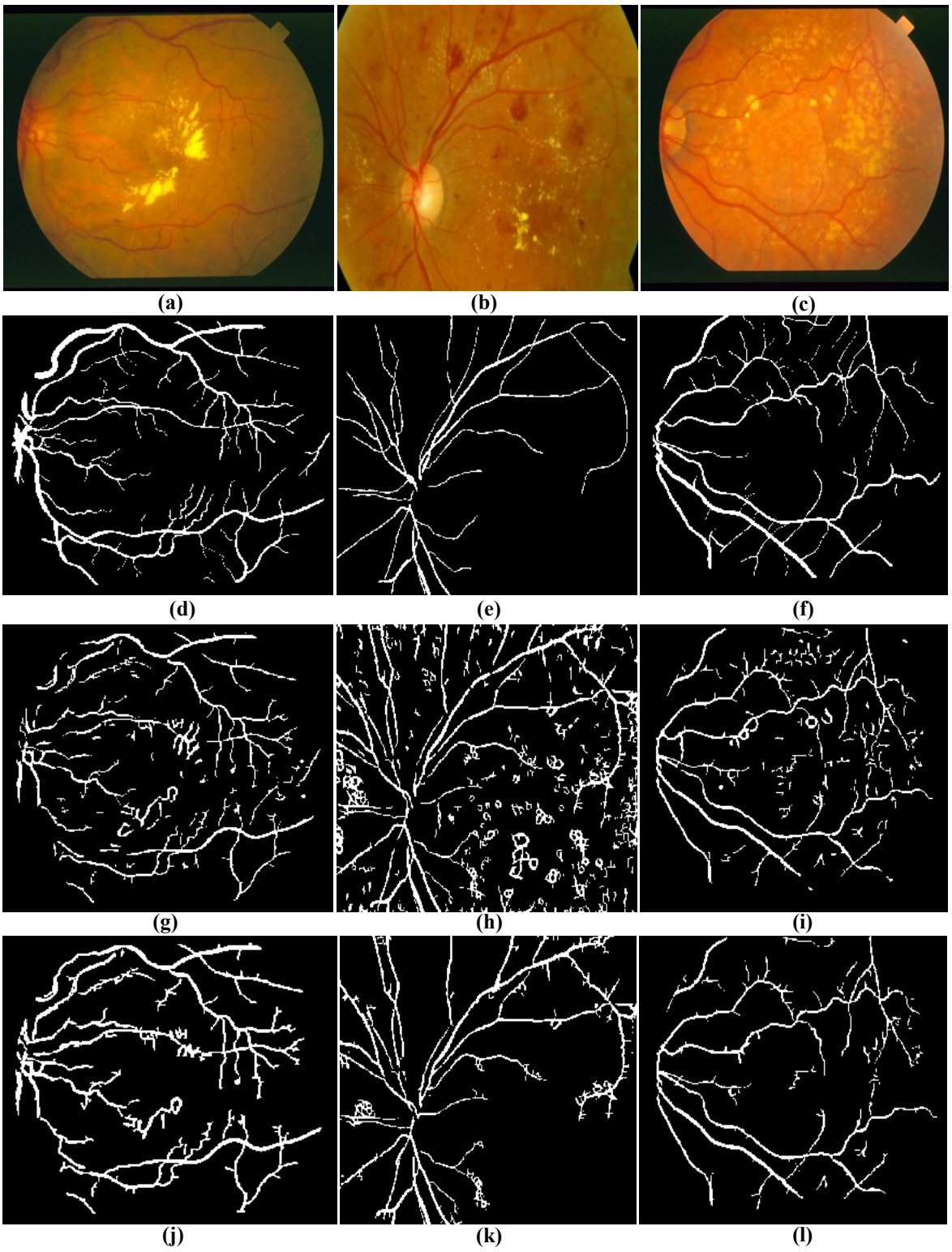

(a), (b), (c): Original Image
(d), (e), (f): Reference Ground Truth
(g), (h), (i): Results of MF-FDOG
(j), (k), (l): Results of the Proposed Method

(a): Image from STARE Database
(b): Clinically Acquired Image
(c): Clinically Acquired Image

Figure 4.8 Original and processed unhealthy images by MF-FDOG and the proposed method

4.5.1 Initial Segmentation of Blood Vasculature Map

In order to extract both thick and thin vessel structures in the initial segmentation of vasculature map, multiscale MF-FDOG method is applied. Large scale values of σ and L are used to detect thick vessel structures, whereas small scale values are used to locate thin vessel structures. The best results are obtained when the spread of intensity profile (σ) is set to 1 and 1.5 for thin and thick and vessel structures respectively. Length of the vessel structures (L) is set to 5 and 9 for thin and thick vessel structures respectively. The mean filter of W = 31 x 31 is used to calculate the local mean of the FDOG response. The filtered images, shown in figure 4.7 (g), (h) and (i), are obtained after the application of MF-FDOG method on healthy retinal fundus images as shown in figure 4.7 (a), (b) and (c) respectively. Figure 4.8 (g), (h) and (i) represents the results of MF-FDOG method on pathological retinal fundus images with mild, intermediate and severe lesions shown in figure 4.8 (a), (b) and (c) respectively. It can be clearly observed that the pathological regions in retinal fundus images are also detected as the part of blood vessels. However, few of the bright lesions are eliminated partially by MF-FDOG method but it is unable to eliminate other dark lesions from the retinal fundus images. Therefore, this method solely is not robust to extract the blood vessels from pathological retinal fundus images. Neural network-based method is used to effectively get rid of these incorrectly classified non-vessel structures as vessel structures.

4.5.2 Feature Extraction and Classification

Initial segmentation of vasculature map obtained from MF-FDOG method, is further processed to eliminate the incorrectly classified regions due to the presence of lesions in the retinal fundus images. This is carried out by selecting the number of geometrical and intensity-based features as described in section 4.3.2. These features are given as inputs for training to a neural network classifier. Neural network classifier classifies the various structures present in the initial segmentation of VM into vessel or non-vessel. Thus, the trained neural network is

able to provide improved extraction of blood vessels in the final segmentation of VM by eliminating all the non-vessel structures. The final segmented images obtained by the neural network classifier on the initial VM from MF-FDOG method, on healthy retinal fundus images are shown in figure 4.7 (j), (k) and (l). These results clearly depict less fragmented vessel segments preserving the connectivity of the vasculature. Figure 4.8 (j), (k) and (l) shows the final segmented images obtained from the VM of pathological retinal fundus images. The results clearly demonstrate the separation of true vessels from non-vessel structures providing appropriate segmentation, especially in pathological retinal fundus images. Thus, the proposed method outperforms the method proposed by Zhang mainly due to following two reasons: (i) It eliminates almost all of the dark and bright lesions from the image. (ii) It has the better ability to detect the correctly classified vessel structures.

4.5.3 Performance Evaluation of Blood Vessels Segmentation Method

Performance Metrics

The performance of the proposed method is enumerated using metrics like sensitivity, specificity and accuracy. These metrics are often used in medical applications to assess the performance of the blood vessels segmentation methods. The higher the value of these parameters better is the performance. Performance metrics are briefly described below:

(i) Sensitivity (SN): Sensitivity, also termed as true positive rate (TPR) is the measure that indicates the ability of the method to detect the correct blood vessel pixels among all the blood vessel pixels. Mathematically it can be expressed as

$$\mathrm{SN} = \frac{\mathrm{TP}}{\mathrm{TP} + \mathrm{FN}} \tag{4.25}$$

where TP represents the number of pixels correctly classified by the method as vessel pixels and FN represents the number of detected pixels which are incorrectly classified by the method as non-vessel pixels.

(ii) Specificity (SP): Specificity is a measure that indicates the ability of the method to detect the correct non-vessel pixels among all the non-vessel pixels and it can be expressed as

$$\mathrm{SP} = \frac{\mathrm{TN}}{\mathrm{TN} + \mathrm{FP}} \tag{4.26}$$

where TN represents the number of pixels correctly classified by the method as non-vessel pixels and FP represents the number of detected pixels which are incorrectly classified by the method as vessel pixels.

(iii) Accuracy (Acc): Accuracy of the method indicates its ability to detect correctly both blood vessels and non-vessels pixels among all the pixels examined. Mathematically it can be expressed as:

$$\mathrm{Acc} = \frac{\mathrm{TN} + \mathrm{TP}}{\mathrm{TN} + \mathrm{TP} + \mathrm{FP} + \mathrm{FN}} \tag{4.27}$$

Table 4.1 shows the segmentation performance of the proposed method and MF-FDOG in terms of three performance metrics sensitivity, specificity and accuracy on the composite database of 5048 retinal fundus images. These performance metrics were calculated by comparing the segmentation results of the methods with that of the reference ground truth images. Table 4.1 clearly illustrates that the overall average segmentation sensitivity, specificity and accuracy on the proposed method are 84.82%, 96.98% and 97.58% respectively on the test images whereas that of MF-FDOG are 71.82%, 94.13% and 93.24% respectively. These values indicate clearly that the proposed method outperforms the method of Zhang mainly in terms of sensitivity and shows comparable results for specificity and accuracy. Table 4.1 also depicts the ability of both the methods to segment blood vessels of retinal fundus image with the various grades of diabetic retinopathy. It is found that the overall average sensitivity of the proposed method for mild diabetic retinopathy (i.e. retinal fundus images with mild lesions) is 85.13% and whereas that of Zhang is only 70.84%. The specificity and accuracy of the proposed method is also comparable to the method of Zhang but with much lesser deviation

around the average value. The segmentation results of the retinal fundus images for moderate diabetic retinopathy (i.e. retinal fundus images with intermediate lesions) and severe diabetic retinopathy (i.e. retinal fundus images with severe lesions) shows the similar trend but with comparatively less values of performance metrics. This is due to the presence of more number of lesions that mainly contributes in incorrect vessel structure detection. On comparing the overall segmentation results in table 4.1, it can be observed that the proposed method has a significant contribution in achieving average sensitivity of $(84.82 \pm 1.93)\%$ which shows an increment of 13.4% over MF-FDOG method. Thus, our method has significantly improved the sensitivity parameter on varying types of retinal fundus images without disturbing the ability to detect the non-vessel pixels correctly (SP) and the ability to classify both vessel and non-vessel pixels correctly (Acc).

The comparative performance analysis of the proposed method for blood vessels segmentation with the existing methods is shown in table 4.2. It is important to note that the existing methods are generally validated on the two open-source databases namely DRIVE and STARE. Therefore, to give an overall idea about the performance comparison of the proposed method with that of existing methods, segmentation results on these two databases are highlighted in table 4.2. The proposed method has clearly outperformed the existing methods mainly in terms of sensitivity that have used DRIVE and STARE databases for evaluation. Overall sensitivity of the DRIVE database (88.23%) is slightly higher than that of STARE database (83.52%) due to the presence of pathological retinal fundus images in STARE database as compared to DRIVE database that mainly comprise of healthy retinal fundus images. Furthermore, the proposed method shows the specificity/accuracy of 97.89/94.83 and 98.20/95.91 for DRIVE and STARE databases respectively which is comparable to almost all the existing methods. It can also be observed that the proposed method is validated with a large composite database as compared to size of the databases of all the existing methods. The

improvement, especially in terms of sensitivity, is supported by the segmentation results of 87.22%, 86.89% and 88.67 on DIARETDB, e-Ophtha and MESSIDOR databases respectively. This is due to the fact that these databases comprise of healthy images and images with mild pathologies similar to DRIVE database. Furthermore, the method is also evaluated on clinically acquired database comprising of large number of healthy images and images with varying types of pathologies. Sensitivity of 87.21% proves the generalization ability of the proposed method. Conclusively, validation of the proposed method on such a large composite database demonstrates the robustness of the proposed method for blood vessels extraction in the presence of varying types of pathologies.

Table 4.1 Evaluation of the proposed method and MF-FDOG on varying grades of diabetic retinopathy

Retinal Image Class (No. of images)	Sensitivity (%) (Average ± SD)	Specificity (%) (Average ± SD)	Accuracy (%) (Average ± SD)
RETINAL IMAGES WITH NO DIABETIC RETINOPATHY (990)			
Zhang [12]	79.8381 ± 2.6521	96.2211 ± 1.2112	92.2313 ± 0.2131
Proposed Method	86.2121 ± 1.3231	97.2312 ± 1.3121	98.12121 ± 1.2121
RETINAL IMAGES WITH MILD DIABETIC RETINOPATHY (1778)			
Zhang [12]	70.8381 ± 4.0979	95.4373 ± 0.3673	93.4743 ± 3.3234
Proposed Method	85.1324 ± 1.4427	98.5985 ± 0.0323	94.8984 ± 1.8448
RETINAL IMAGES WITH MODERATE DIABETIC RETINOPATHY (1321)			
Zhang [12]	70.7304 ± 3.1930	93.9262 ± 2.823	94.3435 ± 4.7283
Proposed Method	85.7333 ± 2.0978	97.8993 ± 0.8728	95.4672 ± 2.8983
RETINAL IMAGES WITH SEVERE DIABETIC RETINOPATHY (959)			
Zhang [12]	65.6813 ± 5.512	91.3493 ± 3.24	92.1697 ± 3.2313
Proposed Method	82.4184 ± 2.289	96.3363 ± 2.244	95.9836 ± 2.3428
OVERALL RESULT ON COMPOSITE DATABASE (5048)			
Zhang [12]	**71.4151 ± 4.4255**	**94.1342 ± 2.4542**	**93.2422 ± 3.4343**
Proposed Method	**84.8180 ± 1.9323**	**96.9757 ± 1.1387**	**97.5797 ± 2.4525**

Table 4.2 Comparative performance of the proposed method on blood vessels segmentation with other existing techniques

Methods	Database	Number of images for validation	Sensitivity/ (True Positive Rate)	Specificity	Accuracy	False positive Rate
Soares [28]	DRIVE	40	----	----	94.66%	----
	STARE	20			94.80%	
Mendonca [29]	DRIVE	40	73.41%	----	94.52%	23.6%
	STARE	20	69.96%		94.40%	27%
Ricci and Perfetti [30]	DRIVE	40	72.46%	----	93.44%	3.45%
	STARE	20	75.05%		94.10%	4.31%
Martinez-Perez[31]	STARE	20	69.48%	----	94.53%	2.62%
Zhang [12]	DRIVE	40	71.20%	----	93.82%	2.76%
	STARE	20	71.77%		94.84%	2.47%
Li [35]	DRIVE	40	71.54%	----	93.43%	2.84%
	STARE	20	71.91%		94.07%	3.13%
Rahebi [39]	DRIVE	40	73.65%	97.07%	94.61%	----
	STARE	20	69.02%	98.04%	95.27%	
Franklin [40]	DRIVE	40	60.7%	97.3%	80.7%	----
Zhao [42]	DRIVE	40	74.2%	98.2%	95.4%	----
	STARE	20	78%	97.8%	87.9%	
Imani [44]	DRIVE	40	75.24%	97.53%	95.23%	----
	STARE	20	75.02%	97.45%	95.90%	
Wang [45]	DRIVE	40	73.9%	98.4%	94.9%	----
	STARE	20	73.2%	98.4%	95.6%	
Proposed Method	**DRIVE**	**40**	**88.23%**	**97.89%**	**94.83%**	**1.31%**
	STARE	**184**	**83.52%**	**98.20%**	**95.91%**	**1.9%**
	DIARETDB	**219**	**87.22%**	**97.72%**	**93.53%**	**1.08%**
	e-Ophtha	**463**	**86.89%**	**98.27%**	**94.34%**	**2.4%**
	MESSIDOR	**1200**	**88.67%**	**97.26%**	**95.82%**	**3.12%**
	Clinical	**2942**	**87.21%**	**95.23%**	**93.12%**	**2.89%**

4.6 CONCLUDING REMARKS

(i) Retinal lesions may have low contrast as compared to the background and other anatomical structures in retinal fundus images. Thus, the objective is to enhance the visualization details with the help of ophthalmologists' interpretation so that retinal lesions are efficiently detected. To achieve this objective, an enhancement method is designed to retain high frequency components and enhance the local contrast of the retinal fundus image. This is accomplished by applying two directional high pass filters followed by adaptive scaling factor. Finally, an optimal value of threshold is chosen by analysing the range of intensity variations in each retinal fundus image database.

(ii) Variations in blood vessels morphology of retinal fundus images is one of the dominant characteristics for the early detection and analysis of retinal abnormalities. Also, the precise segmentation of retinal blood vessels aids in accurate detection of retinal lesions and other anatomical structures. Therefore, the first necessity for designing the computer-aided diagnostic method is the precise segmentation of retinal blood vessels. Keeping this fact in mind, a generalized blood vessels segmentation method is designed to segment blood vessels irrespective of whether the image is healthy or pathological.

(iii) Results of subjective evaluation are supported by the objective medically significant statistical measures. The performance of the proposed method has been validated on composite database of 5048 images comprising of publicly available standard databases and clinically acquired database. The experimental results indicate the high performance of the proposed method with the overall average sensitivity of 84.82% revealing its ability to perform significantly in distinguishing true vessel structures from non-vessel structures. The segmentation results by the proposed method also show a high correlation with the ground truth with an accuracy of 97.58%.

(iv) Furthermore, the method proves its capability on varying grades of retinal fundus images with the sensitivity of 85.13%, 85.73% and 82.41% on mild, moderate and severe diabetic retinopathy respectively. Finally, it can be emphasized that the promising results indicate the generalization ability of the blood vessels segmentation method to aid ophthalmologists in precise detection of retinal lesions for timely treatment of retinal abnormalities.

Chapter 5

Detection of Progressive Diabetic Retinopathy (Study 1)

5.1 INTRODUCTION

Computer-aided detection methods can assist ophthalmologists in the detection of preliminary stages of diabetic retinopathy during mass screening of patients undergoing ophthalmological examinations. The initial stages of diabetic retinopathy, (also termed in literature as background diabetic retinopathy) characterized by irregularity and leakiness of the blood vessels, does not affect vision but may progress to more serious chronic forms of retinopathy. Retinal lesions such as exudates are one of the earliest and most prevalent signs of the onset of chronic diabetic retinopathy termed as progressive diabetic retinopathy. Progressive diabetic retinopathy is a vision threatening complication which may lead to blindness if not treated on time. In order to cease the further development of the disease the physicians determine the precise area of exudates to be exposed to laser for photocoagulation during treatment. Additionally, during mass screening of diabetic retinopathy, it is vital to differentiate retinal images affected with progressive diabetic retinopathy purely based on the presence or absence of exudates. Therefore, proper detection and then segmentation of exudates is important in decision making during treatment of progressive diabetic retinopathy. Thus, to assist ophthalmologists in the process of exudates detection and progressive diabetic retinopathy diagnosis, a robust computer-aided exudates detection and segmentation method is developed in this work that facilitates the smooth and accurate examination of the retinal fundus images. The proposed method is designed with the adaptive image quantization and dynamic decision thresholding to segment the boundaries of exudates irrespective of associated heterogeneity, bright and faint edges. Further, anatomical structures like blood vessels are segmented by the method proposed in section 4.3 and eliminated using the normalization method. Another anatomical structure i.e. optic disk is located, detected and eliminated using

convergence of blood vessels approach. Elimination of these anatomical structures prior to the segmentation of exudates reduces the false responses in the precise exudates segmentation. Finally, to determine the clinical effectiveness of the method, the proposed exudates segmentation method is evaluated on a diversified database of 5048 retinal images using lesion and image-based evaluation criteria.

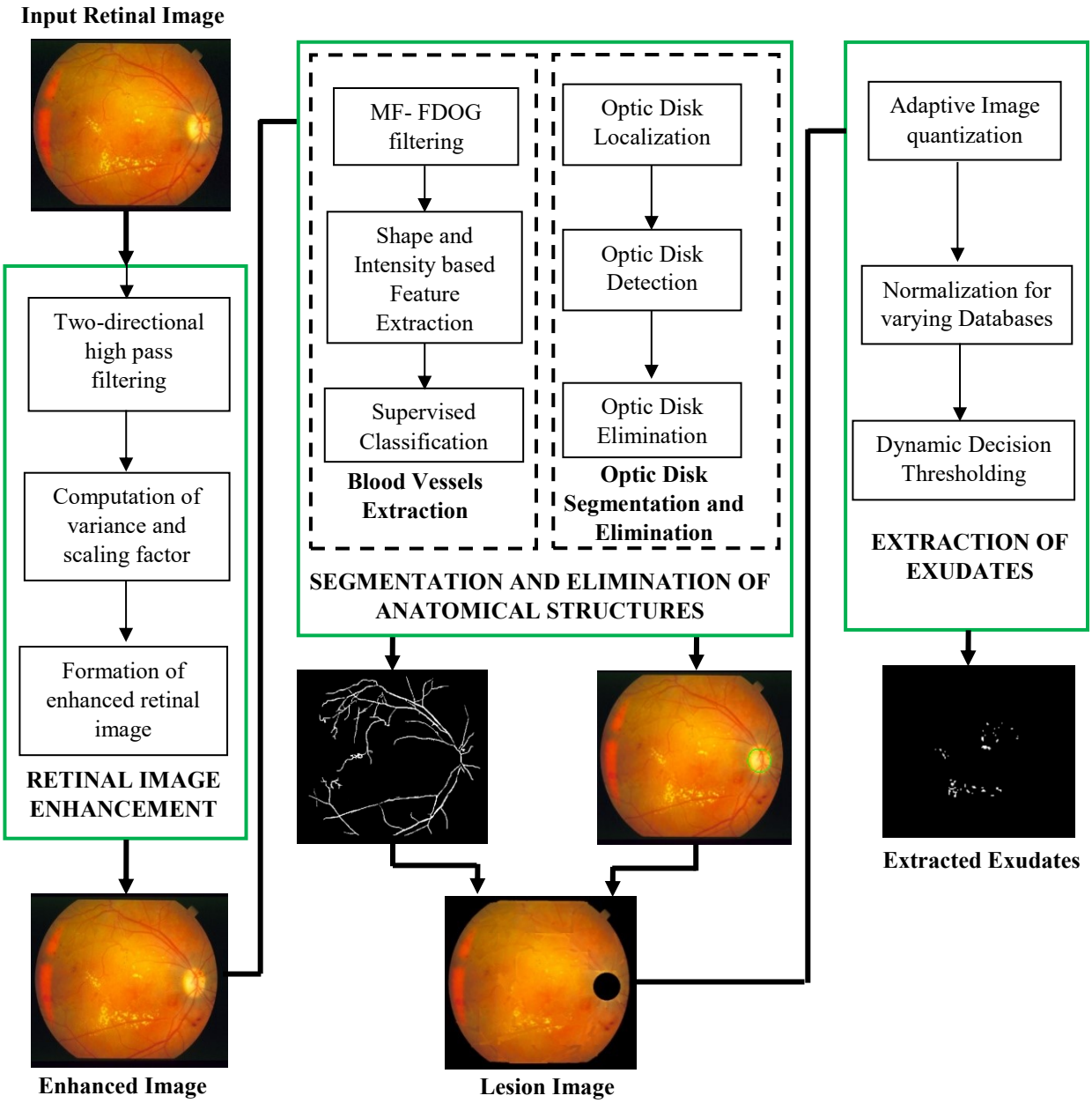

Figure 5.1 Overview of the proposed system for the detection of Progressive Diabetic retinopathy

The proposed method for the detection of progressive diabetic retinopathy, as shown in figure 5.1, consists of three phases, namely (i) retinal image enhancement as described in section 4.2 (ii) segmentation and elimination of anatomical structures, and (iii) segmentation of exudates. The steps followed in these three phases are explained in this section.

5.2 SEGMENTATION AND ELIMINATION OF ANATOMICAL STRUCTURES

The variability within retinal images makes difficult to distinguish exudates in the presence of anatomical structures like blood vessels and optic disk. The brightness of optic disk lies in the same range as that of exudates and retinal blood vessels may interfere in the accurate computer-aided detection of exudates. Therefore, it is necessary to eliminate anatomical structures before the extraction of exudates. This stage consists of two main steps, namely (i) segmentation and elimination of blood vessels and (ii) segmentation and elimination of optic disk. The various stages of the above process applied over an enhanced retinal fundus image are shown in figure 5.2 (a)-(d). Figure 5.2 (a) shows the original retinal image, figure 5.2 (b) depicts the segmented blood vessels, figure 5.2 (c) shows the resultant image after the application of convergence criterion for optic disk location, and figure 5.2 (d) is the resultant image after the detection of optic disk, elimination of optic disk and normalization of blood vessels.

5.2.1 Segmentation and Elimination of Blood vessels

False appearances occur in exudates extraction methods because dark structures such as retinal blood vessels induce local intensity variations, thus misleading the exudates detection methods based on local contrast. The problem that occurs if the local contrast is used to determine regions containing exudates, is that bright regions between dark structures are also characterized by high local contrast. Therefore, the detection process of exudates may produce false positives if blood vessels are not properly eliminated from the retinal fundus image. Thus, the reliable exclusion of retinal blood vessels is one of the significant tasks. In this work, the

generalized blood vessels segmentation method is applied to efficiently eliminate the blood vessels from the retinal fundus images. The step wise procedure for the segmentation of retinal blood vessels is described in section 4.3. Figure 5.2(b) shows the segmented binary blood vessels image, I_{BV}, corresponding to the original pathological retinal fundus image in figure 5.2(a).

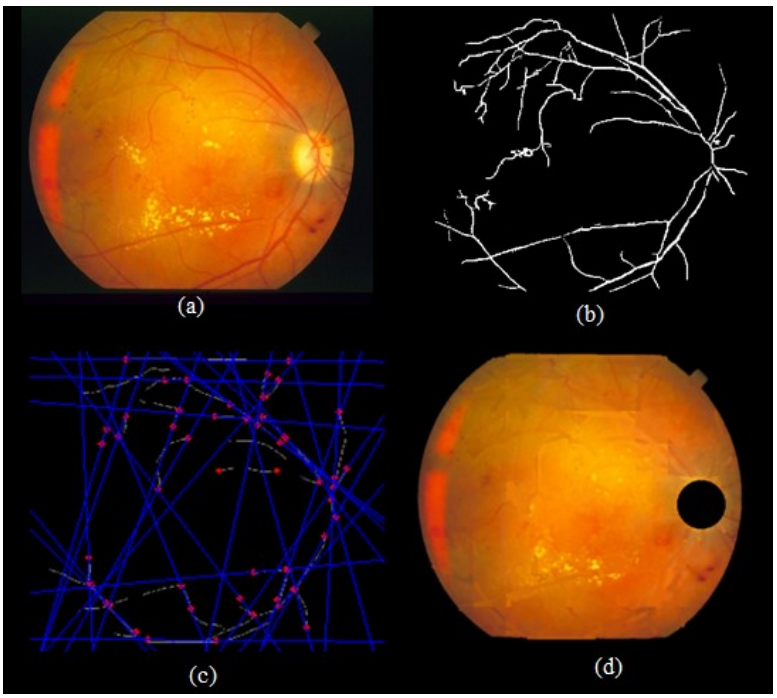

Figure 5.2 (a) Original retinal fundus image, (b) blood vessels segmentation results, (c) depiction of convergence of blood vessels, (d) lesion image obtained after normalization of blood vessels and elimination of optic disk

Afterwards, an adaptive blood vessels normalization method is developed to remove the blood vessel structures from original retinal fundus images. The concept used in the removal of blood vessel structures is basically the replacement of blood vessel pixels from their local background intensity. Therefore, in the process of normalization of detected blood vessel pixels, the estimation of local mean value of its background pixels is made first using 64 x 64 pixels window. Here, the background pixels indicate all other pixels apart from the blood vessel pixels. The local estimate of the background pixels is then used to map the blood vessel pixel

values in such a way that each blood vessel pixel is replaced with the corresponding local mean. An original retinal fundus image has large variation of intensities within an image, therefore the effectiveness of adaptive normalization method is sensitive to the blood vessels neighborhood block size around a pixel. This neighborhood pixel block should have enough number of pixels to provide good normalization with respect to the background. Also, the size of pixel block should be small enough to be able to normalize small blood vessel structures locally. After trial and interaction with ophthalmologists, neighborhood block of 3 x 3 pixels was selected for the present work. This normalization process has two steps. First, the mean values of background pixels from all the three channels, i.e., the red, green and blue, of an input retinal fundus image $I(x, y)$ are computed in 3 x 3 pixels neighborhood block. These mean values are used to calculate the normalization factor, $N(x, y)$, as represented by Eq. (5.1).

$$\begin{aligned} N(x,y) = \quad & \frac{1}{3}\sum_{k=-1}^{1}\sum_{g=-1}^{1} R(x+k, y+g) \times I_{BV}(x+k, y+g) + \\ & \frac{1}{3}\sum_{k=-1}^{1}\sum_{g=-1}^{1} G(x+k, y+g) \times I_{BV}(x+k, y+g) + \\ & \frac{1}{3}\sum_{k=-1}^{1}\sum_{g=-1}^{1} B(x+k, y+g) \times I_{BV}(x+k, y+g) \end{aligned} \tag{5.1}$$

where $R(x, y), G(x, y)$ and $B(x, y)$ are red, green and blue channels respectively of the original retinal fundus image, and I_{BV} is the representation of segmented blood vasculature binary image in which pixels corresponding to blood vessels and non-blood vessels are 1 and 0 respectively. In the second step, the normalized blood vasculature image, N_{BV_img}, is calculated as

$$N_{BV\_img} = \begin{cases} N(x,y) & \text{if } I_{BV}(x,y) = 1 \quad \text{i. e blood vascualture pixel} \\ I(x,y) & \text{otherwise} \end{cases} \tag{5.2}$$

The above expression clearly depicts that if the blood vessel pixel is at the center of 3 x 3 pixels block, then that pixel is replaced by the computed normalization factor at that location otherwise the intensity value of original retinal fundus image will remain preserved at that location. The normalized blood vasculature image is depicted in figure 5.2 (d).

associated with the efficient detection of exudates.

5.2.2 Segmentation and Elimination of Optic Disk

The elimination of optic disk prior to the detection of exudates is indispensable because of the similar attributes of optic disk and exudates in a retinal fundus image in terms of colour, intensity and contrast. Similar attributes of optic disk and exudates will be responsible for false detection at the time of application of exudates segmentation method without removal of optic disk. Therefore, accurate segmentation and elimination of optic disk is necessary to reduce the adverse effects of the presence of optic disk on the segmentation of bright lesions like exudates. The designed method, in this work, for optic disk segmentation and elimination relies on the two benchmark conditions about optic disk: (i) all the main blood vasculature fragments emanates radially outwards from the optic disk as shown in figure 5.3 and (ii) optic disk represents one of the bright regions in retinal fundus image. The methodology of segmentation and elimination of optic disk is graphically represented in figure 5.4.

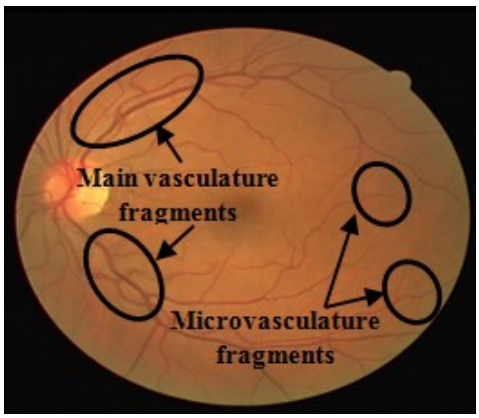

Figure 5.3 Retinal fundus image depicting main and microvasculature fragments

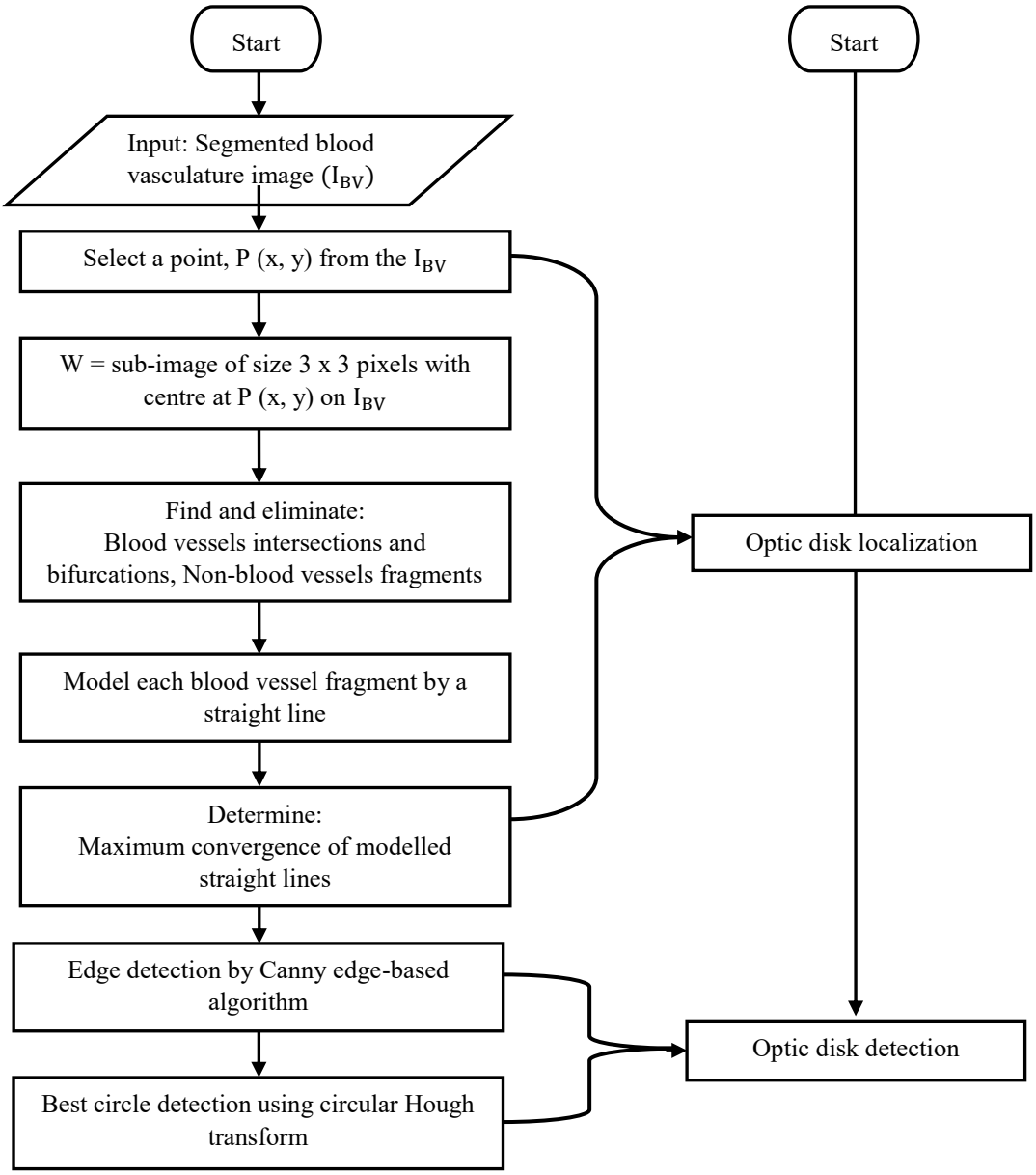

Figure 5.4 Flowchart for the segmentation and elimination of optic disk in retinal fundus image

Optic Disk Localization

The first step in the localization of optic disk is an accurate extraction of blood vessels skeleton from the segmented blood vessels image, I_{BV}. Basically, this blood vessels skeleton is a binary image which contains only the main blood vessel fragments, whereas I_{BV} contains both main and micro blood vessels fragments. Also, I_{BV} may contain small non-blood vessel fragments due to the presence of retinal lesions in pathological retinal fundus images. The

accurate extraction of blood vessels skeleton is performed by the elimination of these non-blood vessels and microvasculature fragments. Afterwards in the next step, the convergence of main blood vessels fragments into optic disk is discovered by calculating the orientations of main blood vessels fragments using a convergence-based technique. The description of proposed optic disk localization method is provided in the following steps:

Step 1: The segmented blood vasculature image, I_{BV}, is taken as an input image.

Step 2: Consider a point $P(x, y)$, as a center pixel, on the image I_{BV}.

Step 3: Select a sub-image around the point P of the size 3 x 3 pixels showing the eight neighbouring pixels around this centre pixel.

Step 4: If the pixel $P(x, y)$ belongs to the blood vessels in the sub-image, then it must decide that this pixel is a part of the main blood vessels or not. If it is not a part of the main blood vessels then it will be either an intersection points of two blood vessels or a bifurcation point of a blood vessel. This decision is made by implementing the fact that main blood vessel fragment appears as linear segment whereas the pixels belonging to intersection point, bifurcations point and other non-blood vessels structure appear as cluster in the sub-image of 3 x 3 pixels and thus will have more than 3 pixels of the same intensity as that of central pixel. Some of the possible main blood vasculature fragments in sub-image of size 3 x 3 pixels are shown in figure 5.5 (a)-(c) and (d) shows an example of the bifurcation point in blood vasculature. This is the reason behind to set a threshold value, T_{BV_pix}, equals to 3 pixels for the identification of main blood vessel segment in the sub-image.

Step 5: Calculate the number of pixels, $Sub\_Num_{pix}(x, y)$, having intensity value equal to one, in the sub-image around the pixel $P(x, y)$ of the segmented binary image, I_{BV}, as

$$Sub\_Num_{pix}(x, y) = \sum_{k=-1}^{1} \sum_{g=-1}^{1} I_{BV}(x + k, y + g) \tag{5.3}$$

Step 6: If the number of pixels, as per Eq. (5.3), in the sub-image lies above the threshold value, then the pixels in the sub-image does not belong to main blood vessel fragment and are eliminated. However, if the number of pixels in the sub-image is either 3 or less than three, it is either a main blood vessel fragment or its end point and thus preserved. The blood vasculature skeleton image (I_{BV_SKT}), obtained after thresholding, is mathematically expressed as:

$$I_{BV_{SKT}} = \quad (5.4)$$

$$\begin{cases} \text{pixel belonging to } I_{BV_{SKT}} & \text{if } Sub_{Num_{pix}}(x,y)^m \leq T_{BV_{pix}} \\ \text{pixel eliminated} & \text{if } Sub_{Num_{pix}}(x,y)^m > T_{BV_{pix}} \end{cases} \forall\ m \in 3 \text{ x } 3 \text{ pixel block}$$

Step 7: Further this blood vasculature skeleton image is used to identify end points, start and end positions, of each main blood vessel fragment. Figure 5.6 (a), (b) and (c) demonstrate the examples of end points in the block of 3 x 3 pixels size and it can be seen clearly that the end points can be identified in the block, if the number of white pixels will be two or less than two. Therefore, each main blood vessel fragment in I_{BV_SKT} is considered as one object and all the pixel locations of this object are stored in a matrix X. Afterwards, a block of 3 x 3 pixels size is traversed throughout the matrix X from left to right and top to bottom to locate the positions of end points by setting a threshold equal to two. If the number of white pixels, representing to blood vessel fragment, are less than or equal to two in that block, then then they are marked as end points.

Step 8: Draw a straight line from the two end points of each main blood vasculature fragment as shown in the image depicted in figure 5.2 (c).

Step 9: Go back to step 7, until all the objects are modelled by the straight lines, otherwise go to next step.

Step 10: Full scan of the image, as obtained after step 9, is performed to determine the region with maximum number of intersections of straight lines. The scanning process is carried out in a block size of 30 x 30 pixels that is determined empirically. Afterwards, the number of intersection points is calculated in each block. The centre pixel of the block, that has maximum number of intersection points, is considered as the centre location of optic disk.

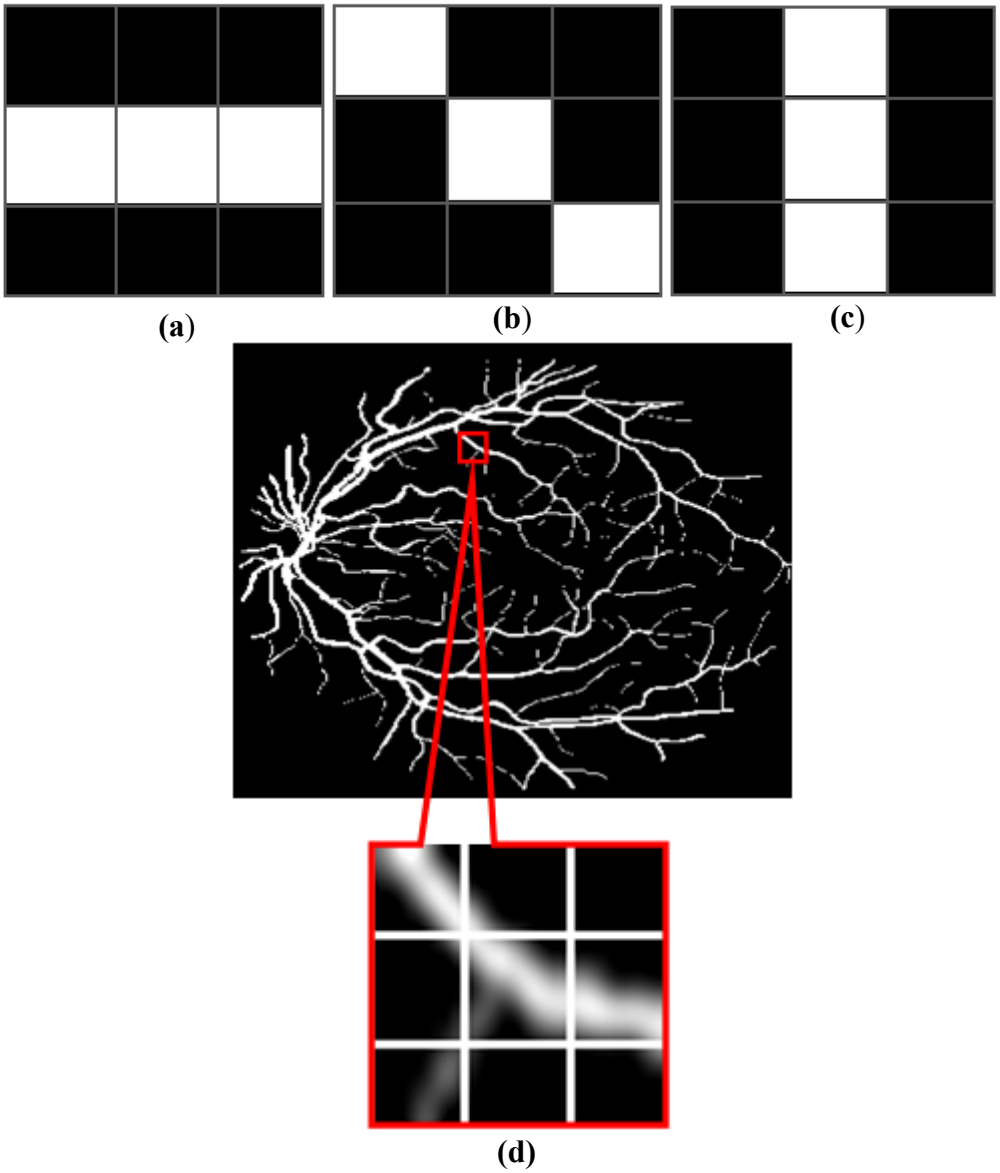

Figure 5.5 (a), (b), (c) Possible main blood vasculature fragments in retinal fundus image and (d) A typical blood vasculature segmented image with a bifurcation zoomed in

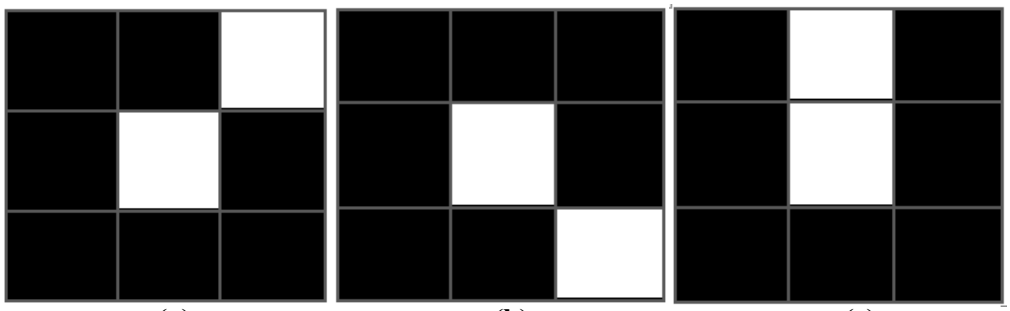

(a) **(b)** **(c)**

Figure 5.6 (a) - (c) Possible corner points of the main blood vasculature fragments

Optic Disk Detection

The previous phase, i.e., optic disk localization determines the optic disk centre in retinal fundus image. To detect the boundary of the optic disk, region of size 130 x 130 pixels is defined around the detected optic disk centre pixel in the original retinal fundus image $I(x, y)$. It was observed during analysis of various retinal image databases the largest optic disk lies within a block of 130 x 130 pixels and therefore the boundary of the optic disk is searched within this area. Optic disk in retinal fundus images appears to be circular in shape. Therefore, the Hough transform is then used to identify the approximate boundary of the optic disk that can be parameterized mathematically as a circle given by

$$(x - x_1)^2 - (y - y_1)^2 = r^2 \tag{5.5}$$

where (x_1, y_1) is the coordinate of the center of the circle that passes through (x, y) and r represent the radius of the circle. The steps carried out for the detection of optic disk boundary are described below.

Step 1: To find the various edges in the specified region of size 130 x 130 pixels in $I(x, y)$, Canny edge detection operator is applied. The application of canny operator eliminates most of the small unwanted structures present due to the fine texture of optic disc. Experimentally, canny operator with $\sigma = 1.5$ and filter of size 4 x 4 pixels provides satisfactory results. The resultant image, namely, edge image contains the edge segments in which many of them would

probably be the actual edges of the optic disk, but some may be not due to other structural variations in the optic disk area.

Step 2: Optic disk in retinal images can be of varying sizes. Therefore, a set of circles depending on the variations of radii of optic disk in different retinal image databases are initialized.

Step 3: Edge image is then scanned to map all the points to circles of varying radii defined by Hough transform using Eq. (5.5).

Step 4: Point of an edge image is preserved if it matches with any approximation of circle defined by Hough transform. The process is repeated until all the points of edge image are scanned.

Step 5: In this step, the set of points obtained in step 4 are compared to the set of circles initialized in step 2. The most fitting circle among the set of circles would be that one that has the maximum number of points coinciding with the circle.

Step 6: The boundary of optic disk is extracted by overlaying the mask of best fitted circle on the normalized blood vasculature image, N_{BV_img}. This image is now termed as mask image.

Optic Disk Elimination

Finally, the optic disk is eliminated from normalized blood vasculature image and the steps used in the optic disk elimination are as follows:

Step 1: The mask image obtained in the previous step is converted to binary image using thresholding. All the pixels except the optic disk boundary are assigned a value one and the corresponding optic disk boundary pixels are assigned a value zero.

Step 2: All the pixels inside the optic disk boundary are filled with a value zero using morphological filling operator.

Step 3: The image is then overlaid on the normalized blood vasculature image, N_{BV_img}.

The image, obtained after the elimination of anatomical structures, is now termed as lesion image, I_{Les_img}, as shown in figure 5.2 (d).

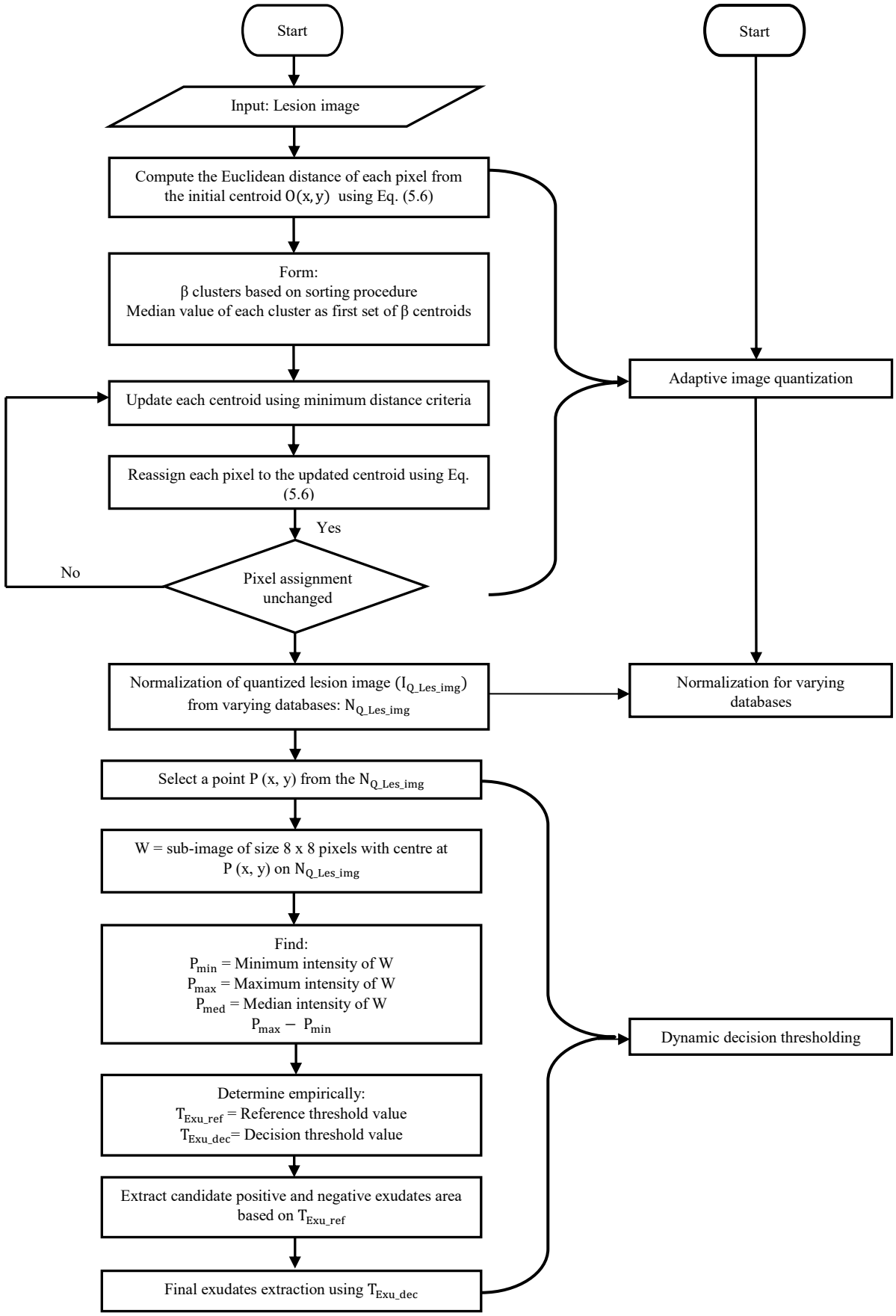

Figure 5.7 Flowchart for the segmentation of exudates on retinal fundus image

5.3 SEGMENTATION OF EXUDATES

The segmentation and elimination of blood vasculature and optic disk, in the previous phase, is designed to improve the accuracy of exudates segmentation method. This is because the image obtained after the removal of these anatomical structures has only the details of the lesions, if any abnormality is associated with this retinal fundus image. The exudates among all the possible lesions have high intensity variations with respect to background and are therefore much visible as bright patterns in I_{Les_img}. The flowchart of the proposed exudates segmentation method is presented in figure 5.7 and the detailed steps used in the implementation of the proposed method are explained as follows:

5.3.1 Adaptive Image Quantization

The image quantization stage reduces the number of distinct colours used in a retinal fundus image. The quantization is carried out by grouping the image pixels with similar attributes. These attributes are basically based on features of retinal fundus images. In this work, a novel adaptive k-means quantization method is developed and used in such a way that the varying intensities of colours in retinal fundus image are uniquely clustered. The basic k-means clustering method randomly partitions the image pixels into colour sets based on k initial centroids, selected arbitrarily, k being the user specified parameter. Then the iterative process is carried out to update centroid of each cluster by taking the mean of pixel values in each cluster. The final clustering results of k-means method highly depend upon the correctness of the initial centroids and do not promise to produce unique clustering results. Therefore, to improve the accuracy and efficiency of basic k-means clustering method, the proposed method divides pixels of image by (i) finding fixed set of initial and final centroids for a set of pixels to provide unique clustering results and (ii) efficiently assigning the pixel intensities to suitable clusters. In the proposed method, k-means quantization for clustering pixel intensities is carried out in such a way that the clusters formed in each iteration are sorted repeatedly until the

clusters meet the specified minimum distance criteria. Since the novel k-means method adapts itself to changes in range of pixel intensities of retinal fundus images, it is called as adaptive k-means method. The step wise description of the proposed method is as follows:

Step 1: The lesion image, I_{Les_img}, is taken as an input image.

Step 2: Select the lower left corner point of I_{Les_img} as origin $O(0,0)$ as shown in figure 5.8.

Step 3: For each pixel coordinate compute the distance from origin, the initial centroid, using the Euclidean distance given by

$$D = \sqrt{\sum_{i=1}^{m} (p_i - c_i)^2} \tag{5.6}$$

where m is the number of pixels in lesion image, p_i denotes the i^{th} pixel in consideration and c_i is the centroid pixel.

Step 4: Then, the pixel values of all coordinates are sorted in accordance with the sorted distances in ascending order.

Step 5: After sorting, partition the sorted pixel values into β equal clusters and take the median value of each cluster as the centroid.

Step 6: Compute the distance between each pixel value $p_i(1 \leq i \leq n)$ and all the centroids $C_j(1 \leq j \leq \beta)$, selected in step 5, using Eq. (5.6).

Step 7: For each pixel p_i, find the closest centroid C_j and assign p_i to cluster C_j.

Step 8: For each cluster $j(1 \leq j \leq \beta)$, recalculate the centroids by taking the mean of its pixel values.

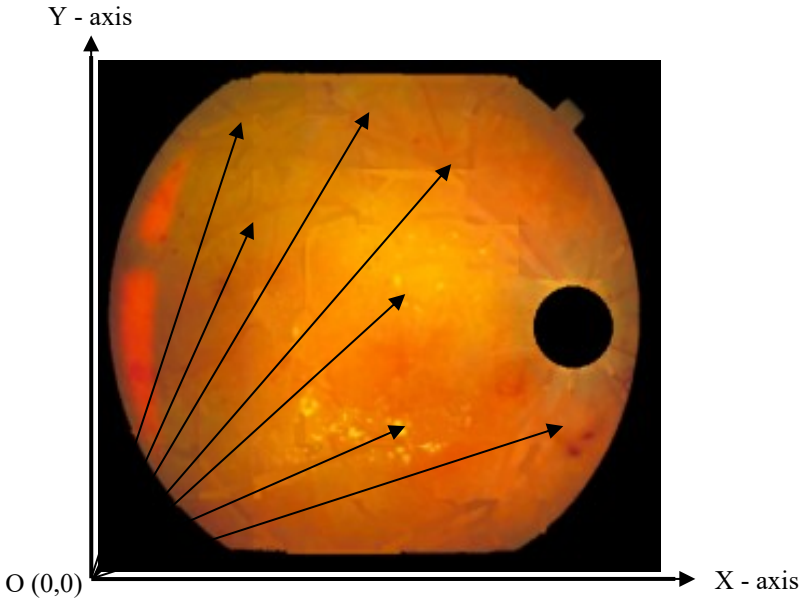

Figure 5.8 Data points in two-dimensional space

Step 9: For each pixel p_i, (i) Compute the distance from the centroid of the present nearest cluster. If the distance is less than or equal to the present nearest distance, the corresponding pixel stays in the same cluster (ii) otherwise for every centroid the distance from the pixel in consideration is computed.

Step 10: This iterative process continues until all the centroid pixels satisfies the convergence criteria. The centroid pixels are convergent if all the pixels of an image are assigned to the clusters having the nearest centroids.

Step 11: Lastly, each pixel value is replaced by its corresponding centroid pixel value, resulting in quantized lesion image ($I_{Q\_Les\_img}$).

5.3.2 Normalization of Quantized Lesion Image

The great variability of pixel intensity values within and among varying databases of retinal fundus images makes it hard to decide the threshold values for the quantized images. Therefore, normalization process is carried out to achieve consistency in the dynamic range of pixel values. The process of normalization of pixel intensity values of each red, green and blue channels of quantized image is carried out in 3 steps.

Step 1: The mean intensities of quantized lesion image, $I_{Q\_Les\_img}$, for each red, green and blue channel is calculated as

$$\mathrm{M_r} = \frac{\sum_{i=1}^{R} \mathrm{I_{RQ_{Les\_img}}(x,y)}}{\mathrm{N_I}}, \mathrm{M_g} = \frac{\sum_{i=1}^{G} \mathrm{I_{GQ_{Les\_img}}(x,y)}}{\mathrm{N_I}} \quad \text{and } \mathrm{M_b} = \frac{\sum_{i=1}^{B} \mathrm{I_{BQ\_Les\_img}(x,y)}}{\mathrm{N_I}} \tag{5.7}$$

where $\mathrm{M_r}, \mathrm{M_g}$ and $\mathrm{M_b}$ are mean intensity values of red, $\mathrm{I_{Rq\_les\_img}(x,y)}$, green, $\mathrm{I_{Gq\_les\_img}(x,y)}$, and blue, $\mathrm{I_{Bq\_les\_img}(x,y)}$ clustered channel images respectively and $\mathrm{N_I}$ represents the number of pixels in $\mathrm{I(x,y)}$.

Step 2: Mean intensity value is then subtracted from the intensity value of each $\mathrm{i^{th}}$ pixel value in the quantized image. It is represented as

$$\mathrm{I_{S\_Q\_Les\_img}} = \mathrm{I_{Q\_Les\_img}(x,y)} - \mathrm{M} \tag{5.8}$$

Step 3: Finally, the intensity values of quantized lesion image are normalized to consistent range of values using

$$\mathrm{N_{Q\_Les\_img}} = \frac{\mathrm{I_{S\_Q\_Les\_img}}}{\max(\mathrm{I_{S\_Q\_Les\_img}})} \tag{5.9}$$

5.3.3 Dynamic Decision Thresholding

The normalized and quantized lesion image, $\mathrm{N_{Q\_Les\_img}}$, consist of fewer number of intensities as compared to original retinal fundus image. The required intensities corresponding to exudates can be obtained only by proper filtering of exudates from other pixels of retinal image corresponding to background and red lesion structures. In addition, exudates are generally brighter than the retinal image background and other lesions present in retinal fundus image. Thus, an appropriate thresholding criterion can differentiate true exudates from other regions of retinal image. Therefore, filtering of exudates pixels is carried out by assessing the range of intensity values of the pixels to be thresholded.

Any retinal fundus image will always have varying number of intensities, i.e., image consists of both foreground and background intensity pixels. Background intensity pixels are the pixels apart from the optic disc, blood vasculature and the lesions present in retinal fundus image. However, foreground intensity pixels can be a part of any lesion present in the retinal fundus image. Therefore, the segmentation of exudates from foreground pixels requires the removal of background pixels and segregation of pixels corresponding to exudates from other red lesions. These unwanted background pixels are removed by computing the mean or median pixel intensity values of $N_{Q\_Les\_img}$. If the retinal fundus image is healthy, the mean and median produce similar values. But, for the pathological retinal fundus images the median produces more accurate estimation of retinal background. Since, the proposed method aims to distinguish exudates from other regions; the thresholding value must be greater than the intensity values of background pixels and other red lesions. However, it is important how bigger the threshold parameter value should be chosen. It is accomplished by empirically choosing two threshold parameters namely: (i) reference threshold value T_{Exu_ref} and (ii) decision threshold parameter T_{Exu_dec} that dynamically segments exudates from each retinal image. The step wise procedure of the dynamic thresholding method is as follows:

Step 1: Consider $N_{Q\_Les\_img}$ obtained from the previous step.

Step 2: Extract a sub-image, W of size 8 x 8 pixels and store the maximum, $P_{max(i)}$, minimum, $P_{min(i)}$, and median, $P_{med(i)}$, intensity value present in W.

Step 3: Compute the difference of maximum and minimum intensity values stored in step 2 and select the reference threshold value T_{Exu_ref}.

Step 4: If the computed difference is greater than the reference threshold value or the median intensity value in W, the region is classified as positive exudates region, Reg_{pos}; otherwise, it

is classified as negative exudates region, $\mathrm{Reg_{neg}}$, and therefore eliminated. The segmented region image thus obtained is represented as

$$I_{\mathrm{Reg_{seg}}} = \begin{cases} \mathrm{Reg_{pos}} & \text{if } \{(P_{max} - P_{min}) > T_{\mathrm{Exu_{ref}}}\} \cup \{P_{max} > P_{med}\} \\ \mathrm{Reg_{neg}} & \text{otherwise} \end{cases} \in 8 \times 8 \text{ pixel block} \quad (5.10)$$

where $P_{max(i)}$, $P_{min(i)}$ and $P_{med(i)}$ are the maximum, minimum and median intensity value present in the sub-image W.

Step 5: From the positive exudates regions, the precise exudates are thresholded using the dynamic threshold value as follows:

$$I_{Exu\_seg} = \begin{cases} 1 \; \forall \; \mathrm{Reg_{pos(i)}} > [P_{max(i)} - (T_{\mathrm{Exu_{dec}}})(P_{max(i)})] \\ 0 \quad \text{otherwise} \end{cases} \forall \, i \in 8 \times 8 \text{ pixel block} \quad (5.11)$$

where dynamic threshold value is represented by $[P_{max(i)} - (T_{Exu\_dec})(P_{max(i)})]$. Dynamic threshold value represents the range of intensity values preserved in each positive exudate region for boundary extraction. It is computed by subtracting the lower bound threshold intensity value from the maximum intensity present in each sub-image ($P_{max(i)}$). Lower bound threshold (T_{Exu_dec}), determined empirically, is the percentage intensity value of $P_{max(i)}$.

5.4 EXPERIMENTAL SET UP

The parameter optimization and the experiments carried out on the proposed exudates segmentation method is described in this section.

5.4.1 Parameters Considered for the Segmentation of Exudates

Three parameters are needed to be optimized in the proposed exudates segmentation method i.e.,

(i) β: Number of clusters, for adaptive image quantization

(ii) T_{Exu_ref}: Reference threshold value for the segregation of positive and negative exudates area

(iii) T_{Exu_dec}: Decision threshold value to determine the final exudates clusters

The retinal fundus images database has large variations of mean intensity difference of inside and outside regions of exudates. Therefore, the optimized visibility of exudates by reducing the number of distinct intensities in the image requires the application of quantization algorithm. Application of adaptive image quantization method on varying database images has shown that the segmentation performance is considered sensitive to the number of clusters selected for grouping image pixels with similar attributes. The choice of number of clusters depends on adherence to the compactness of boundaries of detailed structures of retinal image. Boundary recall, a standard measure for boundary adherence, measures the fraction of ground truth edges lying within two pixels of cluster boundary [171]. The boundary recall for varying number of clusters is plotted in figure 5.9 for sample images from each database. A high boundary recall indicates that very few true edges are missed. It can be observed from the figure that, initially, the boundary recall increases with the increase in number of clusters, indicating the increase in number of varying intensities of exudates for precise segmentation. After a certain value, i.e. ≈30 there is no significant improvement in the boundary recall parameter and the retinal structures are getting over segmented resulting in many insignificant boundaries. This is due to the inclusion of small variations of intensity inside exudates. Thus, the optimized value of β was set to 30.

The dynamic decision thresholding requires two parameters, i.e., reference threshold value and decision threshold value. T_{Exu_ref} controls the classification of sub-images into positive and negative exudates region under consideration. Further, T_{Exu_dec}, representing the percentage value of maximum intensity present in sub-image, thresholds the range of intensities

from histogram of the positive exudates region under consideration. A series of experiments were conducted to determine the optimal threshold values. The optimal intensity thresholds are the ones that achieve best sensitivity/specificity combination. Increase in sensitivity indicates the correct detection of bright as well as subtle exudates, whereas higher specificity shows that the method does not recognize a non-exudates pixel as an exudates pixel. Table 5.1 shows one of the experiments conducted on a sample retinal image to determine the optimal threshold values. It can be observed from this table that initially with the increase in T_{Exu_ref} and T_{Exu_dec}, sensitivity and specificity were improving indicating the higher number of correct detections of exudates and non-exudates structures. However, after a certain value, sensitivity and specificity started decreasing indicating considerable number of false positive detections. A series of experiments were conducted on varying database images and the optimized values of T_{Exu_ref} and T_{Exu_dec} was set to 60 and 20.

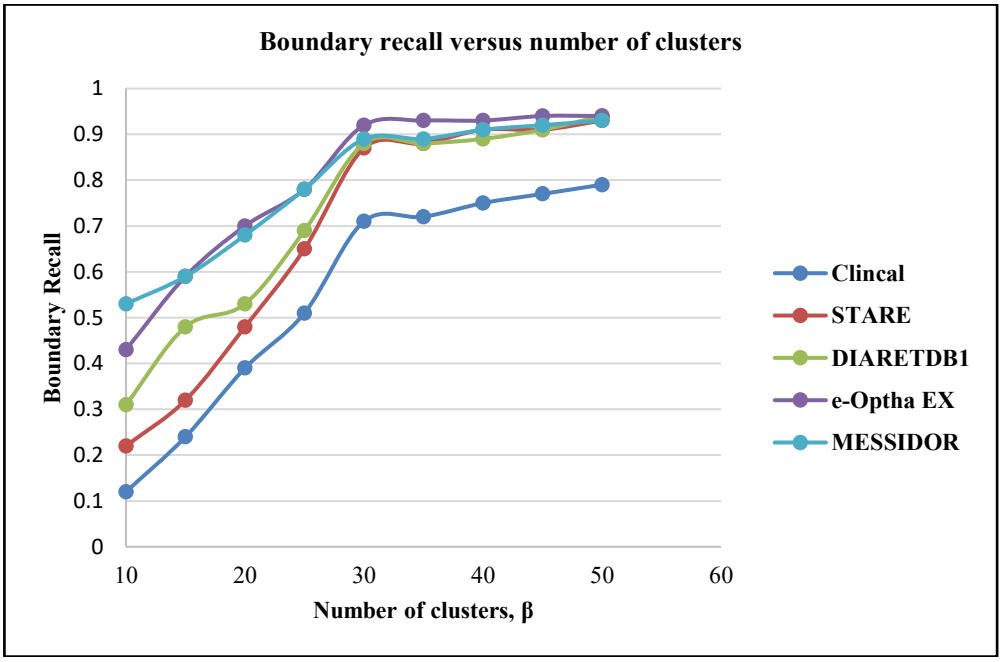

Figure 5.9 Boundary recall vs β for varying database images

Table 5.1 Results corresponding to varying threshold values on a sample retinal fundus image

T_{Exu_dec} \ T_{Exu_ref}	40 SN/SP	50 SN/SP	60 SN/SP	70 SN/SP	80 SN/SP
5%	78.34/84.78	80.54/86.87	82.92/89.32	82.34/88.42	81.32/89.33
10%	79.76/86.45	81.23/87.95	84.19/93.28	83.43/93.23	82.45/91.42
15%	81.77/88.98	85.34/91.23	88.93/95.03	85.93/93.33	85.86/91.01
20%	84.56/91.45	88.55/94.44	**90.43/97.34**	89.02/96.78	88.32/93.67
25%	83.89/91.67	88.11/94.27	89.98/97.32	88.23/95.33	84.23/88.13
30%	80.78/87.12	83.29/87.32	82.92/93.21	82.43/88.23	83.42/84.23

5.4.2 Experiments

The proposed exudates segmentation method is implemented in MATLAB version 2016a on a PC with intel core i7 processor. The performance evaluation of the proposed method is carried out in two ways: subjectively and objectively. First, the segmented exudates structures are examined for the assessment of segmentation performance via visual interpretation by expert ophthalmologist. Visual interpretation is defined as the ability of an ophthalmologist to extract useful lesion information from a retinal fundus image. Visual interpretation of segmented retinal fundus image was assessed by an expert ophthalmologist associated with Sri Guru Harkrishan Sahib Eye Hospital (SGHS), Mohali, India. Objectively, the segmentation performance is evaluated using medically significant statistical measures.

Subjective Evaluation Methodology:

The subjective performance evaluation is carried out on 5048 retinal fundus images comprising of 990 healthy images, 833 images with exudates and 3225 images with other retinal lesions present in retinal fundus images. For subjective evaluation by the ophthalmologists, first, original retinal fundus image and the corresponding segmented exudates images were presented for marking the score of each segmentation result according

to subjective visual perception criterion. Visual perception criterion is based on the quality of segmentation which can be said to be precise if it allows the observer to perceive better the desired information in the image. Four was the score that was assigned for the accurate segmentation of exudates and one was assigned for the worst segmentation results. Two and three were the scores for average and good segmentation results respectively. Finally, a visual evaluation of the segmentation results obtained after the application of method was made.

Objective Evaluation Methodology:

Objectively, the performance evaluation of the proposed method is carried out in two experiments: lesion-based evaluation and image-based evaluation.

Experiment 1: Lesion based evaluation computes the efficiency of the exudates segmentation method to precisely segment the exudates. The performance at lesion level is evaluated quantitatively by comparing the segmented retinal fundus images with reference ground truths, as mentioned earlier, by experienced ophthalmologists. The performance is enumerated using medically significant statistical measures like sensitivity, specificity, accuracy and positive predictive value. These performance measures are briefly described as given below:

(i) Sensitivity: Sensitivity, defined in Eq. 4.25, is the measure that estimates the capability of a method to detect exudates pixels correctly among the true exudates pixels in reference ground truth. TP now represents the exudates pixels correctly detected by the method as exudates pixels in reference ground truth and FN represents the number of exudates pixels which are falsely detected by the method as non-exudates pixels in reference ground truth.

(ii) Specificity: Specificity, defined in Eq. 4.26, is a measure that estimates the capability of a method to detect the non-exudates pixels correctly among the true non-exudates pixels in reference ground truth. TN now represents the number of non-exudates pixels correctly

detected by the method as non-exudates pixels in reference ground truths and FP represents the number of non-exudates pixels which are falsely detected by the method as exudates pixels.

(iii) Accuracy: Accuracy, defined in Eq. 4.27, is a measure that estimates the overall capability of a method to correctly detect exudates and non-exudates pixels among all the exudates and non-exudates pixels in reference ground truth being examined.

(iv) Positive predictive value (PPV): It is a measure that computes the capability of a method to detect the true exudates pixels among all the detected exudates pixels and is expressed as

$$\text{Positive predictive value} = \frac{\text{TP}}{\text{TP} + \text{FP}} \tag{5.12}$$

The range of the performance measures is between 0 to 100%, the best value of 100% is achieved if the segmentation results and the reference ground truths are exactly same. Higher the values of these parameters, the less will be the ambiguity between the original and segmented images.

Experiment 2: Image based evaluation of the proposed method discriminates the retinal fundus images based on the presence or absence of exudates in retinal fundus images. The quantitative image-based evaluation is carried out by evaluating the above mentioned statistical measures i.e. sensitivity, specificity, accuracy and PPV as per Eqs. (4.25) - (4.27) and Eq. (5.12). Further, conditions such as TP, TN, FP and FN now refer to the presence or absence of the disease in the segmented images for image-based evaluation. The definitions of these terms are now modified as given below:

- TP: It refers to the condition when the segmentation result of a method is positive and the reference ground truth condition is also positive.
- TN: Both the segmentation results of a method and reference ground truth represent negative.
- FP: The segmentation result is positive but the reference ground truth is negative.
- FN: The segmentation result is negative but the reference ground truth is positive.

5.5 RESULTS AND DISCUSSION

The results are evaluated subjectively by the expert ophthalmologist and objectively by the statistical measures as given below:

Subjective Evaluation:

Clinically acquired database: The ophthalmologist opined that out of the total of 1351 retinal images containing exudates, the total of 1288 images having good contrast between normal and pathological regions got the highest visual score i.e. four in comparison to other segmented images. The proposed method performs quite well with a visual score of 3 for the total of 52 retinal fundus images having weak contrast between normal and pathological regions. For these cases, ophthalmologist says that the results provide the necessary information required for screening. The segmentation results of the proposed method got a visual score of 1 or 2 for 11 retinal images and ophthalmologist opined that it is very difficult to interpret such retinal images containing exudates with fuzzy boundaries.

Figure 5.10 shows the sample clinically acquired retinal images with varying visual appearance of exudates and their segmentation results obtained after the application of proposed method. From figure 5.10 (a), it is observed that the exudates present in retinal fundus

images have good contrast with respect to the background of retinal fundus images. When such images having good contrast between background and pathological regions are processed for segmentation, it is observed that the segmentation obtained by the proposed method is very close to the reference ground truth of the exudates provided by the expert. A close examination of figure 5.10 (b) and (c) shows that the proposed method can segment those exudates pixels which were not even marked by expert due to poor visual details. From figure 5.10 (d), it is observed that the exudates present in retinal fundus images have weak contrast with the normal region, and hence it becomes difficult to extract the precise boundary of the lesion. When such images with weak contrast between background and pathological regions are processed for segmentation, it is observed that the segmentation results of the proposed method are slightly under-segmented in the regions having small exudates and slightly over-segmented in the regions having large exudates, as depicted in figure 5.10 (e). However, the proposed method can locate all the exudates structures present in retinal fundus images. Finally, it is also observed that the segmentation results of retinal images having varying contrast in different regions gives better visual appearance of exudates in comparison to original retinal images, as shown in figure 5.10 (g) and (h) respectively.

Online acquired databases: The ophthalmologist opined that out of 400 retinal fundus images acquired from publicly available databases, 389 retinal images got the highest visual score i.e. four. Out of remaining 11 cases, 8 cases got the visual score of 3 and 3 cases got the visual score of either 1 or 2. According to ophthalmologist, for these 3 retinal images the exudates structures are either mixed with flash artifacts and are not visible clearly or have very weak contrast with respect to the background.

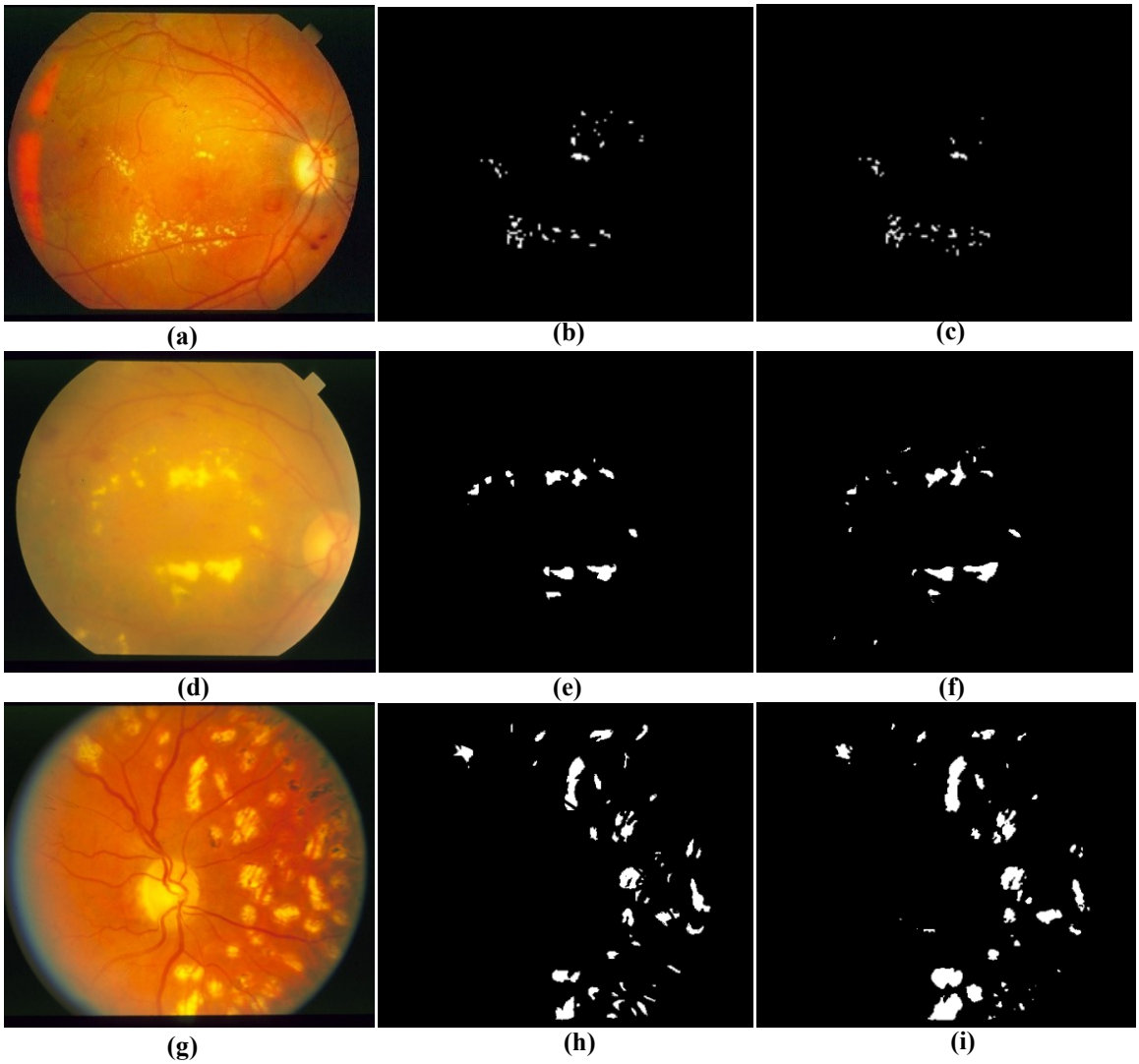

(a), (d), (g): Original retinal fundus images from clinically acquired database
(b), (e), (h): Results of proposed exudates extraction method
(c), (f), (i): Reference ground truths

Figure 5.10 Original and processed pathological images by the proposed exudates extraction method

Segmentation results of sample retinal fundus images randomly selected from publicly available databases by the proposed method are shown in figure 5.11. From figure 5.11 (a) and (d), retinal images from STARE database, it is observed that the boundaries of exudates are slightly blurry and mixed with the normal region. Therefore, in such images it becomes difficult even for the ophthalmologist to segment the exact boundary precisely. When these images having blurred boundaries are processed for segmentation, it is observed that the segmentation obtained by the proposed method is very close to the reference ground truths of the exudates.

From figure 5.11 (b) and (e), it is also observed that the proposed method can segment the prominent and large as well small exudates structures present in retinal fundus images. Also, from an examination of figure 5.11 (g) it is observed that the size of exudates is too small as compared to the overall size of the retinal fundus image. When the images with weak contrast between normal and pathological region is processed for segmentation, it is observed that there is chance of some exudates structures of very few pixels being missed during segmentation. However, the segmentation results of the proposed method are very close to the reference ground truths and provide necessary lesion information.

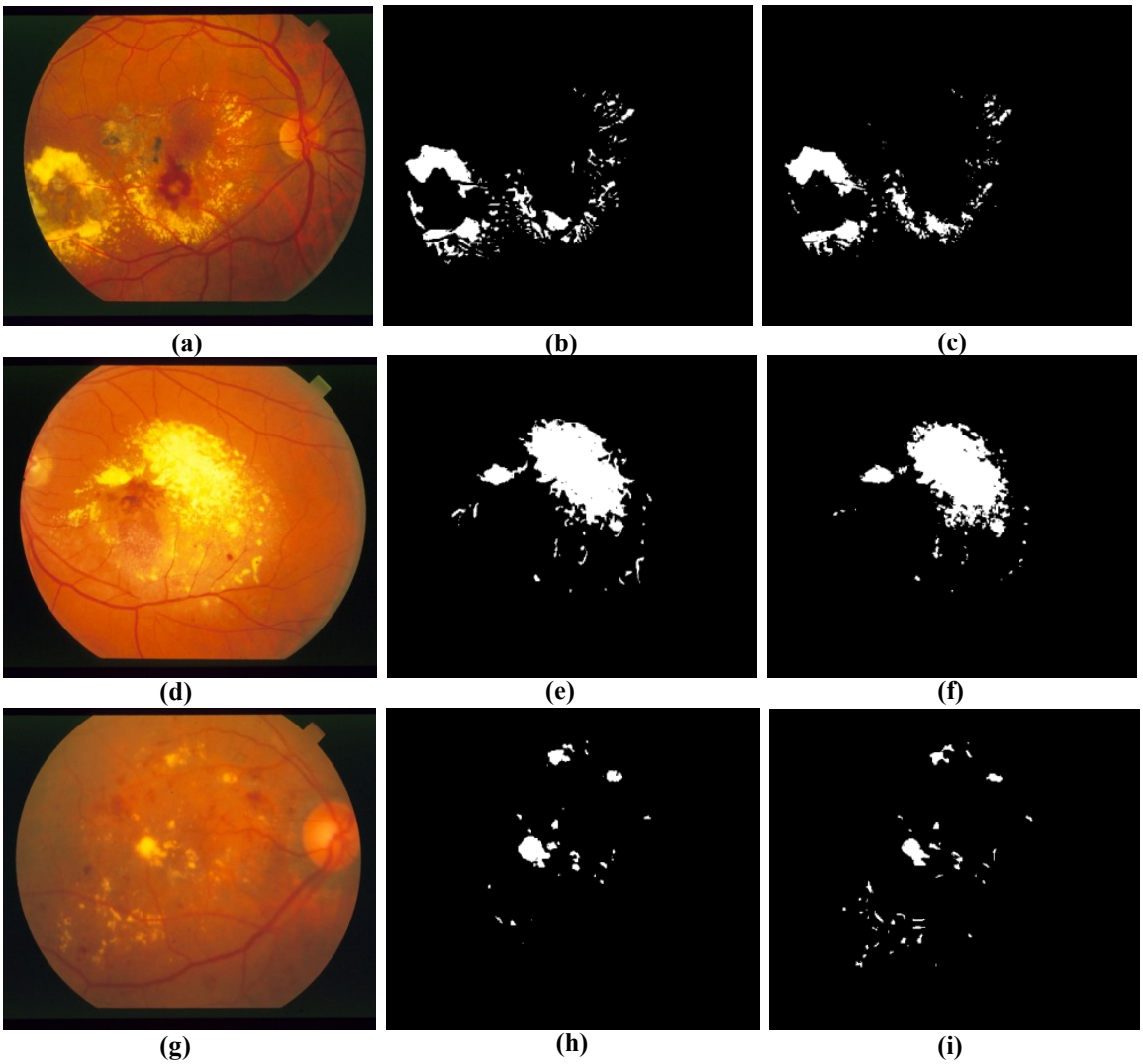

(a), (d), (g): Original retinal fundus images from online datasets
(b), (e), (h): Results of proposed exudates extraction method
(c), (f), (i): Reference ground truths

Figure 5.11 Original and processed pathological images by the proposed exudates extraction method

Table 5.2 Comparative performance of the proposed method concerning the segmentation of exudates with other existing methods

Method	Database	No. of Test Images	Lesion Based Results (%)				Image Based Results (%)				Time (sec.)
			SN	SP	Acc	PPV	SN	SP	Acc	PPV	
Walter [79]	Clinical	15	92.8	----	----	92.4	--	----	----		----
Sopharak [80]	Clinical	60	80	99.46	52.36	----	----	----	----	----	----
Reza [90]	STARE DRIVE	20	94.3	100	----	92	----	----	----	----	----
Sopharak [83]	Clinical	40	87.28	99.24	99.11	42.77	----	----	----	----	1080
Yazid [78]	Clinical STARE	15 15	90.7 97.8	99.4 99	----	74 83.3	----	----	----	----	----
Zhang [82]	Clinical MESSIDOR DIARETDB1 HEI-MED	47 1200 89 169	62.3	----	----	71	----	----	----	----	35
Jaya [97]	Clinical	200	94.1	90	93	----	----	----	----	----	----
Welfer [81]	DIARETDB1	89	70.4	98.84	----	21.32	----	----	----	----	----
Niemeijer [85]	Clinical	300	----	----	----	----	95	86	----	----	----
Youssef [92]	Clinical	7	----	----	----	----	80	100	----	----	----
Lahmiri [95]	STARE	45	----	----	----	----	100	100	100	----	240
Figueiredo [18]	Clinical	607	----	----	----	----	89.81	97.47	----	----	15.97
Wisaeng [96]	Clinical	1220	----	----	----	----	90.42	94.6	93.69	----	----
Osareh [84]	Clinical	142	93	94.1	----	----	95	88.9	----	----	660
García [77]	Clinical	117	88.08	----	----	80.54	100	83.95	93.53	----	----
Sánchez [76]	Clinical	80	90.2	----	----	96.8	100	90	----	----	----
Giancardo [86]	MESSIDOR DIARETDB1 HEI-MED	1200 89 169	----	----	----	----	----	----	----	----	9.3
Harangi [93]	DIARETDB1	89	63	85%	----	----	89	----	----	75	----
Proposed Method	**Clinical**	**2942**	**94.80**	**99.80**	**98.43**	**97.30**	**98.8**	**100**	**100**		**9.36**
	STARE	**184**	**99.65**	**99.12**	**99.13**	**98.76**	**100**	**100**	**100**		
	MESSIDOR	**1200**	**81.32**	**90.47**	**86.00**	**85.87**	**88**	**98**	**93**		
	DIARETDB	**219**	**71.34**	**88.56**	**85.34**	**79.89**	**91**	**94**	**89**		
	e-Ophtha	**463**	**83.00**	**98.80**	**92.00**	**89.40**	**91**	**94**	**93**		
	DRIVE	**40**	**98.43**	**96.34**	**98.23**	**95.12**	**95**	**100**	**97.5**		
	OVERALL	**5048**	**87.95**	**96.45**	**92.64**	**92.34**	**93.25**	**97.64**	**97.48**		

Objective Evaluation: Quantitative performance of the proposed exudates segmentation method in terms of four medically important statistical measures for both the experiments is tabulated in Table 5.2.

Experiment 1: Lesion Based Evaluation

Clinically acquired database: Table 5.2 shows that the proposed exudates segmentation method based on lesion level evaluation achieves average exudates segmentation sensitivity, specificity and accuracy of 94.8%, 99.8% and 98.43% respectively on the clinically acquired retinal images. These values clearly demonstrate the high performance of the proposed method. The bar graphs plots in figure 5.12 highlight the summary of each statistical measure by showing deviation in its value around average value. These plots clearly illustrate the overall high values of performance parameters on the database of 2942 clinically acquired retinal images with least deviation of 0.038% for specificity and highest deviation of 4.73% for sensitivity from their average values. Further figure 5.12 (a), (b) and (c) presents a detailed comparison of the performance of the proposed method with other state of the art methods using clinically acquired databases in terms of bar plots for all four statistical measures. On comparing figure 5.12 (a), (b) and (c), it can be observed that the proposed method shows the best performance among all the state of the art methods using clinically acquired databases. Also, the lowest deviation of 4.73% and 2.31% from average values for sensitivity and PPV, respectively, shows the consistency of the proposed method for segmenting the exudates from retinal fundus images.

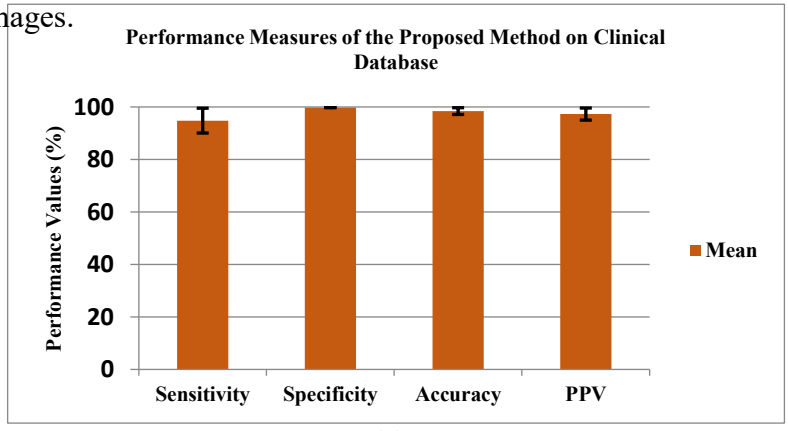

(a)

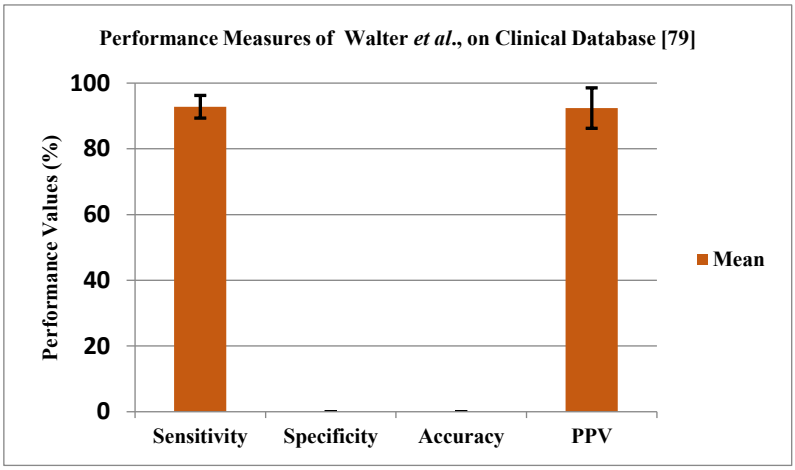
Performance Measures of Walter *et al*., on Clinical Database [79]
Performance Values (%)
100
80
60
40
20
0
Sensitivity
Specificity
Accuracy
PPV
Mean

(b)

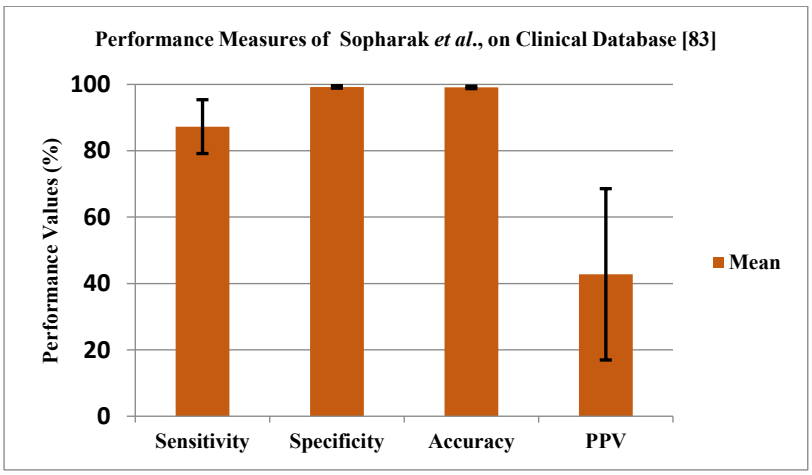
Performance Measures of Sopharak *et al*., on Clinical Database [83]
Performance Values (%)
100
80
60
40
20
0
Sensitivity
Specificity
Accuracy
PPV
Mean

(c)

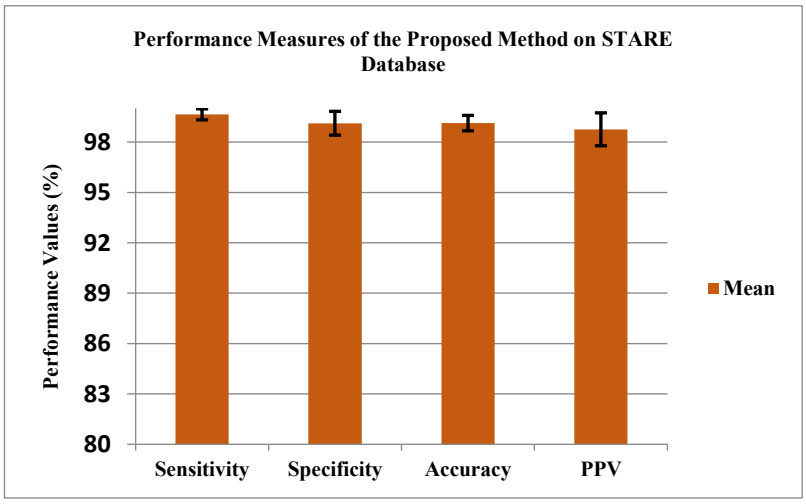
Performance Measures of the Proposed Method on STARE Database
Performance Values (%)
98
95
92
89
86
83
80
Sensitivity
Specificity
Accuracy
PPV
Mean

(d)

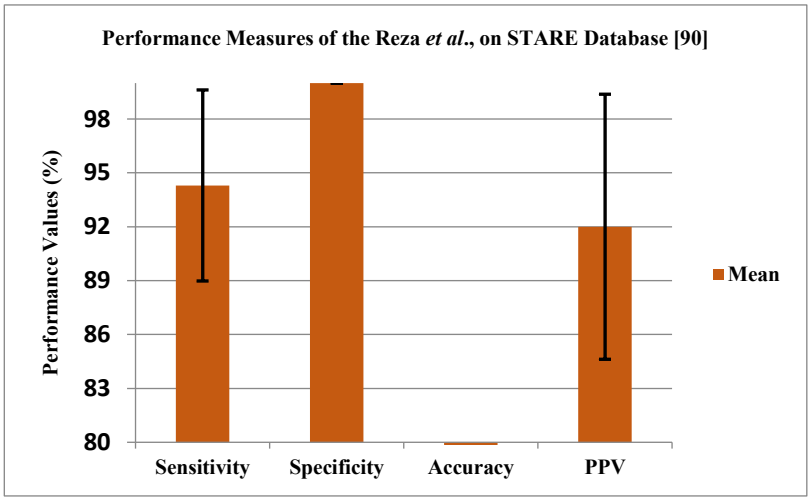

(e)

Figure 5.12 Summary of performance parameters for (a) proposed method on clinical acquired retinal images, (b) Walter *et a*l. on clinical acquired retinal images, (c) Sopharak *et a*l. on clinical acquired retinal images, (d) proposed method on retinal images from STARE database and (e) Reza *et al*. on retinal images from STARE database

Online acquired database: The proposed method shows the lesion-based sensitivity, specificity and accuracy of 99.65%, 99.12% and 99.13% on STARE database and 81.32%, 90.47% and 86% on the MESSIDOR database respectively. The segmentation results of the STARE database are very close to the segmentation results of Reza *et al*. [90]. However, on comparing figure 5.12 (d) and (e), it can be observed that the proposed method has a significant contribution in achieving the deviation of 0.33% and 0.98% from average values for sensitivity and PPV which is sufficiently smaller than the method of Reza by 4.99% and 6.4% respectively. Further, table 5.2 depicts that the proposed method achieved average lesion-based sensitivity and PPV of 81.32% and 84.3% respectively for MESSIDOR database, which exceeds by 19.02% and 13.3% respectively from the method of Zhang [82]. It can also be observed that the proposed method is validated with a larger database as compared to the size of the most of the existing methods except that of Zhang *et al*. [82]. However, the limitation of Zhang is that it has been evaluated with two statistical measures and achieved the sensitivity and PPV of only 62.3% and 71% respectively. Among all the publicly available databases e-

Ophtha EX database is the only database with precisely labeled pixel level ground truths available online. Thus, to establish a fair comparison of lesion-based evaluation methods, results on e-Ophtha EX database are individually depicted in table 5.3. The proposed method achieved average sensitivity of (83 ± 2.34) %, which exceeds by 4% from the method of Welfer *et al*., reported in literature [81]. Additionally, the average PPV of (89.4 ± 3.56) % exceeds by 14.4% from the method of Liu *et al*. [15]. From table 5.3, it can be observed that the proposed method clearly outperformed the existing methods that have used e-Ophtha EX database for evaluation and thus, justifying all the results.

Table 5.3 Comparative results for lesion-based evaluation for the proposed method on e-Ophtha EX dataset

Method	SN (%)	PPV (%)
Zhang [82]	74	72
Welfer [81]	79	55
Liu [15]	76	75
Proposed Method	83 ± 2.34	89.4 ± 3.56

Table 5.4 Comparative results for image-based evaluation for the proposed method on DIARETDB1 dataset

Method	SN (%)	SP (%)	ACC (%)
Walter [79]	86	69	77
Welfer [81]	100	0	45
Liu [15]	83	75	79
Proposed Method	91 ± 3.34	94 ± 2.28	87 ± 4.29

Experiment 2: Image Based Evaluation

Clinically acquired database: Table 5.2 depicts that the overall sensitivity, specificity and accuracy on the clinically acquired database are 98.8%, 100% and 100% respectively, for the image-based evaluation criteria. These results clearly indicate the capability of the proposed method to discriminate retinal images based on the absence or presence of exudates. Moreover, it can also be observed that the proposed method shows the best performance for sensitivity,

specificity and accuracy for clinically acquired database, which exceeds by 8.38%, 5.4% and 6.31% respectively from the method of Wisaeng *et al*. [96].

Online acquired database: In literature, only few methods calculate the statistical measures based on image-based evaluation criteria on STARE database. Lahmiri *et al*. achieved average sensitivity, specificity and accuracy of 100% but validated their method on only 45 retinal images from STARE database and took approximately 240 seconds for execution [95]. In addition to that, the method does not provide any lesion-based evaluation results. Image based evaluation results of the proposed exudates segmentation method in terms of sensitivity, specificity and accuracy are 100% for STARE database and 88%, 98% and 93% respectively for MESSIDOR database. These values clearly indicate high performance of the proposed method for image-based evaluation criteria. Table 5.4 demonstrates the comparative results for image-based evaluation on the DIARETDB1 database. Table 5.4 clearly indicates the significant contribution of the proposed method by achieving average specificity and accuracy of (94 ± 2.28) % and (87 ± 4.29) %, which exceeds by 19% and 8% respectively from the method of Liu *et al*. [15]. Conclusively, tables 5.2, 5.3 and 5.4 shows that the proposed method has achieved higher values of sensitivity, specificity, accuracy in comparison to that of other methods. The improvement especially in terms of sensitivity is supported by the exudates segmentation where removal of false exudates structures resulted in lower number of false positives.

In literature, only few methods computed the execution time of the method for the clinically acquired database. Zhang *et al*. discussed in their work that the computational time for the exudates segmentation in a retinal fundus image by their method is approximately 35 seconds [82]. Also, the time taken by the method proposed by Figueiredo *et al*. is 15.97 seconds. The proposed method takes approximately 4.23 seconds to eliminate the anatomical structures in a retinal fundus image, although this time may vary from image to image

depending on the size of the image and variations of intensities present. In addition to that, the computational time is (approximately) 2.82 seconds for image quantization, 2.31 seconds for dynamic decision thresholding and 9.36 seconds for the total execution of the method as mentioned in table 3. There is a 73.2%-time reduction by the proposed method in comparison to the method of Zhang and 41.4% from the method of Figueiredo. Therefore, the proposed method with this fast segmentation capability is suitable for segmenting the exudates structures in real time. Thus, qualitatively as well as quantitatively, the proposed method proves to be efficient as compared to state of the art methods.

5.2 CONCLUDING REMARKS

A novel and generalized exudates segmentation method for the computer-aided diagnosis of progressive diabetic retinopathy has been proposed and analyzed in this work. The proposed method is designed with the adaptive image quantization and dynamic decision thresholding to segment the boundaries of exudates irrespective of associated heterogeneity, bright and faint edges. The dynamic decision thresholding is robust in the sense that it selects the threshold value dynamically irrespective of the large variations in retinal fundus images. The performance of the proposed method has been evaluated on 5048 retinal fundus images acquired clinically and from publicly available standard databases. Results of subjective evaluation are supported by objective evaluation using two sets of experiments namely: lesion-based evaluation and image-based evaluation criteria. The experimental results for lesion-based evaluation indicate high performance of the proposed method in the segmentation of exudates with sensitivity/specificity/accuracy of 94.80/99.80/98.43 on clinically acquired database images. The image-based evaluation results demonstrate a high precision in correct recognition of pathological images from healthy images with average sensitivity/specificity/accuracy of 98.8/100/100 respectively. The results also reveal that the proposed method performs significantly well for online databases with the sensitivity/accuracy

of 99.65/99.13 on STARE database; 81.32/86.00 on MESSIDOR database; 83/92 on e-Ophtha EX database; 71.34/85.34 on DIARETDB1 database for lesion-based evaluation criteria. Finally, it is emphasized that the proposed exudates segmentation method contributes to the generalization ability and will benefit the ophthalmologists in forming a better decision in diagnosis and controlling the progression of diabetic retinopathy.

Chapter 6

Detection and Grading of Non-Proliferative Diabetic Retinopathy (Study 2)

6.1 INTRODUCTION

Computer-aided severity level detection methods can aid ophthalmologists for appropriate treatment and effective planning in the diagnosis of non-proliferative diabetic retinopathy. Non-proliferative diabetic retinopathy exhibits no characteristic symptoms and might not affect vision until a proliferative stage of diabetic retinopathy is reached. Proliferative diabetic retinopathy, an advanced stage characterized by the growth of new blood vessels in distinct regions of retina, may lead to vision impairment. Also, non-proliferative diabetic retinopathy itself is not a sight threatening condition, but it can trigger other forms of diabetic retinopathy such as diabetic macular edema and diabetic macular ischemia. These diseases may cause rapid vision impairment at any stage of diabetic retinopathy. Also, the treatments at this stage such as laser photocoagulation, vitrectomy, anti-VEGF drugs, corticosteroids etc. have many side effects and possible complications. It is therefore significant to diagnose non-proliferative diabetic retinopathy not only to cease diabetic retinopathy at an initial symptomless clinical stage, but also to diagnose other retinopathies. Experienced ophthalmologists visualize various shape, intensity and texture-based features in retinal images to diagnose and grade non-proliferative diabetic retinopathy. The grading of severity level of non-proliferative diabetic retinopathy requires the subjective and quantitative validation of dark and bright lesions present in retinal image. Moreover, the detection and classification of different retinal lesions is not only helpful for diagnosis but also for treatment preparation. The experts determine the precise area of lesions to be treated. Therefore, efficient detection and classification of retina lesions is significant for fast and precise detection and then grading of non-proliferative diabetic retinopathy. Thus, to

assist ophthalmologists in the process of lesion detection, classification and diagnosis, an efficient computer-aided severity level detection method is developed that enables the precise examination of retinal images. The proposed method judges the severity level of the non-proliferative diabetic retinopathy by segmenting bright and dark lesions irrespective of variations present in diverse retinal image database. Furthermore, in order to achieve high classification accuracy, the computer-aided severity level detection method is designed using a two-step neural network classifier. The proposed method is assessed on a composite database of 5048 retinal images having distinct attributes such as acquisition, field of view, pixel resolution etc. to demonstrate its generalization capability and suitability for practical applications. The segmentation and grading results are verified subjectively by expert ophthalmologist and objectively by medically significant statistical measures.

6.2 SEGMENTATION OF RETINAL LESIONS AND GRADING OF NON-PROLIFERATIVE DIABETIC RETINOPATHY

The proposed method for the grading of non-proliferative diabetic retinopathy, as depicted in figure 6.1 and figure 6.2, consists of five stages, viz. (i) retinal image enhancement described in section 4.2, (ii) segmentation and elimination of anatomical structures described in sections 4.3 and 5.2, (iii) segmentation of candidate objects, (iv) feature extraction, (v) two-step classification module, and (vi) grading of diabetic retinopathy. The steps followed in these stages are elucidated in this section.

6.2.1 Segmentation of Candidate Objects

The segmentation and elimination of blood vessels and optic disk, in the preceding stage, is designed to enhance the accuracy of retinal lesions segmentation. This is due to the image obtained after the elimination of anatomical structures comprise of only retinal lesions, if any retinopathy is present in the retinal fundus image. Retinal lesions comprise of group of pixels,

namely clusters, with homogeneous appearance and are a more perceptually meaningful representation of lesions. Therefore, the use of clusters in subsequent processing for the diagnosis of non-proliferative diabetic retinopathy can reduce the complexity and redundancy as compared to pixel by pixel processing. The clusters termed as candidate objects are obtained by grouping the image pixels with similar color and texture has the ability to adhere to image boundaries. The grouping of pixels is carried out using iterative clustering method proposed by Achanta *et al*. [169]. This method is an adaptation of k-means method for the formation of clusters. The basic k-means clustering process arbitrarily divides the image pixels into color groups based on k initial cluster centers, selected randomly, where k is the user defined parameter. Afterwards, the iterative process is carried out to update center of each cluster by computing the average of pixel values of each cluster. The final clustering results of k-means method mainly rely on the distance calculations of each pixel with all other center pixels of a clustered image. Therefore, to enhance the accuracy and effectiveness of basic k-means clustering method, the proposed method partitions pixels of image by (i) reducing the number of calculations for distance measure by limiting the search space to the region proportional to the size of the cluster required. This results in less computational complexity because it is independent of the number of clusters, k and (ii) by computing the weighted distance measure that combines spatial and color proximity along with providing control over the size and compactness of the clusters.

Given a retinal lesion image, $\mathrm{I_{Les\_img}}$, with the size of M pixels, it is required to partition an image into k group of pixels $\{\Omega_1, \Omega_2, \ldots\ldots, \Omega_k\}$, where $\Omega_p \cap \Omega_q = \emptyset$ (null set), $p, q \in [1, k]$ and $\Omega_1 \cup \Omega_2 \ldots\ldots \cup \Omega_k = \mathrm{I_{Les\_img}}$. The iterative clustering method partitions pixels in a three-dimensional space S^3: $\{x, y, I(x, y)\}$, where x, y are the input image coordinates, and $I(x, y)$ is the intensity of the input image. Assuming the clusters are of approximately equal sizes, there would

be a cluster center at the grid interval defined by $A = \sqrt{\frac{M}{K}}$. The step wise description of the proposed method is as follows:

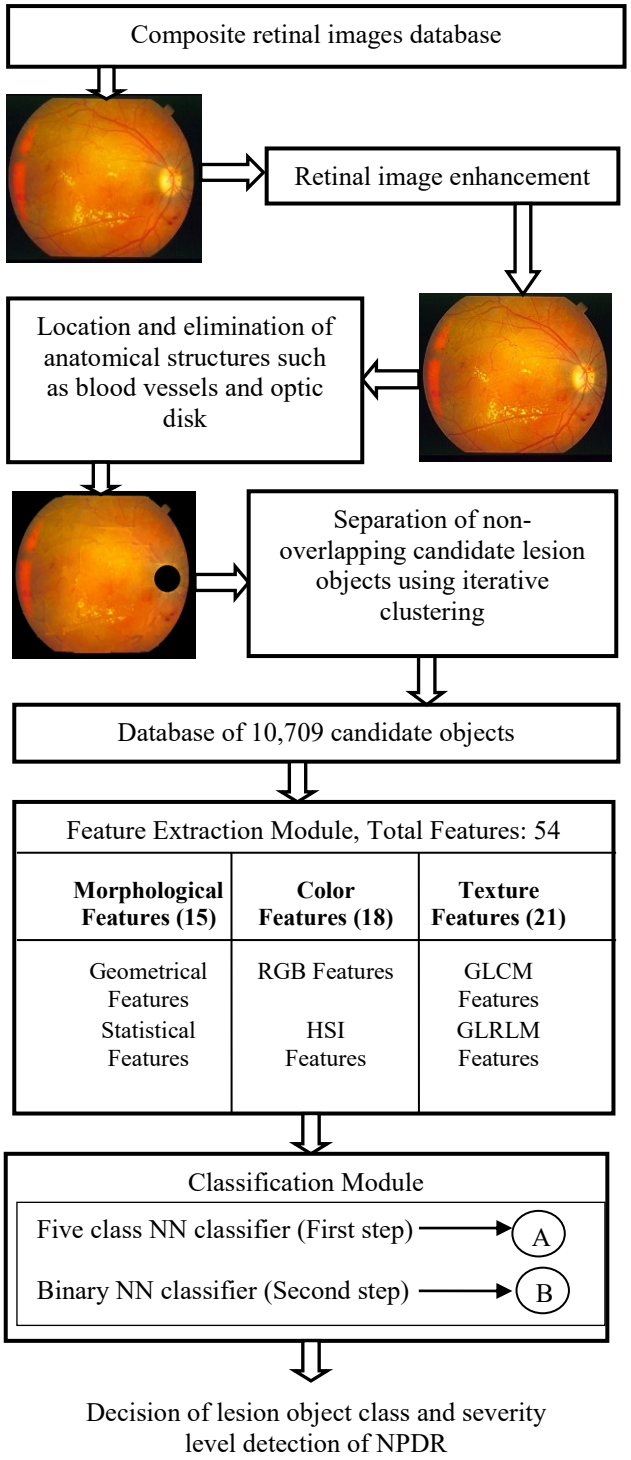

Figure 6.1 Proposed NN based computer-aided severity level detection system

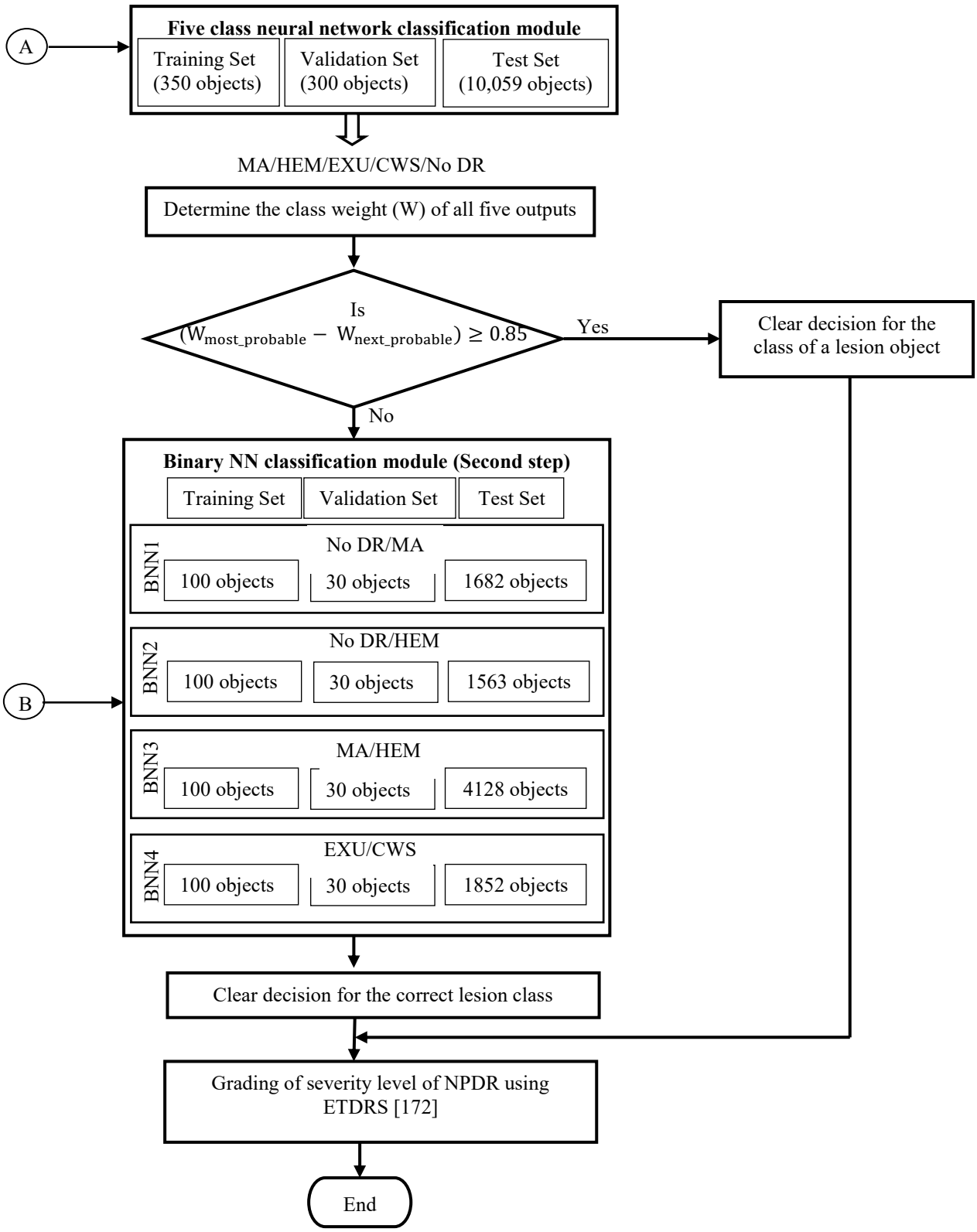

Figure 6.2 Two steps of the classification module, where 'A' indicates five class neural network classifier, and 'B' indicates binary neural network classifier

Step 1: Initially, retinal lesion image, I_{Les_img}, is transformed into the CIELAB color space (L represents lightness component, a and b are green-red and blue-yellow color components respectively) and k initial cluster pixel centers, $C_i = [l_i\ a_i\ b_i\ x_i\ y_i]^T$, are selected evenly on a grid spaced A pixels apart.

where $[l_i\ a_i\ b_i]^T$ are three parameters from CIELAB color space and $[x_i\ y_i]^T$ is the position/space coordinates of the pixels.

Step 2: Each pixel is assigned to its nearest cluster center, and k initial clusters are formed. Similar to k-means method the cluster centers and clusters are iteratively updated, determined by distance measure, D, until they meet the convergence criteria. The new cluster center is obtained by calculating the average $[l_i\ a_i\ b_i\ x_i\ y_i]^T$vector of all the pixels belonging to the cluster.

Step 3: Once new cluster centers are obtained each pixel can be reassigned to the nearest new cluster center in the next iteration so that new clusters are formed. Since the spatial extent of any cluster is approximately A^2, it is assumed that pixels associated with this cluster lie within 2A x 2A area around the cluster center in x, y plane. Therefore, unlike k-means, the searching space of iterative clustering for the computation of the distance between pixels and cluster centers is confined to 2A x 2A region around each cluster center, as depicted in figure 6.3 and not the entire retinal image, thus reducing computations.

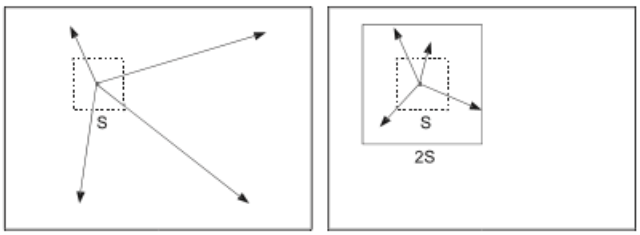

Figure 6.3 (a) k-means searches the entire image, (b) iterative clustering searches the limited region

The distance measure, D, computes the distance between the i^{th} pixel to the k^{th} cluster center in [l a b x y] color image plane space. The range of pixel's color represented in CIELAB color space $[l_i\ a_i\ b_i]^T$ are known, but on the other hand, the pixel's position represented by $[x_i\ y_i]^T$ may take a range of values depending on the size of retinal image from varying databases. Therefore, distance measure as a five-dimensional Euclidean distance in [l a b x y] color space will cause inconsistencies in the clustering process for varying cluster sizes. Also, for large cluster sizes spatial distance will have more importance relative to the color proximity. This results in compact clusters that do not adhere well to the boundaries of different structures of retinal image. For smaller clusters, the converse is true.

To combine both spatial and color proximity in the distance measure, it is required to normalize color and spatial proximity by their respective maximum distances within a cluster, N_c and N_s. Mathematically, distance measure is represented as

$$D = \sqrt{\left(\frac{D_c}{N_c}\right)^2 + \left(\frac{D_s}{N_s}\right)^2} \tag{6.1}$$

where, D_c and D_s represents the color and spatial proximity of each cluster given by

$$D_c = \sqrt{\left(l_i - l_j\right)^2 + \left(a_i - a_j\right)^2 + \left(b_i - b_j\right)^2} \tag{6.2}$$

$$D_s = \sqrt{\left(x_i - x_j\right)^2 + \left(y_i - y_j\right)^2} \tag{6.3}$$

where $(l_i\ a_i\ b_i)$ are the color values of the i^{th}pixel at the coordinates defined by (x_i, y_i) of the lesion image, I_{Les_img}. The maximum spatial distance within a given cluster, N_s , correspond to the grid interval, $A = \sqrt{\frac{M}{K}}$. The maximum color distance, N_c, vary significantly from cluster to cluster and image to image and thus is fixed to a constant value from the range of CIELAB color space values i.e., [1, 40]. In order to determine the optimum value of N_c , the extent of maximum

color distances of detailed structures for all databases are calculated. It can be examined in the figure 6.4 that the range of distance variations in color about the middle value (to ignore the very large and small intensity variations) differs from database to database. Therefore, for the sake of generalization, a specific value, i.e. mean of all middle values ($N_c \approx 30$) is considered for best outcomes.

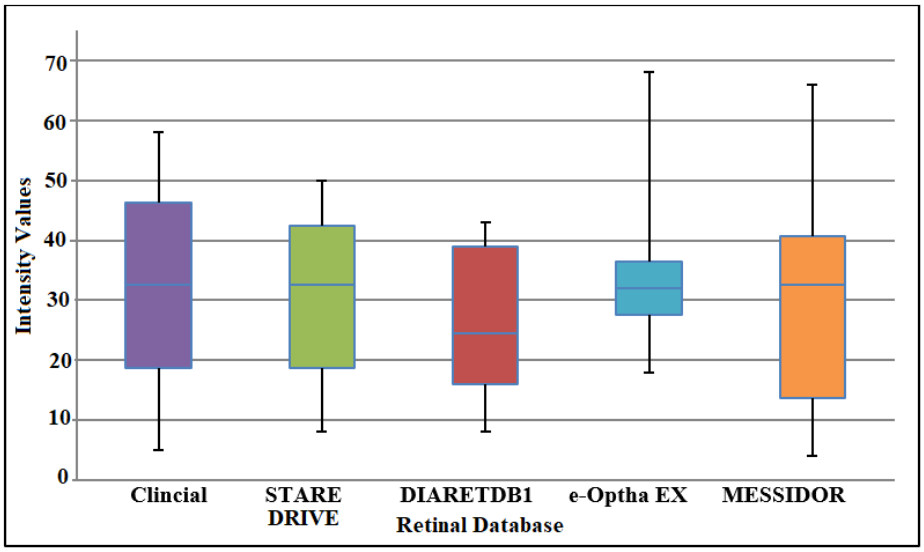

Figure 6.4 Range of intensity variations in detailed regions of sample retinal images from varying databases

The choice of number of clusters, k, relies on adherence to the compactness of contours of detailed regions of retinal fundus image. Therefore, any candidate lesion object should have enough number of pixels to provide good statistical population of spatial proximity. Also, the size of lesion objects should be small enough to be able to include color proximities of lesion objects. Boundary recall, a standard measure for boundary adherence, measures the fraction of ground truth edges lying within two pixels of cluster boundary [171]. The boundary recall for different values of k is plotted in figure 6.5 for few sample retinal images from each database. The large value of boundary recall implies that very few true edges are missed. It can be observed from the figure 6.5 that, primarily, the boundary recall increases with the increase in

the value of k, indicating the precise clustering of retinal structures. After a certain value, i.e. ≈75 there is no substantial enhancement in the boundary recall parameter and the retinal structures are becoming over segmented resulting in many irrelevant boundaries. This is because of the presence of small variations of intensity inside clusters. Thus, the optimized value of k was set to 75 for the present study.

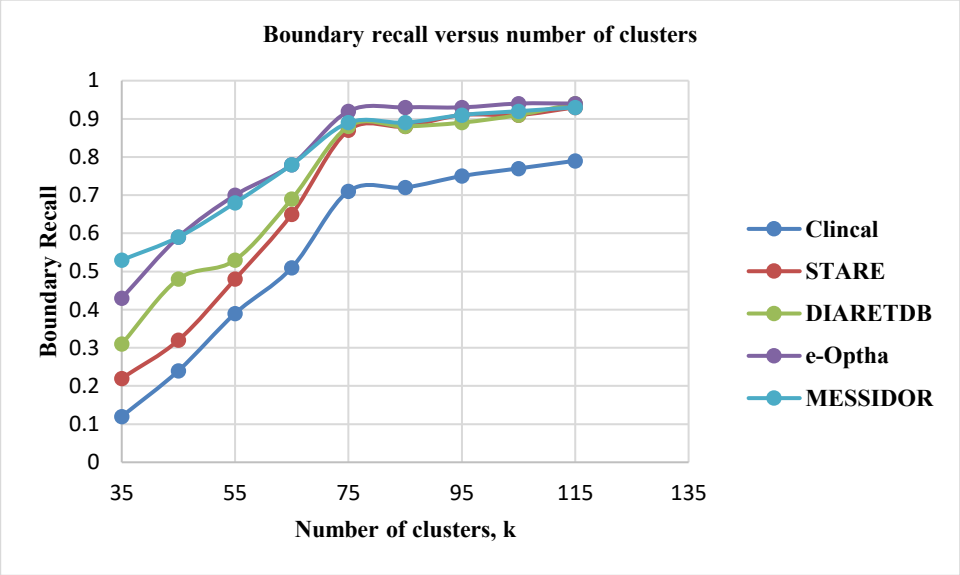

Figure 6.5 Boundary recall vs k for varying database images

Categorization of Candidate Objects:

A collection of 10,709 candidate objects obtained from a composite database of 5048 retinal fundus images are used for the segmentation of bright and dark lesions and subsequently grading of non-proliferative diabetic retinopathy. Candidate object is an area of a retinal fundus image that has pixels of interest to provide diagnostically relevant information. The maximum possible number of non-overlapping candidate objects are segmented, as described in figure 6.6, from clinical and open-source benchmark databases. The distribution of 10,709 candidate objects in retinal image classes as shown in figure 6.6 is as follows: 500 objects of No DR, 3212 objects of MA, 3482 objects of HEM, 2131 of EXU and 389 of CWS. Moreover, two sets of candidate

objects are prepared; one is training data set for the neural network classifier and the other set is prepared for testing the neural network classifier.

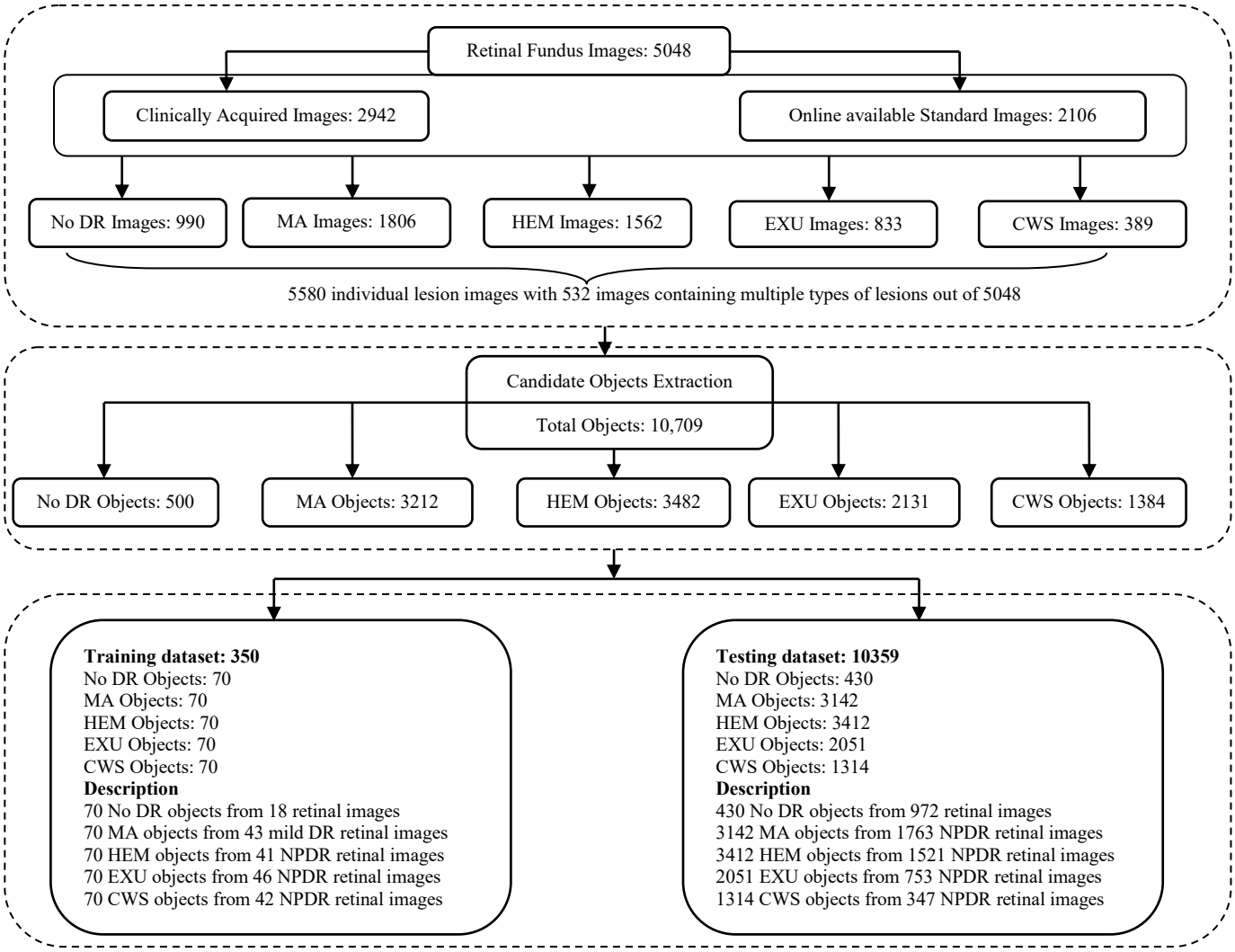

Figure 6.6 Candidate objects database categorization

Table 6.1 summarizes the categorization of the composite image database gathered at two levels namely: image level and lesion level. The image level description contains a single description of the retinal image, i.e., no diabetic retinopathy or with diabetic retinopathy (pathological). This means that if a retinal image contains any type of lesion, it is considered as pathological. The pathological retinal images are further categorized into three categories

depending on the type and number of lesions present in the retinal images. These three non-proliferative diabetic retinopathy severity level categories are: mild, moderate and severe.

Table 6.1 Image level and lesion level retinal image database description

Database	Total Images	Image level		Lesion level		
		No DR	With DR	Mild DR	Moderate DR	Severe DR
DRIVE	40	33	07	02	05	00
STARE	184	25	159	83	43	33
DIARETDB1	219	25	194	141	34	19
e-Ophtha	463	268	195	136	32	27
MESSIDOR	1200	540	660	153	247	260
Clinical	2942	99	2843	1263	960	620

6.2.2 Feature Extraction Module

Experienced ophthalmologists visualize various shape, intensity and texture-based features in retinal images to judge the severity level of diabetic retinopathy. These features are recognized by geometrical, color and texture based visual inspection criteria. Color features are strengthened after contrast enhancement in the discrimination task of five retinal image classes. Geometrical and texture-based features are frequently used in the analysis to extract various distinguishing features to discriminate among retinal image classes. Varying types of features that mathematically represent the visual understanding of ophthalmologists are explored and then selected for the present retinal lesions segmentation and classification study.

The first step of the method extracts the candidate objects of the lesion image, I_{Les_img}, consisting of healthy and pathological objects using iterative clustering method. Mathematical descriptors are then computed for each candidate object of the retinal image. If the lesion image has n candidate objects (one cluster is one sample candidate object), then feature set representation for each lesion i is $FS = \{fs_1, fs_2, fs_3, \ldots\ldots\ldots, fs_{n-1}, fs_n\}$ where fs_i is a feature vector for the i^{th} candidate object comprising of m features as $fs = \{f_1, f_2, f_3, \ldots\ldots, f_m\}$. Out of wide categories of features extraction based methods, relevant set of diagnostically important

mathematical features, based on the pathological details of lesions provided by the ophthalmologists, for retinal lesion classification, 54 features are extracted using three methods namely: (i) morphology based geometrical features based on shape, size and contour of the retinal lesions, (ii) textural features namely: first order statistical (FOS) texture based features, gray level run length matrix (GLRLM) texture based features, and gray level co-occurrence matrix (GLCM) texture based features, and (iii) RGB and HSI model based color features. These sets of features were calculated for each candidate object and combined into one set of features for image characterization. The three sets of features are discussed below:

(i) Morphological features $f_1 - f_{15}$:

Morphological analysis of retinal image compute features related to the shape, structure, color, size etc. of a particular candidate object. Experienced ophthalmologists grade the severity level of non-proliferative diabetic retinopathy by visualizing the geometrical properties of bright and dark lesions. Therefore, in the present work, a total of following 15 morphological features, viz., shape, size and statistical measures are computed for each candidate object extracted.

- Area (pixels) f_1 : Retinal lesions appear as cluster of pixels concentrated over a small region. Thus, this feature calculates the number of pixels inside and including the boundary of a particular candidate object.
- Perimeter (pixels) f_2: This feature is calculated by summing the number of pixels around the circumference of the candidate object.
- Thinness ratio f_3: This feature reflects the regularity of the candidate object. This measure takes a magnitude of 1 for a circle. Candidate objects of regular shape have a higher

thinness ratio than irregular candidate objects. Mathematically, thinness ratio is calculated as

$$\text{Thiness ratio} = \frac{(\text{Perimeter})^2}{4\pi \times (\text{Area})} \tag{6.4}$$

- Bounding length and width f_4: It returns the length and width of the smallest rectangle touching the candidate object.
- Major axis length (pixels) f_5: It is the distance between the end points of the longest line that could be drawn through the candidate object. The major axis end points are obtained by first computing the distance between every combination of pixels at the boundary of the candidate object and then determining the pair with maximum length.
- Minor axis length (pixels) f_6: It computes the distance between the end points of the longest line that could be drawn through the candidate object while maintaining perpendicularity with the major axis.
- Aspect ratio f_7 and rectangular aspect ratio f_8: The aspect ratio defines the proportional relationship between major and minor axis length. Similarly, rectangular aspect ratio defines the relationship between length and width of the bounding rectangle. Mathematically, they are expressed as

$$\text{Aspect ratio} = \frac{\text{major axis length}}{\text{minor axis length}} \tag{6.5}$$

$$\text{Rectangular Aspect ratio} = \frac{\text{length of the bounding rectangle}}{\text{width of the bounding rectangle}} \tag{6.6}$$

- Area ratio f_9: This feature defines the relationship between the area occupied by the bounding rectangle with the actual area of the candidate object and is expressed as

$$\text{Area ratio} = \frac{\text{length} \times \text{width}}{\text{Area}} \tag{6.7}$$

- Maximum f_{10} and minimum radius f_{11}: This feature returns the maximum and the minimum distance between a pixel on the boundary and the center of mass (centroid) pixel coordinate of the candidate object.
- Radius ratio f_{12}: It is given by the ratio of maximum and minimum radius.
- Standard deviation f_{13} and mean of all radii f_{14}: It computes the standard deviation and mean of distances of all pixels on the boundary from the centroid pixel and are denoted by σ_r and μ_r respectively. The mean radii value shows the average of radii values of a candidate object. The standard deviation shows how much variations occur in the candidate object corresponding to mean value.
- Haralick ratio f_{15}: This measure represents the ratio of mean of all radii to the standard deviation of all radii.

$$\text{Haralick ratio} = \frac{\mu_r}{\sigma_r} \tag{6.8}$$

(ii) Texture features $f_{16} - f_{36}$:

Texture is used to analyze the pixels of regions having some consistent probability distribution that is distinguishable from differently textured regions. Texture analysis is suitable for analyzing retinal images because the retina has various differently textured regions and its texture changes in places when affected by the diseases. The visual appearance of the retina changes in the presence of clinical diseases and disturbs the homogeneous texture of the retina. Also, clinicians themselves rely on visual texture to detect abnormalities in a retinal image. Statistical methods of texture characterize the relationship among intensity values of the pixels based on their spatial distribution and

differentiates among the textures of similar appearances. According to the number of intensity points in each observed combination of intensities, methods are classified into first order (one pixel), second order (pair of pixels) and higher order (three or more pixels) statistics. The first order statistical measures are used to characterize the grey-level histogram. The second and higher order statistics describe spatial interpixel correlation to characterize texture pattern [22]. Therefore, in the present work, a total of 21 texture features are selected based on (i) first order statistics (FOS), (ii) Gray level co-occurrence matrix of second order statistics, and (iii) gray level run length matrix of higher order statistics is computed for each candidate object. The three sets of texture features are listed as follows:

First order statistical texture features:

A total of eight first order texture features are measured statistically by identifying a single value as representative for (i) an entire intensity distribution measured by mean, median and mode, (ii) variations in the distribution of intensity computed by range, variance and standard deviation, and (iii) shape of the intensity distribution represented by histogram measured by skewness and kurtosis.

- Mean f_{16}: The mean represents the average intensity values of the pixels in the candidate object. Mathematically, it is given by

$$\text{Mean} = \frac{1}{\text{MN}}\sum_{\text{i=1}}^{\text{M}}\sum_{\text{j=1}}^{\text{N}} \text{I}_{\text{Les\_img}}(\text{i},\text{j}) \tag{6.9}$$

  where $\text{I}_{\text{Les\_img}}(\text{i},\text{j})$ is the lesion image intensity function of two space variables (i,j).

- Median f_{17}: The median computes the middle of the intensity values of all the pixels arranged in ascending order of a particular candidate object. The median is represented as

$$\text{Median} = \begin{cases} (\text{pixel intensity value})_{\frac{(n+1)}{2}} & \text{for odd n} \\ \dfrac{(\text{pixel intensity value})_{\frac{n}{2}} + (\text{pixel intensity value})_{\frac{(n+1)}{2}}}{2} & \text{for even n} \end{cases} \tag{6.10}$$

- Mode f_{18}: The mode returns the intensity value of the pixel with maximum frequency in a candidate object and is represented by

$$\text{Mode} = \text{Max}\left[\sum_{p=0}^{Q-1} \text{Number of occurences of intensity values(Q)}\right] \tag{6.11}$$

where Q is the total number of intensity values in a candidate object.

- Range f_{19}: It computes the difference of maximum and minimum intensity values of a candidate object and is given by

$$\text{Range} = I_{\text{Les\_img}}(i,j)_{\max} - I_{\text{Les}_{\text{img}}}(i,j)_{\min} \tag{6.12}$$

- Variance f_{20}: The variance measures the dispersion of intensity values of pixels ($= M \times N$) around the mean value and is given by

$$\text{Variance} = \frac{1}{MN-1}\sum_{i=1}^{M}\sum_{j=1}^{N}(I_{\text{Les\_img}}(i,j) - \text{mean})^2 \tag{6.13}$$

- Standard deviation f_{21}: Standard deviation, closely related to variance, measures the spread of intensity values of pixels around the mean value and is the positive square root of variance given by

$$\text{Standard deviation} = \sqrt{\text{variance}^2} \tag{6.14}$$

- Skewness f_{22}: Skewness gives the measure of symmetricity of the intensity values about the mean. Bell shaped histogram denotes perfect symmetricity with value zero of skewness. A positive value for the skewness depicts the asymmetric histogram towards right; a negative value indicates that it is asymmetric towards left. It is given by

$$\text{Skewness} = \frac{1}{MN}\sum_{i=1}^{M}\sum_{j=1}^{N}\left(\frac{(I_{Les\_img}(i,j) - \text{mean}}{\text{variance}}\right)^{3} \tag{6.15}$$

- Kurtosis f_{23}: Kurtosis returns the measure of peak in the intensity distribution relative to the normal of the Gaussian curve. Kurtosis with zero value indicates normal, while a positive and negative value indicates peaky and flat to the normal of the Gaussian curve. It is given by

$$\text{Kurtosis} = \frac{1}{MN}\sum_{i=1}^{M}\sum_{j=1}^{N}\left(\frac{(I_{Les\_img}(i,j) - \text{mean}}{\text{variance}}\right)^{4} \tag{6.16}$$

Second and Higher Order Statistical Texture Features:

A single pixel statistic using image histogram focuses on the individual pixel values of a candidate object. In order to capture the spatial interaction between pixels of a candidate object second and higher order statistics are estimated. These features estimate properties of two or more-pixel values occurring at specific locations relative to each other.

Second order statistical texture features: Second order information consider pairs of pixels in spatial relation to each other. Gray level co-occurrence matrix (GLCM) is one of the methods used to derive texture features based on second order statistics. Gray level co-occurrence matrix depicts the relative frequencies (or probabilities), represented by $G_{\theta,d}(i,j)$, with which two pixels separated by a interpixel distance (d) in the direction (θ) appear with intensities i,j. In other words, it basically depicts the grey level histogram of the candidate object in the form of a $M \times M$ matrix, where M represents the number of grey levels in a candidate object. GLCM matrices are calculated over 5×5 region of the candidate object with interpixel distance (d) equals to 1 and in four orientations of $(\theta) = 0, \Pi/4, \Pi/2$ and $3\Pi/4$ radians. Assuming that $p(i,j)$ is the $(i,j)^{th}$ of the co-occurrence matrix that gives the number of times i^{th} and j^{th} pixel values

occur in relation in a candidate object, mean (μ_x, μ_y) and standard deviations (σ_x, σ_y) for rows and columns of the matrix are given by

$$\mu_x = \sum_{i=1}^{M}\sum_{j=1}^{M} i.\,p(i,j) \tag{6.17}$$

$$\mu_y = \sum_{i=1}^{M}\sum_{j=1}^{M} j.\,p(i,j) \tag{6.18}$$

$$\sigma_x = \sum_{i=1}^{M}\sum_{j=1}^{M} (i-\mu_x)^2.\,p(i,j) \tag{6.19}$$

$$\sigma_y = \sum_{i=1}^{M}\sum_{j=1}^{M} (j-\mu_y)^2.\,p(i,j) \tag{6.20}$$

The eight GLCM features are defined as

- Correlation f_{24}: The correlation returns the measure of linear dependence between the neighboring pixels of the candidate object. Correlation value close to zero means no linear dependence, while 1 and -1 indicates good and inverse linear dependence and is given by

$$\text{Correlation(GLCM)} = \sum_{i=0}^{M-1}\sum_{j=0}^{M-1} \frac{(i-\mu_x)(j-\mu_y)p(i,j)}{\sigma_x\sigma_y} \tag{6.21}$$

- Homogeneity f_{25}: Homogeneity measures the uniformity of variations in intensity values of a candidate object. Homogeneity value one indicates that for all pixels in a candidate object, the intensity values in a particular direction and distance is equal to the reference value. Homogeneity uses the weight factor $(1+(i-j)^2)$ related to distance from GLCM diagonal and therefor its value will be small for heterogeneous candidate objects and relatively high for homogeneous candidate objects. Mathematically, it is expressed as

$$\text{Homogeneity(GLCM)} = \sum_{i=0}^{M-1}\sum_{j=0}^{M-1}\frac{1}{1+(i-j)^2}\,p(i,j) \tag{6.22}$$

- Maximum Probability f_{26}: It returns the most probable pixel intensity value between the pixel pairs in a particular direction of a candidate object and is expressed as

$$\text{Maximum probability(GLCM)} = \max\big(p(i,j)\big) \tag{6.23}$$

- Cluster shade f_{27}: It measures the skewness of the GLCM matrix and is expressed as

$$\text{Cluster shade(GLCM)} = \sum_{i=1}^{M}\sum_{j=1}^{M}\big(i-\mu_x+j-\mu_y\big)^3 p(i,j) \tag{6.24}$$

- Entropy f_{28}: Entropy quantifies the measure of randomness in a candidate object and is maximum when all the intensity transitions have equal probability. It is used to distinguish candidate objects with structured appearance (indicating lower value of entropy) from the candidate objects with less structured appearance. It is given by

$$\text{Entorpy(GLCM)} = -\sum_{i=0}^{M-1}\sum_{j=0}^{M-1} p(i,j)\log\big(p(i,j)\big) \tag{6.25}$$

- Cluster prominence f_{29}: It measures the kurtosis of the two-dimensional histogram of a GLCM and is given by

$$\text{Cluster prominence(GLCM)} = \sum_{i=1}^{M}\sum_{j=1}^{M}\big(i-\mu_x+j-\mu_y\big)^4 p(i,j) \tag{6.26}$$

- Autocorrelation f_{30}: This feature is based on the spatial frequencies that describe their organization using a correlation coefficient. This correlation coefficient evaluates the linear spatial relationship between pixels of a candidate object and is given by

$$\text{Autocorrelation(GLCM)} = \sum_{i=1}^{M}\sum_{j=1}^{M}(i\,j)\;p(i,j) \tag{6.27}$$

- Dissimilarity f_{31}: It returns the measure of local variations in a candidate object. It is given by

$$\text{Dissimilarity(GLCM)} = \sum_{i=1}^{M}\sum_{j=1}^{M}|i-j|\;p(i,j) \tag{6.28}$$

Higher order statistical texture features:

Gray level run-length matrix (GLRLM), $p(i,j|\theta)$, returns the higher order statistical features matrix by capturing the coarseness of a texture in a particular direction (θ) by computing the occurrence of runs and its length (j) for each intensity value (i). The run length is the number of pixels in the run and its value is the number of times such a run occurred in a candidate object. Depending on the four directions $\theta = 0, \Pi/4, \Pi/2$ and $3\Pi/4$ radians, varying gray level run-length matrices may be computed for a particular candidate object, one for each direction. In the present work, θ is set to zero radians as the variations in other directions are similar. Assuming that the maximum value of gray level (i) be K, the maximum run length (j) equal to Q and total number of runs be n_r, GLRLM texture descriptors selected for the present work are defined below:

- Long run emphasis f_{32}: It measures the distribution of long runs. Its value is large for coarse textures. It is given by

$$\text{Long run emphasis} = \frac{1}{n_r}\sum_{i=1}^{K}\sum_{j=1}^{Q}p(i,j)*j^2 \tag{6.29}$$

- Short run emphasis f_{33}: It measures the distribution of short runs and its value is large for fine textures. It is given by

$$\text{Short run emphasis} = \frac{1}{n_r}\sum_{i=1}^{K}\sum_{j=1}^{Q}\frac{p(i,j)}{j^2} \tag{6.30}$$

- Gray level non-uniformity f_{34}: It returns the measure of similarity of intensity value of pixels throughout a candidate object. This feature will dominate for long run lengths and will have low value if all intensity values have equal probability of occurrence. It is given by

$$\text{Gray level non uniformity} = \frac{1}{n_r}\sum_{i=1}^{K}\left(\sum_{j=1}^{Q}p(i,j)\right)^2 \tag{6.31}$$

- Run length non-uniformity f_{35}: This feature returns the measure if similarity of the runs in a candidate object and indicates low value if run lengths have equal probabilities. It is given by

$$\text{Run length non uniformity} = \frac{1}{n_r}\sum_{j=1}^{Q}\left(\sum_{i=1}^{K}p(i,j)\right)^2 \tag{6.32}$$

- Run percentage f_{36}: Run percentage returns the homogeneity value and the distribution of runs of a candidate object in a particular direction. The value of run percentage is maximum when the run length is one for all intensity values in a particular direction and is given by

$$\text{Run percentage} = \frac{n_r}{p(i,j) * j} \tag{6.33}$$

(iii) Color features $f_{37} - f_{54}$

Color feature represents statistic of a candidate object in an image plane chosen from a color space representation of a retinal fundus image. Candidate objects are different lesions (e.g. CWS, EXU, HEM, and MA) and regions not containing lesions. Three statistics, i.e.,

mean, intensity and range, are calculated for each candidate object in an image plane. Image planes are (i) Red (R), green (G) and blue (B) chosen from RGB color space representation and (ii) hue (H), saturation (S) and intensity (I) chosen from HSI color space representation of a retinal fundus image. Thus, overall 18 color features (3 statistics × 3 image planes × 2 color space representations) are extracted for each candidate object in a retinal fundus image.

Retinal fundus images are originally in RGB color space (camera output), therefore the mathematical formulations for conversion from RGB to HSI color space are described as follows:

$$\mathrm{I} = \frac{\mathrm{Rn} + \mathrm{Gn} + \mathrm{Bn}}{3} \tag{6.34}$$

$$\mathrm{S} = 1 - \frac{3\min(\mathrm{Rn}, \mathrm{Gn}, \mathrm{Bn})}{\mathrm{I}} \tag{6.35}$$

$$\mathrm{H} = \cos^{-1}\left\{\frac{\frac{1}{2}\left[(\mathrm{Rn} - \mathrm{Gn}) + (\mathrm{Rn} - \mathrm{Bn})\right]}{\left[(\mathrm{Rn} - \mathrm{Gn})^2 + (\mathrm{Rn} - \mathrm{Bn})(\mathrm{Gn} - \mathrm{Bn})\right]^{\frac{1}{2}}}\right\} \tag{6.36}$$

Color in HSI model are defined using normalized R, G, and B, i.e., Rn, Gn, and Bn respectively. The original R, B, and G values are divided by a normalizing constant $((\mathrm{R} + \mathrm{B} + \mathrm{G})/3)$to obtain Rn, Gn, and Bn values.

6.2.3 Classification Module

In the classification module, a two-step classification method was developed using neural networks. These two classifiers are discussed in the following sub sections.

First Step – Five Class Neural Network Classifier:

The set of 54 mathematical features, as mentioned in the previous step, were used as an input to a neural network classifier to classify candidate objects into one of the five classes

namely: EXU, HEM, CWS, MA and No DR. The neural network architecture designed consists of three input layers having input neurons equal to the number of features in the feature set i.e. 54, one hidden layer and an output layer with five neurons corresponding to No DR, EXU, HEM, MA and CWS classes. The optimum value of number of hidden neurons is determined empirically, and it was found that 10 neurons in hidden layer provides appropriate tradeoff between classification accuracy and fast convergence. The desired output neuron was set to one corresponding to the labeled classes and 0 for the other output neurons. Neural network was trained with supervised learning and the weights were adjusted using Levenberg-Marquardt back propagation procedure with adaptive learning rate and momentum in order to obtain a desired input-output relation [22].

A three-stage neural network-based method comprising of training, validation and testing is used for the development of retinal lesion classification system. Sample candidate objects containing lesions and healthy portions of retinal image are randomly distributed into three sets namely: training set, validation set and testing set. The training set, comprising of 350 candidate objects having 70 objects from each of the five classes. These sample objects, collected from the reference ground truths of retinal images, were used to fix the parameters of neural network architecture and weights. These training retinal images with varying shape, size and number of lesions were cautiously selected with the help of expert ophthalmologist to capture the characteristic attributes of each grade of pathology. In order to identify the neural network architecture for best performance with fixed parameters, 300 candidate objects having 60 objects from each class were used for the validation of the trained neural network. The performance of the trained neural network is then evaluated on an independent test set of candidate objects from the composite database of retinal images. It comprises of remaining 10,059 candidate objects

such as: 370 corresponding to No DR, 1991 to EXU, 3352 to HEM, 1254 to CWS and 3082 to MA.

Second Step – Binary Neural Network Classifier:

The output of the neural network for each candidate object signifies the probability of the lesion class representing the output node, ranging from 0 to 1. After analyzing the test results of the first step of the neural network classifier, it was observed that out of 10,059 candidate objects of the testing dataset, 9108 candidate objects, having maximum probability, correspond to correct lesion class. However, 598 candidate objects out of 951 incorrectly classified candidate objects have correct classification with second highest probability. It was also observed that misclassification was present in specific combinations of classes due to similarity of certain features. The incorrect classification was present either among No DR/MA/HEM classes or between EXU/CWS classes. Therefore, to improve the overall classification accuracy, the extracted feature set of the first two most probable classes in the first step of the neural network classifier is passed through the second step of the classification module.

In the second step of the classification module four mutually independent binary classifiers were developed with optimized performance in distinguishing between two classes namely: No DR/MA, No DR/HEM, MA/HEM and EXU/CWS. The candidate objects used for training and validation stages of each binary neural network classifier include candidate objects of corresponding lesion classes from the training and the validation candidate objects used in the first step of the classification module. Therefore, training set for the binary neural network classifier has 100 candidate objects having 50 candidate objects from each of the lesion classes and validation set has 30 candidate objects having 15 objects from each of the classes under consideration. The performance of the designed binary neural network classifiers performance

was tested on the test set of the remaining candidate objects of the two classes. The architecture values of the optimal binary neural network classifier for classification were determined empirically and it has input layer with 54 units, one hidden layer with 20 units and an output layer with one unit. The designed binary classification module is shown in figure 6.2. It shows that, if the difference in the probability of classification between two retinal lesion classes at the output of first neural network classifier is 0.85 or higher, the second step is not required. In such cases, the output of first neural network with maximum probability is the final classification result.

The proposed methodology can be perceived as analogous to the procedure followed by the expert ophthalmologists to classify retinal lesions. The ophthalmologists analyze the retinal images to provide interpretation among five retinal lesion classes and based upon their recommendation on two most probable classes, enquiry from another expert is made for the confirmation of particular type of retinal abnormality. Therefore, two-step lesion classification eliminates the fatigue and inconsistency associated with the subjective interpretation of each retinal lesion class.

6.2.4 Grading of Non-Proliferative Diabetic Retinopathy

A number of grading systems have been established to provide standards for ophthalmologists and researchers in reliable diagnosis and management of diabetic retinopathy using retinal images [172, 173]. These systems grade the severity level of non-proliferative of diabetic retinopathy by objective quantification of retinal lesions. Among these grading systems, Early treatment diabetic retinopathy study (ETDRS) based grading system is used in this work to grade the severity of non-proliferative diabetic retinopathy by quantification of bright and dark lesions detected by the proposed method [172].

In this work, the two-step classification module labels the candidate objects corresponding to regions of retinal lesions as MA/HEM/EXU/CWS and No DR for the candidate object corresponding to healthy region of retinal image. Once the retinal lesions are detected, the number of candidate objects corresponding to HEM, MA, EXU and CWS are computed for each retinal image using a combination function (Ψ) defined in Eq. (6.37). Lesion combination operation (Ψ) is used to generate a diabetic retinopathy severity grade S_G for each retinal image.

$$S_G = \Psi(\mathrm{HEM}, \mathrm{MA}, \mathrm{EXU}, \mathrm{CWS}) \quad (6.37)$$

where, S_G represents the number of candidate objects corresponding to lesions $= \{0,1 \ldots \ldots \ldots . .9\}$.

Following rules, as proposed by ETDRS, are used in the present work to grade the input retinal image into different categories.

- Grade 0 ($S_G = 0$): Absence of diabetic retinopathy and no candidate object of a retinal image correspond to any retinal lesion.
- Grade 1 ($S_G = 0 - 3$): Mild non-proliferative diabetic retinopathy.
- Grade 2 ($S_G = 4 - 8$): Few micro aneurysms, hemorrhages, cotton wool spots and exudates found implies moderate non-proliferative diabetic retinopathy.
- Grade 3 ($S_G > 8$): Micro aneurysms, hemorrhages, cotton wool spots and exudates found in greater quantity than moderate non-proliferative diabetic retinopathy implying severe non-proliferative diabetic retinopathy.

6.3 RESULTS AND DISCUSSION

The proposed exudates segmentation method is implemented in MATLAB version 2016a on a PC with intel core i7 processor. The performance evaluation of the proposed method is carried out in two ways: subjectively and objectively by visual interpretation criteria and medically

significant statistical measures described in section 5.4.2. The direct comparison of the proposed method with other state-of-the-art methods cannot be performed on the composite database as the database includes the clinical retinal images which has not been used by other methods in literature. Similarly, other reported methods have also used their individual collection of datasets and some of them are not made public due to ethical commitments. Therefore, to evaluate the efficiency of the proposed method varying number of experiments were conducted with the composite and individual databases. The results obtained from the experiments based on per-lesion and per-image evaluations and the generalized performance are given in detail in the following subsections:

Experiment 1: Image Level Evaluation for a Composite Database

In this experiment, the generalized performance of the two-step classification method is evaluated by the confusion matrix for per-image evaluation on a composite retinal images database. Table 6.2 shows the confusion matrix of the test results for all the five retinal lesion classes. Individual class accuracies, as shown in table 6.2, delivered by two-step classification module are: No DR-95.9%, MA-98.3%, HEM-98.4%, EXU-97.4% and CWS-97.9%, resulting in the overall accuracy of 97.8%. It is observed from the above results that the misclassification is higher among the retinal classes corresponding to No DR, MA and HEM. This is due to the reason that these retinal lesions such as micro aneurysms and hemorrhages and have visual characteristics similar/showing good resemblance with normal regions of retinal image. The ophthalmologists opined that the differentiation of these lesions from normal regions of retinal image is even difficult for the experts. Similar accuracies are obtained by bright lesions i.e. EXU and CWS, misclassifying only 21 and 2 cases. The method shows the significant contribution with the classification accuracy of 100% between the bright lesion and dark lesion classes.

Table 6.2 Confusion matrix on the test results at image level for a composite database after the two-step neural network classifier module

Class Code	Test results after the two-step neural network classifier module				
	No DR	**MA**	**HEM**	**EXU**	**CWS**
No DR	**950**	12	3	3	3
MA	16	**1776**	21	0	0
HEM	4	18	**1538**	0	0
EXU	11	0	0	**812**	5
CWS	9	0	0	18	**381**
Individual class classification accuracy (%)	95.9(950/990)	98.3(1776/1806)	98.4(1538/1562)	97.4(812/833)	97.9(381/389)
Overall classification accuracy	97.8(5457/5580)				

Experiment 2: Image and Lesion Level Evaluation Concerning the Segmentation of Bright Lesions

In the second experiment, the performance of the proposed method is evaluated by correctly identifying an image containing bright lesions namely: exudates and cotton wool spots. In this experiment, retinal images containing bright lesions are considered as positive and all healthy retinal images and containing dark lesions as negative.

Clinically acquired database: Table 6.3 demonstrates that the overall sensitivity, specificity and accuracy on the clinically acquired database are 100%, 100% and 100% respectively, for per-image based evaluation criteria. These results clearly signify the capacity of the proposed method to differentiate retinal fundus images based on the absence or presence of bright lesions. Additionally, it can also be observed that the proposed method depicts the best performance in terms of specificity for clinically acquired database, which exceeds by 22.22% and 5.4% from the method of Gracia *et al*. and Osareh *et al*. using clinically acquired databases [174, 77]. Table 4 also shows that the proposed method based on per-lesion evaluation achieved average sensitivity/specificity/accuracy of 95.80/98.80/95.43 respectively on clinically acquired database images. Further, on comparing all the state-of-the-art methods using clinically acquired

databases, it is observed that the proposed method shows the highest performance with the largest database of 1470 clinically acquired retinal images.

Table 6.3 Comparative Performance of the Proposed Method concerning the Segmentation of Bright Lesions with other Existing Methods

Detection method	Database	Number of Test Images for Validation	Lesion Based Results (%)				Image Based Results (%)		
			SN	SP	Acc	PPV	SN	SP	Acc
Niemeijer [85]	Clinical	300	95.0	88	----	----	----	----	----
Osareh [174]	Clinical	150	93.5	92.1	----	----	96	94.6	----
Gracia [77]	Clinical	67	87.61	----	----	83.51	100	77.78	91.04
Kuivalainen [175]	DIARETDB MESSIDOR DRIVE	139 17 34	91.2	99.3	99.5	----	----	----	----
Giancardo [86]	DIARETDB1 HEI-MED MESSIDOR	89 169 1200	----	----	-----		88 88 77	90 90 90	---- ---- ----
Roychowdhury [156]	DIARETDB1	89	74.2	98	----	----	----	----	----
Zhang [14]	e-Ophtha	82	74	----	----	72	96	89	----
Akram [157]	DRIVE STARE DIARETDB MESSIDOR	40 81 89 1200	97.39	98.02	97.56	----	----	----	----
Figueiredo [18]	Clinical HEI-MED	2870 169	89.81 ----	97.47 ----	---- ----	---- ----	---- 66	---- 87.8	---- ----
Proposed Method	**Clinical**	**1470**	**95.80**	**98.80**	**95.43**	**96.30**	**100**	**100**	**100**
	STARE	**88**	**97.85**	**99.62**	**96.23**	**97.86**	**98.6**	**100**	**100**
	MESSIDOR	**1200**	**97.58**	**93.27**	**94.12**	**87.78**	**87.4**	**96**	**93.4**
	DIARETDB	**219**	**94.83**	**97.63**	**96.43**	**94.34**	**98**	**96.1**	**93.3**
	e-Ophtha EX	**82**	**91.78**	**97.80**	**94.31**	**86.40**	**96.1**	**96**	**95.6**
	DRIVE	**40**	**98.98**	**98.33**	**93.65**	**88.43**	**98.3**	**100**	**98**
	OVERALL	**3099**	**96.41**	**96.57**	**94.96**	**92.54**	**94.81**	**98.07**	**98.63**

Online acquired database: The proposed method depicts the per-lesion based sensitivity/specificity/ accuracy of 97.85/99.62/96.23 respectively for STARE database and 97.58/93.27/94.12 respectively for MESSIDOR database. The segmentation results of the STARE database are comparable to the segmentation results of Akram *et al* [157]. However, on

comparing the results, it can be observed that the proposed method has a substantial contribution in the generalization ability in achieving the overall sensitivity/specificity/accuracy of 96.41/96.57/94.96 respectively on a database of 3099 retinal images which is sufficiently larger as compared to the size of Akram *et al* [157]. Table 6.3 also demonstrates the comparative results on open source benchmark databases for image-based evaluation. The improvement specifically in terms of sensitivity over the state-of-the-art methods is supported by the efficient segmentation of bright lesion structures where removal of false bright lesions resulted in lower number of false positives.

Experiment 3: Image and Lesion Level Evaluation Concerning the Segmentation of Dark Lesions

The third experiment aims at evaluating the performance of the proposed method in correctly identifying an image containing dark lesions namely: micro aneurysms and hemorrhages. In this experiment, retinal images containing dark lesions are considered as positive and all healthy retinal images and containing bright lesions as negative.

Clinically acquired database: In literature, only few methods calculate the statistical measures for dark lesions on clinically acquired database, as shown in Table 6.4. Gracia *et al*. achieved average sensitivity of 86.01% and 100% for per-lesion and per-image based evaluation criteria respectively [110]. However, the low specificity of 56% on per-image evaluation for 65 clinically acquired retinal images depicts that there are higher number of spurious responses. In addition to that, the method does not provide per-lesion based specificity and accuracy results. Lastly, the average sensitivity/specificity/accuracy of 94.80/99.80/98.43 respectively for per-lesion evaluation and 98.8/100/100 respectively for per-image evaluation shows the consistency of the method for segmenting the dark lesions from retinal images.

Table 6.4 Comparative Performance of the Proposed Method concerning the Segmentation of Dark Lesions with other Existing Methods

Detection method	Database	Number of Test Images for Validation	Lesion Based Results (%)				Image Based Results (%)		
			SN	SP	Acc	PPV	SN	SP	Acc
Niemeijer [108]	Clinical	100	31.0	----	----	----	100	87	----
Quellec [107]	Clinical	35	89.62	----	----	89.50	----	----	----
García [110]	Clinical	65	86.01	----	----	51.99	100	56	83.08
Jaafar [176]	DIARETDB0 DIARETDB1	130 89	87.70	98.60	----	----	98.80	86.20	----
Roychowdhury [156]	DIARETDB1	89	80	85	-----		----	----	----
Akram [157]	DRIVE STARE DIARETDB MESSIDOR	40 81 89 1200	97.83	98.36	98.12	----	----	----	----
Kauppi [177]	DIARETDB1	89	80	39.0	----	----	80	55.5	----
Kuivalainen [175]	DIARETDB0	128	----	----	----	----	82.5	72.5	----
Figueiredo [18]	Clinical DIARETDB MESSIDOR	2870 219 1200	89.89 ---- ----	89.55 ---- ----	---- ---- ----	---- ---- ----	---- 74.45 75.11	---- 86.25 91.81	---- ---- ----
Proposed Method	**Clinical**	**1472**	**94.80**	**99.80**	**98.43**	**97.30**	**98.8**	**100**	**100**
	STARE	**96**	**99.65**	**99.12**	**99.13**	**98.76**	**100**	**100**	**100**
	MESSIDOR	**1200**	**96.58**	**90.47**	**95.02**	**85.87**	**88**	**98**	**93**
	DIARETDB	**219**	**97.34**	**97.56**	**98.34**	**93.68**	**98**	**99**	**97**
	e-Ophtha MA	**381**	**89.89**	**98.80**	**92.00**	**89.40**	**91**	**94**	**93**
	DRIVE	**40**	**95.98**	**99.53**	**94.65**	**88.95**	**98**	**99**	**98**
	OVERALL	**3408**	**95.19**	**96.24**	**96.50**	**92.10**	**94.10**	**98.55**	**96.02**

Online acquired database: The comparative performance analysis of the proposed method for the segmentation of dark lesions on publicly available databases with existing methods is shown in Table 6.4. It is important to note that among all the publicly available databases DIARETDB database is the only database on which the existing methods are generally validated. Thus, to establish a fair comparison of the state-of-the-art methods, results on DIARETDB database are highlighted in Table 6.4. The proposed method has clearly outperformed the existing methods mainly in terms of sensitivity for per-lesion evaluation and specificity for per-image evaluation.

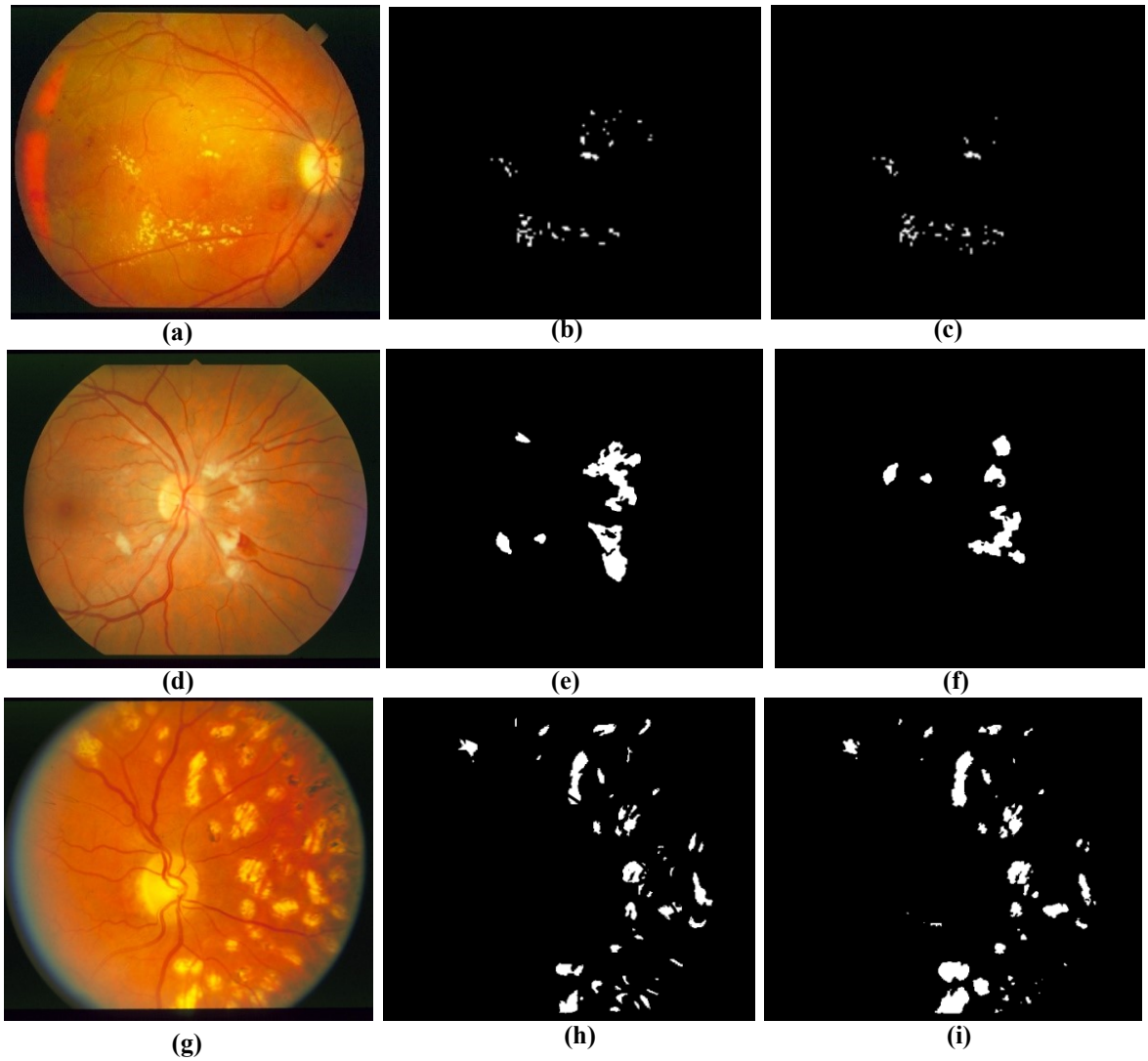

(a), (d), (g): Original retinal fundus images containing bright lesions
(b), (e), (h): Results of proposed computer aided detection and classification method
(c), (f), (i): Reference ground truths

Figure 6.7 Original and processed pathological images by the proposed computer-aided severity level detection method

The proposed method achieves average per-lesion sensitivity of 97.34% which exceeds by 9.64% from the method of Jaafar *et al*., reported in literature [176]. Additionally, the average per-image accuracy and positive predictive value of 99% and 97% respectively, shows the reliability of the proposed method to obtain accurate assessment as to whether dark lesions are present or not. Conclusively, validation of the proposed method on such a large composite database

demonstrates the generalization capability of the proposed method for retinal segmentation in the presence of varying types of pathologies.

Experiment 4: Subjective Evaluation

In the fourth experiment, the results obtained for dark and bright lesions segmentation are observed for the evaluation of the proposed method via visual interpretation by expert ophthalmologist. Visual interpretation is the capability of an ophthalmologist to extract significant information from a retinal image. Interpretation based on visual perception criteria of segmented retinal image was assessed by an expert ophthalmologist associated with Sri Guru Harkrishan Sahib Eye Hospital, Mohali, India. Visual perception criterion is dependent on the quality of segmentation which is considered to be accurate if it permits the observer to identify better the desired information in the retinal image.

Bright lesions: Figure 6.7 shows the sample retinal images with varying visual appearance of retinal lesions and their segmentation results obtained after the application of the proposed method. From figure 6.7 (a), it is observed that the exudates present in retinal images have better contrast as compared to the background of retinal fundus images. When such images having fair contrast between background and detailed regions are processed for segmentation, it is perceived that the segmentation results of the proposed method are comparable to the reference ground truth of the exudates marked by the experts. The detailed examination of figure 6.7 (b) and (c) shows that the proposed method is able to segment those exudates pixels which were not even indicated by expert because of poor visual details. From figure 6.7 (d), it is observed that the cotton wool spots present in retinal images have poor contrast with respect to the normal region, and therefore it becomes hard to segment the exact boundary of the lesion. When images with poor contrast between background and detailed regions are processed for segmentation, it is perceived that the segmentation results of the proposed method are somewhat under-segmented in the regions comprising of small cotton wool spots and slightly over-segmented in the regions

having large cotton wool spots, as depicted in figure 6.7 (e). However, the proposed method is able to locate all the bright lesions appearing in retinal images. Lastly, it is also perceived that the segmentation outcomes of retinal images having variable contrast in different regions provides improved visual appearance of exudates in comparison to original retinal fundus images, as shown in figure 6.7 (g) and (h) respectively.

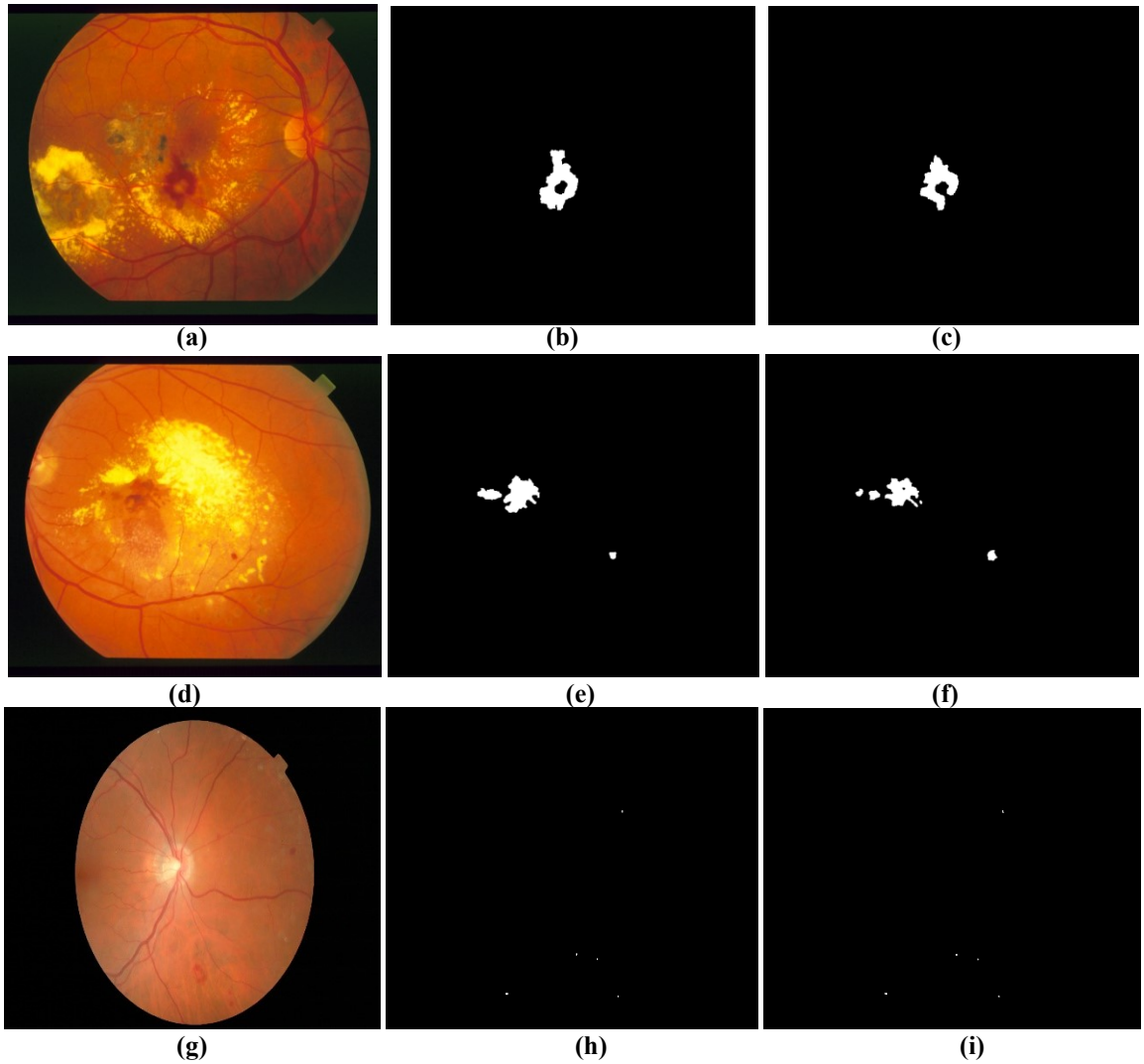

(a), (d), (g): Original retinal fundus images containing red lesions
(b), (e), (h): Results of proposed computer aided detection and classification method
(c), (f), (i): Reference ground truths

Figure 6.8 Original and processed pathological images by the computer-aided severity level detection method

Table 6.5 Confusion matrix, showing the NPDR grading at image level for each database

Class Code (CLINCIAL)	No DR	MILD	MODERATE	SEVERE
No DR	**94**	33	3	7
MILD	4	**1216**	25	21
MODERATE	1	14	**928**	43
SEVERE	0	0	4	**549**
Individual class classification accuracy (%)	95(94/99)	96.3(1216/1263)	96.7(928/960)	88.5(549/620)
Overall classification accuracy	94.7(2787/2942)			

Class Code (DRIVE)	No DR	MILD	MODERATE	SEVERE
No DR	**31**	0	0	0
MILD	2	**2**	1	0
MODERATE	0	0	**4**	0
SEVERE	0	0	0	**0**
Individual class classification accuracy (%)	93.9(31/33)	100(2/2)	80(4/5)	100(0/0)
Overall classification accuracy	92.5(37/40)			

Class Code (STARE)	No DR	MILD	MODERATE	SEVERE
No DR	**24**	2	0	1
MILD	1	**80**	1	1
MODERATE	1	1	**40**	1
SEVERE	0	0	1	**30**
Individual class classification accuracy (%)	92.3(23/25)	96.4(80/83)	95.3(40/42)	91(30/33)
Overall classification accuracy	94.1(173/184)			

Class Code (DIARETDB1)	No DR	MILD	MODERATE	SEVERE
No DR	**5**	1	0	0
MILD	0	**29**	1	0
MODERATE	0	1	**32**	1
SEVERE	0	0	1	**18**
Individual class classification accuracy (%)	100(5/5)	93.5(29/31)	94.1(32/34)	94.7(18/19)
Overall classification accuracy	94.4(84/89)			

Class Code (e-OPHTHA)	No DR	MILD	MODERATE	SEVERE
No DR	**254**	3	0	0
MILD	12	**131**	1	1
MODERATE	2	2	**31**	1
SEVERE	0	0	0	**25**
Individual class classification accuracy (%)	94.8(254/268)	96.3(131/136)	96.9(31/32)	92.6(25/27)
Overall classification accuracy	95.2(441/463)			

Dark lesions: Segmentation results of retinal images randomly selected from the composite database by the proposed method are shown in figure 6.8. From figure 6.8 (a) and (d), retinal images from STARE database, it can be seen that the boundaries of hemorrhages are slightly blurry and mixed with the bright lesions such as exudates and blood vessels region. Therefore, in such retinal images it becomes ambiguous even for the expert ophthalmologist to extract the exact boundary accurately. When these retinal images having fuzzy boundaries are processed for segmentation, it is perceived that the segmentation results obtained by the proposed method is comparable to the reference ground truths of the hemorrhages. From figure 6.8 (b) and (e), it is also observed that the proposed method is capable of segmenting the clear and large as well small hemorrhages (micro aneurysms) present in retinal images. Also, from an examination of figure 6.8 (g) it is observed that the size of micro aneurysms is too small as compared to the overall size of the retinal image. When the images with poor contrast between normal and detailed region is processed for segmentation, it is observed that there is possibility of micro aneurysms of very few pixels being missed during segmentation. However, the segmentation outcomes of the proposed method are comparatively very similar to the reference ground truths and provide essential lesion information.

Experiment 5: Evaluation Concerning the Grading of Diabetic retinopathy

In the last experiment, further evaluation for the performance of the proposed method in correctly grading the retinal image in the different severity levels is carried out. Table 6 shows the confusion matrices for the total number of retinal images which are graded correctly or incorrectly in the different severity levels for clinically and publicly acquired database. The proposed method shows the high classification performance for mild, moderate and severe clinically acquired retinal images with accuracy of 96.3%, 96.7% and 88.5% respectively. The

reason for misclassification of few samples of mild, moderate and severe in each other is due to the overlapping pathological appearances among dark lesions or bright lesions. It can also be observed from the results depicted in Table 6.5, that the proposed method performs efficiently in grading the publicly acquired databases, justifying its ability to correctly identify the severity level of the retinopathy present. Conclusively, the comparative performance analysis of the proposed method in grading the severity level with the existing methods is shown in Table 6.6. The overall sensitivity/specificity/accuracy of 95.74/97.31/96.33 respectively shows the capacity of the method in accurately determining the severity level of diabetic retinopathy as compared to the methods of Akram *et al*. and Figueiredo *et al.* [18,157].

Table 6.6 Performance evaluation of proposed system for grading of NPDR

Detection method	Database	Image Based Results (%)		
		SN	SP	Acc
Figueiredo [18]	Clinical	95.32%	64.89%	----
	DIARETDB	74.45%	86.25%	----
	MESSIDOR	75.11%	91.81%	----
	HEI-MED	66.00%	87.80%	----
Akram [157]	DRIVE	95.23%	94.73%	95.00%
	STARE	100%	91.30%	97.50%
	DIARETDB	96.42%	95.02%	95.50%
	MESSIDOR	99.50%	95.50%	98.90%
Proposed Method	**Clinical**	**99.49%**	**100%**	**100%**
	STARE	**99.33%**	**100%**	**100%**
	MESSIDOR	**87.50%**	**97.00%**	**93.00%**
	DIARETDB	**92.5%**	**93.00%**	**89.50%**
	e-Ophtha	**97.64%**	**94.35%**	**97.47%**
	DRIVE	**98.00%**	**99.50%**	**98.00%**
	OVERALL	**95.74%**	**97.31%**	**96.33%**

6.4 CONCLUDING REMARKS

A generalized computer-aided severity level detection method for the diagnosis of non-proliferative diabetic retinopathy has been proposed and examined in this work. The proposed method reliably judges the severity level by segmenting dark and bright lesions present in retinal fundus images regardless of types of lesions, blurred and well-contrasted lesions. The two-step

hierarchical classification is efficient in the sense that it segments retinal lesions irrespective of the large variations in retinal fundus images from varying databases. Therefore, the proposed method decreases inter-expert observability in the diagnosis of non-proliferative diabetic retinopathy to large extent.

The proposed methodology is designed and assessed with 5048 clinical retinal images acquired from hospital and six other open source benchmark databases, having distinct attributes like acquisition manner, field of view angle, pixel resolution etc. to demonstrate its generalization capacity and appropriateness for practical applications. Qualitative evaluation results by the visual interpretation of ophthalmologists are supported by quantitative evaluation using two sets of evaluation criteria: per-lesion and per-image based evaluation. The experimental results for per-lesion based evaluation reveals high performance of the proposed method in the segmentation of dark and bright lesions with sensitivity/specificity/accuracy of 94.80/99.80/98.43 and 95.80/98.80/95.43 respectively on clinically acquired database retinal images. The per-image evaluation outcomes show the high precision in precise recognition of clinically acquired pathological images from healthy retinal images with average sensitivity/specificity/accuracy of 98.8/100/100 and 100/100/100 for dark and bright lesions respectively. The overall results of per-lesion and per-image evaluation criteria reveals the capability of the proposed framework in the efficient grading of severity level of non-proliferative diabetic retinopathy based on the detection of red and bright lesions which are subtle and tough to distinguish. Lastly, it is emphasized that the proposed severity level detection method contributes to the generalization capacity and will aid ophthalmologists in making a better decision in diagnosis and regulating the development of non-proliferative diabetic retinopathy.

Chapter 7

Conclusions

This chapter summarizes the conclusions drawn from the experiments done for the computer-aided retinal disease diagnosis. The proposed work was conducted to diagnose retinal diseases, i.e. progressive and non-proliferative diabetic retinopathy using retinal fundus images. The conclusions drawn from the present research work and future scopes are mentioned in this section. The key conclusions on retinal image enhancement and blood vessels segmentation are also summarized along with the separate description of conclusions for the detection of progressive and non-proliferative diabetic retinopathy.

7.1 RETINAL IMAGE ENHANCEMENT AND BLOOD VESSELS SEGMENTATION

(i) Performance Investigation of Retinal Image Enhancement Method:

The following conclusions are drawn from the proposed image enhancement work done for retinal fundus images:

- The proposed retinal image enhancement method is designed to improve the visual quality of retinal fundus image and evaluated subjectively by the expert ophthalmologist. It was observed, from the visual judgement of the expert ophthalmologist, that the processed images provide better visual appearance in comparison to the original retinal images in terms of enhanced contrast and reduced blurring. Subsequently with this subjective assessment by the ophthalmologist, it can be concluded that the proposed enhancement method is suitable for precise lesion and anatomical structures segmentation as required in the designing of computer-aided methods for retinal disease detection and grading.
- The optimization in visual quality by proposed enhancement method was achieved by varying two parameters: (a) adaptive scaling factor for global contrast enhancement and (b) threshold value for local contrast enhancement. Adaptive scaling factor is optimized

subjectively by the expert ophthalmologist whereas threshold value is optimized by analyzing the range of intensity variations in each retinal image database present in the composite database. Final optimized values of adaptive scaling factor and threshold value for the proposed enhancement method are 3 and 120 respectively. These values are optimized in terms of reduction of blurring with contrast enhancement of retinal structures allowing the fine details of image to be visualized clearly.

(ii) Performance Investigation of Blood Vessels Segmentation Method:

- The performance of proposed blood vessels segmentation method, as evaluated with diverse and extensive database of 5048 retinal fundus images is 84.82% in terms of overall sensitivity. That much sensitivity reveals that the effectiveness of proposed method in segmenting blood vessels irrespective of healthy or pathological types of retinal fundus images. The subjective performance evaluation results of the proposed method are supported by objective medically significant statistical measures. Furthermore, the average accuracy of 97.58% on a composite database shows that there is high correlation of the segmented blood vessels with the ground truth provided by expert ophthalmologist.
- The proposed method outperforms the other methods in literature by showing significant improvement in sensitivity while preserving the ability to detect non-blood vessels structures (showing specificity 96.98%) and true blood vessel structures (showing accuracy 97.58%) with the evaluation on a comparatively large set of images. In addition, the method proves its capability in distinguishing true blood vessels from non-blood vessels on varying grades on retinal fundus images with the sensitivity of 85.13%, 85.73% and 82.41% on mild, moderate and severe diabetic retinopathy respectively. After the final evaluation, it can be concluded that the promising blood vessel segmentation results

obtained in the present work indicate its generalization ability to aid ophthalmologists in accurate detection of retinal lesions and subsequently retinal abnormalities.

7.2 PERFORMANCE OF PROGRESSIVE DIABETIC RETINOPATHY DETECTION METHOD

The proposed method reliably segments exudates using adaptive image quantization and subsequently dynamic decision thresholding irrespective of variations present in diverse retinal image database. The conclusions drawn from the detection of progressive diabetic retinopathy work are as follows:

- Performance effectiveness of the proposed exudates segmentation method is summarized on a diversified database of 5048 retinal fundus images using two sets of experiments namely: lesion-based evaluation and image-based evaluation. The overall average lesion-based sensitivity/specificity/accuracy of 94.80/99.80/98.43 on 2942 clinically acquired retinal fundus images indicates efficient pixel level segmentation of exudates by the proposed method. The image-based average sensitivity/specificity/accuracy of 98.8/100/100 demonstrates the effectiveness of the method in correct identification of pathological images from healthy images during mass screening.
- Additionally, the segmentation results on open-source benchmark databases reveals the ability of the method to segment exudates in comparison to other state-of-the art methods. The experimental results on open-source benchmark databases shows the sensitivity/accuracy of 99.65/99.13 on STARE database; 81.32/86.00 on MESSIDOR database; 83/92 on e-Ophtha EX database; 71.34/85.34 on DIARETDB1 database for lesion-based evaluation criteria. These results reveal that the proposed method performs significantly well irrespective of varying attributes of retinal images from different databases such as locations, shape, color, size etc. Finally, it can be emphasized that the

significant collective performance of the proposed exudates segmentation method on a composite database contributes to the generalization capability and proves the strong candidature in real-time diagnosis of progressive diabetic retinopathy.

7.3 PERFORMANCE OF NON-PROLIFERATIVE DIABETIC RETINOPATHY DETECTION AND GRADING METHOD

The proposed computer-aided method judges the severity level of the non-proliferative diabetic retinopathy by segmenting bright and dark lesions irrespective of associated heterogeneity, bright and faint edges. The conclusions drawn from the detection and grading method of non-proliferative diabetic retinopathy work are as follows:

- The performance of the proposed non-proliferative diabetic retinopathy detection method, as assessed on a composite database of 5048 retinal images having distinct attributes such as acquisition, field of view, pixel resolution etc., demonstrates its generalization capability and suitability for practical applications. The segmentation and grading results were verified subjectively by the visual interpretation of expert ophthalmologists and quantitatively by medically significant statistical measures using lesion and image-based evaluation criteria. The overall lesion and image-based evaluation of the proposed method reveals high performance in the segmentation of dark and bright lesions with SN/SP/ACC of 94.80/99.80/98.43 and 95.80/98.80/95.43 respectively on clinically acquired retinal images database. Furthermore, the image-based evaluation results demonstrate the high precision in precise recognition of pathological images from healthy retinal images with overall SN/SP/ACC of 98.8/100/100 and 100/100/100 for dark and bright lesions respectively.
- Finally, it can be concluded that the proposed method efficiently grades the severity level of non-proliferative diabetic retinopathy in spite of huge variations in retinal images of

different databases. Therefore, the proposed method reduces the interobserver variabilities in the diagnosis of non-proliferative diabetic retinopathy to a large extent. Additionally, the substantial combined lesion and image-based performance of the proposed method on clinical and open-source benchmark databases contributes to the generalization ability in diagnosing and controlling the progression of non-proliferative diabetic retinopathy.

7.4 SCOPE FOR FUTURE WORK

The following are the recommendations for future work:

(i) In the present work, the ground truths are marked manually by the expert ophthalmologists. In future work, an automatic clustering-based segmentation method can be implemented to identify ground truths of various retinal structures automatically because each retinal structure has different features from surrounding regions of retinal fundus image.

(ii) The classification system can be designed with more number of retinal diseases that appear in retinal fundus images.

(iii) In order to improve the generalized performance of the computer-aided system and to provide a system for real clinical practice, the same proposed system can be designed with a larger clinically acquired database acquired from different fundus cameras. Image data sets obtained from one clinical source do limit in representing the medical variety needed for large clinical studies (variance in sex, age, compliance etc.). Therefore, clinical retinal image database should be acquired from different medical centres so that a more generalized and robust system can be designed for real clinical need in this medical domain.

REFERENCES

[1] W. Sarah, R. Gojka, G. Anders, S. Richard, and K. Hilary, "Global Prevalence of Diabetes: Estimates for the year 2000 and projection for 2030," *Diabetes Care*, vol. 27, no. 5, pp. 1047–1053, 2004

[2] N. H. Cho *et al.*, "IDF Diabetes Atlas: Global estimates of diabetes prevalence for 2017 and projections for 2045," *Diabetes Research and Clinical Practice*, vol. 138, pp. 271–281, 2018.

[3] International Diabetes Federation, "Diabetes Complications" [Online] Available: https://www.idf.org/aboutdiabetes/what-is-diabetes/complications.html. [Accessed: Jan. 10, 2018].

[4] FIRSTPOST [Online] Available: https://www.firstpost.com/india/diabetes-is-indias-fastest-growing-disease-72-million-cases-recorded-in-2017-figure-expected-to-nearly-double-by-2025-4435203.html. [Accessed: Dec. 3, 2017].

[5] J. Chu, Y. Ali, "Diabetic Retinopathy: A Review," *Drug Development Research*., vol. 2, no. 4, pp. 226-237, 1989.

[6] DA. Salz, AJ. Witkin, "Identifying and Monitoring Diabetic Retinopathy," [Online] Available:http://retinatoday.com/2016/03/identifying-and-monitoring-diabetic-retinopathy/ [Accessed: Dec. 5, 2017].

[7] RxList- Fluorescite Side Effects Center [Online] Available: https://www.rxlist.com/fluorescite-side-effects-drug-center.htm [Accessed: Jan. 3, 2015].

[8] A. Sjølie, J. Stephenson, S. Aldington, E. Kohner, H. Janka, L. Stevens, J. Fuller, "Retinopathy and vision loss in insulin-dependent diabetes in Europe. The EURODIAB IDDM Complications Study," 1997; *Ophthalmology*, vol. 2, pp. 252-260, 1997.

[9] P. Frith, R. Gray, S. MacLennan, P. Ambler, *The Eye in Clinical Practice*, 2nd ed., Blackwell Science ltd., London, 2001.

[10] J. G. Hollyfield, R. E. Anderson, M. M LaVail (Eds.). Retinal Degenerative Diseases, Springer. *Laser Photocoagulation: Ocular Research and Therapy in Diabetic Retinopathy*, vol. 572, pp. 195-200, 2006.

[11] P. M. Rokade and R. R. Manza, "Automatic Detection of Hard Exudates in Retinal Images Using Haar Wavelet Transform," *International Journal of Application or Innovation Engineering and Management*, vol. 4, no. 5, pp. 402–410, 2015.

[12] B. Zhang, L. Zhang, L. Zhang, and F. Karray, "Retinal vessel extraction by matched filter with first-order derivative of Gaussian," *Computers in Biology and Medicine*, vol. 40, no. 4, pp. 438–445, 2010.

[13] D. Welfer, J. Scharcanski, and D. R. Marinho, "A coarse-to-fine strategy for automatically detecting exudates in color eye fundus images," *Computerized Medical Imaging and Graphics*, vol. 34, no. 3, pp. 228–235, 2010.

[14] X. Zhang *et al.*, "Exudate detection in color retinal images for mass screening of diabetic retinopathy," *Medical Image Analysis*, vol. 18, no. 7, pp. 1026–1043, 2014.

[15] Q. Liu *et al.*, "A location-to-segmentation strategy for automatic exudate segmentation in colour retinal fundus images," *Computerized Medical Imaging Graphics*, vol. 55, pp. 78–86, 2017.

[16] Habib *et al*., "Incorporating spatial information for microaneurysm detection in retinal images," *Advances in Science, Technology and Engineering Systems Journal*, vol. 2, no. 3, pp. 642-649, 2017.

[17] M. Usman Akram, S. Khalid, A. Tariq, S. A. Khan, and F. Azam, "Detection and classification of retinal lesions for grading of diabetic retinopathy," *Computers in Biology and Medicine*, vol. 45, no. 1, pp. 161–171, 2014.

[18] I. N. Figueiredo, S. Kumar, C. M. Oliveira, J. D. Ramos, and B. Engquist, "Automated lesion detectors in retinal fundus images," *Computers in Biology and Medicine*, vol. 66, pp. 47–65, 2015.

[19] D. Santhi, D. Manimegalai, S. Parvathi, and S. Karkuzhali, "Segmentation and classification of bright lesions to diagnose diabetic retinopathy in retinal images," *Biomedical Engineering*, vol. 61, no. 4, pp. 443–453, 2016.

[20] N. M. Salem and A. K. Nandi, "Segmentation of retinal blood vessels using scale-space features and K-nearest neighbour classifier," *International Conference on Acoustics, Speech, Signal Processing*, pp. 1001–1004, 2006.

[21] M. Garcia, C. Valverde, M. I. Lopez, J. Poza, and R. Hornero, "Comparison of logistic regression and neural network classifiers in the detection of hard exudates in retinal images," *35th Annual International Conference of the IEEE Engineering in Medicine and Biology Society (EMBC),* pp. 5891–5894, 2013.

[22] D. Mittal, V. Kumar, S. C. Saxena, N. Khandelwal, and N. Kalra, "Neural network based focal liver lesion diagnosis using ultrasound images," *Computerized Medical Imaging and Graphics,* vol. 35, no.4, pp. 315–323, 2011.

[23] K. Kharat, P. Kulkarni, and M. Nagori, "Brain tumor classification using neural network based methods," *International Journal of Computer Science and Informatics*, vol. 1, no. 4, pp. 85–90, 2012.

[24] I. I. Esener, S. Ergin, and T. Yuksel, "A New Feature Ensemble with a Multistage Classification Scheme for Breast Cancer Diagnosis," *Journal of Healthcare Engineering*, vol. 2017, 2017.

[25] S. Chaudhuri, S. Chatterjee, N. Katz, M. Nelson, M. Goldbaum, "Detection of blood vessels in retinal images using two-dimensional matched filters," *IEEE Transactions on Medical Imaging*, vol. 8, pp. 263–269, 1989.

[26] A. Hoover, "Locating blood vessels in retinal images by piecewise threshold probing of a matched filter response," *IEEE Transactions on Medical Imaging*, vol. 19, pp. 203-210, 2000.

[27] JJ. Staal, MD. Abramoff, M. Niemeijer, MA. Viergever, B. Van Ginneken, "Ridge based vessel segmentation in color images of the retina," *IEEE Transactions on Medical Imaging,* vol. 23, pp. 501–509, 2005.

[28] J. Soares, J. Leandro, RJ. Cesar, H. Jelinek H, M. Cree, "Retinal vessel segmentation using the {2-D} Gabor wavelet and supervised classification," *IEEE Transactions on Medical Imaging*, vol. 25, pp. 1214-1222, 2006.

[29] AM. Mendonça, A. Campilho, "Segmentation of retinal blood vessels by combining the detection of centerlines and morphological reconstruction," *IEEE Transactions on Medical Imaging*, vol. 25, pp. 1200-1213, 2006.

[30] E. Ricci, R. Perfetti, "Retinal blood vessel segmentation using line operators and support vector classification," *IEEE Transactions on Medical Imaging,* vol. 26, pp. 1357-1365, 2007.

[31] ME. Martinez-Perez, AD. Hughes, SA. Thom, AA. Bharath, KH. Parker, "Segmentation of blood vessels from red-free and fluorescein retinal images," *Medical Image Analysis*, vol. 11, pp. 47-61, 2007.

[32] L. Zhang, Q. Li, J. You, and D. Zhang, "A modified matched filter with double-sided thresholding for screening proliferative diabetic retinopathy," *IEEE Transactions on Information Technology in Biomedicine*, vol. 13, no. 4, pp. 528–534, 2009.

[33] T. E. F. Lupascu AC, D. Tegolo, "Retinal Vessel Segmentation Using AdaBoost," *IEEE Transactions on Information Technology in Biomedicine*, vol. 14, no. 5, pp. 1267–1274, 2010.

[34] F. Muhammad Moazam *et al.*, "An ensemble classification-based approach applied to retinal blood vessel segmentation," *IEEE Transactions on Biomedical Engineering.*, vol. 59, no. 9, pp. 2538–2548, 2012.

[35] Q. Li, J. You, and D. Zhang, "Vessel segmentation and width estimation in retinal images using multiscale production of matched filter responses," *Expert Systems with Applications*, vol. 39, no. 9, pp. 7600–7610, 2012.

[36] Y. Wang, G. Ji, P. Lin, and E. Trucco, "Retinal vessel segmentation using multiwavelet kernels and multiscale hierarchical decomposition," *Pattern Recognition Letters*, vol. 46, no. 8, pp. 2117–2133, 2013.

[37] U. T. V. Nguyen, A. Bhuiyan, L. A. F. Park, and K. Ramamohanarao, "An Effective Retinal Blood Vessel Segmentation Method Using Multi-Scale Line Detection," *Pattern Recognition Letters.*, vol. 46, no. 3, pp. 703–715, 2012.

[38] A. Salazar-Gonzalez, D. Kaba, and X. Liu, "Segmentation of the blood vessels and optic disc in retinal images," *IEEE Journal of Biomedical and Health Informatics*, vol. 18, no.6, pp. 1874-1886, 2014.

[39] J. Rahebi and F. Hardalaç, "Retinal Blood Vessel Segmentation with Neural Network by Using Gray-Level Co-Occurrence Matrix-Based Features," *Journal of Medical Systems*, vol. 38, no. 8, p. 85, 2014.

[40] S.W. Franklin, "Computerized screening of diabetic retinopathy employing blood vessel segmentation in retinal images," *Biocybernetics and Biomedical Engineering*, vol. 34, no. 2, pp. 117–124, 2014.

[41] Y. Qian, X. Hong, X. Fang, and F. Y. Shih, "Retinal vessels segmentation based on level set and region growing," *Pattern Recognition Letters*, vol. 47, no. 7, pp. 2437–2446, 2014.

[42] Y. Zhao, L. Rada, K. Chen, S. P. Harding, and Y. Zheng, "Automated Vessel Segmentation Using Infinite Perimeter Active Contour Model with Hybrid Region Information with Application to Retinal Images," *IEEE Transactions on Medical Imaging*, vol. 34, no. 9, pp. 1797–1807, 2015.

[43] S. Roychowdhury, D. D. Koozekanani, and K. K. Parhi, "Iterative Vessel Segmentation of Fundus Images," *IEEE Transactions on Biomedical Engineering*, vol. 62, no. 7, pp. 1738–1749, 2015.

[44] E. Imani, M. Javidi, and H.-R. Pourreza, "Improvement of retinal blood vessel detection using morphological component analysis," *Computer Methods and Programs in Biomedicine*, vol. 118, no. 3, pp. 263–279, 2015.

[45] S. Wang, Y. Yin, G. Cao, B. Wei, Y. Zheng, and G. Yang, "Hierarchical Retinal Blood Vessel Segmentation Based on Feature and Ensemble Learning," *Neurocomputing*, vol. 149, no. PB, pp. 708–717, 2015.

[46] X. Jiang and D. Mojon, “Adaptive local thresholding by verification based multithreshold probing with application to vessel detection in retinal images,” *IEEE Transactions on Pattern Analysis and Machine Intelligence*, vol. 25, no. 1, pp. 131–137, 2003.

[47] M. Sofka and C. V. Stewart, “Retinal vessel centerline extraction using multiscale matched filters, confidence and edge measures,” *IEEE Transactions on Medical Imaging*, vol. 25, no. 12, pp. 1531–1546, 2006.

[48] Liang Zhou, M. S. Rzeszotarski, L. J. Singerman, and J. M. Chokreff, “The detection and quantification of retinopathy using digital angiograms,” *IEEE Transactions on Medical Imaging*, vol. 13, no. 4, pp. 619–626, 1994.

[49] O. Chutatape, Liu Zheng, and S. M. Krishnan, “Retinal blood vessel detection and tracking by matched Gaussian and Kalman filters,” *Proceedings of 20th Annual International Conference IEEE Engineering in Medicine and Biology Society*, vol. 6, pp. 3144–3149.

[50] Y. A. Tolias and S. M. Panas, “A fuzzy vessel tracking algorithm for retinal images based on fuzzy clustering,” *IEEE Transactions on Medical Imaging*, vol. 17, no. 2, pp. 263–273.

[51] A. Can, H. Shen, J. Turner, H. Tanenbaum, and B. Roysam, “Rapid automated tracing and feature extraction from retinal fundus images using direct exploratory algorithms,” *IEEE Transactions on Information Technology in Biomedicine*, vol. 3, no. 1, pp. 1–15, 1999.

[52] X. You, Q. Peng, Y. Yuan, Y. M. Cheung, and J. Lei, “Segmentation of retinal blood vessels using the radial projection and semi-supervised approach,” *Pattern Recognition Letters.*, vol. 44, no. 10–11, pp. 2314–2324, 2011.

[53] M. G. Cinsdikici and D. Aydin, “Detection of blood vessels in ophthalmoscope images using MF/ant (matched filter/ant colony) algorithm,” *Computer Methods and Programs in Biomedicine*, vol. 96, no. 2, pp. 85–95, 2009.

[54] C. Yao and H. J. Chen, “Automated retinal blood vessels segmentation based on simplified PCNN and fast 2D-Otsu algorithm,” *Journal of Central South University of Technology (English Ed.*, vol. 16, no. 4, pp. 640–646, 2009.

[55] R. J. Winder, P. J. Morrow, I. N. McRitchie, J. R. Bailie, and P. M. Hart, "Algorithms for digital image processing in diabetic retinopathy.," *Computerized Medical Imaging Graphics*, vol. 33, no. 8, pp. 608–22, 2009.

[56] B. Kochner, D. Schuhmann, M. Michaelis, G. Mann, and K.-H. Englmeier, "Course tracking and contour extraction of retinal vessels from color fundus photographs: Most efficient use of steerable filters for model-based image analysis," *Proceedings SPIE - International Society for Optics and Photonics Engineering*, vol. 3338, pp. 755–761, 1998.

[57] A. Pinz, S. Bern, P. Datlinger, and A. Kruger, "Mapping the Human Retina," *Ophthalmology*, vol. 17, no. 4, pp. 606–619, 1998.

[58] S. C. Lee, Y. Wang, and E. T. Lee, "Computer algorithm for automated detection and quantification of microaneurysms and hemorrhages (HMAs) in color retinal images.," *Medical Imaging'99. International Society for Optics and Photonics*, pp. 61–71, 1999.

[59] M. Lalonde, M. Beaulieu, and L. Gagnon, "Fast and robust optic disc detection using pyramidal decomposition and hausdorff-based template matching," *IEEE Transactions on Medical Imaging*, vol. 20, no. 11, pp. 1193–1200, 2001.

[60] C. Sinthanayothin, J. F. Boyce, H. L. Cook, and T. H. Williamson, "Automated localisation of the optic disc, fovea, and retinal blood vessels from digital colour fundus images," *British Journal of Ophthalmology*, vol. 83, no. 8, pp. 902–910, 1999.

[61] C. Sinthanayothin, J. F. Boyce, H. L. Cook, and T. H. Williamson, "Automated localisation of the optic disc, fovea, and retinal blood vessels from digital colour fundus images," *British Journal of Ophthalmology*, vol. 83, no. 8, pp. 902–910, 1999.

[62] A. Hoover and M. Goldbaum, "Locating the optic nerve in a retinal image using the fuzzy convergence of the blood vessels," *IEEE Transactions on Medical Imaging.*, vol. 22, no. 8, pp. 951–958, 2003.

[63] K. W. Tobin, E. Chaum, V. Priya Govindasamy, and T. P. Karnowski, “Detection of anatomic structures in human retinal imagery,” *IEEE Transactions on Medical Imaging*, vol. 26, no. 12, pp. 1729–1739, 2007.

[64] A. A. H. A. R. Youssif, A. Z. Ghalwash, and A. A. S. A. R. Ghoneim, “Optic disc detection from normalized digital fundus images by means of a vessels’ direction matched filter,” *IEEE Transactions on Medical Imaging*, vol. 27, no. 1, pp. 11–18, 2008.

[65] M. Niemeijer, M. D. Abramoff, and B. van Ginneken, “Automated localization of the optic disc and the fovea.,” *Conference Proceedings IEEE Engineering in Medicine and Biology Society*, vol. 2008, pp. 3538–41, 2008.

[66] T. Kauppi and H. Kälviäinen, “Simple and robust optic disc localisation using colour decorrelated templates,” *Lecture Notes in Computer Science (including Lecture Notes in Artificial Intelligence and Lecture Notes in Bioinformatics)*, vol. 5259 LNCS, pp. 719–729, 2008.

[67] M. Niemeijer, M. D. Abràmoff, and B. Van Ginneken, “Segmentation of the optic disc, macula and vascular arch in fundus photographs,” *IEEE Transactions on Medical Imaging*, vol. 26, no. 1, pp. 116–127, 2007.

[68] D.Welfer; J.Scharcanski; C.M. Kitamura;M.M.D.Pizzol;L.W.B.Ludwig; D.R. Marinho, “Segmentation of the optic disc in color eye fundus images using an adaptive morphological approach,” *Computers in Biology and Medicine*, vol. 40, pp. 124–137, 2010.

[69] S. Lu, “Accurate and efficient optic disc detection and segmentation by a circular transformation,” *IEEE Transactions on Medical Imaging*, vol. 30, no. 12, pp. 2126–2133, 2011.

[70] H. Yu *et al.*, “Fast localization and segmentation of optic disk in retinal images using directional matched filtering and level sets,” *IEEE Transactions on Information Technology in Biomedicine*, vol. 16, no. 4, pp. 644–657, 2012.

[71] A. Kauri and P. Kaur, “A Comparative Review of Various Segmentation Techniques for Early Detection of Exudates in Retinal Fundus Images,” *IEEE 1st International Conference on Power Electronics, Intelligent Control and Energy Systems (ICPEICES),* pp. 1–4, 2016.

[72] J. G. Hollyfield, R. E. Anderson, M. M LaVail (Eds.). Retinal Degenerative Diseases, Springer. Laser Photocoagulation: Ocular Research and Therapy in Diabetic Retinopathy. 2006; 195-200.

[73] R. Phillips, J. Forrester, and P. Sharp, "Automated detection and quantification of retinal exudates," *Graefe's Archive for Clinical and Experimental Ophthalmology*, vol. 231, no. 2, pp. 90–94, 1993.

[74] B. M. Ege *et al.*, "Screening for diabetic retinopathy using computer based image analysis and statistical classification," *Computer Methods and Programs in Biomedicine*, vol. 62, no. 0169–2607, pp. 165–175, 2000.

[75] H. W. H. Wang, W. H. W. Hsu, K. G. G. K. G. Goh, and M. L. L. M. L. Lee, "An effective approach to detect lesions in color retinal images," *Proceedings IEEE Conference on Computer Vision and Pattern Recognition. CVPR 2000 (Cat. No.PR00662)*, vol. 2, pp. 1–6, 2000.

[76] C. I. Sanchez, M. Garcia, A. Mayo, M. I. Lopez, and R. Hornero, "Retinal image analysis based on mixture models to detect hard exudates.," *Medical Image Analysis*, vol. 13, no. 4, pp. 650–658, 2009.

[77] G. Maria, S. C. I, L. M. I, A. Daniel, and H. Roberto, "Neural network based detection of hard exudates in retinal images," *Computer Methods and Programs in Biomedicine.*, no. 1, pp. 9–19, 2009.

[78] H. Yazid, H. Arof, and H. M. Isa, "Automated identification of exudates and optic disc based on inverse surface thresholding," *Journal of Medical Systems*, vol. 36, no. 3, pp. 1997–2004, 2012.

[79] T. Walter, J.-C. Klein, P. Massin, and A. Erginay, "A contribution of image processing to the diagnosis of diabetic retinopathy-detection of exudates in color fundus images of the human retina," *IEEE Transactions on Medical Imaging*, vol. 21, no. 10, pp. 1236–1243, 2002.

[80] A. Sopharak, B. Uyyanonvara, S. Barman, and T. H. Williamson, "Automatic detection of diabetic retinopathy exudates from non-dilated retinal images using mathematical morphology methods," *Computerized Medical Imaging and Graphics*, vol. 32, no. 8, pp. 720–727, 2008.

[81] D. Welfer, J. Scharcanski, and D. R. Marinho, “A coarse-to-fine strategy for automatically detecting exudates in color eye fundus images,” *Computerized Medical Imaging and Graphics*, vol. 34, no. 3, pp. 228–235, 2010.

[82] X. Zhang *et al.*, “Exudate detection in color retinal images for mass screening of diabetic retinopathy,” *Medcal Image Analysis*, vol. 18, no. 7, pp. 1026–1043, 2014.

[83] A. Sopharak, B. Uyyanonvara, and S. Barman, “Automatic Exudate Detection from Non-dilated Diabetic Retinopathy Retinal Images Using Fuzzy C-means Clustering,” *Sensors (Peterborough, NH)*, pp. 2148–2161, 2009.

[84] A. Osareh, M. Mirmehdi, B. Thomas, R. Markham: Scientific Report. Digital Colour Images: Image (Rochester, N.Y.) pp. 1220–1223, 2003.

[85] M. Niemeijer, B. van Ginneken, S. R. Russell, M. S. A. Suttorp-Schulten, and M. D. Abramoff, “Automated Detection and Differentiation of Drusen, Exudates, and Cottonwool Spots in Digital Color Fundus Photographs for Early Diagnosis of Diabetic Retinopathy,” *Investigative Ophthalmology and Visual Science*, vol. 48, no. 5, pp. 2260–7, 2007.

[86] L. Giancardo *et al.*, “Exudate-based diabetic macular edema detection in fundus images using publicly available datasets,” *Medical Image Analysis*, vol. 16, no. 1, pp. 216–226, 2012.

[87] D. Sidibé, I. Sadek, and F. Mériaudeau, “Discrimination of retinal images containing bright lesions using sparse coded features and SVM,” *Computers in Biology and Medicine*, vol. 62, pp. 175–184, 2015.

[88] A. Osareh and M. Mirmehdi, “Automatic recognition of exudative maculopathy using fuzzy c-means clustering and neural networks,” *Medical Image Understanding and Analysis,* vol. 3, pp. 49-52, 2001.

[89] D. Usher, M. Dumsky, M. Himaga, T. H. Williamson, S. Nussey, and J. Boyce, “Automated Detection of Diabetic Retinopathy in Digital Retinal Images: A Tool for Diabetic Retinopathy Screening,” *Diabetic Medicine*, vol. 21, pp. 84–90, 2004.

[90] A. W. Reza, C. Eswaran, and S. Hati, “Automatic tracing of optic disc and exudates from color fundus images using fixed and variable thresholds,” *Journal of Medical Systems*, vol. 33, no. 1, pp. 73–80, 2009.

[91] A. W. Reza, C. Eswaran, and K. Dimyati, “Diagnosis of diabetic retinopathy: Automatic extraction of optic disc and exudates from retinal images using marker-controlled watershed transformation,” *Journal of Medical Systems*, vol. 35, no. 6, pp. 1491–1501, 2011.

[92] D. Youssef and N. H. Solouma, “Accurate detection of blood vessels improves the detection of exudates in color fundus images,” *Computer Methods and Programs in Biomedicine*, vol. 108, no. 3, pp. 1052–1061, 2015.

[93] B. Harangi, B. Antal, and A. Hajdu, “Automatic exudate detection with improved naive-Bayes classifier,” *Proceedings - IEEE Symposium Computer-Based Medical Systems*, 2012.

[94] G. G. Rajput and P. N. Patil, “Detection and classification of exudates using k-means clustering in color retinal images,” *Proceedings - 2014 5th International Conference on Signal and Image Processing, ICSIP 2014*, pp. 126–130, 2014.

[95] S. Lahmiri and M. Boukadoum, “Automated detection of circinate exudates in retina digital images using empirical mode decomposition and the entropy and uniformity of the intrinsic mode functions,” *Biomedical Technik*, vol. 59, no. 4, pp. 357–366, 2014.

[96] K. Wisaeng, N. Hiransakolwong, and E. Pothiruk, “Automatic detection of exudates in retinal images based on threshold moving average models,” *Biophysics (Oxford).*, vol. 60, no. 2, pp. 288–297, 2015.

[97] T. Jaya, J. Dheeba, and N. A. Singh, “Detection of Hard Exudates in Colour Fundus Images Using Fuzzy Support Vector Machine-Based Expert System,” *Journal of Digital Imaging*, vol. 28, no. 6, pp. 761–768, 2015.

[98] S. Chugh, J. Kaur, D. Mittal, “Exudates Segmentation in Retinal Fundus Images for the Detection of Diabetic Retinopathy,” *International Journal of Engineering Research and Technology*, vol. 3, pp. 673–677, 2014.

[99] S. K. Mishra, D. Mittal, R. K. Sunkaria, "Designing of Computer Aided Diagnostic System for the Identification of Exudates in Retinal Fundus Images," *Journal of Biomedical Engineering and Medical Imaging*, vol. 2, no. 3, pp. 29-40, 2015.

[100] D. Mittal and K. Kumari, "Automated detection and segmentation of drusen in retinal fundus images," *Computers and Electrical Engineering*, vol. 47, pp. 82–95, 2015.

[101] I. N. Figueiredo and S. Kumar, "Wavelet-based computer-aided detection of bright lesions in retinal fundus images," *Lecture Notes in Computer Science (including Lecture Notes in Artificial Intelligence and Lecture Notes in Bioinformatics)*, vol. 8641 LNCS, pp. 234–240, 2014.

[102] M. J. Cree, J. A. Olson, K. C. Mchardy, P. F. Sharp, and J. V. Forrester, "A fully automated comparative microaneurysm digital detection system," *Eye*, vol. 11, no. 5, pp. 622–628, 1997.

[103] T. Spencer, J. A. Olson, K. C. McHardy, P. F. Sharp, and J. V. Forrester, "An image-processing strategy for the segmentation and quantification of microaneurysms in fluorescein angiograms of the ocular fundus," *Computers and Biomedical Research*, vol. 29, no. 4, pp. 284–302, 1996.

[104] T. Walter and J.-C. Klein, "Automatic Detection of Microaneurysms in Color Fundus Images of the Human Retina by Means of the Bounding Box Closing," *International Symposium Medical Data Analysis*, vol. 2526, pp. 210–220, 2002.

[105] T. Walter and J. C. Klein, "A computational approach to diagnosis of diabetic retinopathy," *Proceedings of the 6th Conference on Systemics, Cybernetics and Informatics (SCI2002)*, pp. 521-526, 2002.

[106] C. Sinthanayothin, J. Boyce, and T. Williamson, "Automated detection of diabetic retinopathy on digital fundus images," *Diabetic*, pp. 105–112, 2002.

[107] G. Quellec, M. Lamard, P. M. Josselin, G. Cazuguel, B. Cochener, and C. Roux, "Optimal Wavelet Transform for the Detection of Microaneurysms in Retina Photographs," *IEEE Transactions on Medical Imaging*, vol. 27, no. 9, pp. 1230–1241, 2008.

[108] M. Niemeijer, B. Van Ginneken, J. Staal, M. S. A. Suttorp-Schulten, and M. D. Abràmoff, "Automatic detection of red lesions in digital color fundus photographs," *IEEE Transactions on Medical Imaging*, vol. 24, no. 5, pp. 584–592, 2005.

[109] D. Usher, M. Dumsky, M. Himaga, T. H. Williamson, S. Nussey, and J. Boyce, "Automated Detection of Diabetic Retinopathy in Digital Retinal Images: A Tool for Diabetic Retinopathy Screening," vol. 21, pp. 84–90, 2004.

[110] M. García, M. I. López, D. Álvarez, and R. Hornero, "Assessment of four neural network based classifiers to automatically detect red lesions in retinal images," *Medical Engineering and Physics*, vol. 32, no. 10, pp. 1085–1093, 2010.

[111] L. Seoud, T. Hurtut, J. Chelbi, F. Cheriet, and J. M. P. Langlois, "Red Lesion Detection using Dynamic Shape Features for Diabetic Retinopathy Screening," *IEEE Transactions on Medical Imaging*, vol. XX, no. XX, pp. 1–1, 2015.

[112] A. J. Frame *et al.*, "A comparison of computer based classification methods applied to the detection of microaneurysms in ophthalmic fluorescein angiograms," *Computers in Biology and Medicine*, vol. 28, no. 3, pp. 225–238, 1998.

[113] J. H. Hipwell, F. Strachan, J. A. Olson, K. C. McHardy, P. F. Sharp, and J. V. Forrester, "Automated detection of microaneurysms in digital red-free photographs: A diabetic retinopathy screening tool," *Diabetic Medicine*, vol. 17, no. 8, pp. 588–594, 2000.

[114] G. Yang, L. Gangnon, S. Wang, and M. C. Boucher, "Algorithm for detection microaneurysms in low resolution color retinal images," *Proceedings of the International Conference on Visualization Interface*, pp. 265–271, 2001.

[115] P. M. D. S. Pallawala, W. Hsu, M. L. Lee, and S. S. Goh, "Automated microaneurysm segmentation and detection using generalized eigenvectors," *Proceedings of the Seventh IEEE International Conference on Computer Vision and Work Applications, WACV 2005*, pp. 322–327, 2007.

[116] G. Quellec, M. Lamard, P. M. Josselin, G. Cazuguel, B. Cochener, and C. Roux, "Detection of lesions in retina photographs based on the wavelet transform," *Proceedings of Annual International Conference on IEEE Engineering in Medicine and Biology*, pp. 2618–2621, 2006.

[117] T. Walter, P. Massin, A. Erginay, R. Ordonez, C. Jeulin, and J. C. Klein, "Automatic detection of microaneurysms in color fundus images," *Medical Image Analysis*, vol. 11, no. 6, pp. 555–566, 2007.

[118] A. Bhalerao, A. Patanaik, S. Anand, and P. Saravanan, "Robust detection of microaneurysms for sight threatening retinopathy screening," *Proceedings 6th Indian Conference Computer Vision, Graphics and Image Processing ICVGIP 2008*, pp. 520–527, 2008.

[119] B. Zhang, X. Wu, J. You, Q. Li, and F. Karray, "Detection of microaneurysms using multi-scale correlation coefficients," *Pattern Recognition*, vol. 43, no. 6, pp. 2237–2248, 2010.

[120] C. I. Sánchez, R. Hornero, A. Mayo, and M. García, "Mixture model-based clustering and logistic regression for automatic detection of microaneurysms in retinal images," *Proceedings of SPIE – The International Society for Optical Engineering*, vol. 72601M, 2009.

[121] L. Giancardo, F. Mériaudeau, T. P. Karnowski, K. W. Tobin, Y. Li, and E. Chaum, "Microaneurysms detection with the radon cliff operator in retinal fundus images," *Proceedings of SPIE Medical Imaging 2010: Image Processing*, vol. 76230U, 2010.

[122] X. Zhang, G. Thibault, and E. Decencière, "Application of the morphological ultimate opening to the detection of microaneurysms on eye fundus images from clinical databases,"*13th International Congress of Stereology (ICS'13)*, 2011.

[123] Y. Hatanaka, T. Inoue, S. Okumura, C. Muramatsu, and H. Fujita, "Automated microaneurysm detection method based on double-ring filter and feature analysis in retinal fundus images," *Proceedings of IEEE Symposium on Computer based Medical Systems*, 2012.

[124] A. T. E. G.G. Gardner, D. Keating, T.H. Williamson, "Automatic detection of diabetic retinopathy using an artificial neural network: a screening tool," *Ophthalmology*, pp. 940–944, 1996.

[125] X. Zhang and O. Chutatape, “Top-down and bottom-up strategies in lesion detection of background diabetic retinopathy,” *Proceedings on IEEE Computer Society Conference on Computer Vision and Pattern Recognition, CVPR 2005*, vol. II, pp. 422–428, 2005.

[126] Y. Hatanaka, T. Nakagawa, and Y. Hayashi, “CAD scheme to detect hemorrhages and exudates in ocular fundus images,” *Proceedings of the SPIE Medical Imaging*, vol. 6514, pp. 1–8, 2007.

[127] Y. Hatanaka, T. Nakagawa, Y. Hayashi, T. Hara, and H. Fujita, “Improvement of automated detection method of hemorrhages in fundus images.,” *Proceedings of the 30th Annual International Conference of the IEEE Engineering in Medicine and Biology Society*, pp. 5429–5432, 2008.

[128] K. A. Goatman, G. J. Williams, S. Philip, P. F. Sharp, and J. A. Olson, “Automated Detection of Blot Haemorrhages as a Sign of Referable Diabetic Retinopathy,” *Proceedings of the Medical Image Understanding and Analysis*, no. February 2016, pp. 4–8, 2008.

[129] J.P. Bae, K.G. Kim, H.C. Kang, C.B. Jeong, K. H. Park, and J.M. Hwang, “A study on hemorrhage detection using hybrid method in fundus images,” *Journal of Digital Imaging*, vol. 24, no. 3, pp. 394–404, 2011.

[130] V. S. Joshi *et al.*, “Automated detection of malarial retinopathy-associated retinal hemorrhages,” *Investigative Ophthalmology and Visual Science*, vol. 53, no. 10, pp. 6582–6588, 2012.

[131] L. Tang, M. Niemeijer, J. M. Reinhardt, M. K. Garvin, and M. D. Abramoff, “Splat feature classification with application to retinal hemorrhage detection in fundus images,” *IEEE Transactions on Medical Imaging*, vol. 32, no. 2, pp. 364–375, 2013.

[132] C. Sinthanayothin, J. Boyce, and T. Williamson, “Automated detection of diabetic retinopathy on digital fundus images,” *Diabetic*, pp. 105–112, 2002.

[133] X. Zhang and G. Fan, “Retinal spot lesion detection using adaptive multiscale morphological processing,” *Advances in Visual Computing*, pp. 1–12, 2006.

[134] M. Foracchia, E. Grisan, and A. Ruggeri, “Luminosity and contrast normalization in retinal images,” *Medical Image Analysis*, vol. 9, no. 3, pp. 179–190, 2005.

[135] C. Mariño, E. Ares, M. G. Penedo, M. Ortega, N. Barreira, and F. Gomez-Ulla, "Automated three stage red lesions detection in digital color fundus images," *WSEAS Transactions on Computers*, vol. 7, no. 4, pp. 207–215, 2008.

[136] S. Pradhan, S. Balasubramanian, and V. Chandrasekaran, "An integrated approach using automatic seed generation and hybrid classification for the detection of red lesions in digital fundus images," *Proceedings on IEEE International Conference of Computer and Information Technology Workshops CIT Work. 2008*, pp. 462–467, 2008.

[137] G. B. Kande, T. S. Savithri, P. V. Subbaiah, and M. R. N. Tagore, "Detection of red lesions in digital fundus images," *Proceedings on IEEE International Symposium on Biomedical Imaging from Nano to Macro, ISBI 2009*, pp. 558–561, 2009.

[138] M. García, S. Member, C. I. Sánchez, M. I. López, and R. Hornero, "Automatic Detection of Red Lesions in Retinal Images Using a Multilayer Perceptron Neural Network," *30th Annual International Conference of the IEEE Engineering in Medicine and Biology Society*, pp. 5425–5428, 2008.

[139] G. B. Kande, T. S. Savithri, and P. V. Subbaiah, "Automatic detection of microaneurysms and hemorrhages in digital fundus images," *Journal of Digital Imaging*, vol. 23, no. 4, pp. 430–437, 2010.

[140] M. M. Habib *et al.*, "Incorporating Spatial Information for Microaneurysm Detection in Retinal Images," *Advances in Science, Technology and Engineering Systems Journal*, vol. 2, no. 3, pp. 642–649, 2017.

[141] C. Köse, U. Şevik, C. Ikibaş, and H. Erdöl, "Simple methods for segmentation and measurement of diabetic retinopathy lesions in retinal fundus images," *Computer Methods and Programs in Biomedicine*, vol. 107, no. 2, pp. 274–293, 2012.

[142] V. P. Singh, S. Srivastava, and R. Srivastava, "Effective mammogram classification based on center symmetric-LBP features in wavelet domain using random forests," *Technology and Health Care*, vol. 25, no. 4, pp. 709–727, 2017.

[143] S. Chaudhuri, S. Chatterjee, N. Katz, M. Nelson, and M. Goldbaum, "Detection of blood vessels in retinal images using two dimensional matched filters," *IEEE Transactions on Medical Imaging*, vol. 8, pp. 263–269, 1989.

[144] M. S. Manikandan and S. Dandapat, "Multiscale entropy based weighted distortion measure for ECG coding", *IEEE Signal Processing Letters*, vol. 15, pp. 829-832, 2008.

[145] A. Thakur and R.S. Anand, "A Local statistics based region growing segmentation method for ultrasound medical images", *International Journal of Signal Processing (IJSP),* vol. 1, no. 2, pp 141-146, 2004.

[146] J. D. Bremner, P. Randall, E. Vermetten, and L. Staib, "Magnetic resonance imaging-based measurement of hippocampal volume in posttraumatic stress disorder related to childhood physical and sexual abuse: A preliminary report," *Biological Psychiatry*, vol. 41, no. 1, pp. 23–32, 1997.

[147] R. R. Winkel *et al.*, "Mammographic density and structural features can individually and jointly contribute to breast cancer risk assessment in mammography screening: A case-control study," *BMC Cancer*, vol. 16, no. 1, 2016.

[148] H. Alahmer and A. Ahmed, "Computer-aided Classification of Liver Lesions from CT Images Based on Multiple ROI," *Procedia Computer Science*, vol. 90, pp. 80–86, 2016.

[149] D. Mittal, V. Kumar, S. C. Saxena, N. Khandelwal, and N. Kalra, "Neural network based focal liver lesion diagnosis using ultrasound images," *Computerized Medical Imaging and Graphics,* vol. 35, no.4, pp. 315–323, 2011.

[150] Pathak, A.N., and Sunkaria, R.K., Multiclass Brain Tumour Classification using SVM. *International Journal of Computer Applications*, vol. 97, no. 23, pp. 34-38, 2014.

[151] V. K. Shrivastava, N. D. Londhe, R. S. Sonawane, and J. S. Suri, "Computer-aided diagnosis of psoriasis skin images with HOS, texture and color features: A first comparative study of its kind," *Computer Methods and Programs in Biomedicine*, vol. 126, pp. 98–109, 2016.

[152] R. Pires, H. F. Jelinek, J. Wainer, E. Valle, and A. Rocha, "Advancing bag-of-visual-words representations for lesion classification in retinal images," *PLoS One*, vol. 9, no. 6, 2014.

[153] M. R. K. Mookiah, C. K. Chua, L. C. Min, E. Y. K. Ng, and A. Laude, "Computer aided diagnosis of diabetic retinopathy using multi-resolution analysis and feature ranking frame work," *Journal of Medical Imaging and Health Informatics*, vol. 3, no. 4, pp. 598–606, 2013.

[154] R. A. Welikala *et al.*, "Genetic algorithm based feature selection combined with dual classification for the automated detection of proliferative diabetic retinopathy," *Computerized Medical Imaging and Graphics*, vol. 43, pp. 64–77, 2015.

[155] N. B. Prakash, D. Selvathi, and G. R. Hemalakshmi, "Development of algorithm for dual stage classification to estimate severity level of diabetic retinopathy in retinal images using soft computing techniques," *International Journal of Electrical Engineering and Informatics*, vol. 6, no. 4, pp. 717–739, 2014.

[156] S. Roychowdhury, D. Koozekanani, and K. Parhi, "DREAM: Diabetic Retinopathy Analysis using Machine Learning," *IEEE Journal of Biomedical and Health Informatics*, vol. 18, pp. 1717–28, 2014.

[157] M. Usman Akram, S. Khalid, A. Tariq, S. A. Khan, and F. Azam, "Detection and classification of retinal lesions for grading of diabetic retinopathy," *Computers in Biology and Medicine*, vol. 45, no. 1, pp. 161–171, 2014.

[158] W. L. Yuna, U. R. Acharyab, Y. V Venkatesha, C. Cheec, L. C. Minb, and E. Y. K. Ngd, "Identification of different stages of diabetic retinopathy using retinal optical images," *Information Sciences (Ny).*, vol. 178, pp. 106–121, 2008.

[159] P. K. Mishra, A. Sinha, K. R. Teja, N. Bhojwani, S. Sahu, and A. Kumar, "A computational modeling for the detection of diabetic retinopathy severity," *Bioinformation*, vol. 10, no. 9, pp. 556–561, 2014.

[160] K. Verma, P. Deep, and A. G. Ramakrishnan, "Detection and classification of diabetic retinopathy using retinal images," *Proceedings on Annual IEEE India Conference of Engineering Sustainable Solutions INDICON-2011*, 2011.

[161] M. A. Fadzil, L. Izhar, H. Nugroho, and H. Nugroho, "Analysis of retinal fundus images for grading of diabetic retinopathy severity," *Medical & Biological Engineering & Computing*, pp. 1–8, 2011.

[162] B. van Staal, J.J. Abramoff, M.D. Niemeijer, M. Viergever, M.A. Ginneken, "DRIVE: Digital Retinal Images for Vessel Extraction," *IEEE Transactions on Medical Imaging*, pp. 501–509, 2004.

[163] T. Kauppi *et al.*, "DIARETDB1 : Standard Diabetic Retinopathy Database," 2007. http://www.it.lut.fi/project/imageret/diaretdb1/ [Accessed: Jan. 10, 2018].

[164] Messidor, "Methods to evaluate segmentation and indexing techniques in the field of retinal ophthalmology," *Adcis*, 2004. http://www.adcis.net/en/Download-Third-Party/Messidor.html [Accessed: Jan. 13, 2014].

[165] ADCIS, "e-optha: A Color Fundus Image Database." ADCIS, http://www.adcis.net/en/Download-Third-Party/E-Ophtha.html [Accessed: Jan. 8, 2014].

[166] M. Goldbaum, "STructured Analysis of the Retina (STARE)," 2000. http://www.ces.clemson.edu/~ahoover/stare/ [Accessed: Dec. 10, 2013].

[167] B. Dupas *et al.*, "Evaluation of automated fundus photograph analysis algorithms for detecting microaneurysms, haemorrhages and exudates, and of a computer-assisted diagnostic system for grading diabetic retinopathy," *Diabetes & Metabolism*, vol. 36, no. 3, pp. 213–220, 2010.

[168] L. Tang, M. Niemeijer, J.M. Reinhardt, M.K. Garvin, M.D. and Abramoff, "Splat feature classification with application to retinal hemorrhage detection in fundus images," *IEEE transactions on medical imaging*, vol. 32, no. 2, pp. 364-375, 2013.

[169] R. Achanta, A. Shaji, K. Smith, A. Lucchi, P. Fua, and S. Süsstrunk, "SLIC superpixels compared to state-of-the-art superpixel methods," *IEEE Transactions on Pattern Analysis and Machine Intelligence*, vol. 34, no. 11, pp. 2274–2281, 2012.

[170] M. Al-Rawi, M. Qutaishat, and M. Arrar, "An improved matched filter for blood vessel detection of digital retinal images," *Computers in biology and medicine,* vol. 37, pp. 262-267, 2007.

[171] A. Levinshtein, A. Stere, K. N. Kutulakos, D. J. Fleet, S. J. Dickinson, and K. Siddiqi, "TurboPixels: Fast superpixels using geometric flows," *IEEE Transactions on Pattern Analysis and Machine Intelligence*, vol. 31, no. 12, pp. 2290–2297, 2009.

[172] American Academy of Ophthalmology, "International clinical diabetic retinopathy disease severity scale," *American Academy of Ophthalmology*, 2002.

[173] C. P. Wilkinson *et al.*, "Proposed international clinical diabetic retinopathy and diabetic macular edema disease severity scales," *Ophthalmology*, vol. 110, no. 9, pp. 1677–1682, 2003.

[174] A. Osareh, B. Shadgar, and R. Markham, "A computational-intelligence-based approach for detection of exudates in diabetic retinopathy images," *IEEE Transactions on Information Technology and Biomedicine*, vol. 13, no. 4, pp. 535–545, 2009.

[175] Kuivalainen, M., others, "Retinal image analysis using machine vision," Master's Thesis, Lappeenranta University of Technology, *Department of Information Technology,* Lappeenranta 2005.

[176] H. F. Jaafar, A. K. Nandi, and W. Al-Nuaimy, "Automated detection of red lesions from digital colour fundus photographs," *Proceedings of Annual International Conference on IEEE Engineering in Medicine and Biology Society EMBS*, pp. 6232–6235, 2011.

[177] T. Kauppi *et al.*, "Constructing benchmark databases and protocols for medical image analysis: Diabetic retinopathy," *Computational and Mathematical Methods in Medicine*, 2013.

[178] X. Zhang, G. Thibault, E. Decencière, G. Quellec, G. Cazuguel, et al., "Spatial normalization of eye fundus images," *ISBI 2012: 9th IEEE International Symposium on Biomedical Imaging*, 2012.

Appendix A

Segmentation Results

The mean sensitivity, specificity, accuracy results for blood vessels segmentation, bright and dark lesions segmentation are given in the appendix. The mean and standard deviation values are provided for each retinal fundus image database corresponding to different grades and types of lesions in diabetic retinopathy

Clinical DATABASE (2942 Retinal Images)						
Lesion type (No. of Images)		**Blood vessels Mean±S.D.**	**Exudates (study 1) Mean±S.D.**	**Bright lesions (study 2) Mean±S.D.**	**Dark lesions (study 2) Mean±S.D.**	**Grading Mean±S.D.**
No Diabetic Retinopathy (99 Retinal Images)						
No lesion (99)	SN	96.56±0.1233	99.24±1.287	95.23±1.0854	99.24±1.244	98.24±1.014
	SP	98.13±0.0232	99.43±0.277	97.76±1.3851	97.56±1.8549	99.64±1.414
	Acc	95.43±2.4231	98.44±1.512	96.85±1.274	96.35±1.204	97.34±1.245
Mild Diabetic Retinopathy (1263 Retinal Images)						
MA (373 Retinal Images)						
MA (373)	SN	94.86±2.1432	98.56±2.365	98.73±3.0874	93.47±2.154	100
	SP	99.23±3.1212	99.87±2.176	99.68±3.2854	95.45±2.241	99.63±2.154
	Acc	95.64±1.1121	99.67±2.174	99.24±4.951	92.54±1.24	99.85±2.124
HEM (135 Retinal Images)						
HEM (135)	SN	90.46±2.9432	97.56±1.365	98.76±2.1274	89.08±1.214	100
	SP	96.23±1.4232	98.87±1.204	97.35±2.3951	90.78±1.204	100
	Acc	94.36±2.1411	96.34±1.385	98.24±1.074	94.98±1.854	100
CWS (95 Retinal Images)						
CWS (95)	SN	91.23±1.0311	95.67±1.074	93.76±1.074	88.87±1.247	100
	SP	95.65±0.1231	99.26±1.025	95.45±1.3985	89.44±1.854	100
	Acc	94.96±0.7313	97.87±1.024	92.74±1.854	89.36±1.012	100
EXU (196 Retinal Images)						
EXU (196)	SN	92.89±2.1232	95.67±2.014	92.87±1.074	95.45±1.287	100
	SP	96.98±3.4275	99.56±1.0254	95.67±1.0398	98.65±1.854	99.32±1.823
	Acc	95.65±1.3913	95.34±1.398	93.85±1.274	93.64±1.041	99.89±1.972
MA + HEM (118 Retinal Images)						
MA+HEM (118)	SN	87.44±1.3135	98.46±0.351	98.76±1.8541	96.56±1.247	100
	SP	94.97±3.4245	97.32±0.324	97.35±1.3207	98.23±1.584	100
	Acc	97.34±2.3452	98.78±1.352	97.25±1.0854	94.45±1.041	100
CWS + EXU (3 Retinal Images)						
CWS+EXU (03)	SN	90.75±0.0454	98.67±0.0384	92.34±0.0214	98.87±0.025	100
	SP	98.65±0.0665	97.25±0.214	94.34±0.0258	99.53±0.084	100
	Acc	94.34±0.0655	96.75±0.017	92.68±0.0267	99.56±0.014	100
HEM + EXU (198 Retinal Images)						
HEM+EXU (198)	SN	86.66±2.3422	96.35±1.3241	94.75±1.074	95.57±1.074	98.56±2.104
	SP	95.98±2.1246	96.13±2.365	99.45±2.385	92.35±1.854	99.57±1.247
	Acc	92.44±3.5333	97.76±2.147	98.36±2.174	94.57±1.021	99.74±1.014
MA + CWS (22 Retinal Images)						
MA+CWS (22)	SN	91.31±1.0121	95.43±0.3258	93.76±0.074	95.63±1.210	99.57±0.108
	SP	90.98±1.7275	97.77±0.214	96.45±0.325	98.74±0.014	97.63±0.145
	Acc	91.76±3.3412	96.35±1.354	95.30±0.24	92.64±1.010	98.74±0.454
MA + HEM + CWS (10 Retinal Images)						

Contd…

MA+HEM+EXU (10)	SN	83.89±1.8563	93.87±0.325	92.70±0.074	89.98±0.04	97.13±0.014
	SP	93.54±1.4275	96.56±0.327	93.68±0.365	86.67±0.048	98.48±0.078
	Acc	91.53±1.1213	94.34±0.145	95.74±0.014	84.87±0.094	97.68±0.414
MA+ HEM + EXU (113 Retinal Images)						
MA+HEM+EXU (113)	SN	85.89±3.1231	95.75±1.0398	94.74±1.074	96.86±1.546	98.35±1.045
	SP	89.98±3.2211	99.65±1.2475	95.81±1.287	94.45±1.854	98.56±1.865
	Acc	93.41±2.1212	97.86±1.3968	93.21±1.074	85.76±1.0214	97.24±1.784
Moderate Diabetic Retinopathy (960 Retinal Images)						
HEM (162 Retinal Images)						
HEM (162)	SN	86.98±3.2321	98.45±2.2014	95.76±3.074	95.45±2.415	99.87±2.543
	SP	90.65±1.9832	99.75±2.0241	97.45±2.174	98.76±1.854	98.36±2.634
	Acc	92.86±2.4212	97.89±1.9684	96.35±2.017	95.54±3.154	99.46±2.523
CWS (98 Retinal Images)						
CWS (98)	SN	88.33±2.3167	95.98±1.3287	90.64±1.98	97.75±1.615	100
	SP	90.99±2.1865	99.77±1.2074	92.67±1.54	98.75±1.06	100
	Acc	92.67±1.5463	99.47±1.0274	93.36±1.34	97.74±1.064	100
EXU (208 Retinal Images)						
EXU (208)	SN	89.45±2.1654	94.75±2.3574	89.24±2.074	95.74±1.0521	100
	SP	91.67±3.4692	95.74±2.1027	88.64±2.358	97.68±1.854	100
	Acc	92.67±1.4531	93.93±2.3698	91.74±2.1463	96.35±1.0557	100
MA + HEM (106 Retinal Images)						
MA+HEM (106)	SN	89.23±2.1314	94.37±1.085	97.35±1.074	94.98±1.0247	98.86±2.564
	SP	93.21±2.6904	99.75±1.0274	92.76±1.352	92.46±2.041	98.74±3.0452
	Acc	92.41±1.9583	96.84±1.395	95.35±1.240	94.97±1.784	99.75±3.14
CWS + EXU (9 Retinal Images)						
CWS+EXU (09)	SN	80.89±0.3423	94.47±0.3214	93.74±0.0541	98.34±0.0451	97.60±0.785
	SP	91.04±0.3232	98.85±0.0284	95.56±0.0128	99.67±0.085	98.75±0.0141
	Acc	96.42±0.0645	94.38±0.0241	92.35±0.047	99.45±0.0485	98.56±0.0241
HEM + EXU (205 Retinal Images)						
HEM+EXU (205)	SN	84.44±3.4924	96.85±2.3851	94.09±2.0174	89.67±2.864	98.07±2.154
	SP	93.93±3.0932	97.84±2.174	93.89±2.174	86.47±2.741	96.63±2.7854
	Acc	94.36±1.4242	94.37±2.385	92.97±2.3258	84.89±2.7412	97.21±2.451
MA + CWS (35 Retinal Images)						
MA+CWS (35)	SN	85.89±3.1231	92.75±1.047	91.97±0.145	92.67±1.854	95.86±1.74
	SP	89.98±3.2211	99.75±1.025	93.86±0.358	94.75±1.074	96.47±1.05
	Acc	93.41±2.1212	94.37±0.954	92.68±1.124	92.47±0.71	97.47±0.41
MA + HEM + CWS (14 Retinal Images)						
MA+HEM+CWS (14)	SN	90.31±0.3231	94.76±0.2174	89.04±0.385	89.47±0.784	99.84±0.7854
	SP	94.33±0.3923	99.46±1.3654	90.25±0.014	88.47±0.89	98.65±0.724
	Acc	95.92±0.1912	98.85±0.984	93.36±0.214	91.85±0.074	97.34±0.711
MA+ HEM + EXU (116 Retinal Images)						
MA+HEM+EXU (116)	SN	89.01±1.1212	95.73±1.9854	96.68±1.074	94.85±1.074	100
	SP	92.78±2.1931	99.75±1.3574	94.46±1.258	96.75±1.854	100
	Acc	92.43±1.1903	99.63±1.3684	96.09±1.240	93.89±1.741	100
CWS + HEM + EXU (5 Retinal Images)						
CWS+HEM+EXU (05)	SN	87.89±0.9344	93.74±0.321	96.60±0.021	89.85±0.017	98.76±0.025
	SP	90.92±0.2121	98.75±0.0174	96.86±0.0014	86.63±0.254	97.74±0.014
	Acc	91.83±0.0122	97.36±0.0285	93.91±0.074	84.85±0.014	96.85±0.074
MA+ HEM + CWS + EXU (2 Retinal Images)						
MA+HEM+CWS+EXU (02)	SN	84.91±0.0012	95.46±0.0012	82.98±0.0054	86.75±0.0001	95.56±0.045
	SP	92.91±0.0215	99.74±0.047	87.67±0.074	89.75±0.085	97.88±0.041
	Acc	94.91±0.0121	95.48±0.014	81.90±0.014	87.85±0.014	96.85±0.075
Severe Diabetic Retinopathy (620 Retinal Images)						
HEM (87 Retinal Images)						
HEM	SN	84.43±1.3232	97.25±1.0247	97.97±1.0854	79.34±1.075	94.98±1.087

Contd…

(87)	SP	96.68±2.0957	99.17±1.028	93.87±1.8547	74.24±1.8554	95.68±1.0574
	Acc	92.18±1.0936	95.08±1.8274	95.56±1.632	81.56±1.047	96.63±1.584
CWS (93 Retinal Images)						
CWS	SN	88.33±1.9838	95.08±1.0174	87.83±1.074	98.75±1.327	93.36±1.274
(93)	SP	98.32±1.9382	99.45±1.685	82.24±1.365	99.75±1.740	94.64±1.854
	Acc	94.67±1.8973	99.75±1.354	90.87±1.241	99.35±1.048	93.23±1.027
EXU (87 Retinal Images)						
EXU	SN	82.98±1.9288	94.24±1.874	89.08±0.074	95.67±1.546	100
(87)	SP	97.92±1.0873	97.34±1.638	85.70±1.385	97.54±1.287	100
	Acc	94.12±0.9832	95.54±2.147	84.68±1.098	96.64±1.07	100
MA + HEM (99 Retinal Images)						
MA+HEM	SN	81.53±0.9871	95.45±2.174	98.71±1.288	92.65±1.07	96.94±1.25
(99)	SP	95.72±1.9438	99.87±2.3698	99.23±1.074	94.45±1.45	94.76±1.07
	Acc	90.84±1.7822	98.12±2.258	99.65±1.385	92.34±1.74	93.45±1.2458
CWS + EXU (4 Retinal Images)						
CWS+EXU	SN	79.93±0.0323	95.09±0.2147	90.87±0.0041	91.76±0.056	99.43±0.047
(04)	SP	89.92±0.0281	98.78±0.385	84.56±0.0078	94.56±0.045	98.87±0.14
	Acc	89.99±0.0912	96.64±0.965	89.98±0.085	92.35±0.74	98.12±0.46
HEM + EXU (90 Retinal Images)						
HEM+EXU	SN	83.94±1.0822	95.34±1.0857	79.23±1.074	89.35±1.74	97.64±1.75
(90)	SP	93.18±1.882	99.24±1.398	86.54±1.35	88.56±1.08	97.76±1.74
	Acc	92.13±1.0483	99.65±2.385	90.43±1.74	91.35±1.04	96.45±1.85
MA + CWS (31 Retinal Images)						
MA+CWS	SN	88.19±0.3293	95.76±0.2874	87.54±1.074	89.56±1.24	97.63±1.24
(31)	SP	96.24±1.3913	99.45±0.3694	93.35±1.36	86.46±1.285	96.54±1.74
	Acc	95.28±1.0328	97.75±0.9874	96.35±1.85	84.76±0.74	96.23±1.04
MA + HEM + CWS (14 Retinal Images)						
MA+HEM+CWS	SN	85.28±0.2831	95.76±0.385	85.67±0.074	92.67±0.014	96.73±0.74
(14)	SP	94.42±0.0131	99.34±0.274	93.45±0.085	94.46±0.850	97.64±0.14
	Acc	93.42±0.3213	95.74±0.4127	96.35±0.074	91.35±0.84	97.25±0.42
MA+ HEM + EXU (104 Retinal Images)						
MA+HEM+EXU	SN	87.32±1.0381	95.23±2.7841	87.89±1.078	92.65±2.751	93.95±1.5275
(104)	SP	95.23±1.0931	99.65±2.0174	94.75±1.258	94.43±2.155	94.68±2.01
	Acc	94.13±0.7943	99.35±1.0874	94.67±1.074	92.64±1.085	93.08±2.017
CWS + HEM + EXU (3 Retinal Images)						
CWS+HEM+EXU	SN	87.98±0.0812	96.65±0.3854	90.46±0.074	79.65±0.784	99.86±0.842
(03)	SP	97.93±0.0123	99.45±0.741	97.75±0.0025	86.35±0.745	100
	Acc	95.82±0.0371	97.87±0.9854	90.35±0.0041	90.67±0.754	99.23±0.754
MA+ CWS + EXU (1 Retinal Images)						
MA+CWS+EXU	SN	84.39±0.00	97.09±0.00	85.09±0.00	91.34±0.00	97.83±0.00
(01)	SP	98.38±0.00	96.89±0.00	89.86±0.00	94.65±0.00	96.86±0.00
	Acc	95.29±0.00	98.08±0.00	87.87±0.00	92.74±0.00	96.24±0.00
MA+ HEM + CWS + EXU (7 Retinal Images)						
MA+HEM+CWS+EXU	SN	85.32±0.0381	93.76±0.0174	87.85±0.074	86.35±0.0241	98.06±0.84
(07)	SP	95.32±0.1031	99.80±0.085	85.74±0.098	83.35±0.078	94.97±0.74
	Acc	93.49±0.1391	96.45±0.0836	89.86±0.085	85.73±0.8544	92.64±0.784

DRIVE DATABASE (40 Retinal Images)						
Lesion type (No. of Images)		**Blood vessels Mean±S.D.**	**Exudates (study 1) Mean±S.D.**	**Bright lesions (study 2) Mean±S.D.**	**Dark lesions (study 2) Mean±S.D.**	**Grading Mean±S.D.**
No Diabetic Retinopathy (33 Retinal Images)						
No lesion	SN	91.39±0.2918	99.67±0.0241	95.85±0.074	98.78±0.741	100
(33)	SP	98.32±0.3392	98.56±0.0124	97.96±0.41	99.45±0.987	100
	Acc	95.23±0.3232	98.46±0.175	96.46±0.85	99.76±0.274	100

Contd…

Mild Diabetic Retinopathy (2 Retinal Images)						
Only MA (02)	SN	89.03±0.003	99.23±0.041	98.96±0.074	95.58±0.085	100
	SP	98.12±0.011	97.22±0.002	96.01±0.025	97.78±0.065	100
	Acc	95.39±0.0004	98.88±0.014	95.96±0.07	96.82±0.041	100
Moderate Diabetic Retinopathy (5 Retinal Images)						
MA/HEM (02)	SN	88.01±0.004	95.98±0.052	98.96±0.078	91.51±0.0458	98.47±0.0411
	SP	97.84±0.012	97.75±0.045	99.35±0.041	94.78±0.0241	99. 01±0.065
	Acc	94.92±0.048	98.06±0.054	99.64±0.045	92.45±0.045	89.72±0.044
EXU/CWS (02)	SN	87.12±0.0043	96.87±0.0021	95.78±0.01	95.01±0.074	98.14±0.028
	SP	82.18±0.024	94.46±0.014	99.78±0.028	97.78±0.084	99. 01±0.032
	Acc	92.72±0.0248	95.66±0.018	94.75±0.004	96.24±0.024	98.77±0.054
Dark/Bright (01)	SN	87.83±0.00	97.76±0.00	92.01±0.00	89.01±0.00	97.47±0.00
	SP	95.17±0.00	95.54±0.00	95.62±0.00	86.71±0.00	96.78±0.00
	Acc	95.93±0.00	94.23±0.00	91.76±0.00	84.89±0.00	96.65±0.00
STARE DATABASE (184 Retinal Images)						
Lesion type (No. of Images)		**Blood vessels Mean±S.D.**	**Exudates (study 1) Mean±S.D.**	**Bright lesions (study 2) Mean±S.D.**	**Dark lesions (study 2) Mean±S.D.**	**Grading Mean±S.D.**
No Diabetic Retinopathy (25 Retinal Images)						
No lesion (25)	SN	84.87±0.0124	99.65±0.110	98.56±0.147	97.78±0.0454	100
	SP	99.54±0.045	99.34±0.141	98.78±0.5847	90.58±0.0147	100
	Acc	96.65±0.054	98.35±0.184	96.64±0.451	97.53±0.1524	100
Mild Diabetic Retinopathy (83 Retinal Images)						
Only MA (72)	SN	84.63±1.017	99.65±1.054	98.67±1.541	95.84±1.542	98.23±1.045
	SP	98.36±1.0274	99.34±1.4524	98.48±1.4521	97.01±2.041	99.01±1.7475
	Acc	95.46±1.758	99.66±1.354	94.97±1.2015	96.71±2.214	89.34±1.512
MA+HEM (11)	SN	82.75±0.174	97.87±0.214	95.78±0.212	79.78±0.45	100
	SP	96.35±0.424	98.54±0.1245	97.74±0.258	86.78±0.0152	100
	Acc	94.44±0.454	97.43±0.242	96.01±0.7446	90.29±0.021	100
Moderate Diabetic Retinopathy (43 Retinal Images)						
MA/HEM (23)	SN	83.46±0.142	98.65±0.251	97.68±0.144	95.32±0.5241	95.11±0.212
	SP	95.45±0.154	97.33±0.4558	90.41±0.2421	98.23±0.4521	98.78±0.217
	Acc	93.09±0.554	97.54±0.155	97.30±0.225	92.84±0.024	97.55±0.245
EXU/CWS (12)	SN	84.75±0.014	94.23±0.014	89.78±0.025	98.08±0.045	93.45±0.0127
	SP	96.64±0.110	93.76±0.140	86.78±0.0212	99.23±0.0475	95.01±0.027
	Acc	93.87±0.0127	96.46±0.212	82.87±0.0.45	99.07±0.0124	96.51±0.014
Dark/Bright (08)	SN	85.90±0.078	97.74±0.075	87.48±0.055	92.00±0.045	97.84±0.047
	SP	99.75±0.0124	96.73±0.047	85.01±0.0475	94.48±0.0454	98.64±0.054
	Acc	96.43±0.045	95.97±0.065	83.85±0.054	92.51±0.104	99.21±0.054
Severe Diabetic Retinopathy (33 Retinal Images)						
MA/HEM (03)	SN	85.09±0.0041	97.35±0.0054	98.75±0.044	96.47±0.041	97.64±0.0154
	SP	97.75±0.00235	97.48±0.0042	99.04±0.041	93.23±0.054	96.48±0.0454
	Acc	99.78±0.0054	96.83±0.0145	99.23±0.0425	92.41±0.045	96.74±0.045
EXU/CWS (11)	SN	85.34±0.124	95.84±0.456	78.70±0.1254	97.10±0.128	94.74±0.045
	SP	99.64±0.454	94.73±0.365	89.78±0.127	90.58±0.078	97. 78±0.057
	Acc	95.75±0.045	94.98±0.127	86.54±0.879	97.48±0.045	99.71±0.0554
Dark and Bright (19)	SN	82.97±1.0245	96.23±0.1452	81.21±0.214	89.78±0.245	98.48±0.512
	SP	94.35±1.045	96.86±0.452	86.01±0.247	86.78±0.4586	96.11±0.412
	Acc	93.36±0.452	94.24±0.5745	84.23±0.1747	84.56±0.5452	98.54±0.241
DIARETDB DATABASE (219 Retinal Images)						
Lesion type (No. of Images)		**Blood vessels Mean±S.D.**	**Exudates (study 1) Mean±S.D.**	**Bright lesions (study 2) Mean±S.D.**	**Dark lesions (study 2) Mean±S.D.**	**Grading Mean±S.D.**

Contd…

No Diabetic Retinopathy (25 Retinal Images)						
No lesion (25)	SN	88.25±1.021	86.45±1.784	98.57±1.254	97.78±1.045	94.65±1.027
	SP	98.35±1.241	97.78±1.241	98.54±1.015	90.48±1.24	99 23±1.274
	Acc	94.86±1.274	95.57±1.047	99.37±1.27	97.45±1.785	96.12±1.528
Mild Diabetic Retinopathy (141 Retinal Images)						
Only MA (98)	SN	87.24±1.547	97.35±1.027	98.45±1.285	89.54±1.274	97.71±1.0174
	SP	97.51±1.044	90.45±1.024	99.78±1.274	88.42±1.024	98.45±1.274
	Acc	93.65±1.274	97.48±1.274	99.78±1.365	91.84±1.274	95.86±1.965
MA+HEM (43)	SN	86.45±0.274	94.78±1.024	95.23±0.274	89.05±0.754	92.21±0.844
	SP	96.01±0.874	97.23±1.2710	97.75±0.741	86.78±0.574	93.45±0.544
	Acc	93.57±0.844	96.04±0.985	96.12±0.844	84.45±0.245	89.78±0.214
Moderate Diabetic Retinopathy (34 Retinal Images)						
MA/HEM (06)	SN	85.04±0.041	84.47±0.154	97.54±0.064	79.78±0.054	97.32±0.075
	SP	95.45±0.078	90.48±0.014	99.24±0.045	86.54±0.024	95.78±0.047
	Acc	92.45±0.0758	89.24±0.0285	97.48±0.024	90.45±0.054	97.45±0.0247
EXU/CWS (20)	SN	86.14±0.0174	68.57±0.0258	93.34±0.078	95.86±0.041	91.78±0.074
	SP	93.45±0.014	85.86±0.025	96.78±0.0222	97.47±0.054	92.78±0.087
	Acc	91.87±0.078	83.14±0.078	93.01±0.085	96.57±0.0748	96.21±0.054
Dark and Bright (08)	SN	87.35±0.074	83.54±0.047	90.85±0.0365	91.27±0.0574	92.89±0.054
	SP	94.15±0.054	85.52±0.077	92.45±0.087	94.48±0.045	93.68±0.041
	Acc	93.78±0.025	80.17±0.07	91.75±0.078	92.45±0.0477	87.01±0.084
Severe Diabetic Retinopathy (19 Retinal Images)						
MA/HEM (02)	SN	88.25±0.001	70.72±0.007	97.01±0.04	92.10±0.074	97.64±0.024
	SP	97.15±0.004	85.86±0.04	94.78±0.085	94.23±0.070	96.04±0.014
	Acc	95.28±0.045	82.14±0.004	92.85±0.075	92.04±0.058	96.17±0.058
EXU/CWS (04)	SN	87.84±0.027	80.17±0.0584	95.45±0.078	98.21±0.074	92.42±0.078
	SP	93.10±0.085	89.23±0.074	97.78±0.085	99.77±0.096	96.23±0.024
	Acc	92.47±0.074	91.78±0.075	96.55±0.078	99.74±0.04	87.47±0.064
Dark and Bright (13)	SN	84.58±0.148	74.14±0.175	96.78±0.174	98.04±0.741	90.46±0.174
	SP	93.27±0.0174	91.17±0.741	90.47±0.457	98.48±0.144	78.14±0.474
	Acc	89.05±0.755	88.87±0.475	90.14±0.743	96.21±0.754	90.05±0.487
MESSIDOR DATABASE (1200 Retinal Images)						
Lesion type (No. of Images)		**Blood vessels Mean±S.D.**	**Exudates (study 1) Mean±S.D.**	**Bright lesions (study 2) Mean±S.D.**	**Dark lesions (study 2) Mean±S.D.**	**Grading Mean±S.D.**
No Diabetic Retinopathy (540 Retinal Images)						
No lesion (540)	SN	90.25±3.044	90.24±3.241	93.24±3.215	99.24±3.9475	97.25±3.574
	SP	99.24±3.2154	95.75±2.547	99.23±3.744	97.24±3.4557	98.42±3.784
	Acc	95.44±4.242	94.42±3.287	97.78±2.584	98.01±3.527	96.14±3.478
Mild Diabetic Retinopathy (153 Retinal Images)						
Only MA (89)	SN	89.21±1.234	95.45±1.274	98.57±1.745	92.78±1.745	87.84±1.274
	SP	98.54±1.204	95.78±1.247	99.86±1.247	94.86±1.244	97.48±1.584
	Acc	95. 86±1.0274	97.24±1.965	99.48±1.357	92.45±1.365	93.45±1.345
MA+HEM (64)	SN	88.01±1.024	94.51±1.741	95.58±1.711	79.87±1.045	88.21±1.074
	SP	97.04±1.274	95.78±1.357	97.23±1.274	86.78±1.274	92.47±1.027
	Acc	95.48±1.385	95.27±1.274	96.78±1.287	90.54±1.024	95.54±1.278
Moderate Diabetic Retinopathy (247 Retinal Images)						
MA/HEM (23)	SN	87.87±0.014	94.86±0.147	97.69±0.255	89.75±0.254	88.87±0.584
	SP	97.54±0.147	98.04±0.856	98.76±0.575	86.78±0.8745	86.23±0.1578
	Acc	94.21±0.4557	96.14±0.274	97.12±0.147	84.45±0.542	89.47±0.2148
EXU/CWS (98)	SN	84.87±1.784	74.78±1.274	91.87±1.0475	93.78±1.854	87.48±1.057
	SP	93.65±1.545	89.46±1.895	94.86±1.7854	99.54±1.078	97.75±1.74
	Acc	92.45±1.274	85.45±1.024	92.98±1.027	97.15±1.044	94.41±1.457

Contd…

Dark and Bright (143)	SN	86.86±2.5487	75.23±3.57	89.87±2.544	97.51±2.05	89.64±2.0825
	SP	96.21±3.245	85.48±3.784	90.64±2.870	94.78±2.698	87.78±2.085
	Acc	93.24±2.875	83.64±3.875	89.86±2.457	94.87±2.054	89.54±2.520
Severe Diabetic Retinopathy (260 Retinal Images).						
MA/HEM (19)	SN	88.45±0.2578	85.14±0.555	93.01±0.255	89.78±0.6556	97.21±0.085
	SP	97.21±0.5455	90.23±0.074	99.78±0.745	88.01±0.874	96.45±0.327
	Acc	95.01±0.1475	94.57±0.325	97.87±0.211	91.54±0.585	96.82±0.248
EXU/CWS (98)	SN	95.85±1.0278	75.48±1.0274	95.76±1.259	98.11±1.085	90.21±1.652
	SP	93.54±1.274	83.48±1.985	97.42±1.0274	99.23±1.5874	95.55±1.274
	Acc	91.01±1.028	81.86±1.287	96.01±1.078	99.01±1.274	93.45±1.658
Dark and Bright (143)	SN	88.87±2.385	81.85±1.965	79.87±1.385	91.45±1.654	90.87±2.174
	SP	98.12±2.0174	90.45±1.274	90.44±1.74	94.05±1.257	91.86±2.385
	Acc	96.24±2.014	86.32±1.0285	89.54±1.095	92.48±1.274	87.98±2.072

e-Optha DATABASE (463 Retinal Images)						
Lesion type (No. of Images)		**Blood vessels Mean±S.D.**	**Exudates (study 1) Mean±S.D.**	**Bright lesions (study 2) Mean±S.D.**	**Dark lesions (study 2) Mean±S.D.**	**Grading Mean±S.D.**
No Diabetic Retinopathy (268 Retinal Images)						
No lesion (268)	SN	90.54±2.074	93.86±2.0174	93.45±2.365	98.07±2.745	94.74±2.874
	SP	98.86±3.274	99.78±2.745	98.21±2.745	99.01±2.654	96.47±2.654
	Acc	95.55±2.968	97.23±2.878	96.18±2.985	99.16±2.331	97.65±2.214
Mild Diabetic Retinopathy (136 Retinal Images)						
Only MA (104)	SN	87.54±1.285	90.32±1.457	93.45±1.074	92.54±1.085	97.85±1.074
	SP	98.58±1.274	97.86±1.124	99.78±1.385	94.78±1.741	94.46±1.647
	Acc	94.21±1.352	95.33±1.985	97.12±1.0147	92.46±1.952	97.23±1.325
MA+HEM (32)	SN	87.98±0.96	92.76±0.528	95.31±1.074	79.23±1.0285	98.78±0.074
	SP	98.54±0.854	98.48±0.965	97.43±0.985	86.86±1.074	96.54±0.985
	Acc	94.58±0.574	96.24±1.027	96.32±0.2745	90.48±1.241	97.87±1.052
Moderate Diabetic Retinopathy (32 Retinal Images)						
MA/HEM (09)	SN	89.54±0.074	94.75±0.096	98.55±0.074	89.76±0.087	95.87±0.041
	SP	98.64±0.085	97.86±0.088	99.23±0.052	88.45±0.041	97.54±0.074
	Acc	93.42±0.078	91.57±0.054	99.57±0.014	91.64±0.085	95.87±0.0985
EXU/CWS (23)	SN	89.78±0.521	75.23±0.041	89.01±0.0451	93.45±0.0214	98.54±0.0127
	SP	98.45±0.85	89.42±0.0865	93.46±0.0985	99.12±0.032	96.86±0.0352
	Acc	96.54±0.074	86.16±0.0451	94.57±0.0741	97.23±0.0154	97.87±0.055
Severe Diabetic Retinopathy (27 Retinal Images)						
MA/HEM (03)	SN	84.24±0.021	89.48±0.054	92.86±0.074	89.86±0.041	97.78±0.041
	SP	95.78±0.012	96.58±0.021	94.76±0.051	88.01±0.055	99.65±0.047
	Acc	93.78±0.098	90.54±0.035	92.48±0.098	90.75±0.036	96.45±0.041
EXU/CWS (24)	SN	86.97±0.74	81.86±0.52	79.85±0.385	98.84±0.854	91.86±0.741
	SP	98.78±0.41	96.76±0.071	84.54±0.754	99.58±0.341	94.48±0.364
	Acc	94.45±0.85	89.87±0.74	86.23±0.174	99.57±0.354	96.24±0.241

Appendix B

Sample Images

The example images from composite database and their corresponding results are given below:

(i) Enhancement results on sample images are shown below:

Image class	Original image	Enhanced image
Healthy (clinical)	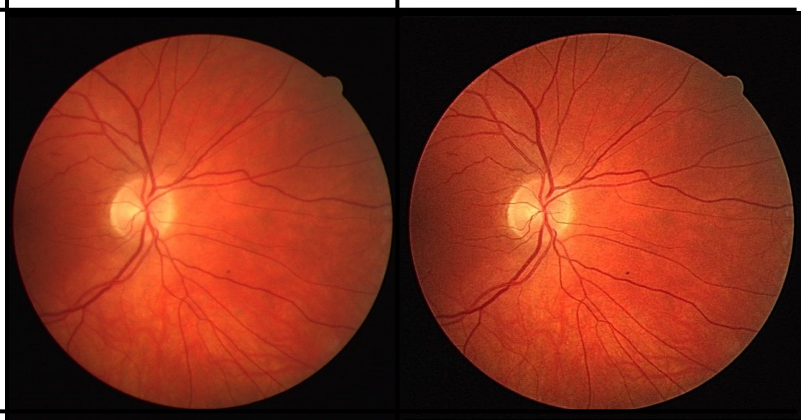	
Healthy (DRIVE)	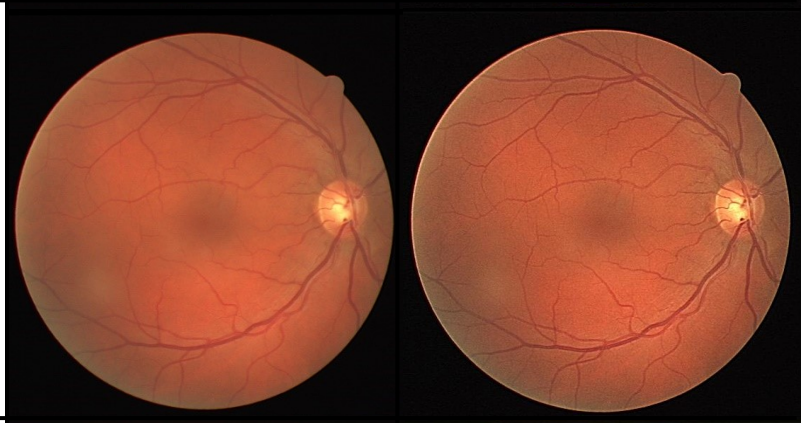	
Moderate DR (STARE)	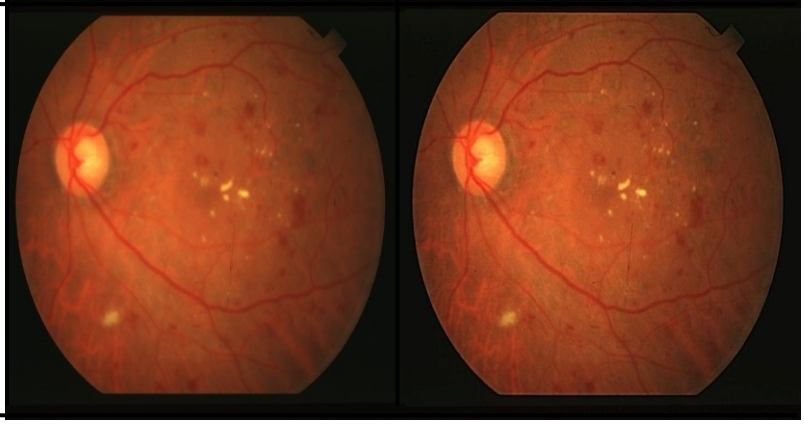	

Image class	Original image	Enhanced image
Severe DR (Clinical)	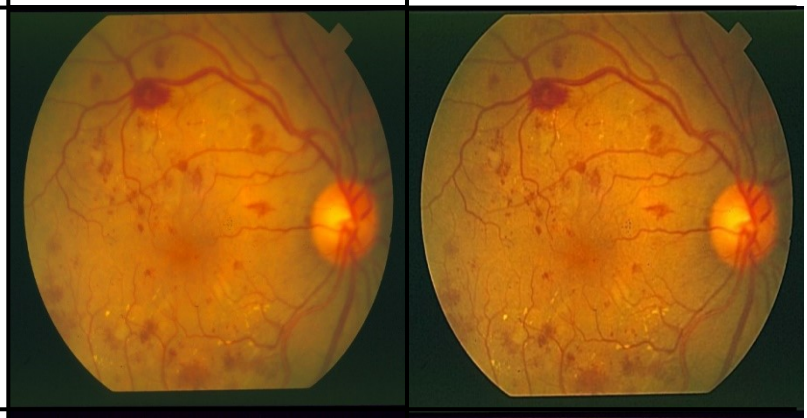	
Mild DR (DIARETDB)	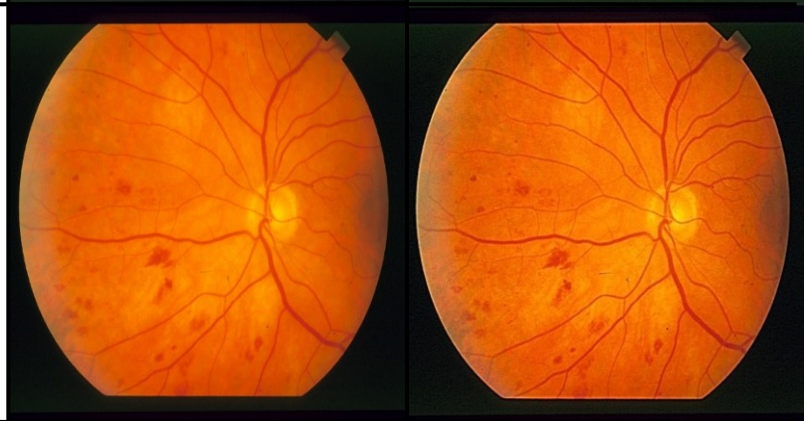	
Severe DR (Clinical)	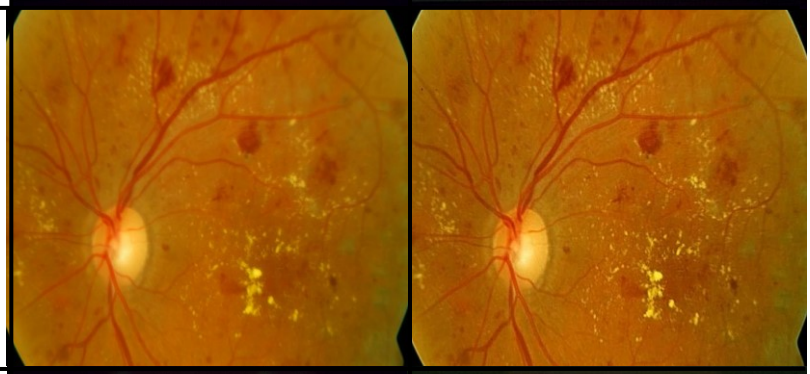	
Severe DR (STARE)	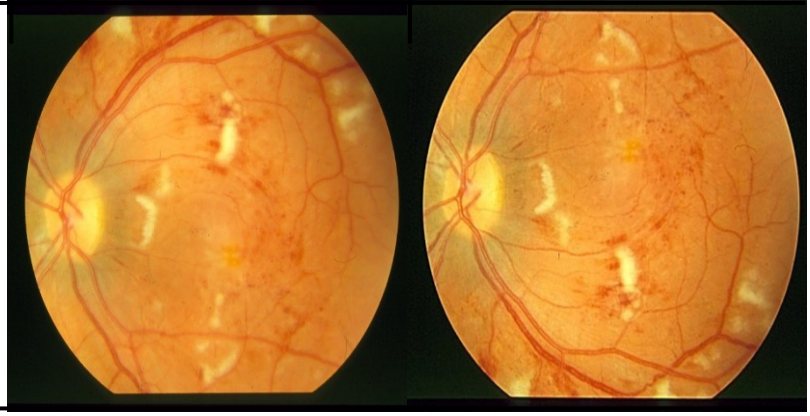	

(ii) Optic disk detection results on sample images are shown below:

Image class	Original image	Segmented optic disk
Moderate DR (clinical)		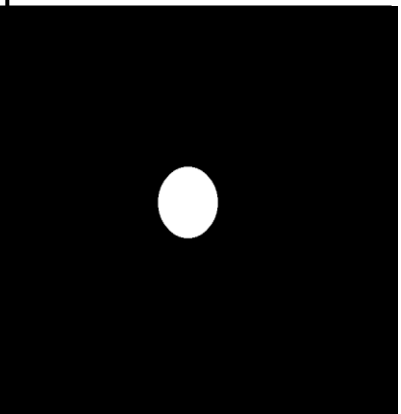
Severe DR (STARE)		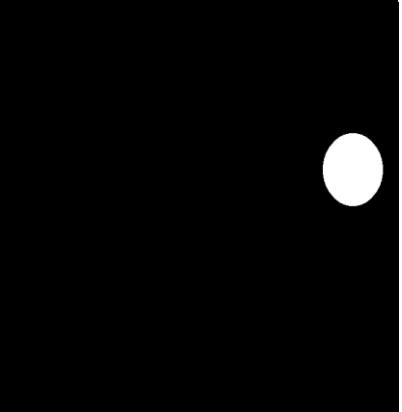
Moderate DR (STARE)		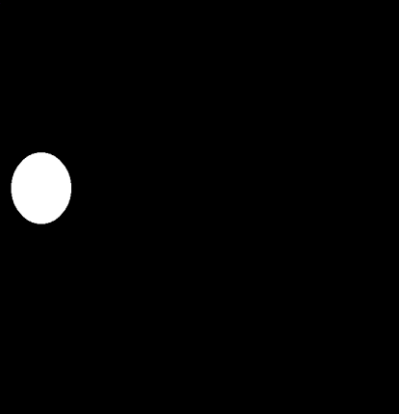
Moderate DR (e-Optha)		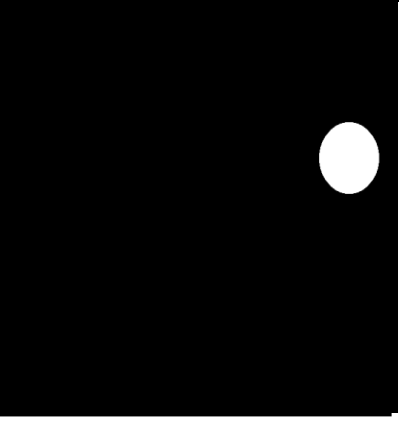

Image class	Original image	Segmented optic disk
Severe DR (e-Optha)		
Moderate DR (DIARETDB)		
Severe DR (STARE)		
Moderate DR (Clinical)		

(iii) Blood vessels segmentation results on sample images are shown below:

Image class	Original image	Segmented blood vessels
Mild DR (Clinical)		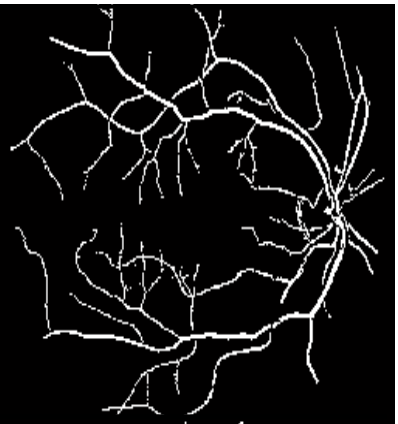
Mild DR (MESSIDOR)		
Moderate DR (STARE)		
Moderate DR (STARE)	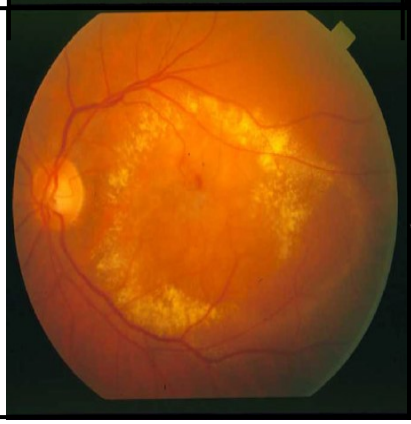	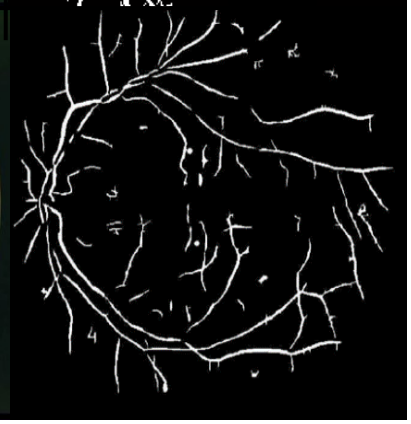

Image class	Original image	Segmented blood vessels
Healthy (Clinical)	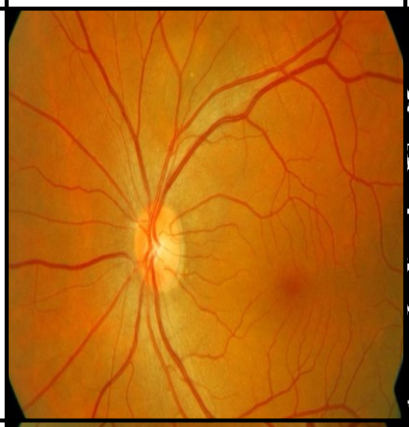	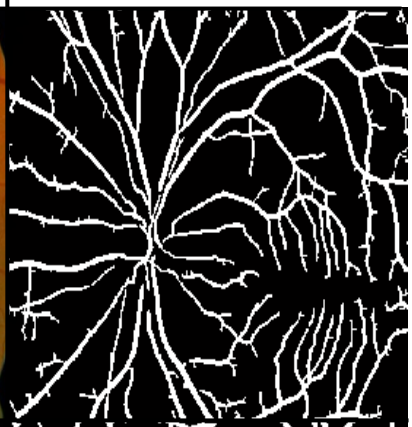
Healthy (Clinical)		
Severe DR (DIABRETDB)		
Mild DR (DRIVE)		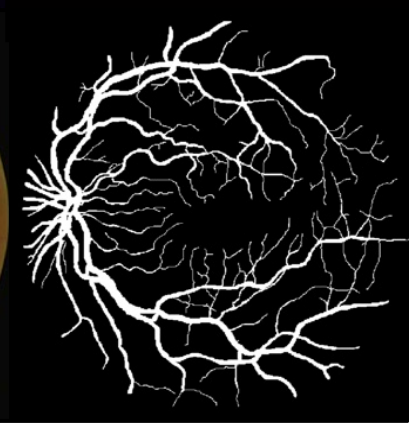

(iv) Bright lesions segmentation results on sample images are shown below:

Image class	Original image	Segmented lesions
Severe DR (STARE)		
Moderate DR (STARE)	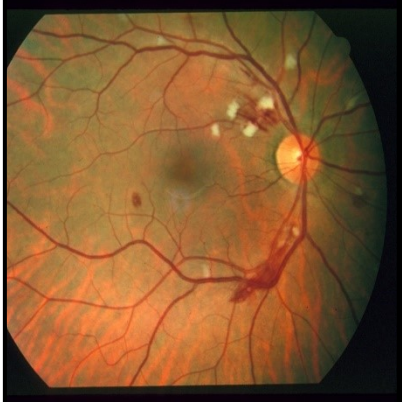	
Moderate DR (e-Optha)	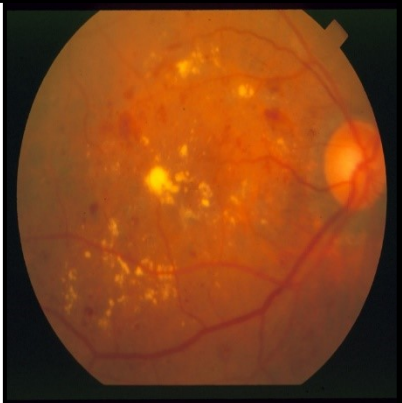	
Severe DR (STARE)		

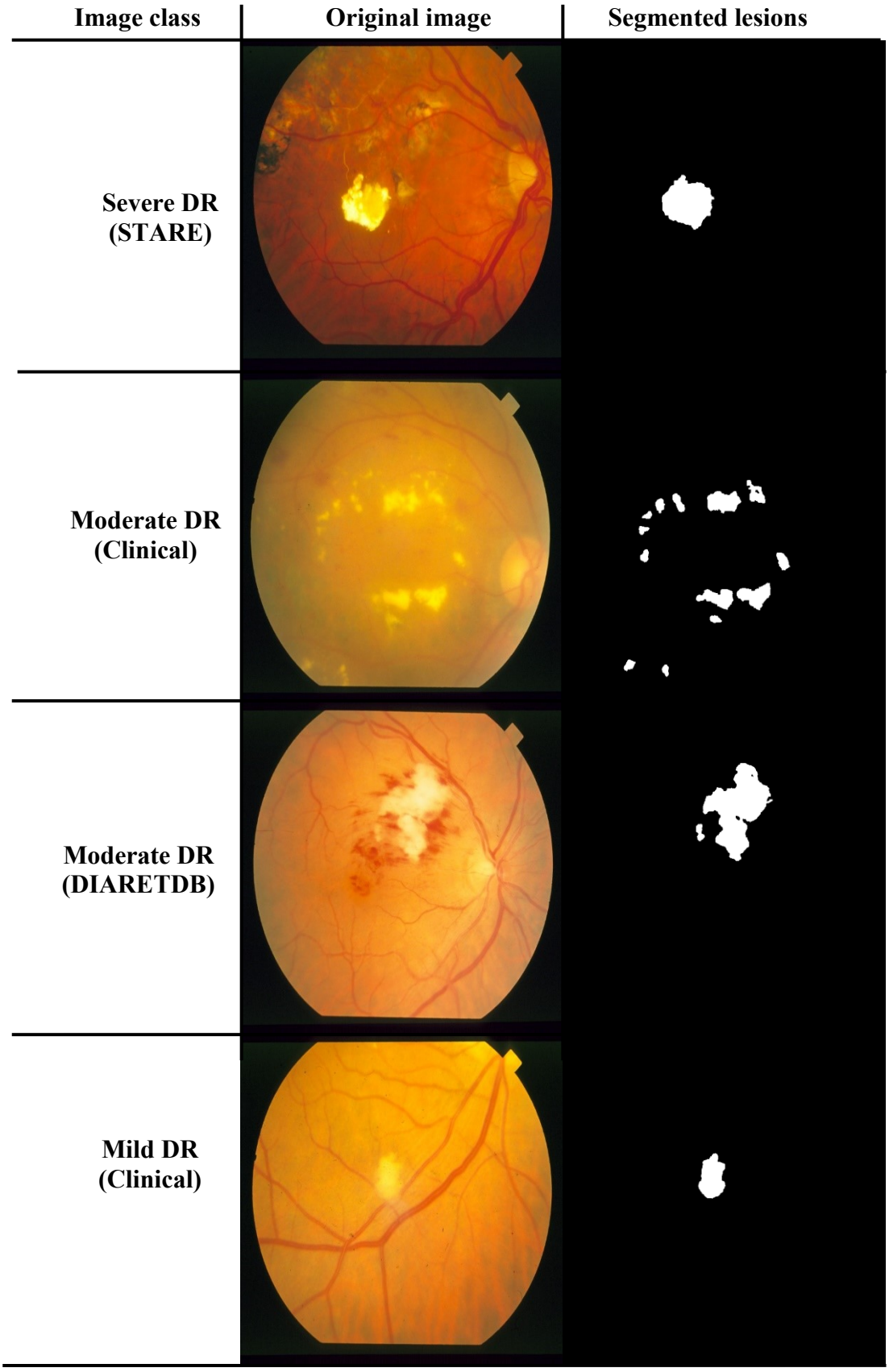
Image class
Original image
Segmented lesions
Severe DR (STARE)
Moderate DR (Clinical)
Moderate DR (DIARETDB)
Mild DR (Clinical)

(v) Dark Lesions segmentation results on sample images are shown below:

Image class	Original image	Segmented lesions
Severe DR (e-Optha)		
Mild DR (DIARETDB)		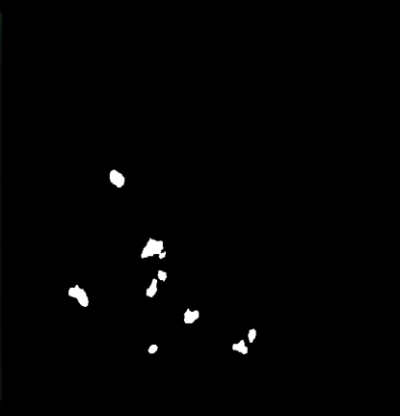
Severe DR (Clinical)	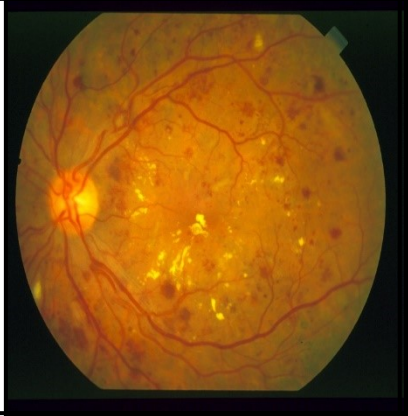	
Mild DR (e-Optha)		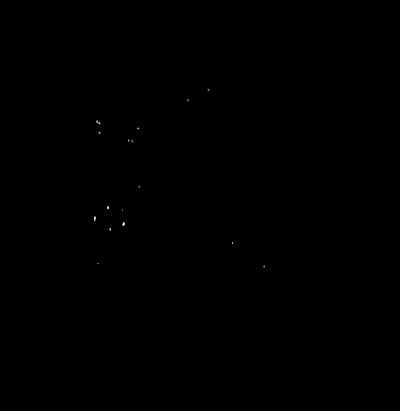

Image class	Original image	Segmented lesions
Mild DR (STARE)		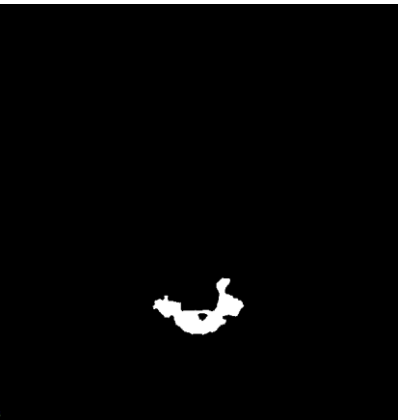
Severe DR (STARE)		
Moderate DR (Clinical)		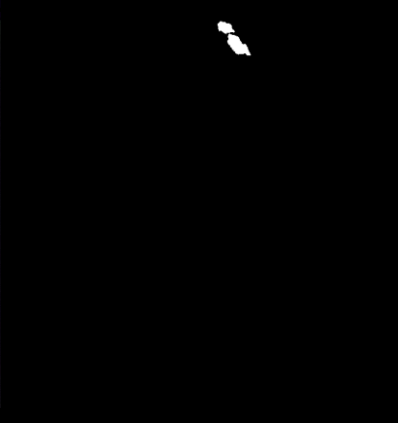
Mild DR (e-Optha)		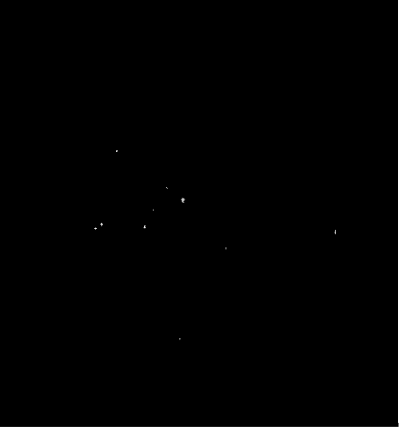

List of publications from present work

(i) J. Kaur, D. Mittal, "**A generalized method for the detection of vascular structure in pathological retinal images**," Biocybernetics and Biomedical Engineering, vol. 15, no. 1, pp. 184-200, 2017.
https://doi.org/10.1016/j.bbe.2016.09.002
Publisher: Elsevier
Impact factor: 1.374

(ii) J. Kaur, D. Mittal, "**A generalized method for the segmentation of exudates from pathological retinal fundus images**," Biocybernetics and Biomedical Engineering, vol. 38, no. 1, pp. 27-53, 2018.
https://doi.org/10.1016/j.bbe.2017.10.003
Publisher: Elsevier
Impact factor: 1.374

(iii) J. Kaur, D. Mittal, "**Estimation of severity level of non-proliferative diabetic retinopathy for clinical aid**," Biocybernetics and Biomedical Engineering, vol. 38, no. 3, pp. 708-732, 2018.
https://doi.org/10.1016/j.bbe.2018.05.006
Publisher: Elsevier
Impact factor: 1.374

(iv) J. Kaur, D. Mittal, "**Construction of benchmark retinal image database for diabetic retinopathy analysis**," Biomedical Engineering (Submitted after minor revision)
Publisher: De Gruyter
Impact factor: 1.096

(v) J. Kaur, D. Mittal, "**Diabetic retinopathy diagnosis using computer-aided fundus image analysis – A review**," Artificial Intelligence Reviews. (Under Review)
Publisher: Springer
Impact factor: 3.814

(vi) J. Kaur, D. Mittal, "**Segmentation and Measurement of Exudates in Fundus Images of the Retina for Detection of Retinal**," Journal of Biomedical Engineering and Medical Imaging, vol. 2, no. 1, pp. 27-38, 2015.
http://dx.doi.org/10.14738/jbemi. 21.987
Publisher: Society for Science and Education